Karlsruher Institut für Technologie

Linking Cosmology with Collider Phenomenology

Zur Erlangung des akademischen Grades eines

DOKTORS DER NATURWISSENSCHAFTEN

von der KIT-Fakultät für Physik
des Karlsruher Instituts für Technologie (KIT)

genehmigte

DISSERTATION

von

M.Sc. Jonas Müller

aus Karlsruhe

Referentin: Prof. Dr. M.Mühlleitner

Korreferent: PD Dr. S.Gieseke

Tag der mündlichen Prüfung: 22. Januar 2021

Eidesstattliche Versicherung gemäß § 13 Absatz 2 Ziffer 3 der Promotionsordnung des Karlsruher Instituts für Technologie (KIT) für die KIT-Fakultät für Physik:

1. Bei der eingereichten Dissertation zu dem Thema

   Linking Cosmology with Collider Phenomenology

   handelt es sich um meine eigenständig erbrachte Leistung.

2. Ich habe nur die angegebenen Quellen und Hilfsmittel benutzt und mich keiner unzulässigen Hilfe Dritter bedient. Insbesondere habe ich wörtlich oder sinngemäß aus anderen Werken übernommene Inhalte als solche kenntlich gemacht.

3. Die Arbeit oder Teile davon habe ich bislang nicht an einer Hochschule des In- oder Auslands als Bestandteil einer Prüfungs- oder Qualifikationsleistung vorgelegt.

4. Die Richtigkeit der vorstehenden Erklärungen bestätige ich.

5. Die Bedeutung der eidesstattlichen Versicherung und die strafrechtlichen Folgen einer unrichtigen oder unvollständigen eidesstattlichen Versicherung sind mir bekannt.

Ich versichere an Eides statt, dass ich nach bestem Wissen die reine Wahrheit erklärt und nichts verschwiegen habe.

Karlsruhe, den 05. Januar 2021

. . . . . .

(Müller Jonas)

For my parents and grandmother

Abstract

The discovery of the Higgs boson in 2012 was a major milestone of modern particle physics. The Higgs boson was the last puzzle piece of the Standard Model (SM) required for consistent description of all properties and interactions of the fundamental particles in terms of a quantum field theory. Up to now the SM was confirmed to a remarkable precision, however, the SM does not provide solutions to all open remaining questions of modern physics. Non-minimal extended Higgs sector are a promising approach to overcome certain open issues of the SM. Four different non-minimal extended Higgs sector models are considered in the context of this thesis.

We investigate the Pseudo-Nambu Goldstone Dark Matter and the Vector Dark Matter model as two possible extensions of the SM yielding a Dark Matter candidate. We calculate the electroweak next-to leading order corrections to the spin-independent cross-section for both models. We analyze the impact of the quantum corrections on the blind spots of the direct detection experiments and discuss the phenomenological consequences of the derived model parameter space. Furthermore, we compare different approaches to include the higher-order corrections and comment on related issues.

The parameter space of the Next-to-Minimal Two-Higgs Doublet model is explored with the additional requirement of a strong first-order electroweak phase transition. The interplay between the theoretical and experimental constraints as well as the electroweak phase transition narrows down the compatible parameter space of the model significantly. For a sufficient large and efficient parameter scan of the model parameters, the `C++ BSMPT` code was extended and further improved. The major update to the second release version `BSMPT v2` is published.

In addition, the possibility to calculate the produced baryon asymmetry of the universe in the Complex Two-Higgs doublet (C2HDM) model is included in `BSMPT v2`. Two non-local electroweak baryogenesis approaches are investigated and systematically compared within the C2HDM. We argue why the interplay between the constraints on the electric dipole moment, the requirement of an electroweak phase transition as well as a sufficient produced baryon asymmetry of the universe significantly reduces the viable parameter space of the C2HDM.

Zusammenfassung

Die Entdeckung des Higgs Bosons in 2012 war einer der grundlegenden Meilensteine der modernen Teilchenphysik. Das Higgs Boson war das letzte Puzzleteil des Standard Models (SM), das für eine konsistente Beschreibung aller Eigenschaften und Wechselwirkungen zwischen den fundamentalen Teilchen innerhalb einer Quantenfeldtheorie benötigt wurde. Bis zum heutigen Tag wurde das SM bis hin zu einer bemerkenswerten Präzession bestätigt, jedoch vermag das SM nicht alle offenen Fragen der modernen Physik zu beantworten. Nichtminimale Erweiterungen des Higgs Sektors liefern einen vielversprechenden Ansatz, um bestimmte offene Probleme des SM zu lösen. Innerhalb dieser Thesis werden insgesamt vier verschiedene Modelle mit nichtminimale Erweiterungen des Higgs Sektors betrachtet.
Als zwei mögliche SM Erweiterungen untersuchen wir das Pseudo-Nambu Goldstone Dunkle Materie und das Vektor Dunkle Materie Modell, welche jeweils einen Dunkle Materie Kandidaten liefern. Wir berechnen für beide Modelle die nächst führenden elektroschwachen Korrekturen zum Spin-unabhängigen Wirkungsquerschnittes. Wir analysieren den Einfluss der Quantenkorrekturen auf die insensitiven Bereiche der direkten Dunklen Materie Suchen und diskutieren die phänomenologischen Konsequenzen der abgeleiteten möglichen Parameterbereiche. Weiterhin werden wir verschiedene Ansätze, die Korrekturen höherer Ordnung

einzubinden vergleichen und auf etwaige Probleme eingehen.
Der Parameterbereich des Nichtminimalen Zwei-Higgs-Dublett-Modell wird mit der Zusatzbedingung eines starken elektroschwachen Phasenüberganges erster Ordnung untersucht. Das Zusammenspiel zwischen theoretischen und experimentellen Einschränkungen wie auch der elektroschwache Phasenübergang schränkt den möglichen Parameter Bereich des Modells signifikant ein. Für einen hinreichend großen und effektiven Parameterscan der Modellparameter wurde das `C++` Programm `BSMPT` erweitert und optimiert. Das Update zur zweiten Release-Version `BSMPT v2` ist veröffentlicht.
Zusätzlich wurde die Möglichkeit der Berechnung der Baryon Asymmetrie des Universums für das komplexe Zwei-Higgs-Doublet Modell (C2HDM) in `BSMPT v2` entwickelt. Zwei nichtlokale elektroschwache Baryogenese Ansätze wurden hierzu untersucht und systematisch innerhalb des C2HDM verglichen. Wir begründen, wieso das Zusammenspiel zwischen den Beschränkungen induziert durch die Messungen des elektrischen Dipol Moments, die Zusatzbedingung eines elektroschwachen Phasenübergangs sowie die Forderung einer hinreichender Baryon Asymmetrie des Universums signifikant den kompatiblen Parameter Bereich des C2HDM einschränkt.

List of Publications

This thesis is based on the following publications:

1. S. Glaus, M. Mühlleitner, J. Müller, S. Patel, and R. Santos, "Electroweak Corrections to Dark Matter Direct Detection in a Vector Dark Matter Model," *JHEP* **10** (2019) 152, arXiv:1908.09249 [hep-ph]
2. S. Glaus, M. Mühlleitner, J. Müller, S. Patel, and R. Santos, "NLO corrections to Vector Dark Matter Direct Detection – An update," *PoS* **CORFU2019** (2020) 046, arXiv:2005.11540 [hep-ph]
3. S. Glaus, M. Mühlleitner, J. Müller, S. Patel, T. Römer, and R. Santos, "Electroweak Corrections in a Pseudo-Nambu Goldstone Dark Matter Model Revisited," arXiv:2008.12985 [hep-ph]
4. P. Basler, M. Mühlleitner, and J. Müller, "Electroweak Phase Transition in Non-Minimal Higgs Sectors," *JHEP* **05** (2020) 016, arXiv:1912.10477 [hep-ph]
5. P. Basler, M. Muhlleitner, and J. Müller, "BSMPT v2 A Tool for the Electroweak Phase Transition and the Baryon Asymmetry of the Universe in Extended Higgs Sectors," arXiv:2007.01725 [hep-ph]
6. P. Basler, M. Mühlleitner, and J. Müller, "Electroweak Baryogenesis Revisited in the Complex Two-Higgs Doublet Models," arXiv:tba.

List of Abbreviations

2HDM Two-Higgs-Doublet Model

C2HDM CP-violating Two-Higgs-Doublet Model

PNGDM Pseudo-Nambu-Goldstone Dark Matter

VDM Vector Dark Matter

BAU baryon asymmetry of the universe

BSM beyond the Standard Model

CB charge breaking

DM Dark Matter

EDM electric dipole moment

EWBG electroweak baryogenesis

EWPT electroweak phase transition

FCNC Flavour Changing Neutral Current

LO leading-order

N2HDM Next-to-Two-Higgs-Doublet Model

NLO next-to-leading-order

QED quantum electrodynamics

QCD quantum chronodynamics

SFOEWPT strong first-order electroweak phase transition

SM Standard Model

VEV vacuum expectation value

EW electroweak

SI-cxn spin-independent cross-section

BEH Brout-Englert-Higgs

QFT quantum field theory

QCD quantum chromodynamics

CMB Cosmic Microwave Background

WIMP weakly interacting massive particle

SUSY Supersymmetry

LHC Large Hadron Collider

OS on-shell

WFRC wave-function renormalization constant

VIA VEV insertion approximation

Contents

CHAPTER 1

Introduction

The Standard Model (SM) of particle physics is a quantum field theory describing the properties and interactions of the fundamental particles [7–14]. With the discovery of an SM-like Higgs boson at the Large Hadron Collider (LHC) in 2012, the last remaining puzzle piece of the SM was found [15, 16]. The Higgs boson is the first observed elementary spin-zero particle. The associated field is responsible for the mass generation of all massive SM-fields. Thus, the properties of the SM-like Higgs boson are indeed the crucial input required for a consistent description of particle interactions. So far the predictions of the SM have been all confirmed to remarkable precision and no significant deviations are observed [17–19].
Despite the enormous success, it is not possible to explain all observed physical phenomena within the SM. The evolution of our universe after the *Big Bang* can be described within the Λ-Cold-Dark-Matter model, the standard model of Big Bang cosmology. It allows for a consistent description of the structure formation and the Cosmic Microwave Background (CMB). In particular, the measurement of the CMB predicts the abundance of the different constituents of our universe [20]. Astonishingly only roughly 5% of the mass-energy of our universe is baryonic matter, while $\sim 27\%$ consists of the so-called *Dark Matter* (DM). The DM is assumed to be non-baryonic (electrically neutral), cold, dissipationless and collisionless. The DM interaction proceeds solely through gravitation and at most *weakly interacts* with the SM particle content. The SM does not provide a DM candidate.

While the nature of DM is unknown, *Weakly-Interacting-Massive particle* (WIMP) models provide a promising solution to incorporate the particle nature of DM in the SM. The use of a *Higgs portal* is an economic realization of a WIMP model. The DM and SM particles are coupled through a Higgs boson mediator. On the one hand, these Higgs portal models feature a rich phenomenology at the LHC. On the other hand they allow for further experimental approaches to probe the parameter space of the new physics models. Direct detection experiments utilize the Higgs portal to probe the effective DM-nucleus coupling in a recoil experiment [21]. Up to now, no significant signals could be observed within a direct detection experiment. However, the absence of such signal can be used to derive constraints on the model parameter space. Even though there is a remarkable precision in experiments as well as in theoretical calculations for the SM at the LHC, higher-order corrections to DM observables, like the spin-independent cross-section in a direct detection experiment, are lacking in the literature.

In this thesis we calculate the electroweak next-to-leading order corrections to the spin-independent cross-section (SI-cxn) in two different Higgs-portal DM models. Higher-order corrections play an important role in the discussion of the sensitivity of experimental results and the derived parameter constraints. Especially in one of the models, the SI-cxn is vanishing in the leading-order prediction, hence there is no possibility to extract information from a direct detection experiment without higher-order corrections.

Besides a non-zero DM relic density, also a non-zero baryon asymmetry is observed by the CMB measurement. Sakharov introduced three conditions a model needs to fulfill in order to be able to provide a dynamical generation of a baryon asymmetry [22]: *(i)* a particle physics model needs to have C- and CP-violation, *(ii)* B-violating processes as well as *(iii)* a departure from thermal equilibrium in the early universe. The two former conditions can be realized within the SM, the latter could be achieved through a *strong first-order electroweak phase transition* (SFOEWPT). An SFOEWPT is only possible in the SM for Higgs boson masses below $\sim 70\,\text{GeV}$ [23–25]. Singlet and doublet extensions of the Higgs potential are a promising approach, that allow us to fulfill the Sakharov conditions without violating the gauge symmetries of the SM while being compatible with electroweak precision measurements, such as the ρ-parameter [26]. With increasing precision in the Higgs property measurements, the new physics extensions get more and more constrained. However, there is still plenty of freedom in the parameter space. The additional demand to fulfill further conditions derived from cosmological considerations, like the requirement of an SFOEWPT, helps to narrow down the parameter space of new physics models significantly. In the context of this thesis, we investigate the impact of the additional requirement of an SFOEWPT in the Next-to-Minimal Two-Higgs-Doublet (N2HDM) [27], which is a model extending the SM Higgs potential with a doublet and a singlet field.
The SFOEWPT is only the first step to achieve a successful generation of the baryon asymmetry of the universe (BAU). The predicted amount of the produced BAU requires a consistent description of the non-equilibrium thermal system of the early universe. There are several attempts to calculate the BAU, for instance leptogenesis [28,29], local and non-local electroweak baryogenesis [24, 30–32]. Two non-local electroweak baryogenesis approaches are considered in the context of this thesis. Both approaches derive quantum transport equations describing the thermal system of the early universe [33–39]. The solution of these transport equations allows us to predict the BAU by utilizing electroweak sphaleron transitions.

This thesis is divided into four different parts.
In Part I of the thesis, we first briefly introduce the SM and discuss the shortcomings as well as the open questions of the SM. Afterwards, we discuss the theoretical and experimental constraints, that all SM-extensions need to fulfill. Subsequently, we introduce in Chapter 3 the non-minimal extensions of the SM used in the thesis: the complex Two-Higgs Doublet Model (C2HDM) in Sec. 3.2, the Pseudo-Nambu Goldstone DM (PNGDM) model in Sec. 3.3, the vector DM model (VDM) in Sec. 3.4 and the Next-to-Minimal Two-Higgs Doublet model (N2HDM) in Sec. 3.5.
In Part II of the thesis we present the electroweak next-to-leading order corrections of DM direct detection. We start with a brief theoretical introduction in Chapter 4 by discussing the renormalization of non-minimal extended Higgs sectors in Sec. 4.1, followed by the discussion of the DM phenomenology required DM direct detection in Sec. 4.2. We conclude the theoretical introduction with the description of the calculation of DM direct detection in the different DM models in Sec. 4.3. The calculation and results of the PNGDM and the VDM model are presented in Chapter 5 and Chapter 6, respectively.
The Part III deals with the combination of the additional requirement of a strong first-order electroweak phase transition and the collider phenomenology in the N2HDM. Again, we start with a brief theoretical introduction of the one-loop effective potential at finite temperatures

in Sec. 7.1 as well of the electroweak phase transition in Sec. 7.2. We show the results for the `Type I` and `Type II` N2HDM in Chapter 8, respectively.
The combination of electroweak baryogenesis with the most recent collider phenomenology is presented in Part IV. After a brief theoretical introduction in electroweak baryogenesis and the corresponding quantum transport equations in Chapter 9, we present the results obtained in the C2HDM in Chapter 10.
We conclude in Chapter 11.

Part I.

Non-Minimal Extensions of the Standard Model

CHAPTER 2

The Standard Model

The Standard Model (SM) of particle physics is the most successful theory describing the interplay between all observed elementary particles and their interactions mediated by the fundamental forces, namely the electroweak and the strong force. The former is the unification of quantum electrodynamics and the weak force. Gravitational interactions are not included in the SM.
In the following we will give a short overview of the SM especially its gauge structure and the Brout-Englert-Higgs (BEH) mechanism [8–10]. We conclude the chapter with the shortcomings and open questions not answered by the SM.

2.1. Gauge Invariance

The SM is a renormalizable quantum field theory (QFT) describing all observed particles as excitations of quantized fields. The gauge group which reflects the local symmetries of the SM Lagrangian is given by the direct product of

$$SU(3)_C \otimes SU(2)_L \otimes \mathrm{U}_Y \ . \tag{2.1}$$

The gauge group $SU(3)_C$ corresponds to quantum chromodynamics (QCD) describing the interactions between particles with a color charge [40–42]. The direct product of $SU(2)_L \otimes \mathrm{U}_Y$ forms the electroweak (EW) gauge group describing the EW interactions [14, 43, 44]. Left-chiral fields (indicated by the index L) carrying a hypercharge (Y) transform accordingly under the electroweak gauge group. The particle content of the SM can be categorized into fermions (spin 1/2), gauge bosons (spin 1) and scalar fields (spin 0). The mediators of the strong force are the gluon fields denoted by G^a_μ where a is the $SU(3)_C$ index of the adjoint representation. The $SU(2)_L$ gauge group yields the gauge field W^a_μ and U_Y the field B_μ, respectively. All gauge bosons have a spin of one.
The SM fermions can be split into quarks forming a triplet under $SU(3)_C$ and leptons, which are $SU(3)_C$ singlets. All fermions come with two chiralities, left- and right-handed, where the left-handed fields are charged under the gauge group $SU(2)_L$, while the right-handed fields are $SU(2)_L$ singlets. Both chiralities also carry a $U(1)$ hypercharge.
With the discovery of the Higgs boson the first fundamental spin-0 particle was discovered [15, 16]. The role of the Higgs boson will be discussed later on.

For a generic QFT with fermions represented as Ψ, gauge fields A^a_μ and a scalar ϕ, the kinetic Lagrangian reads

$$\mathcal{L}_{\text{kin}} = \bar{\psi} i \not{\partial} \psi - \frac{1}{4} F^a_{\mu\nu} F^{\mu\nu,a} + (\partial_\mu \phi)^\dagger (\partial^\mu \phi) \ , \tag{2.2}$$

with the Dirac spinors $\bar{\psi} = \psi^\dagger \gamma^0$ and the slash notation $\not{\partial} = \gamma_\mu \partial^\mu$. The field-strength tensors of the gauge fields are defined as

$$F^a_{\mu\nu} = \partial_\mu A^a_\nu - \partial_\nu A^a_\mu + g f^{abc} A^b_\mu A^c_\nu \ , \tag{2.3}$$

where g is the respective gauge coupling and f^{abc} the structure constant of the gauge group. Local gauge transformations can be represented with the generators t^a of the respective Lie-group[1]

$$\Psi \to (1 + i\alpha^a t^a)\, \psi \ , \tag{2.4a}$$

$$A^a_\mu \to A^a_\mu + \frac{1}{g} \partial_\mu \alpha^a + f^{abc} A^b_\mu \alpha^c \ , \tag{2.4b}$$

$$\phi \to (1 + i\alpha^a t^a)\, \phi \ . \tag{2.4c}$$

Demanding local gauge invariance of Eq. (2.2) under the gauge transformations defined in Eq. (2.4) requires the introduction of a covariant derivative defined for the SM as

$$D_\mu \equiv \partial_\mu - i g_s \frac{\lambda_2}{2} G^a_\mu - i g_2 \frac{\sigma^a}{2} W^a_\mu - i g_1 \frac{Y}{2} B_\mu \ . \tag{2.5}$$

The gauge coupling g_s corresponds to the $SU(3)_C$, g_2 to $SU(2)_L$ and g_1 to U_Y, respectively. The Gell-Mann matrices λ_a are eight linear-independent 3×3 matrices and span the Lie algebra of $SU(3)_C$. Analogously, the Pauli matrices σ^a form the Lie-algebra of the $SU(2)_L$ gauge group. For the SM particle content Eq. (2.2) reads

$$\mathcal{L}_{\text{kin}} = \sum_{\text{Fermions}} \bar{\psi} i \not{D} \psi - \frac{1}{4} \left(G^a_{\mu\nu} G^{\mu\nu,a} + W^a_{\mu\nu} W^{\mu\nu,a} + B_{\mu\nu} B^{\mu\nu} \right) + (D_\mu \Phi)^\dagger (D^\mu \Phi) \ . \tag{2.6}$$

The field-strength tensors $G^a_{\mu\nu}$, $W^a_{\mu\nu}$ and $B_{\mu\nu}$ correspond to the gauge fields of the $SU(3)_C$ G^a_μ $(a = 1, \ldots, 8)$, $SU(2)_L$ W^a_μ $(a = 1, 2, 3)$ and $U(1)_Y$ B_μ, respectively. The structure constants and the respective indices a are in accordance with the gauge group and representations.
After the rotation to the mass eigenstates the fields W^a_μ and B_μ yield the W- and Z-gauge bosons as well as the photon. Note that Eq. (2.6) is indeed gauge invariant under the SM gauge group, but does not include explicit mass terms for the respective particles. It is not possible to write down explicit mass terms in a gauge invariant way. To generate masses for the fermions and bosons, the spontaneous electroweak symmetry breaking formalism is utilized discussed in the following.

2.2. Electroweak Symmetry Breaking of the SM

Spontaneous electroweak symmetry breaking (BEH mechanism) yields a possibility to generate mass terms for the gauge bosons and fermions of the SM in a gauge invariant way. For this purpose, a $SU(2)_L$ doublet

$$\Phi = \begin{pmatrix} \phi^+ \\ \frac{1}{\sqrt{2}} (\rho + i\eta) \end{pmatrix} \ , \tag{2.7}$$

[1] Note that the Einstein sum convention is implicitly assumed.

is introduced in the SM, with the weak hypercharge $Y = 1$. All field components of this doublet are color singlets, implying no strong interactions. The upper component ϕ^+ denotes a complex field and the normalization is chosen such that the real and imaginary part are canonically normalized. The lower components ρ and η are real fields.
Given that only one Higgs doublet Φ breaks the SM symmetry groups, the most general scalar potential reads

$$V(\Phi) = -\mu^2 \Phi^\dagger \Phi + \lambda \left(\Phi^\dagger \Phi\right)^2 \ , \tag{2.8}$$

with the mass parameter μ^2 and the Higgs self-coupling λ. For $\mu^2, \lambda > 0$ the minimum of the potential in Eq. (2.8) is not at the origin. Hence, the ground state of the potential corresponds to a non-zero expectation value of the field component denoted as

$$\langle \Phi \rangle = \frac{1}{\sqrt{2}} \begin{pmatrix} 0 \\ v \end{pmatrix} \ , \tag{2.9}$$

with the vacuum expectation value (VEV)

$$|v|^2 = \frac{\mu^2}{2\lambda} \ . \tag{2.10}$$

Note that the condition in Eq. (2.10) applies on the absolute value, hence there is an infinite number of equivalent minima of the Higgs potential, related through an $SU(2)$ transformation. By expanding the Higgs field around the VEV as

$$\Phi = \begin{pmatrix} \phi^+ \\ \frac{1}{\sqrt{2}} \left(v + \rho + i\eta\right) \end{pmatrix} \ , \tag{2.11}$$

and therefore choosing an explicit direction in the (ρ, η) plane the EW symmetry is spontaneously broken. Additionally by choosing the VEV to lie in the neutral component, the residual $\mathrm{U}(1)_{\mathrm{em}}$ remains unbroken, so that the symmetry of quantum electrodynamics (QED) persists.
According to the Goldstone theorem [45–47], breaking the EW symmetries by Eq. (2.11) yields three massless Nambu-Goldstone bosons, however this is only true for global symmetries. Gauging (demanding local gauge invariance) causes the Nambu-Goldstone bosons to be associated with the gauge bosons. In particular, the remaining degrees of freedom of the $SU(2)_L \otimes U(1)_Y$-fields after the spontaneous symmetry breaking, are transformed into longitudinal components of the gauge fields. In this way the gauge bosons receive mass terms. This is related with the common phrase *the Nambu-Goldstones are eaten up by the gauge bosons.*
In the unitary gauge[2], the bosonic mass terms are given as

$$\mathcal{L} \supset \frac{v^2}{8} \left[g_2^2 \left(W_\mu^1\right)^2 + g_1^2 \left(W_\mu^2\right)^2 + \left(g_1 B_\mu - g_2 W_\mu^3\right)^2 \right] - \lambda v^2 \rho^2 \ . \tag{2.12}$$

Introducing the Weinberg angle θ_W allows us to diagonalize the resulting mass matrix yielding the mass eigenstates

$$W_\mu^\pm = \frac{W_\mu^{(1)} \mp W_\mu^{(2)}}{\sqrt{2}} \ , \tag{2.13a}$$

[2] In principle, an additional term is needed to fix the gauge condition. The usual approach is to introduce an R_ξ gauge term. However, for simplicity the unitarity gauge is chosen, where the limit of the gauge parameter $\xi \to \infty$ is taken. This is equivalent to integrating out the Goldstone field with mass ξm_a $(a = W, Z)$ which thus decouples in all quantum corrections.

$$Z_\mu = \frac{g_2 W_\mu^{(3)} - g_1 B_\mu}{\sqrt{g_2^2 + g_1^2}} = \cos\theta_W W_\mu^3 - \sin\theta_W B_\mu \ , \tag{2.13b}$$

$$A_\mu = \frac{g_2 W_\mu^{(3)} + g_1 B_\mu}{\sqrt{g_2^2 + g_1^2}} = \sin\theta_W W_\mu^3 + \cos\theta_W B_\mu \ , \tag{2.13c}$$

with the relation between the Weinberg angle and the gauge couplings

$$\cos\theta_W = \frac{g_2}{\sqrt{g_2^2 + g_1^2}} \ . \tag{2.14}$$

The masses of the bosonic states are given by

$$m_W = g_2 \frac{v}{2} \ , \tag{2.15a}$$

$$m_Z = \sqrt{g_1^2 + g_2^2}\frac{v}{2} \ , \tag{2.15b}$$

$$m_h = \sqrt{2\lambda v^2} = \sqrt{2\mu^2} \ . \tag{2.15c}$$

The photon field A_μ is massless and the Higgs boson h is identified with the field component ρ. The mass terms for the fermions can be realized by the introduction of Yukawa terms in the Lagrangian coupling the $SU(2)_L$ Higgs doublet with the $SU(2)_L$ fermion doublet and the respective right-handed fermion singlet

$$\mathcal{L}_{\text{Yuk}} = -\sum_f y_f \psi_L^{(f)} \psi_R^{(f)} \frac{v+h}{\sqrt{2}} \ , \tag{2.16}$$

with the corresponding Yukawa coupling y_f. Note that these terms on the one hand generate mass terms for the fermions scaling with the coupling strength

$$m_f = \frac{v}{\sqrt{2}} y_f \ , \tag{2.17}$$

and on the other hand introduce Higgs interactions with a pair of left- and right-handed fermions

$$g_{hff} = -i\frac{m_f}{v} \ . \tag{2.18}$$

Introducing the covariant derivative in Eq. (2.5) also gives rise to Higgs-gauge-boson vertices proportional to the respective mass squared ($V = Z, W$)

$$g_{hVV} = 2i\frac{m_V^2}{v} \ , \tag{2.19}$$

note that the coupling scales with the mass squared in contrast to Eq. (2.18).

2.3. Open Questions of the Standard Model

Regardless of the success of the SM and its power in making falsifiable predictions, there are still open problems in modern physics, which cannot be explained within the SM framework. To name the most obvious one, the gravitational force is not embedded in the SM. Due to its relatively weak strength (on short distances), the gravitational force is mostly neglected in particle physics phenomena.

Further, the SM of particle physics does not provide a suitable candidate for Dark Matter (DM). Cosmological observations indicate that baryonic matter accounts only for a small fraction of the matter content of the universe [48, 49], the remaining part, roughly 84%, consists of non-luminous matter, Dark Matter [20]. There are several attempts to solve the

missing mass problem like *modified newtonian gravity* [50–52] or introducing new particles interacting only gravitationally with the SM particle content. Extending on this idea, one possible solution is to have weakly interacting massive particle (WIMP) allowing us to explain the missing mass in the universe. At the same time, there is the possibility to search for new interactions between WIMPs and SM particles. The general idea of a WIMPs will be discussed in Sec. 4.2.2.

Besides the DM problem it is also unknown how the baryon asymmetry of the universe (BAU) is generated. The matter-antimatter asymmetry can be estimated by assuming that all Cosmic Microwave Background (CMB) photons are the result of thermal annihilation of the baryon pairs [26]

$$\frac{n_b - n_{\bar{b}}}{n_b + n_{\bar{b}}} \approx \eta \equiv \frac{n_B}{n_\gamma} = (6.2 \pm 0.4) \cdot 10^{-10} \ , \tag{2.20}$$

where n_b ($n_{\bar{b}}$) indicates the (anti-) baryon density and n_γ the photon density of today's universe. The baryon-to-photon ratio is the crucial tuning parameter for the prediction of the abundance of light elements in the Big-Bang nucleosynthesis. Hence, the measurement of deuterium and hydrogen distributions gives the precise value in Eq. (2.20). Further, it is possible to relate η to the fraction of the cosmological density parameter Ω given by the baryons [26]

$$\Omega_b = 3.66 \times 10^7 \eta h^{-2} \ , \tag{2.21}$$

or reformulated as $10^{10}\eta = 274\Omega_b h^2$. The *Planck* measurement of the baryon fraction $\Omega_b = 0.0224 \pm 0.0002$ directly translates to an even tighter limit of $\eta = (6.12 \pm 0.04) \cdot 10^{-10}$.

Explaining the dynamical generation of the BAU is a demanding theoretical task. Sakharov proposed three necessary conditions a model needs to fulfill in order to enable a dynamical production of the BAU in the early universe [22]. The first condition of baryon-number violating processes can be achieved in the SM through sphaleron transitions (discussed in Sec. 9.1.1). The second condition, C- and CP-violation, is present in the SM as well, but the amount of CP-violation is not sufficient [53]. The last condition is the departure from thermal equilibrium. As we will discuss later, the non-equilibrium state can be reached through a strong first-order electroweak phase transition. However, the SM provides only a smooth crossover implying that the third Sakharov condition is not fulfilled in the SM.

CHAPTER 3

Non-Minimal Extensions of the Standard Model

The SM does not provide a sufficient framework to solve all remaining open problems of modern physics as mentioned already in Sec. 2.3. Thus, it is interesting to study beyond the Standard Model (BSM) models. However, the great success of the SM describing all particle interactions indicates that the SM somehow has to be embedded in the new physics models. There are attempts to utilize further symmetry relations to extend the SM to a full theory, as done for instance in Supersymmetry (SUSY) models. SUSY models as *e.g.* the Minimal-Supersymmetric Standard Model (MSSM) introduce for each SM particle a superpartner extending the particle content of the SM significantly. These newly introduced particles could yield a DM candidate, and in addition the new degrees of freedom in the spectrum could change the thermodynamical properties of the early universe. SUSY models have the capability to solve several remaining problems at once, however SUSY models also introduce a plethora of new particles. Due to missing new signatures at the Large Hadron Collider (LHC), it might be a more pragmatic approach to start with *smaller* models to attack the open questions.
A *bottom-up* approach are the non-minimal extended Higgs sector models. The SM Higgs potential is the least well studied sector experimentally. Hence, the experimental constraints on the Higgs potential parameters are rather weak. Especially the trilinear and quartic couplings of the Higgs boson are predicted by the SM. They read expressed in Feynman rules

$$g_{hhh} = -3i\frac{m_h^2}{v} \ , \tag{3.1a}$$

$$g_{hhhh} = \frac{g_{hhh}}{v} \ , \tag{3.1b}$$

but are not validated by experiment. Thus, it is a pragmatic approach to extend the SM Higgs potential in a minimal way while respecting the gauge structure of the SM and requiring that the extended Higgs sector remains renormalizable. By respecting the gauge structure of the SM, it is ensured that the electroweak symmetry breaking yields the same SM particles as the gauge bosons and fermions, while the Higgs sector is extended with non-SM like Higgs bosons. The renormalizability ensures that no divergences occur in higher order corrections, allowing for accurate and precise predictions.

One of the strongest constraints for extended Higgs sector BSM models comes from the ρ parameter [54]

$$\rho \equiv \frac{\sum_i v_i^2 \left[4I_{W,i}\left(I_{W,i}+1\right) - Y_i^2\right]}{\sum_i 2Y_{W,i}^2 v_i^2} \ , \tag{3.2}$$

where the sum runs over any scalar Higgs multiplet i with the corresponding VEV v_i, weak isospin $I_{W,i}$ and weak hypercharge Y_i. The experimentally measured value for this parameter comes from precise EW measurements and is given by [26]

$$\rho_{\text{exp.}} = 1.00039 \pm 0.00019 \ . \tag{3.3}$$

The SM provides by construction a ρ parameter at tree level

$$\rho = \frac{m_W^2}{m_Z^2 \cos\theta_W} \underbrace{=}_{\text{Eq. (2.15c)}} 1 \ , \tag{3.4}$$

so that the SM automatically fulfills the experimental value. The Eq. (3.2) implies that it is possible to add an arbitrary number of $SU(2)_L$ scalar doublets with $I_W = 1/2$ and a hypercharge of $Y = +1$, fulfilling automatically Eq. (3.3). Further, $SU(2)_L$ singlets with vanishing hypercharge $Y = 0$ can also be added arbitrarily. Consequently, doublet and singlet extensions providing a renormalizable Lagrangian are viable model candidates to look for BSM physics. In the context of this thesis, several doublet and singlet extensions are considered.
The following chapter is structured as follows: We start with the discussion of the theoretical and experimental constraints applied on the BSM models in Sec. 3.1. We will comment shortly on the theoretical constraints on the general Higgs potential giving first requirements on the model parameters, followed by the experimental constraints governed by the precise measurements present today. Subsequently, we introduce the complex two-Higgs doublet model in Sec. 3.2, the complex singlet extension in Sec. 3.3, the vector dark matter model in Sec. 3.4 and finally the next-to-minimal two-Higgs doublet model in Sec. 3.5. We restrict the introduction to the minimum required for the phenomenological discussion in this thesis and refer to the literature accordingly.

3.1. Theoretical and Experimental Constraints

Extending the SM Higgs sector yields a large plethora of possibilities, hence it is important to constrain the models under investigation. In the following the different constraints applied on the various non-minimal extended Higgs sector models are presented. The constraints can be categorized by theoretical and experimental constraints.
Unitarity is one of the theoretical constraints. The mechanism of electroweak symmetry breaking does not solely give mass to the fermions and gauge bosons, but provides a mechanism to unitarize the scattering of *e.g.* longitudinal gauge bosons at high energies. The scattering amplitude of longitudinal gauge bosons is proportional to the center-of-mass energy squared s in the high-energy limit, thus the resulting cross section would be divergent. However, the electroweak symmetry breaking also introduces additional Higgs boson contributions canceling the terms proportional to s. The resulting cross section gives a finite limit for $s \to \infty$. Extending the Higgs sector also introduces additional Higgs bosons, hence the newly introduced couplings have to fulfill the same cancellation mechanism in order to unitarize the cross section in the high-energy limit. The unitarity requirements are usually expressed as constraints on the Higgs self-coupling λ_i.
Quantum tunneling allows for transitions between different vacuum states. Consequently, if there is a deeper vacuum state of the Higgs potential, there exists a non-zero possibility that

	d_R	L	l_R	d-type	leptons
`Type I`	-	+	-	ϕ_2	ϕ_2
`Type II`	+	+	+	ϕ_1	ϕ_1
`lepton-specific`	-	+	+	ϕ_2	ϕ_1
`flipped`	+	+	-	ϕ_1	ϕ_2

Table 3.1.: The first three columns provide the fermionic $\mathbb{Z}_2$ charge assignments in order to obtain the coupling structure given in the last two columns. For instance, in the `Type I` the down-type and leptons are simultaneously coupled to the second Higgs doublet.

the known Higgs vacuum state tunnels to the deeper one. Since we obviously live in a rather stable universe, it is presumed that our Higgs vacuum state is at least meta-stable[3], implying that the *tunnel time* is longer than the age of the universe. For simplicity, we demand that the chosen Higgs vacuum state in the extended Higgs sector models yields a global (tree-level) minimum by construction. In this way it is ensured that the predicted vacuum state of the models is a stable one. Further, we impose that the model is *bounded from below*. Boundedness from below implies that the ground state is the true global minimum of the potential, hence there are no falling field directions. Both the global minimum condition and boundedness from below conditions are usually expressed in constraints in terms of the Lagrange parameters of the model. For more complex Higgs sectors, there is also the possibility to check these conditions numerically [58].

3.1.1. Flavor-Changing Neutral Currents

Besides the theoretical considerations, there are many experimental results which have to be accounted for. An important set of constraints is given by the absence of Flavour Changing Neutral Currents (FCNCs). In the SM, FCNCs are avoided at tree level and highly suppressed at one-loop level. However, BSM extensions might introduce FCNCs already at tree level requiring fine-tuning in order to be compatible with the experimental findings. It is possible, however, to ensure that such BSM contributions to FCNC remain small *e.g.* due to additional (flavor) symmetries. Another possibility is the so-called natural flavor conservation requiring each fermion multiplet to be coupled to exactly one scalar mutliplet. For doublet and singlet extensions, the coupling structure can be enforced by imposing discrete or continuous symmetries on the Yukawa and Higgs sector. Additional symmetries in the potentials are often used to reduce the number of free parameters or *e.g.* to ensure the stability of DM candidates as discussed later on. These symmetries can be extended to the Yukawa sector to ensure the absence of FCNCs.
Suppose in a theory, two $SU(2)_L$ Higgs doublets ϕ_1 and ϕ_2 are introduced with the $\mathbb{Z}_2$ symmetry

$$\phi_1 \to \phi_1 \ , \quad \phi_2 \to -\phi_2 \ . \tag{3.5}$$

Without loss of generality, the up-type quark can be assumed to be coupled solely to the second Higgs doublet. This can be achieved by extending the $\mathbb{Z}_2$ to the Yukawa sector

$$Q_L \to Q_L \ , \quad u_R \to -u_R \ , \tag{3.6}$$

with the left-handed $SU(2)_L$ quark doublet Q_L and the right-handed up-type quark singlet

[3]For a detailed discussion of the vacuum stability of the Higgs potential we refer to *e.g.* [55–57].

u_R. The remaining down-type quarks and leptons can be coupled to the Higgs doublets in four different combinations. The corresponding coupling structures and the respective $\mathbb{Z}_2$ assignments are listed in Tab. 3.1. Consequently, in `Type I` models all fermions are coupled to the same Higgs doublet, whereby `Type II` models differentiate. The up-type quarks are coupled to the second Higgs doublet and the down-type quarks and leptons to the first Higgs doublet, respectively. This coupling structure corresponds to the structure obtained in supersymmetric models such as the MSSM. The remaining types `lepton-specific` and `flipped` are not discussed in the context of this thesis.

3.1.2. S,T,U Oblique Parameters

The oblique parameters S, T, U are a generalization of the ρ parameter defined in Eq. (3.2) taking higher-order corrections into account. The experimental values can be extracted from a global fit to electroweak precision measurements [59]

$$S = 0.04 \pm 0.11 \ , \quad T = 0.09 \pm 0.14 \ , \quad U = -0.02 \pm 0.11 \ . \tag{3.7}$$

These quantities are sensitive to BSM contributions altering the gauge boson self energies, and hence provide a strict limit for BSM models. The predictions for the oblique parameters are calculated for a large variety of BSM models, especially for doublet and singlets extensions, allowing us to check the model predictions with the experimentally measured values. The `C++` code `ScannerS` [60,61] provides an implementation of the oblique parameter S, T, U for several doublet and singlet extensions. Furthermore, it allows us to generate benchmark scenarios fulfilling theoretical and experimental constraints presented subsequently in this section. Doublet extensions of the SM provide additional charged scalars in the Higgs spectrum. The T parameter sets a strict upper bound on the mass difference between the charged and the corresponding closest-in-mass neutral Higgs boson, whereas the S parameter on the other hand provides a constraint on the mass differences between mixing scalars.

3.1.3. Flavor Constraints

Even in the absence of FCNCs at tree level, there is the possibility for loop-induced FCNC processes. Moreover, in doublet extensions typically also charged Higgs bosons are a part of the Higgs spectrum giving rise to charge currents in the flavor sector, even at tree level. Precise flavor observables are especially sensitive to the charged Higgs boson, allowing us to constraint the parameter space concerning the charged Higgs significantly. In Fig. 3.1, the results of a fit to flavor observables within the Two-Higgs Doublet Model are shown. Both plots depict the plane spanned by the charged Higgs boson mass and $\tan\beta$, one mixing angle of the model. The details will be discussed in Sec. 3.2. These results are applicable to all models with one additional $SU(2)_L$ Higgs doublet and the respective Yukawa type (as listed in Tab. 3.1). Additional singlets in the model do not alter these results (as discussed in Sec. 3.5). The color code indicates the excluded parameter regions by the respective decay channels. For the `Type I` model the exclusion limit shows a stronger dependence on $\tan\beta$ and the charged Higgs mass $M_{H^\pm}$, whereas for the `Type II` models only charged Higgs masses above $\gtrsim 580\,\text{GeV}$ are allowed regardless of $\tan\beta$. Additionally, $B_s \to \mu\mu$ decays also give an upper bound on $\tan\beta$ in `Type II` models.

3.1.4. Electric Dipole Moment

One of the striking experimental constraints to be accounted for in the context of electroweak baryogenesis is given by the electric dipole moment (EDM). Within the SM the CP-violating sources are expected to be tiny, since these effects arise at the multi-loop level. Moreover, the precise measurement of the electron EDM by the ACME collaboration [62]

$$d_e < 1.11 \times 10^{-29}\, e\,\text{cm} \ , \tag{3.8}$$

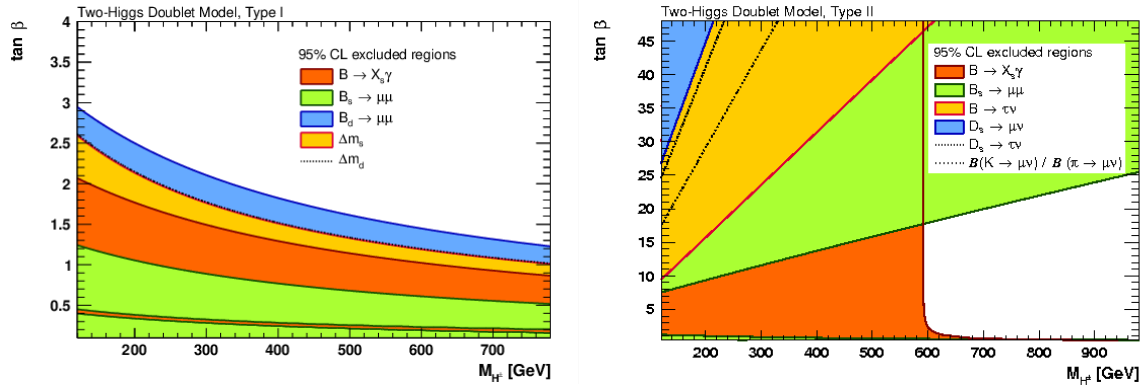

(a) (b)

Figure 3.1.: Result of a fit to flavor observables within the Two-Higgs doublet model for the plane of the charged Higgs mass versus $\tan\beta$, one mixing angle of the model. The results are taken from [59].

puts severe constraints on BSM models with additional CP-violating sources in the scalar sector. The electric charge of the electron is denoted as e. Again the theoretical predictions are calculated in many models, where we use the implementation in `ScannerS`.

3.1.5. Higgs Measurements

With the discovery of the Higgs boson in 2012, the search for additional scalars did not end. The ATLAS and CMS experiments at the LHC as well as the older experiments *e.g.* Tevatron and LEP put an enormous effort in the search for new scalars.
The program `HiggsBounds` [63–67] provides a framework to test the theory predictions for all Higgs production processes and decay rates of the model and compares it to several phenomenological studies. The predictions are compared to the experimental results as expected and observed limits at 2σ or 95% confidence level as function of the model parameters.
To check for the validity of the SM-like Higgs boson in the BSM model, the code `HiggsSignals` [68, 69] provides a framework to compute the χ^2 value of the given parameter point, where the χ^2 values allows us to quantify the agreement between prediction and observation. For the proper interpretation of the statistical significance of a parameter point in `HiggsSignals`, we refer to [68–70].
Both programs are linked within `ScannerS` allowing for an extensive parameter region scan for BSM models with extended Higgs sectors.

3.2. The (Complex) Two-Higgs Doublet Model

The scalar sector of the SM is extended by an additional $SU(2)_L$ Higgs doublet with a softly-broken $\mathbb{Z}_2$ symmetry, yielding the CP-violating Two-Higgs-Doublet Model (C2HDM) [71,72]. The general Lagrangian of the CP-violating C2HDM is built of

$$\mathcal{L}^{\rm EW}_{\rm C2HDM} = \mathcal{L}_{YM} + \mathcal{L}_{\rm F} + \mathcal{L}_S^{\rm C2HDM} + \mathcal{L}_{\rm Yuk} + \mathcal{L}_{\rm GF} + \mathcal{L}_{\rm FP}\ . \tag{3.9}$$

The *Yang-Mills Lagrangian* $\mathcal{L}_{YM}$ and the fermion Lagrangian $\mathcal{L}_{\rm F}$ contain the kinetic terms for the gauge bosons and fermions, respectively. They describe the interactions between the gauge bosons with fermions and themselves. Since these parts of the Lagrangian do not differ compared to the SM, we do not list them explicitly here.
The scalar Lagrangian $\mathcal{L}_S^{\rm C2HDM}$ contains the covariant derivatives of the Higgs fields and the

corresponding Higgs potential. The explicit form will be discussed in the following subsection. The Yukawa Lagrangian $\mathcal{L}_{\text{Yuk}}$ provides the terms describing the Higgs interactions with the fermions and the fermion mass terms, respectively. Due to the second $SU(2)_L$ Higgs doublet compared to the SM, the avoidance of FCNCs at tree level allows for four different possibilities to extend the $\mathbb{Z}_2$ symmetry to the Yukawa sector. The resulting coupling structure is discussed in Sec. 3.1.1.
The gauge-fixing and the *Fadeev-Popov* Lagrangian are not needed in their full form, hence we refer to [73] for the explicit definition.
In order to define the gauge condition to remove the redundant degrees of freedom of the gauge boson fields, we use the renormalizable R_ξ gauge[4]. Thereby, gauge-fixing parameters ξ_V $(V = W, Z, \gamma)$ are introduced for each gauge boson. The inclusion of the nonphysical *Fadeev-Popov ghost fields* $u_{W^\pm}$, u_Z and u_γ allows us to cancel the nonphysical degrees of freedom of the gauge bosons, resulting physical observables that are independent of the gauge fixing parameters. We follow the approach of [73], where $\mathcal{L}_{\text{GF}}$ and $\mathcal{L}_{\text{FP}}$ are introduced after the renormalization of the rest of the Lagrangian. Therefore, all introduced fields in $\mathcal{L}_{\text{GF}}$ and $\mathcal{L}_{\text{FP}}$ are already considered to be renormalized and hence no introduction of counterterms is needed.

3.2.1. The Scalar Lagrangian of the C2HDM

The scalar Lagrangian of the CP-violating C2HDM contains the kinetic terms of the Higgs bosons and their respective interactions with the gauge bosons and the self-interactions. The corresponding Lagrangian reads

$$\mathcal{L}_S^{\text{C2HDM}} = \sum_{i=1}^{2} \left(D_\mu \Phi_i\right)^\dagger \left(D^\mu \Phi_i\right) - V_{\text{C2HDM}}^{(0)} \,, \tag{3.10}$$

with two $SU(2)_L$ Higgs doublets Φ_i $(i = 1, 2)$ and the covariant derivative defined in Eq. (2.5). The scalar Higgs potential of the C2HDM is given by (for a phenomenological discussion see *e.g.* [71])

$$\begin{aligned} V_{\text{C2HDM}}^{(0)} = {} & m_{11}^2 \Phi_1^\dagger \Phi_1 + m_{22}^2 \Phi_2^\dagger \Phi_2 + \frac{\lambda_1}{2}\left(\Phi_1^\dagger \Phi_1\right)^2 + \frac{\lambda_2}{2}\left(\Phi_1^\dagger \Phi_1\right)^2 + \lambda_3 \left(\Phi_1^\dagger \Phi_1\right)\left(\Phi_2^\dagger \Phi_2\right) \\ & + \lambda_4 \left(\Phi_1^\dagger \Phi_2\right)^2 + \left[\frac{\lambda_5}{2}\left(\Phi_1^\dagger \Phi_2\right)^2 - m_{12}^2 \left(\Phi_1^\dagger \Phi_2\right) + h.c.\right] \,, \end{aligned} \tag{3.11}$$

where all Lagrange parameter are real due to the hermicity of the potential except for m_{12} and λ_5. These two complex parameters give rise to the CP-violation in the C2HDM. The potential obeys a softly broken discrete $\mathbb{Z}_2$ symmetry under which the doublets transform as $\Phi_1 \to \Phi_1$ and $\Phi_2 \to -\Phi_2$. The mass parameter m_{12}^2 softly breaks this symmetry. The extension of this $\mathbb{Z}_2$ to the Yukawa sector ensures the absence of tree-level FCNCs as discussed in Sec. 3.1.1. The spontaneous EW symmetry breaking requires the field expansion of the two Higgs doublets around its VEVs in terms of the charged CP-even and CP-odd field components ζ_i and η_i and the neutral CP-even and CP-odd fields ρ_i and ψ_i $(i = 1, 2)$

$$\Phi_1 = \frac{1}{\sqrt{2}} \begin{pmatrix} \zeta_1 + i\eta_1 \\ \rho_1 + \omega_1 + i\psi_1 \end{pmatrix} \,, \qquad \Phi_2 = \frac{1}{\sqrt{2}} \begin{pmatrix} \zeta_2 + \omega_{\text{CB}} + i\eta_2 \\ \rho_2 + \omega_2 + i\left(\psi_2 + \omega_{\text{CP}}\right) \end{pmatrix} \,, \tag{3.12}$$

[4] We emphasize that the framework of the effective potential is using the Landau gauge. It is also possible to formulate the effective potential in the general R_ξ gauge. However, the renormalization of the Pseudo-Nambu-Goldstone Dark Matter (PNGDM) and Vector Dark Matter (VDM) requires the discussion of the gauge-fixing terms, where the treatment is analogous to the C2HDM.

with the most general vacuum structure of the C2HDM

$$\langle\Phi_1\rangle = \frac{1}{\sqrt{2}}\begin{pmatrix}0\\ \omega_1\end{pmatrix} \quad \text{and} \quad \langle\Phi_2\rangle = \frac{1}{\sqrt{2}}\begin{pmatrix}\omega_{\text{CB}}\\ \omega_2 + i\omega_{\text{CP}}\end{pmatrix} . \tag{3.13}$$

The general tree-level vacuum structure of the 2HDM allows for three different possible vacua, the normal EW-breaking, a CP-breaking and a charge breaking (CB) vacuum. It was shown that these vacua cannot coexist simultaneously at tree-level [74–76]. However, higher-order corrections or finite temperature effects might alter these statements and we allow for the most general vacuum structure by including ω_{CB} and ω_{CP} in the VEV structure defined in Eq. (3.13). In this way, it is possible to check for next-to-leading-order (NLO) vacuum stability or investigate the vacuum structure at finite temperature. To identify the correct EW-breaking tree-level vacuum at zero temperature, we enforce

$$v_i \equiv \omega_i\big|_{T=0} , \qquad i = 1, 2, \text{CP}, \text{CB} , \tag{3.14}$$

with

$$v_{\text{CP}} = v_{\text{CB}} \equiv 0 . \tag{3.15}$$

The SM VEV v is related to the VEV components of the two Higgs doublets through

$$v_1^2 + v_2^2 \equiv v^2 = (246.22\text{GeV})^2 . \tag{3.16}$$

The ratio of the VEV components is defined by the mixing angle β as

$$\tan\beta = \frac{v_2}{v_1} . \tag{3.17}$$

After the EW symmetry breaking three of the eight degrees of freedom introduced through the two Higgs doublets become the would-be Goldstone bosons. They are *absorbed* by the EW gauge bosons in order to give them mass. The remaining degrees of freedom ζ_i and η_i can be diagonalized to the charged sector with the rotation matrix

$$R_\beta = \begin{pmatrix}\cos\beta & \sin\beta\\ -\sin\beta & \cos\beta\end{pmatrix} . \tag{3.18}$$

The mass eigenstates are the charged Goldstone bosons $G^\pm$ and the charged Higgs bosons $H^\pm$. The remaining neutral scalar sector consists of three neutral Higgs bosons. In a CP-conserving 2HDM these mass eigenstates correspond to two CP-even neutral Higgs bosons h, H and the pseudoscalar A [77,78]. However, in the C2HDM the neutral mass eigenstates are CP-mixed states.
The tree-level minimum conditions on the tree-level potential

$$\frac{\partial V^{(0)}_{\text{C2HDM}}}{\partial\Phi_i^\dagger}\Big|_{\Phi_j=\langle\Phi_j\rangle} \overset{!}{=} 0 , \quad i,j \in \{1,2\} , \tag{3.19}$$

yield the following relations between the Lagrange parameters

$$m_{11}^2 = \text{Re}\; m_{12}^2\frac{v_2}{v_1} - \frac{\lambda_1}{2}v_1^2 - \frac{\lambda_3+\lambda_4+\text{Re}\;\lambda_5}{2}v_2^2 , \tag{3.20a}$$

$$m_{22}^2 = \text{Re}\; m_{12}^2\frac{v_1}{v_2} - \frac{\lambda_2}{2}v_2^2 - \frac{\lambda_3+\lambda_4+\text{Re}\;\lambda_5}{2}v_1^2 , \tag{3.20b}$$

$$\text{Im}\; m_{12}^2 = \text{Im}\;\lambda_5\frac{v_1 v_2}{2} , \tag{3.20c}$$

allowing us to express the mass parameters m_{11}^2 and m_{22}^2 in terms of the Higgs self-couplings λ_i, the VEVs v_1,v_2 and the soft breaking parameter m_{12}^2. Because of two complex Lagrange parameters, two complex phases $\phi(m_{12}^2)$ and $\phi(\lambda_5)$ can give rise to CP-violation. The phases are defined by

$$m_{12}^2 = \left|m_{12}^2\right| \exp(i\phi(m_{12}^2)) \quad \text{and } \lambda_5 = |\lambda_5| \exp(i\lambda_5) \ , \tag{3.21}$$

where Eq. (3.20c) can be used to relate the two phases to each other [71]

$$2\text{Re } (m_{12}^2) \tan\phi(m_{12}^2) = v_1 v_2 \text{Re } (\lambda_5) \tan\phi(\lambda_5) \ . \tag{3.22}$$

By requiring $\phi(\lambda_5) \neq 2\phi(m_{12}^2)$, it is ensured that both phases cannot be removed simultaneously [79].
The diagonalization of the mass matrix of the neutral sector requires the introduction of three mixing angles α_i $(i = 1, 2, 3)$ and the rotation matrix

$$R = \begin{pmatrix} c_1 c_2 & s_1 c_2 & s_s \\ -(c_1 s_2 s_3 + s_1 c_3) & c_1 c_3 - s_1 s_2 s_3 & c_2 s_3 \\ -c_1 s_2 c_3 + s_1 s_3 & -(c_1 s_3 + s_1 s_2 c_3) & c_2 c_3 \end{pmatrix} \ , \tag{3.23}$$

with the shorthand notation $c_i \equiv \cos\alpha_i$ and $s_i \equiv \sin\alpha_i$, respectively. The mixing angles can be chosen without loss of generality in the range of

$$-\frac{\pi}{2} \leq \alpha_i < \frac{\pi}{2} \, . \tag{3.24}$$

The resulting diagonalised mass matrix

$$R\mathcal{M}^2 R^T = \text{diag}(m_{H_1}^2, m_{H_2}^2, m_{H_3}^2) \ , \tag{3.25}$$

is assumed to be mass ordered, $m_{H_1} \leq m_{H_2} \leq m_{H_3}$. Note that one of the three neutral Higgs bosons will be identified to be the SM Higgs boson, hence three different mass hierachies are possible, where the SM-like Higgs boson is the lightest, heaviest or lies in between of the two non-SM like neutral Higgs bosons. The nine independent input parameters of the C2HDM are given by

$$v \ , \tan\beta \ , \alpha_{1,2,3} \ , m_{H_1} \ , m_{H_2} \ , m_{H^\pm} \ , \text{Re } \left(m_{12}^2\right) \ , \tag{3.26}$$

where the remaining heaviest neutral Higgs boson mass can be expressed as [71]

$$m_{H_3}^2 = \frac{m_{H_1}^2 R_{13} \left(R_{12} \tan\beta - R_{11}\right) + m_{H_2}^2 R_{23} \left(R_{22} \tan\beta - R_{21}\right)}{R_{33} \left(R_{31} - R_{32} \tan\beta\right)} \ . \tag{3.27}$$

3.2.2. The Yukawa Sector of the C2HDM

In order to avoid the presence of FCNCs at tree level, the natural flavor conservation allows us to extend the $\mathbb{Z}_2$ symmetry in four different ways to the Yukawa sector. The Yukawa Lagrangian has the following form in the mass basis $(i = 1, 2, 3)$ [71]

$$\mathcal{L}_{\text{Yuk}} \supset -\frac{m_f}{v} \overline{\psi}_f \left[c^e(H_i f f) + i c^o(H_i f f)\gamma_5\right] \psi_f H_i \ , \tag{3.28}$$

with the respective SM fermion mass m_f and spinor ψ_f. The effective CP-even (odd) Higgs fermion couplings $c^{e(o)}$ are given in Tab. 3.2. However, the effective Higgs fermion couplings can also be interpreted as complex fermion masses which allows for the extraction of the corresponding source term required for electroweak baryogenesis as discussed in Chapter 9.

	Type I		Type II		FL		LS	
	c^e	c^o	c^e	c^o	c^e	c^o	c^e	c^o
up-type quarks	$\frac{R_{i2}}{\sin\beta}$	$-\frac{R_{i3}}{\tan\beta}$	$\frac{R_{i2}}{\sin\beta}$	$-\frac{R_{i3}}{\tan\beta}$	$\frac{R_{i2}}{\sin\beta}$	$-\frac{R_{i3}}{\tan\beta}$	$\frac{R_{i2}}{\sin\beta}$	$-\frac{R_{i3}}{\tan\beta}$
down-type quarks	$\frac{R_{i2}}{\sin\beta}$	$\frac{R_{i3}}{\tan\beta}$	$\frac{R_{i1}}{\cos\beta}$	$-R_{i3}\tan\beta$	$\frac{R_{i1}}{\cos\beta}$	$R_{i3}\tan\beta$	$\frac{R_{i2}}{\sin\beta}$	$-\frac{R_{i3}}{\tan\beta}$
leptons	$\frac{R_{i2}}{\sin\beta}$	$\frac{R_{i3}}{\tan\beta}$	$\frac{R_{i1}}{\cos\beta}$	$-R_{i3}\tan\beta$	$\frac{R_{i2}}{\sin\beta}$	$-\frac{R_{i3}}{\tan\beta}$	$\frac{R_{i1}}{\cos\beta}$	$R_{i3}\tan\beta$

Table 3.2.: The effective CP-even and CP-odd couplings between the Higgs boson H_i ($i = 1,2,3$) and the SM fermions ψ_f for `Type I`, `Type II`, `Lepton-specific` (LS) and `Flipped (FL)`.

3.3. The Singlet Extension of the Standard Model

Another possibility to extend the SM Higgs sector while automatically fulfilling the experimental results for the ρ parameter defined in Eq. (3.2), is to extend the SM with additional singlets. Singlet extensions yield a rich phenomenology at the LHC. Since the additional singlet is not charged under the SM gauge groups $SU(3)_C \otimes SU(2)_L \otimes U(1)_Y$, it is not coupled to fermions or gauge bosons. Hence, the only SM interaction is through the Higgs field itself. The mixing of the singlet with the Higgs doublet allows for modifications of the Higgs interactions and changes the Higgs decay processes compared to the ones expected in the SM. In the following we introduce a complex singlet extension of the SM providing a DM WIMP candidate in the Higgs spectrum. The Yang-Mills Lagrangian and the kinetic Lagrangian $\mathcal{L}_{YM}$ and $\mathcal{L}_{\rm F}$ are the same as in the SM, hence we do not show their explicit form. Also the gauge-fixing and Fadeev-Popov Lagrangian are analogous to the C2HDM. The scalar Lagrangian for the PNGDM reads

$$\mathcal{L}_{\rm S}^{\rm PNGDM} = (D_\mu \Phi)^\dagger (D^\mu \Phi) + (\partial_\mu S)^* (\partial^\mu S) - V^{(0)}_{\rm PNGDM} \,, \tag{3.29}$$

with the Higgs doublet Φ and the complex singlet S. Note that the singlet field S does not have a charge under the SM group, consequently the covariant derivative reduces to the conventional partial derivative. The tree-level Higgs potential $V^{(0)}_{\rm PNGDM}$ is given by

$$V^{(0)}_{\rm PNGDM} = -\frac{\mu_H^2}{2}|\Phi|^2 + \frac{\lambda_H}{2}|\Phi|^4 - \frac{\mu_S^2}{2}|S|^2 + \frac{\lambda_S}{2}|S|^4 + \lambda_{HS}|\Phi|^2|S|^2 - \frac{m_\chi^2}{4}(S^2 + S^{*2}) \,. \tag{3.30}$$

The first two terms in the potential reflect the SM Higgs potential for a single Higgs doublet Φ and the following two terms correspond to a singlet scalar Higgs potential. The term proportional to λ_{HS} corresponds to a *Higgs portal* mixing the singlet field S with the Higgs doublet. Note that the potential without the last term is symmetric under a global $U(1)$ gauge transformation

$$S \to \exp(i\alpha) S \,, \quad \Phi \to \exp(i\alpha)\Phi \,. \tag{3.31}$$

However, the mass term $\sim \frac{m_\chi^2}{4}(S^2 + S^{*2})$ breaks explicitly the $U(1)$ symmetry of the potential. This $U(1)$ breaking gives rise to the Pseudo-Nambu Goldstone nature of the DM candidate and yields interesting phenomenological consequences [80]. They will be discussed in Chapter 5. The boundedeness from below condition as discussed in Sec. 3.1 implies that the self-couplings obey

$$\lambda_H > 0, \qquad \lambda_S > 0, \qquad \lambda_{HS} > -\sqrt{\lambda_H \lambda_S} \,. \tag{3.32}$$

The vacuum structure of the PNGDM is chosen to be the normal EW breaking vacuum with the additional singlet contribution,

$$\langle H \rangle = \frac{1}{\sqrt{2}} \begin{pmatrix} 0 \\ v \end{pmatrix} , \quad \langle S \rangle = \frac{v_s}{\sqrt{2}} , \tag{3.33}$$

with the EW VEV $v = 246.22\,\text{GeV}$ and the singlet VEV v_s. The singlet VEV v_s is an open input parameter in the PNGDM and chosen to be real and positive.
The minimum conditions analogous to Eq. (3.19) are given by

$$\begin{aligned} \left\langle \frac{\partial V^{(0)}_{\text{PNGDM}}}{\partial \Phi} \right\rangle = 0 \qquad &\Longleftrightarrow \qquad T_\Phi \equiv \frac{v}{2}\left(-\mu_H^2 + \lambda_H v^2 + \lambda_{HS} v_s^2\right) = 0 \,, \\ \left\langle \frac{\partial V^{(0)}_{\text{PNGDM}}}{\partial S} \right\rangle = 0 \qquad &\Longleftrightarrow \qquad T_S \equiv \frac{v_s}{2}\left(-\mu_S^2 + \lambda_S v_s^2 + \lambda HS v^2 - m_\chi^2\right) = 0 \,, \end{aligned} \tag{3.34}$$

where the tadpoles T_Φ and T_S are explicitly kept. They are required to formulate the proper renormalization conditions and the correct treatment of the VEV renormalization. The details will be discussed in Sec. 4.1. The singlet and doublet are expanded around their VEV with the fields according to

$$\Phi = \begin{pmatrix} G^+ \\ \frac{1}{\sqrt{2}}\left(v + \Phi_H + i G^0\right) \end{pmatrix} , \qquad S = \frac{1}{\sqrt{2}}\left(v_s + \Phi_S + i\chi\right) \,, \tag{3.35}$$

with the scalar fields in the gauge basis $\{\Phi_H, \Phi_S\}$, the VEVs v, v_s, the charged and neutral Goldstone bosons G^+,G^0 and the DM field χ. Note that the imaginary component of the singlet does not obtain a VEV contribution, hence it is not coupled to the SM particle content. Solely, an interaction between the Higgs bosons with the DM field χ is present in this model. This kind of models is often referred to as *Higgs portal* models.
The neutral Higgs mass matrix is given by

$$\mathcal{M}_T^2 = \mathcal{M}^2 + \mathcal{T} \,, \quad \mathcal{M}^2 = \begin{pmatrix} \lambda_H v^2 & \lambda_{HS} v v_s \\ \lambda_{HS} v v_s & \lambda_S v_s^2 \end{pmatrix} , \quad \mathcal{T} = \begin{pmatrix} T_H/v & 0 \\ 0 & T_S/v_s \end{pmatrix} , \tag{3.36}$$

where the explicit tadpole contributions are kept. The diagonalization of the mass matrix can be achieved by introducing a mixing angle α with the rotation matrix

$$R(\alpha) \equiv \begin{pmatrix} \cos\alpha & \sin\alpha \\ -\sin\alpha & \cos\alpha \end{pmatrix} , \tag{3.37}$$

yielding the diagonal mass matrix and the mass eigenstates h_i $(i = 1, 2)$,

$$M^2 \equiv R(\alpha)\, \mathcal{M}^2\, R^{-1}(\alpha) = \begin{pmatrix} m_{h_1}^2 & 0 \\ 0 & m_{h_2}^2 \end{pmatrix} , \qquad \begin{pmatrix} h_1 \\ h_2 \end{pmatrix} \equiv R(\alpha) \begin{pmatrix} \Phi_H \\ \Phi_S \end{pmatrix} . \tag{3.38}$$

Note that the explicit tadpole contribution in Eq. (3.36) is dropped in Eq. (3.38). The mass terms in Eq. (3.38) correspond to the tree-level masses of the PNGDM parameters.
The PNGDM can be described with eight independent input parameter given by

$$v \,,\; v_s \,,\; \alpha \,,\; m_{h_1}^2 \,,\; m_{h_2}^2 \,,\; m_\chi^2 \,,\; T_H \,,\; T_S \,, \tag{3.39}$$

where the Lagrange parameters can be determined via

$$\begin{aligned}\lambda_{HS} &= -\frac{m_{h_2}^2 - m_{h_1}^2}{2vv_s}\sin 2\alpha\,,\\ \lambda_H &= \frac{m_{h_2}^2\sin^2\alpha + m_{h_1}^2\cos^2\alpha}{v^2}\,,\\ \lambda_S &= \frac{m_{h_2}^2\cos^2\alpha + m_{h_1}^2\sin^2\alpha}{v_s^2}\,.\end{aligned} \tag{3.40}$$

Analogous to the C2HDM, FCNCs can be avoided by extending the $\mathbb{Z}_2$ symmetry of the Higgs doublet $\Phi \to -\Phi$ to the Yukawa sector. Since there is only one Higgs doublet Φ in the PNGDM, all quark types (up- and down-type) and leptons have to be coupled to the Higgs doublet in order to enable the BEH mechanism giving mass to the fermions. Hence, the PNGDM corresponds effectively to a `Type I` model.

3.4. The Vector Dark Matter Model

The nature of possible DM particles remains an open question in modern physics. However, the framework of non-minimal extended Higgs sector models allows us to investigate all the different spin constellations for the DM candidate. By demanding renormalizability of the model, there remain three different spin natures of the DM candidate, spin 0, 1/2 and 1. The PNGDM presented in Sec. 3.3 yields a spin 0 DM candidate. In the following we will present a possible spin 1 DM candidate, thus the DM candidate corresponds to a vector DM candidate. The VDM model is similar to the complex singlet extension in Sec. 3.3, however the *dark* $U(1)_\chi$ is gauged. Thus, the covariant derivative in the scalar Lagrangian of the VDM model

$$\mathcal{L}_{\mathrm{S}}^{\mathrm{VDM}} = (D_\mu\Phi)^\dagger\,(D^\mu\Phi) + (d_\mu S)^*\,(d^\mu S) - V_{\mathrm{VDM}}^{(0)}\,, \tag{3.41}$$

is extended by the new gauge field χ_μ and the respective gauge coupling g_χ

$$d_\mu \equiv \partial_\mu + ig_\chi\chi_\mu\,. \tag{3.42}$$

Note that the Higgs doublet is not charged under the dark $U(1)_\chi$, hence the covariant derivative D_μ applied on the Higgs doublet is given by Eq. (2.5), while the covariant derivative d_μ acting on the singlet field solely consists of the partial derivative plus the additional DM gauge field χ. The tree-level Higgs potential reads

$$V = -\mu_H^2|\Phi|^2 + \lambda_H|\Phi|^4 - \mu_S^2|S|^2 + \lambda_S|S|^4 + \kappa|S|^2|\Phi|^2\,, \tag{3.43}$$

with the Higgs doublet Φ and the complex singlet S. All parameters in the potential are real. Contrary to Eq. (3.30), there is no soft-breaking mass term present in the potential. Consequently, the dark $U(1)_\chi$ is not broken explicitly.
The field expansion is analogous to the PNGDM given by

$$H = \begin{pmatrix} G^+ \\ \frac{1}{\sqrt{2}}\left(v + \Phi_H + i\sigma_H\right)\end{pmatrix} \quad \text{and} \quad S = \frac{1}{\sqrt{2}}\left(v_S + \Phi_S + i\sigma_S\right)\,, \tag{3.44}$$

with the real scalar fields Φ_H, Φ_S, σ_H and σ_S. The VEVs are denoted by $v = 246.22\mathrm{GeV}$ and the singlet VEV as v_s.
The neutral scalar mass matrix is given by

$$\mathcal{M}_{\Phi_h\Phi_S} = \begin{pmatrix} 2\lambda_H v^2 & \kappa v v_S \\ \kappa v v_S & 2\lambda_S v_S^2\end{pmatrix} + \begin{pmatrix} \frac{T_{\Phi_H}}{v} & 0 \\ 0 & \frac{T_{\Phi_S}}{v_S}\end{pmatrix}\,, \tag{3.45}$$

where again the explicit tadpole contributions are kept in the mass matrix. The tadpoles are defined through the minimum conditions of the tree-level potential

$$\left\langle \frac{\partial V}{\partial \Phi_H} \right\rangle \equiv \frac{T_{\Phi_H}}{v} = \left(\frac{\kappa v_S^2}{2} + \lambda_H v^2 - \mu_H^2 \right) , \tag{3.46}$$

$$\left\langle \frac{\partial V}{\partial \Phi_S} \right\rangle \equiv \frac{T_{\Phi_S}}{v_S} = \left(\frac{\kappa v^2}{2} + \lambda_S v_S^2 - \mu_S^2 \right) . \tag{3.47}$$

These contributions are needed in order to renormalize the EW VEV consistently. Defining a mixing angle α as in Eq. (3.38) makes it possible to diagonalize the mass matrix and with the help of the minimum conditions it is possible to relate the Lagrange parameters to the masses masses, the VEVs and the mixing angle α

$$\lambda_H = \frac{m_{h_1}^2 \cos^2\alpha + m_{h_2}^2 \sin^2\alpha}{2v^2} , \tag{3.48a}$$

$$\kappa = \frac{\left(m_{h_1}^2 - m_{h_2}^2\right) \cos\alpha \sin\alpha}{v v_S} , \tag{3.48b}$$

$$\lambda_S = \frac{m_{h_1}^2 \sin^2\alpha + m_{h_2}^2 \cos^2\alpha}{2v_S} , \tag{3.48c}$$

$$v_S = \frac{m_\chi}{g_\chi} . \tag{3.48d}$$

We emphasize, that the singlet VEV is now a function of the DM mass and the gauge coupling contrary to the PNGDM, where the singlet VEV was an input parameter. The resulting input parameters of the VDM model are chosen to be

$$m_{h_1} , m_{h_2} , m_\chi , \alpha , v , g_\chi , T_{\Phi_H} , T_{\Phi_S} . \tag{3.49}$$

3.5. The Next-to Minimal Two-Higgs Doublet Model

The last non-minimal extended Higgs sector model presented in this thesis is a combination of a doublet and singlet extension, the Next-to-Two-Higgs-Doublet Model (N2HDM). It consists of a CP-conserving Two-Higgs-Doublet Model (2HDM) with a softly broken $\mathbb{Z}_2$ symmetry between the two Higgs doublets Φ_i $(i = 1, 2)$ analogous to the C2HDM, while the singlet field does not transform,

$$\Phi_1 \to \Phi_1 , \quad \Phi_2 \to -\Phi_2 , \quad \Phi_S \to \Phi_S . \tag{3.50}$$

Another $\mathbb{Z}_2'$ symmetry is introduced under which the fields transform as

$$\Phi_1 \to \Phi_1 , \quad \Phi_2 \to \Phi_2 , \quad \Phi_S \to -\Phi_S . \tag{3.51}$$

The overall EW Lagrangian remains unchanged compared to Eq. (3.9). Note that the singlet field is not charged under the SM gauge groups $SU(3)_C \otimes SU(2) \otimes U(1)_Y$, yet the covariant derivatives for the two Higgs doublets are the same as in the C2HDM in Eq. (2.5).
The tree-level potential of the N2HDM is given by

$$\begin{aligned} V_{\text{N2HDM}}^{(0)} = {} & m_{11}^2 \Phi_1^\dagger \Phi_1 + m_{22}^2 \Phi_2^\dagger \Phi_2 - m_{12}^2 \left(\Phi_1^\dagger \Phi_2 + \text{h.c.} \right) + \frac{\lambda_1}{2} \left(\Phi_1^\dagger \Phi_1 \right)^2 + \frac{\lambda_2}{2} \left(\Phi_2^\dagger \Phi_2 \right)^2 \\ & + \lambda_3 \Phi_1^\dagger \Phi_1 \Phi_2^\dagger \Phi_2 + \lambda_4 \Phi_1^\dagger \Phi_2 \Phi_2^\dagger \Phi_1 + \frac{\lambda_5}{2} \left((\Phi_1^\dagger \Phi_2)^2 + \text{h.c.} \right) \\ & + \frac{1}{2} m_S^2 \Phi_S^2 + \frac{\lambda_6}{8} \Phi_S^4 + \lambda_7 \left(\Phi_1^\dagger \Phi_1 \right) \Phi_S^2 + \lambda_8 \left(\Phi_2^\dagger \Phi_2 \right) \Phi_S^2 , \end{aligned} \tag{3.52}$$

with the two Higgs doublets Φ_i $(i = 1, 2)$ and the singlet field Φ_S. All Lagrange parameters are real due to hermicity implying that the N2HDM is a CP-conserving extension of the SM. The mass parameter m_{12}^2 breaks the $\mathbb{Z}_2$ symmetry, while the terms proportional to λ_7 and λ_8 induce the mixing of the doublet fields and the singlet field.
The field expansions around the VEV are defined as

$$\Phi_1 = \frac{1}{\sqrt{2}} \begin{pmatrix} \zeta_1 + i\eta_1 \\ \rho_1 + \omega_1 + i\psi_1 \end{pmatrix}, \qquad \Phi_2 = \frac{1}{\sqrt{2}} \begin{pmatrix} \zeta_2 + \omega_{\mathrm{CB}} + i\eta_2 \\ \rho_2 + \omega_2 + i\left(\psi_2 + \omega_{\mathrm{CP}}\right) \end{pmatrix}, \qquad \Phi_S = \rho_3 + \omega_S\,, \tag{3.53}$$

with the CP-even (odd) charged components ζ_i (η_i) and the CP-even (odd) neutral components ρ_i (ψ_i). The singlet field is assumed to be real. The general tree-level vacuum structure of the 2HDM is shown to be either a normal EW-breaking, CP-violating or a CB-vacuum [74–76], however this does not generalize to the N2HDM. In [81, 82] explicit counter examples are given, where the CP/CB-vacua coexist next to EW-breaking vacua. Thus, we include the most general vacuum structure in Eq. (3.53) with the EW-breaking VEVs ω_i $(i = 1, 2)$, the CP-violating VEV ω_{CP} and the CB VEV ω_{CB}. The inclusion of the general vacuum structures allows for the investigation of the NLO stability of the EW minimum and furthermore the stability concerning finite temperature effects on the Higgs potential. To obtain the EW-breaking vacuum at zero temperature, we enforce

$$\langle\Phi_1\rangle\big|_{T=0} = \frac{1}{\sqrt{2}} \begin{pmatrix} 0 \\ v_1 \end{pmatrix}, \qquad \langle\Phi_2\rangle\big|_{T=0} = \frac{1}{\sqrt{2}} \begin{pmatrix} 0 \\ v_2 \end{pmatrix}, \qquad \langle S\rangle\big|_{T=0} = v_S\,, \tag{3.54}$$

with the VEV definitions

$$v_i \equiv \omega_i\big|_{T=0}\,, \quad i = 1, 2, S, \mathrm{CP}, \mathrm{CB}\,. \tag{3.55}$$

The CP-violating and CB VEVs are hence chosen to be vanishing at zero temperature

$$v_{\mathrm{CP}} = v_{\mathrm{CB}} = 0\,. \tag{3.56}$$

Requiring the tree-level potential to be minimized at the EW VEV leads to three minimum conditions given by

$$v_2 m_{12}^2 - v_1 m_{11}^2 = \frac{v_1}{2}\left(v_1^2\lambda_1 + v_2^2\lambda_{345} + v_S^2\lambda_7\right) \tag{3.57a}$$

$$v_1 m_{12}^2 - v_2 m_{22}^2 = \frac{v_2}{2}\left(v_1^2\lambda_{345} + v_2^2\lambda_2 + v_S^2\lambda_8\right) \tag{3.57b}$$

$$-m_S^2 v_s = \frac{v_s}{2}\left(v_1^2\lambda_7 + v_2^2\lambda_8 + v_S^2\lambda_6\right)\,, \tag{3.57c}$$

where the shorthand notation

$$\lambda_{345} \equiv \lambda_3 + \lambda_4 + \lambda_5 \tag{3.58}$$

is introduced. With the introduction of the singlet field and the mixing terms ($\sim \lambda_7, \lambda_8$) in Eq. (3.52), the CP-even neutral Higgs sector of the N2HDM is extended with respect to the real CP-conserving 2HDM. The resulting 3×3 neutral scalar Higgs mass matrix is given by

$$\mathcal{M}^2 = \begin{pmatrix} v^2\lambda_1 c_\beta^2 + m_{12}^2 t_\beta & v^2\lambda_{345}c_\beta s_\beta - m_{12}^2 & v v_S \lambda_7 c_\beta \\ v^2\lambda_{345}c_\beta s_\beta - m_{12}^2 & v^2\lambda_2 s_\beta^2 + m_{12}^2/t_\beta & v v_S \lambda_8 s_\beta \\ v v_S \lambda_7 c_\beta & v v_S \lambda_8 s_\beta & v_S^2\lambda_6 \end{pmatrix}. \tag{3.59}$$

By introducing three mixing angles α_i $(i = 1, 2, 3)$ and using the same parametrization as in Eq. (3.23) the mass matrix can be diagonalized,

$$R\mathcal{M}^2 R^T = \text{diag}(m_{H_1}^2, m_{H_2}^2, m_{H_3}^2) \,, \tag{3.60}$$

with three Higgs mass eigenstates

$$\begin{pmatrix} h_1 \\ h_2 \\ h_3 \end{pmatrix} = R \begin{pmatrix} \rho_1 \\ \rho_2 \\ \rho_S \end{pmatrix} \,. \tag{3.61}$$

An explicit mass ordering is assumed for the mass eigenstates with

$$m_{H_1} \leq m_{H_2} \leq m_{H_3} \,. \tag{3.62}$$

Both neutral Higgs sectors of the C2HDM and N2HDM yield three neutral Higgs bosons h_i $(i = 1, 2, 3)$. Note that the mass eigenstates of the C2HDM are CP-mixed states, contrary to the Higgs mass eigenstates in the N2HDM. The fields h_i $(i = 1, 2, 3)$ are all CP-even fields. The diagonalization of the CP-odd part of the N2HDM requires the introduction of

$$\tan\beta \equiv {}^{v_2}/_{v_1} \,, \tag{3.63}$$

yielding the mass eigenstates of the charged Goldstone boson, the charged Higgs boson and the pseudo-scalar Higgs boson A [81]. In the end, the following input parameters for the N2HDM are chosen

$$\alpha_1 \,, \quad \alpha_2 \,, \quad \alpha_3 \,, \quad \tan\beta \,, \quad v \,, \quad v_S \,, \quad m_{H_{1,2,3}} \,, \quad m_A \,, \quad m_{H^\pm} \,, \quad m_{12}^2 \,, \tag{3.64}$$

where the soft-breaking mass scale m_{12}^2 is kept as open input parameter.

Part II.

Electroweak Corrections to the Spin-Independent Cross Section

CHAPTER 4

Theoretical Foundations

Dark Matter (DM) is one of the remaining open questions in modern physics. While its nature and properties are unknown, one thing we know is that there must be some sort of matter interacting gravitationally with observable matter. One possibility to explain the non-observable mass is through the introduction of *weakly interacting massive particles* (WIMPs). These additional massive particles contribute to the mass density of the universe, however their weak interactions with the Standard Model (SM) particle content would explain why we have not observed them (yet). There is a substantial effort to develop search strategies for DM to derive its properties and nature. Such experiments rely on precise predictions of the underlying DM models. So far, most of the WIMP DM model predictions are based on tree-level calculations, where NLO corrections might play an important role, or even alter the derived constraints on the parameter space of the underlying models. Hence, we want to investigate the electroweak (EW) next-to-leading-order (NLO) corrections on one possible observable, the spin-independent cross-section (SI-cxn). In particular, the predicted SI-cxns are calculated with the respective EW NLO corrections taken into account and compared to the recent Xenon-1T results. For that purpose, we introduce the basic idea of regularization and renormalization of UV divergences in Sec. 4.1. We introduce the on-shell (OS) counterterms required to cancel all emerging UV poles in a consistent way in Secs. 4.1.1 to 4.1.5. We further introduce some basics in DM phenomenology required for the derivation of the expected signals in a direct detection experiment in Sec. 4.2.2. We conclude our introduction with the discussion of the theoretical prediction of the SI-cxn in terms of effective Wilson coefficients, which can be identified with Feynman diagrams of the underlying DM model in Sec. 4.3. In the end, we explain how do we extract the Wilson coefficients for the models Pseudo-Nambu-Goldstone Dark Matter (PNGDM) and Vector Dark Matter (VDM).

4.1. Regularization and Renormalization of Non-minimal Extended Higgs Sectors

An example to illustrate the problem of renormalization is given by the following simple diagram in a ϕ^4 theory

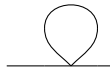

$$= -\frac{i\lambda}{2} \int \frac{d^4k}{(2\pi)^4} \frac{i}{k^2 - m^2} \ , \tag{4.1}$$

with the quartic self-coupling λ, the mass m of the field ϕ and the loop momentum k, respectively. This kind of diagrams occurs in higher-order corrections. However, the integral is explicitly UV divergent, as we show in the following. Performing a Wick rotation $k^0 \to ik_E^0$ and identifying the components of the 4-momentum as $\mathbf{k} \to \mathbf{k}_E$, yields the integral in a Euclidean metric

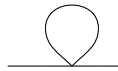

$$= \frac{i\lambda}{2} \cdot i \int \frac{d^4k_E}{(2\pi)^4} \frac{i}{k^2 + m^2} = -\frac{4\pi i\lambda}{2} \int_0^\infty \frac{dk_E}{(2\pi)^4} \frac{k_E^3}{k_E^2 + m^2} \ . \tag{4.2}$$

Introducing a cut-off on the loop momentum Λ,

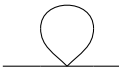

$$= -\frac{4\pi i\lambda}{2} \int_0^\Lambda \frac{dk_E}{(2\pi)^4} \frac{k_E^3}{k_E^2 + m^2} = -\frac{i\pi\lambda}{(2\pi)^4} \left(\Lambda^2 - m^2 \ln \frac{m^2 + \Lambda^2}{m^2} \right) \ , \tag{4.3}$$

makes the UV divergence explicit. The appearance of the divergences cannot be circumvented in a fixed-order calculation. However, higher-order predictions of physical observables are indeed finite, due to the cancellation of all emerging divergences.

The systematic cancellation of the divergences can be achieved by regularization and renormalization. In the process of the regularization the contributing UV poles are isolated from their finite contributions in a self-consistent way. A possible approach to regularize the UV poles is shown in Eq. (4.3). By introducing a cut-off for the loop momentum Λ, the UV poles are explicitly given in terms of Λ. If this regularization is applied on all contributions, the dependence on the cut-off scale Λ is canceled leaving the physical observable finite. However, the introduction of a cut-off scale is inconvenient especially for a gauge theory, due to the breaking of internal symmetries.

A more convenient method to regularize the UV poles is given by *dimensional regularization* (DimReg). The actual calculation of the integrals is performed in $d = 4 - 2\epsilon$ dimensions introducing an infinitesimal parameter ε. The introduced parameter restores the 4-dimensional result for $\epsilon \to 0$ and thus serves as a regulator. To ensure the correct mass dimension in the integration, an additional mass scale, the renormalization scale μ, has to be introduced

$$\int \frac{d^4p}{(2\pi)^4} \to \mu^{4-d} \int \frac{d^dp}{(2\pi)^d} \ . \tag{4.4}$$

Performing the d-dimensional integral and expanding the result for small ϵ allows us to calculate the above integral to be

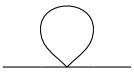

$$= -\frac{\lambda}{2} \left(-\frac{i}{16\pi^2} m^2 \left[\frac{1}{\epsilon} - \gamma_E + \log(4\pi) + \log\left(\frac{\mu^2}{m^2}\right) + 1 \right] + \mathcal{O}(\epsilon) \right) \tag{4.5a}$$

$$= i \frac{\lambda}{32\pi^2} m^2 \left(\Delta_\epsilon + 1 + \mathcal{O}(\epsilon) \right) \ , \tag{4.5b}$$

with the Euler-Mascheroni constant $\gamma_E \simeq 0.577$. In this way, the UV pole of the integral becomes explicit in terms of $1/\epsilon$, where the additional typical constants are taken in the definition of

$$\Delta_\epsilon \equiv \frac{1}{\varepsilon} - \gamma_E + \log(4\pi) \ . \tag{4.6}$$

In this way, it is possible to isolate all UV divergences in a fixed order calculation in terms of Δ_ϵ. In a second step, we need to cancel all UV divergences. The systematic cancellation method is called renormalization.

The basic assumption is that the independent input parameters of the underlying (renormalizable[5]) model are *bare* parameters. These bare parameters are not related to the physical

[5] In the context of this thesis, we deal only with renormalizable QFTs. It is also possible to cancel all UV divergences in a non-renormalizable QFT, however this has to be achieved *order-by-order* and thus requires the introduction of an infinite number of counterterms.

observed parameters and still contain the infinities. By expanding the bare parameters in terms of the renormalized parameters and the respective counterterms,

$$\rho_{i,0} \to \rho_i + \delta\rho_i \ , \tag{4.7a}$$

$$\phi_{j,0} = \sqrt{Z_{\phi_j}}\phi_j \simeq \left(1 + \frac{\delta Z_{\phi_j}}{2}\right)\phi_j \ , \tag{4.7b}$$

$$T_{i,0} \to T_i + \delta T_i \ , \tag{4.7c}$$

it is possible to separate the infinities in the counterterms and interpret the renormalized parameters to be the physical (finite) observables. In Eq. (4.7) we differentiate between three different kinds of counterterms. The first kind in Eq. (4.7a) corresponds to the input parameters *e.g.* the masses of the respective particles. Eq. (4.7b) indicates the wave-function renormalization constant (WFRC) $\sqrt{Z_\phi}$ ensuring the field renormalization, and the tadpole counterterms are introduced in Eq. (4.7c). These tadpole counterterms yield the *proper* treatment of the quantum corrections affecting the EW minimum. We will comment on this, while discussing the explicit form of the tadpole counterterms.
The renormalization scheme, or rather the renormalization condition, determines the finite parts of the counterterms. For example, in the *minimal subtraction ($\overline{MS}$) renormalization scheme* the respective counterterms are expected to exactly contain solely the UV poles (*e.g.* the Δ_ϵ part in Eq. (4.5)) and thus they do not have finite pieces apart from the universal constants defined in Δ_ϵ. Thus, the resulting renormalized parameter is finite.
Another approach is the so-called OS *scheme*. In the OS scheme three renormalization conditions are imposed

- the mixing of fields with same quantum numbers vanishes on the mass shells $p^2 = m^2_{\phi_i}$
- the physical masses are defined as the real parts of the poles of the renormalized propagator
- the normalization of the fields ϕ_i is such that the residue of the corresponding propagator at its pole is i.

We assume a scalar multiplet with the fields ϕ_i ($i = 1, \ldots, N$). These conditions allow us to determine the counterterms in terms of the self-energies evaluated at the respective mass shells.
In the following, we will introduce the explicit counterterms required for the renormalization of the VDM and PNGDM. Both models yield a similar scalar sector consisting of an $SU(2)$ doublet with an additional singlet field. The corresponding neutral Higgs sector consists of two mixing mass eigenstates h_i ($i = 1, 2$) with the mixing angle α. The fermion sector is equivalent in both models, hence the counterterms have the same form[6]. Furthermore, the SM-like gauge boson sector is the same in both models. For this reason, we can formulate the counterterms for both models simultaneously. The renormalization of the *dark sector* differs in the models, which we discuss at the end of this section.

4.1.1. Scalar Sector

We start the introduction with the scalar sector. We choose to renormalize the model in the mass basis, implying that we renormalize the input parameters listed in Eqs. (3.39) and (3.49).

[6]Note, however that the corresponding self-energies required for the determination of the counterterms are indeed different for both models.

Both models yield a CP-even neutral sector consisting of two mass-ordered mass eigenstates h_i $(i = 1, 2)$. The WFRC are defined as

$$\begin{pmatrix} h_1 \\ h_2 \end{pmatrix} \to \begin{pmatrix} 1 + \frac{1}{2}\delta Z_{h_1 h_1} & \frac{1}{2}\delta Z_{h_1 h_2} \\ \frac{1}{2}\delta Z_{h_2 h_1} & 1 + \frac{1}{2}\delta Z_{h_2 h_2} \end{pmatrix} \begin{pmatrix} h_1 \\ h_2 \end{pmatrix} . \tag{4.8}$$

The (bare) mass matrix is split into the mass terms and the respective tadpole matrix

$$\mathcal{M}_{h_1 h_2} = \begin{pmatrix} m_{h_1}^2 & 0 \\ 0 & m_{h_2}^2 \end{pmatrix} + \underbrace{R(\alpha) \begin{pmatrix} T_H/v & 0 \\ 0 & T_S/v_S \end{pmatrix} R(\alpha)^T}_{\equiv \delta T} . \tag{4.9}$$

Note that T_H and T_S correspond to the tadpoles of the scalar field of the doublet Φ_H and the singlet field Φ_S, respectively. The rotation matrix $R(\alpha)$ transforms from the gauge basis to the mass basis. The resulting tadpole matrix contributing to the mass matrix is referred to as δT.
EW corrections might alter the structure of the EW vacuum. To conserve the tree-level relations between the VEVs and input parameters, it is required to introduce tadpole counterterms, so that the renormalized tadpole $\hat{T}_i$ vanishes

$$\hat{T}_i = T_i - \delta T_i \stackrel{!}{=} 0 . \tag{4.10}$$

Note that this renormalization condition in Eq. (4.10) can be imposed on the gauge basis $(i = H, S)$ or the mass basis $(i = h_1, h_2)$, since the tadpoles are related through the rotation

$$\begin{pmatrix} T_{h_1} \\ T_{h_2} \end{pmatrix} = R(\alpha) \cdot \begin{pmatrix} T_H \\ T_S \end{pmatrix} . \tag{4.11}$$

This allows for the expansion of Eq. (4.9) to strict one-loop order

$$\mathcal{M}_{h_1 h_2} \to \mathcal{M}_{h_1 h_2} + \delta\mathcal{M}_{h_1 h_2} , \tag{4.12}$$

with the renormalized mass matrix $\mathcal{M}_{h_1 h_2}$ and the required counterterms

$$\delta\mathcal{M}_{h_1 h_2} = \begin{pmatrix} \delta m_{h_1}^2 & 0 \\ 0 & \delta m_{h_2}^2 \end{pmatrix} + R(\alpha) \begin{pmatrix} \frac{\delta T_H}{v} & 0 \\ 0 & \frac{\delta T_S}{v_S} \end{pmatrix} R(\alpha)^T \equiv \begin{pmatrix} \delta m_{h_1}^2 & 0 \\ 0 & \delta m_{h_2}^2 \end{pmatrix} + \begin{pmatrix} \delta T_{h_1 h_1} & \delta T_{h_1 h_2} \\ \delta T_{h_2 h_1} & \delta T_{h_2 h_2} \end{pmatrix} . \tag{4.13}$$

The terms of the order $\mathcal{O}(\delta\alpha\delta T_i)$ are dropped, since they are beyond the one-loop expansion. Imposing the OS condition yields the following set of counterterms for the CP-even neutral Higgs bosons h_i $(i = 1, 2)$ [83]

$$\delta m_{h_i}^2 = \mathrm{Re}\ \left[\Sigma_{h_i h_i}(m_{h_i}^2) - \delta T_{h_i h_i}\right] , \tag{4.14a}$$

$$\delta Z_{h_i h_i} = -\mathrm{Re}\ \left[\frac{\partial \Sigma_{h_i h_i}(p^2)}{\partial p^2}\right]_{p^2 = m_{h_i}^2} , \tag{4.14b}$$

$$\delta Z_{h_i h_j} = \frac{2}{m_{h_i}^2 - m_{h_j}^2} \mathrm{Re}\ \left[\Sigma_{h_i h_j}(m_{h_j}^2) - \delta T_{h_i h_j}\right] , \quad i \neq j . \tag{4.14c}$$

We emphasize again, that the equations are valid for both models PNGDM and VDM, however the explicit scalar self-energies $\Sigma_{h_i h_j}$ depend on the underlying model.

4.1.2. Renormalization of the Mixing Angle

The diagonalization of the mass matrix requires the introduction of a mixing angle. The mixing angle as an input parameter is promoted to one-loop order by splitting the mixing angle into a renormalized part and its respective counterterm,

$$\alpha_0 = \alpha + \delta\alpha\,. \tag{4.15}$$

However, there is no obvious physical observable that can be used to impose an OS scheme. Thus the renormalization is a non-trivial task.
One possible approach is proposed in [84], which we refer to as the KOSY scheme. The basic idea of the KOSY scheme is to relate the counterterms of the mixing angle to the off-diagonal elements of the OS WFRCs of the scalar sector. To do so, it is assumed that $\sqrt{Z_\Phi}$ contains the WFRCs of the gauge basis $\{\phi_H, \phi_S\}$, which can be related to the mass basis after the rotation

$$\begin{pmatrix} h_1 \\ h_2 \end{pmatrix} = R\left(\alpha + \delta\alpha\right) \sqrt{Z_\Phi} \begin{pmatrix} \Phi_H \\ \Phi_S \end{pmatrix}\,. \tag{4.16}$$

Expanding Eq. (4.16) to strict one-loop level yields

$$R\left(\alpha + \delta\alpha\right) \sqrt{Z_\Phi} \begin{pmatrix} \Phi_H \\ \Phi_S \end{pmatrix} = \underbrace{R(\delta\alpha)R(\alpha)\sqrt{Z_\Phi}R(\alpha)^T}_{\stackrel{!}{=}\sqrt{Z_H}} R(\alpha) \begin{pmatrix} \Phi_H \\ \Phi_S \end{pmatrix} + \mathcal{O}(\delta\alpha^2) = \sqrt{Z_H} \begin{pmatrix} h_1 \\ h_2 \end{pmatrix}\,, \tag{4.17}$$

allowing us to express the alternative WFRC matrix in the mass basis as

$$\sqrt{Z_H} = R(\delta\alpha) \begin{pmatrix} 1 + \dfrac{\delta Z_{h_1h_1}}{2} & \delta C_h \\ \delta C_h & 1 + \dfrac{\delta Z_{h_2h_2}}{2} \end{pmatrix} \approx \begin{pmatrix} 1 + \dfrac{\delta Z_{h_1h_1}}{2} & \delta C_h + \delta\alpha \\ \delta C_h - \delta\alpha & 1 + \dfrac{\delta Z_{h_2h_2}}{2} \end{pmatrix}\,, \tag{4.18}$$

with some constants δC_h, the respective WFRCs $\delta Z_{h_ih_j}$ of the mass basis and the mixing angle counterterm $\delta\alpha$. Note that the specific form of δC_h is not of importance, since $\sqrt{Z_\Phi}$ is only required to be symmetric. Imposing the OS conditions on the WFRCs in Eq. (4.18) yields

$$\frac{\delta Z_{h_1h_2}}{2} \stackrel{!}{=} \delta C_h + \delta\alpha \qquad \text{and} \qquad \frac{\delta Z_{h_2h_1}}{2} \stackrel{!}{=} \delta C_h - \delta\alpha\,, \tag{4.19}$$

and finally the mixing counterterm in the KOSY scheme [84] is given by

$$\delta\alpha = \frac{1}{4}\left(\delta Z_{h_1h_2} - \delta Z_{h_2h_1}\right) \tag{4.20}$$

$$= \frac{1}{2(m_{h_1}^2 - m_{h_2}^2)} \mathrm{Re}\,\left(\Sigma_{h_1h_2}(m_{h_2}^2) + \Sigma_{h_2h_1}(m_{h_1}^2) - 2\delta T_{h_1h_2}\right)\,. \tag{4.21}$$

Note that the explicit form of the KOSY counterterm of the mixing angle α in Eq. (4.20) requires exactly the same parametrization of the rotation matrix as the one defined in Eq. (3.18).

Another approach to renormalize the mixing angle is a process-dependent scheme. While the KOSY mixing angle counterterm is universal in the sense that the counterterm is unambiguous, a process-dependent scheme is as the name already suggests dependent on the process chosen to renormalize the angle. A specific process is taken. In particular, the SM-like Higgs boson decay $h \to \tau\tau$ is chosen for the renormalization of $\delta\alpha$ in the VDM model. The NLO corrections involve infrared (IR) divergences stemming from the QED corrections[7]. Since the

[7] We refer to NLO corrections with internal photon lines as QED corrections.

corresponding QED corrections form a UV-finite subset, it is possible to impose the renormalization conditions solely on the *weak* subset of diagrams. Hence, we require that the NLO and LO amplitude of the process are the same

$$\mathcal{A}^{\text{NLO,weak}}_{h\to\tau\tau} \stackrel{!}{=} \mathcal{A}^{\text{LO}}_{h\to\tau\tau}\,, \tag{4.22}$$

where the 'weak' indicates the NLO EW corrections without the QED subset. The NLO amplitude consists of the LO amplitude $\mathcal{A}^{\text{LO}}$, the genuine one-loop vertex corrections $\mathcal{A}^{\text{virt,weak}}$ and the respective vertex counterterm $\mathcal{A}^{\text{ct}}$

$$\mathcal{A}^{\text{NLO,weak}}_{h\to\tau\tau} = \mathcal{A}^{\text{LO}} + \mathcal{A}^{\text{virt,weak}} + \mathcal{A}^{\text{ct}}\,. \tag{4.23}$$

Imposing the process-dependent renormalization condition allows us to express the mixing angle counterterm as

$$\delta\alpha = -\left(\frac{\partial g_{h\tau\tau}}{\partial\alpha}\right)^{-1}\left[\mathcal{A}^{\text{virt,weak}} + \mathcal{A}^{\text{ct}}\big|_{\delta\alpha=0}\right]\,. \tag{4.24}$$

Here $\mathcal{A}^{\text{ct}}\big|_{\delta\alpha=0}$ denotes the complete counterterm amplitude but without the contribution from $\delta\alpha$ and $g_{h\tau\tau}$ indicates the LO coupling of the respective process.
The $\overline{\text{MS}}$ scheme yields another approach to express the mixing angle counterterm. Since the UV pole of the respective counterterm is unambiguous, the $\overline{\text{MS}}$ counterterm can be extracted from the the process-dependent counterterm by taking solely the UV-pole. The resulting $\overline{\text{MS}}$ counterterm does not contain any finite pieces, thus it is not dependent on the chosen process. In [85–88] different approaches to renormalize the mixing angle are discussed for the 2HDM and N2HDM, respectively. It turned out that process-dependent and $\overline{\text{MS}}$ renormalization scheme yield unphysically large counterterms, where the KOSY scheme tends to produce moderate NLO corrections. Nevertheless, all mentioned renormalization schemes for the mixing angle counterterm introduce explicit gauge parameter dependence in the counterterm. For a detailed discussion of this gauge dependence issue we refer to [85, 87].
The choice of the renormalization scheme for the mixing angle affects the NLO predictions (see *e.g.* [89,90]). We treat this freedom of choice as a theoretical uncertainty and compare different renormalization schemes for the mixing angle in the VDM model. This might allow for a rough estimate of the overall impact of theoretical uncertainty on the NLO EW predictions for the SI-cxn due to missing higher-order corrections beyond NLO.

4.1.3. Renormalization of the Gauge Sector

The VDM and PNGDM incorporate the SM gauge sector and the renormalization is not required to be changed compared to the SM. However, we introduce in the following our notation and conventions for the renormalization of the SM gauge sector. For a detailed introduction of EW radiative corrections we refer to [83, 91].
Analogous to the previous section, the bare input parameters are split into the renormalized parameter and its counterterm, respectively,

$$m_W^2 \to m_W^2 + \delta m_W^2\,, \tag{4.25a}$$
$$m_Z^2 \to m_Z^2 + \delta m_Z^2\,, \tag{4.25b}$$
$$e \to e + \delta Z_e e\,, \tag{4.25c}$$
$$g \to g + \delta g\,, \tag{4.25d}$$

with the masses m_W and m_Z of the SM gauge bosons W and Z, the electrical charge e and the $SU(2)$ gauge coupling g. The photon γ and Z gauge boson are allowed to mix with each other, hence the corresponding WFRCs have to form a 2×2 matrix,

$$\begin{pmatrix} Z \\ \gamma \end{pmatrix} \to \begin{pmatrix} 1+\frac{1}{2}\delta Z_{ZZ} & \frac{1}{2}\delta Z_{Z\gamma} \\ \frac{1}{2}\delta Z_{\gamma Z} & 1+\frac{1}{2}\delta Z_{\gamma\gamma} \end{pmatrix}\begin{pmatrix} Z \\ \gamma \end{pmatrix}\,, \tag{4.26a}$$

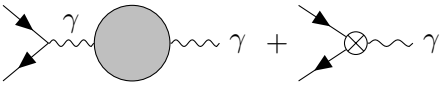

Figure 4.1.: The QED vertex counterterm of the three-point interaction of a photon with two fermions cancel the external leg corrections of the photon line if δZ_e is related to $\delta Z_{\gamma\gamma}$.

$$W^{\pm} \to \left(1 + \frac{1}{2}\delta Z_{WW}\right) W^{\pm}\,, \tag{4.26b}$$

where the W boson does not require a matrix structure. In the general R_ξ gauge, the renormalized two-point correlation function of the gauge bosons $V_i, V_j \in \{W^{\pm}, Z, \gamma\}$ can be brought into the following form [83]

$$\begin{aligned}\hat{\Gamma}^{\mu\nu}_{ij} = -i\left(g^{\mu\nu} - \frac{p^\mu p^\nu}{p^2}\right)\left(p^2 - m_V^2\right)\delta_{ij} - i\frac{p^\mu p^\nu}{p^2}\frac{1}{\xi_V}\left(p^2 - \xi_V m_V^2\right)\delta_{ij} \\ -i\left(g^{\mu\nu} - \frac{p^\mu p^\nu}{p^2}\right)\hat{\Sigma}^T_{ij}(p^2) - i\frac{p^\mu p^\nu}{p^2}\hat{\Sigma}^L_{ij}(p^2)\,,\end{aligned} \tag{4.27}$$

with the respective mass of the vector boson m_V, the corresponding gauge parameter ξ_V and the momentum p. The renormalized self-energies $\hat{\Sigma}^x_{ij}(p^2)$ are separated into a transversal ($x = T$) and longitudinal ($x = L$) contribution. Imposing OS conditions permits us to derive the corresponding OS counterterms for the gauge boson masses and WFRCs [83]

$$\delta m_W^2 = \mathrm{Re}\ \Sigma^T_{WW}\left(m_W^2\right) \quad \text{and} \quad \delta m_Z^2 = \mathrm{Re}\ \Sigma^T_{ZZ}\left(m_Z^2\right)\,, \tag{4.28}$$

and

$$\delta Z_{WW} = -\mathrm{Re}\ \left.\frac{\partial \Sigma^T_{WW}(p^2)}{\partial p^2}\right|_{p^2=m_W^2}\,, \tag{4.29a}$$

$$\begin{pmatrix}\delta Z_{ZZ} & \delta Z_{Z\gamma} \\ \delta Z_{\gamma Z} & \delta Z_{\gamma\gamma}\end{pmatrix} = \begin{pmatrix} -\mathrm{Re}\ \left.\frac{\partial \Sigma^T_{ZZ}(p^2)}{\partial p^2}\right|_{p^2=m_Z^2} & 2\frac{\Sigma^T_{Z\gamma}(0)}{m_Z^2} \\ -2\frac{\Sigma^T_{Z\gamma}(0)}{m_Z^2} & -\mathrm{Re}\ \left.\frac{\partial \Sigma^T_{\gamma\gamma}(p^2)}{\partial p^2}\right|_{p^2=0} \end{pmatrix}. \tag{4.29b}$$

Note that the self-energies correspond to the genuine one-loop self-energies. In order to fix the counterterm δZ_e in Eq. (4.25) an additional condition is required. The electric charge is fixed or required to reproduce the physical value in the so-called *Thomson limit*. This corresponds to the limit of vanishing photon momentum in the Thomson scattering between a photon and an electron [92]. In Fig. 4.1 the corresponding process is shown. The gray blob indicates the genuine EW one-loop corrections to the photon line, the crossed blob depicts the vertex counterterm, required to cancel all UV divergences. However, due to the mixing of the photon with the Z boson in the SM, an additional contribution occurs. This contribution can be related to the photon-photon external leg corrections which allows us to derive the counterterm as [83]

$$\delta Z_e = \frac{1}{2}\left.\frac{\partial \Sigma^T_{\gamma\gamma}(p^2)}{\partial p^2}\right|_{p^2=0} + \frac{s_W}{c_W}\frac{\Sigma^T_{\gamma Z}(0)}{m_Z^2}\,, \tag{4.30}$$

with the abbreviation $s_W = \sin\theta_W$ and $c_W = \cos\theta_W$, where θ_W stands for the Weinberg angle. The $SU(2)$ gauge coupling g is related to the electric charge and the Weinberg angle through

$$e = g\sin\theta_W\,, \quad \text{with} \quad \cos\theta_W = \frac{m_W}{m_Z}\,, \tag{4.31}$$

which allows us to derive the counterterm of the gauge coupling

$$\frac{\delta g}{g} = \delta Z_e + \frac{1}{2}\frac{1}{m_Z^2 - m_W^2}\left(\delta m_W^2 - c_W^2 \delta m_Z^2\right) . \tag{4.32}$$

4.1.4. Renormalization of the Quark Sector

For simplicity, we consider the fermion sector to be flavor diagonal, thus the mixing through the CKM matrix is neglected. This implies, that the renormalization and respectively the counterterms can be formulated for each quark generation separately. Further, both models under investigation do not provide CP-violation, hence the derivation of the counterterms is simplified. For a detailed introduction and discussion of the counterterms of the EW corrections see *e.g.* [83].
In the following, we present the renormalization of the quark sector of the SM. The respective counterterms for the lepton sector can be directly taken over, since the CKM matrix is neglected in this work.
A WFRCs and a mass counterterm is introduced for each chiral quark,

$$q_{L/R} \to \left(1 + \frac{1}{2}\delta Z_{qq}^{L/R}\right) q_{L/R} , \tag{4.33}$$

and

$$m_q \to m_q + \delta m_q . \tag{4.34}$$

Analogous to the gauge sector, also the two-point correlation function of the quarks can be split into different tensor structures. For the quarks, we find left-/right-handed and a scalar part

$$\Gamma_{qq}(p) = i\left(\not{p} - m_q\right) + i\left[\not{p}\omega_- \Sigma_{qq}^L(p^2) + \not{p}\omega_+ \Sigma_{qq}^R(p^2) + m_q\left(\omega_+ + \omega_-\right)\Sigma_{qq}^S(p^2)\right] , \tag{4.35}$$

with the chiral projectors $\omega_\pm = \frac{1}{2}\left(1 \pm \gamma_5\right)$. The mass of the corresponding quark is denoted as m_q. Σ_{qq}^x indicates the genuine one-loop self-energy of the quark q with the projected chirality x, respectively. Note that there is no flavor mixing, hence there are no off-diagonal self-energy contributions. The momentum p denotes the in- and out-going momentum of the self-energy. Imposing the OS renormalization conditions yields the following set of OS counterterms for a quark q [83]

$$\delta m_q = \frac{m_q}{2}\mathrm{Re}\left[\Sigma_{qq}^L(m_q^2) + \Sigma_{qq}^R(m_q^2) + 2\Sigma_{qq}^S(m_q^2)\right] , \tag{4.36a}$$

$$\delta Z_{qq}^L = -\mathrm{Re}\left[\Sigma_{qq}^L(m_q^2)\right] - m_q^2 \mathrm{Re}\left[\frac{\partial\Sigma_{qq}^L(p^2)}{\partial p^2} + \frac{\partial\Sigma_{qq}^R(p^2)}{\partial p^2} + 2\frac{\partial\Sigma_{qq}^S(p^2)}{\partial p^2}\right]\Bigg|_{p^2=m_q^2} , \tag{4.36b}$$

$$\delta Z_{qq}^R = -\mathrm{Re}\left[\Sigma_{qq}^R(m_q^2)\right] - m_q^2 \mathrm{Re}\left[\frac{\partial\Sigma_{qq}^L(p^2)}{\partial p^2} + \frac{\partial\Sigma_{qq}^R(p^2)}{\partial p^2} + 2\frac{\partial\Sigma_{qq}^S(p^2)}{\partial p^2}\right]\Bigg|_{p^2=m_q^2} . \tag{4.36c}$$

4.1.5. Renormalization of the Dark Sector

Both models PNGDM and VDM provide two different kinds of DM candidates. The $U(1)$ symmetry in the PNGDM yields a Pseudo-Nambu Goldstone DM candidate χ, where the gauged $U(1)_\chi$ present in the VDM model provides an additional vector χ_μ. The scalar DM candidate in the PNGDM can be renormalized analogously to the scalar sector of the Higgs sector, hence the corresponding OS counterms read

$$\delta Z_{\chi\chi} = -\mathrm{Re}\left[\frac{\partial\Sigma_{\chi\chi}(p^2)}{\partial p^2}\right]\Bigg|_{p^=m_\chi^2} , \qquad \delta m_\chi^2 = \mathrm{Re}\left[\Sigma_{\chi\chi}(p^2 = m_\chi^2) - \frac{\delta T_S}{v_S}\right] . \tag{4.37}$$

Since the scalar DM candidate χ does not mix with any other particle, there are no off-diagonal contributions to the genuine one-loop self-energy $\Sigma_{\chi\chi}$. The singlet tadpole counterterm δT_S can be related to the mass eigenstate tadpole by Eq. (4.11).
The renormalization of the input parameters of the dark sector of the VDM is a bit more involved. The WFRC can be derived accordingly to the WFRC of the W-gauge boson, resulting in

$$\delta Z_{\chi\chi} = -\,\mathrm{Re}\,\frac{\partial \Sigma^T_{\chi\chi}(p^2)}{\partial p^2}\bigg|_{p^2=m_\chi^2} \,. \tag{4.38}$$

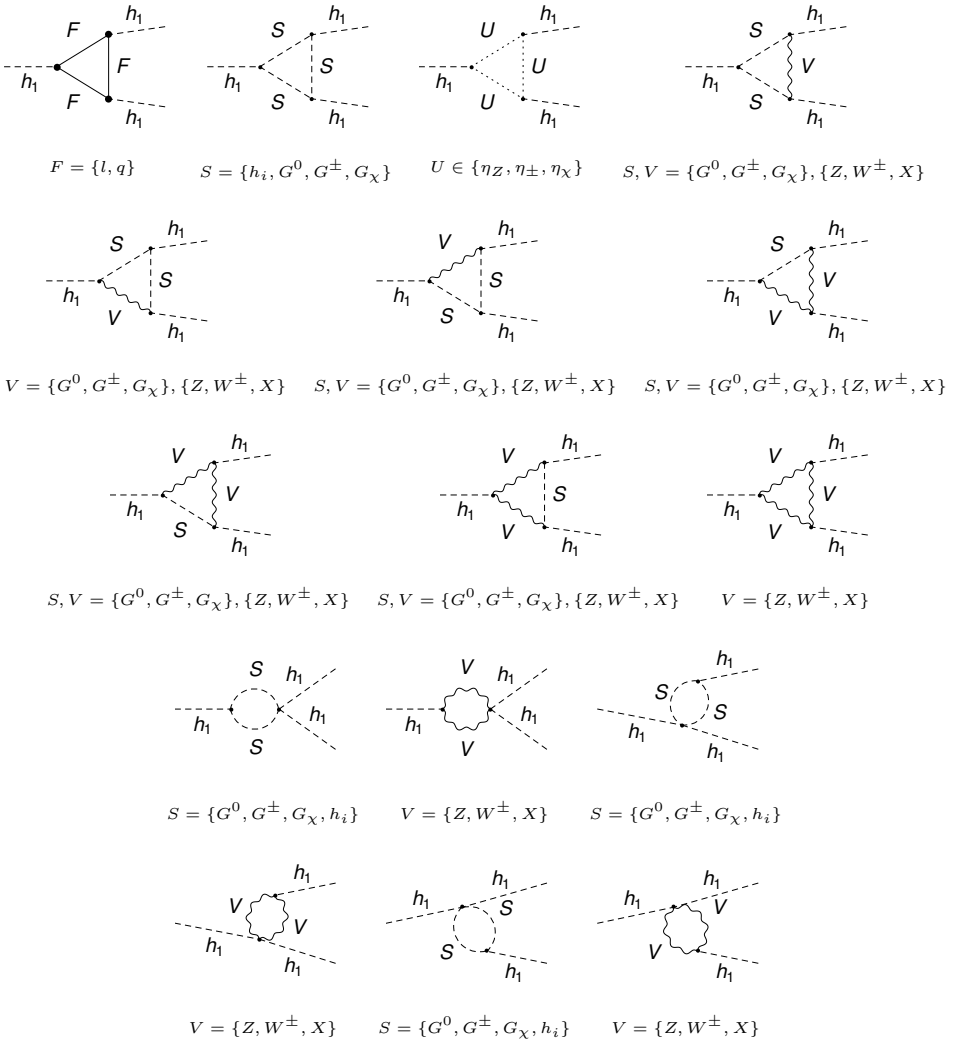

Figure 4.2.: Generic diagrams contributing to $\mathcal{A}^{\mathrm{VC}}_{h_1h_1h_1}$. Here F denotes fermions, S scalars, V gauge bosons, and U ghost fields.

Note that the self-energy in Eq. (4.37) is a scalar self-energy, whereas in Eq. (4.38) the transversal part of the vector self-energy has to be projected. The mass of the DM candidate of the VDM is related to the dark gauge coupling g_χ through Eq. (3.48d). Due to the chosen treatment of the tadpole renormalization, it is not required to renormalize the singlet VEV v_s[8]. Thus, either the dark gauge coupling or the dark mass can be chosen to be renormalized. We take the dark gauge coupling g_χ to be the independent input parameter. However, the

[8] In the *alternative tadpole scheme* as proposed by Fleischer and Jegerlehner [93], the singlet VEV requires an introduction of a singlet VEV counterterm Δv_s [87].

dark gauge coupling g_χ cannot be linked to a physical observable, which prevents the usage of OS conditions for the renormalization. For the derivation we use a process-dependent renormalization scheme, which also enables to extract the $\overline{\text{MS}}$ counterterm $\delta g_\chi^{\overline{\text{MS}}}$ since the UV divergence is universal. We use the process $h_1 \to h_1 h_1$ to extract the counterterm. The EW NLO amplitude $\mathcal{A}^{\text{NLO}}_{h_1h_1h_1}$ of this trilinear vertex consists of the LO amplitude $\mathcal{A}^{\text{LO}}_{h_1h_1h_1}$, the genuine one-loop virtual corrections $\mathcal{A}^{\text{VC}}_{h_1h_1h_1}$ and the respective vertex counterterm $\mathcal{A}^{\text{CT}}_{h_1h_1h_1}$,

$$\mathcal{A}^{\text{NLO}}_{h_1h_1h_1} = \mathcal{A}^{\text{LO}}_{h_1h_1h_1} + \mathcal{A}^{\text{VC}}_{h_1h_1h_1} + \mathcal{A}^{\text{CT}}_{h_1h_1h_1} \ . \tag{4.39}$$

We will drop the index $h_1h_1h_1$ for better readability. The counterterm amplitude is split into the vertex counterterm δg^{CT} and the external leg corrections δ^{mix}

$$\mathcal{A}^{\text{CT}} = \delta^{\text{mix}} + \delta g^{\text{CT}} \ , \tag{4.40}$$

with

$$\delta^{\text{mix}} = \frac{3}{2} g_{h_1h_1h_1} \delta Z_{h_1h_1} + \frac{3}{2} g_{h_1h_1h_2} \delta Z_{h_2h_1} \ . \tag{4.41}$$

The trilinear LO coupling $g_{h_ih_jh_k}$ denotes the coupling between three neutral Higgs bosons h_i, h_j and h_k. In the VDM the trilinear LO coupling between three h_1 reads

$$g_{h_1h_1h_1} = -\frac{3gm_{h_1}^2 \cos^3\alpha}{2m_W} - \frac{3g_\chi m_{h_1}^2 \sin^3\alpha}{m_\chi} \ , \tag{4.42}$$

hence the vertex counterterm is given by

$$\delta g^{\text{CT}} = \sum_p \frac{\partial g_{h_1h_1h_1}}{\delta p} \delta p \ , \quad p \in \{m_{h_1}, m_\chi, \alpha, g_\chi, g, m_W\} \ . \tag{4.43}$$

The genuine one-loop virtual corrections are depicted in Fig. 4.2. The counterterm in the process-dependent scheme then reads

$$\delta g_\chi = \left(\frac{m_\chi}{3m_{h_1}^2 s_\alpha^3}\right) \left(\mathcal{A}^{\text{VC}} + \mathcal{A}^{\text{CT}}|_{\delta g_\chi = 0}\right) \ , \tag{4.44}$$

with $s_\alpha = \sin\alpha$ and the subscript $\delta g_\chi = 0$ indicating the counterterm amplitude without the contribution of g_χ. Eq. (4.44) contains finite pieces induced by the virtual corrections and counterterms, hence the counterterm is dependent on the chosen process. By solely extracting the UV poles (terms proportional to Δ_ϵ) of δg_χ in Eq. (4.44), the corresponding $\overline{\text{MS}}$ counterterm is found to be

$$\delta g_\chi^{\overline{\text{MS}}} = \delta g_\chi|_{\Delta_\epsilon} = \frac{g_\chi^3}{96\pi^2} \Delta_\epsilon \ . \tag{4.45}$$

The $\overline{\text{MS}}$ counterterm can also be derived from the β function of the respective RGE evolution of g_χ. The result in Eq. (4.45) was checked against the RGE obtained from `SARAH` [94–97]. We now have all the required counterterms for the PNGDM and VDM.

4.2. Dark Matter Phenomenology

The existence of DM is one of the most demanding open questions in modern physics. So far there is only bare knowledge about the nature and properties of DM, however there is a plethora of evidences for the existence of DM. In the following, we discuss one phenomenon requiring the introduction of additional mass in the content of the universe - the Cosmic Microwave Background (CMB). By discussing the CMB, we will introduce the basics of the

ΛCDM model needed for the discussion of the SI-cxn in Sec. 4.2.2. We will restrict the DM phenomenology to the discussion of WIMPs. Without doubt, there exists a substantial amount of possible other solutions for DM models. For a broad overview and introduction in DM, we recommend *e.g.* [98, 99].
The expansion of our universe is dictated by the content of the universe, where the different contributions scale differently with respect to the scale factor of the universe a. The scale factor $a(t)$ is time dependent and describes the change in the three dimensional Euclidean spatial coordinates in the Friedmann-Lemaître-Robertson-Walker metric [100]. By using the equations of state for non-relativistic matter, radiation and the cosmological constant, the Friedmann-Lemaître equation can be cast in the following form [100]

$$\frac{H^2}{H_0^2} = \Omega_r a^{-4} + \Omega_m a^{-3} + \Omega_k a^{-2} + \Omega_\Lambda \ . \tag{4.46}$$

The Hubble constant is defined as $H \equiv \frac{\dot{a}}{a}$ and the reference value H_0 indicates the Hubble constant of today's universe $H_0 \simeq 70 \frac{km}{sMps}$. The densities Ω_i are normalized to the critical mass density ρ_c which separates the collapsing and expanding universe

$$\Omega_i \equiv \frac{\rho_i}{\rho_c} \ . \tag{4.47}$$

The radiation density Ω_r scales with a to the power of minus four, the non-relativistic mass density Ω_m with the power of minus three, the curvature density Ω_k with minus two and the cosmological density does not scale at all, hence all different contributions show a different behavior. Starting with the radiation dominated universe in the Big Bang and the different scaling behavior of the different contributions in Eq. (4.46) immediately implies, that there are epochs of the universe, where the non-relativistic matter starts to dominate the expansion of the universe until the dictating contribution is the non-relativistic matter density. The dynamics of the universe and especially the structure formation can be described within the ΛCDM model which acts as the Standard Model of Big Bang Cosmology [100].
The non-relativistic matter density consists of two contributions, namely the baryonic matter, which makes up for the observable matter and DM

$$\Omega_m = \Omega_b + \Omega_\chi \ . \tag{4.48}$$

The isotropic photon background - the CMB - yields an efficient way to probe the parameters of the ΛCDM model. The origin could be interpreted as the sphere of last photon scattering before the decoupling of the photons. The small temperature fluctuations in the CMB

$$\frac{\delta T}{T_0} \lesssim 10^{-5} \ , \tag{4.49}$$

however, indicate that the photons have to be causally connected at some point of the history of the universe. The measurement of the CMB is given as a power spectrum, where the temperature fluctuation is expanded in spherical coordinates

$$\frac{\delta T(\theta,\phi)}{T_0} \equiv \frac{T(\theta,\phi) - T_0}{T_0} = \sum_{l=0}^{\infty} \sum_{m=-l}^{l} a_{lm} Y_l m(\theta,\phi) \ , \tag{4.50}$$

with the normalization T_0 as the decoupling temperature of the photons, the spherical angles θ, ϕ and the spherical surface functions Y_{ml}. This allows us to investigate the correlations of the temperature fluctuations on the sky sphere. Since there is no special direction in an

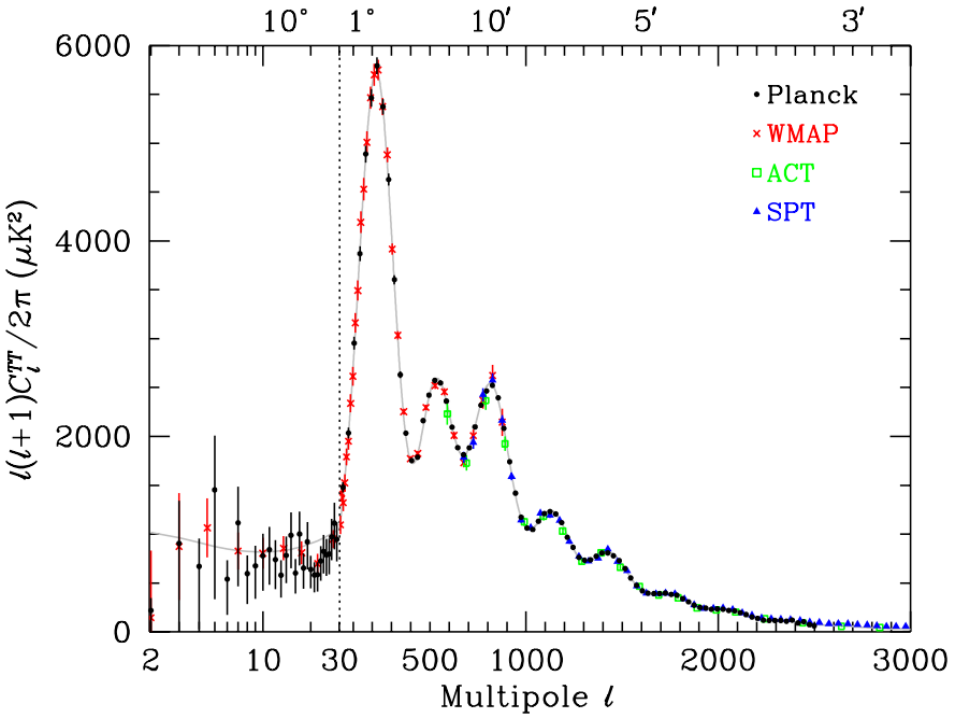

Figure 4.3.: CMB temperature anisotropy band-power estimates from the *Planck*, *WMAP*, *ACT*, and SPT experiments as a function of the multipole parameter l. The plotted curve indicates the best-fit *Planck* ΛCDM model. This plot is taken from [100].

isotropic universe, the average over the magnetic number m can be taken and only the mean values of the temperature fluctuation are of interest

$$\frac{1}{4\pi}\int d\Omega \left(\frac{\delta T}{T_0}\right)^2 = \sum_{l=0}^{\infty}\frac{2l+1}{4\pi}C_l \ , \tag{4.51}$$

with

$$C_l = \frac{1}{2l+1}\sum_{m=-l}^{l}|a_{lm}|^2 \ . \tag{4.52}$$

The power spectrum of the CMB is shown in Fig. 4.3 as a function of the multipole parameter l. A peak structure is observable for $l \gtrsim 30$. These peaks can be associated with the *acoustic oscillation* of the baryon-photon fluid before the decoupling. The interplay of gravitational and electromagnetic forces acting on baryonic matter does not allow for structure formation. Simply because the compression of baryonic matter due to gravity yields immediately a counter acting radiation pressure induced by the Coulomb interaction. Without further mass content, this would end in an endless oscillation of compression and rarefaction of the baryonic matter. To account for forming structures in the universe, it is essential that there exists a neutral mass interacting solely gravitationally. This neutral mass, the DM, acts as an gravitational well, since the corresponding mass is not affected by radiation pressure, hence it can clump together. The gravitational well pulls the baryon-photon fluid, which results in temperature fluctuations in the photon gas due to the compression. The first peak, the fundamental tone, indicates a sound wave corresponding to the horizon at decoupling. This sound wave just compressed once. The second peak in Fig. 4.3 is induced by the sound wave undergoing one compression followed by one rarefaction induced by the radiation pressure. In this way, the even peaks are associated with the process of compression due to the gravitational potential, odd-numbered peaks correspond to the rarefaction induced by the radiation

pressure. Due to the different dependence on gravity and radiation pressure, the relative difference of the peak structure allows us to extract Ω_m and Ω_b[9]. Furthermore, the height of the peaks is sensitive to the cosmological constant Λ, permitting the extraction of Ω_Λ. The measurement of the CMB by *Planck* determines [103]

$$\Omega_b h^2 = 0.02225 \pm 0.00023 \ , \quad \Omega_m = 0.308 \pm 0.012 \ , \tag{4.53}$$

which allows us to estimate the DM density to be

$$\Omega_\chi h^2 \simeq 0.12 \ . \tag{4.54}$$

Up to this point, the DM is only required to be electric neutral[10] and interacting gravitationally. However, an additional requirement to account for is, that the DM has to be *cold* (non-relativistic). This implies the decoupling of the cold DM from the thermal bath well before recombination, due to the requirements of the formation of the gravitational wells. The generation of DM is another open question in modern physics. In the context of WIMPs, the freeze-out mechanism is one possible solution, corresponding to thermal production of DM. Analogous to the neutrinos, photons and all other SM particles, the DM is *frozen* out of the high-density thermal bath if the respective interaction rate of the particle drops below the expansion rate of the universe, the Hubble rate H. In this case, the particle cannot interact with the thermal bath anymore and is *chemically* decoupled. A rough estimate of the freeze-out temperature can be obtained by equating the interaction rate with the Hubble rate, however a more sophisticated calculation requires the solution of the Boltzmann equations [99, 100],

$$\frac{dn}{dt} - 3Hn = -\langle \sigma v \rangle \left(n^2 - n_{\rm eq}^2 \right) \ , \tag{4.55}$$

with n being the particle distribution function, $\langle \sigma v \rangle$ the thermally averaged cross-section multiplied with the particle velocity v and the equilibrium density $n_{\rm eq}$. It is convenient to switch the variables to $Y = {}^{n}/_{s}$ and $x = {}^{m}/_{T}$. Solving Eq. (4.55) allows us to determine the freeze-out temperature $x_{\rm fo}$ and evaluate the density expected today for the respective particle. The relic density of a (cold) WIMP-like DM candidate is given by [100]

$$\Omega_{\rm cold} h^2 \simeq 0.1 \left(\frac{x_{\rm fo}}{20} \right) \left(\frac{10^{-8} {\rm GeV}^{-2}}{\sigma_{\rm DM+DM \to anything}} \right) \ , \tag{4.56}$$

with $\sigma_{\rm DM+DM \to anything}$ corresponding to the cross-section obtained for an arbitrary $2 \to 2$ process $\chi\chi \to SM + SM$. The freeze-out temperature can be approximated by the solution of

$$\sqrt{x} \cdot e^{-x} = \left(m_{\rm DM} \cdot M_{Pl} \cdot \sigma_{\rm DM+DM \to anything} \right)^{-1} \ , \tag{4.57}$$

and is given as a number between 10 and 50. Eq. (4.56) is often referred to as the "*WIMP miracle*". For typical EW-scale cross-sections of the order $\mathcal{O}\left(10^{-8} {\rm GeV}^{-2}\right)$ and masses, Eq. (4.56) predicts the correct amount of DM in Eq. (4.54).

4.2.1. Density and Velocity Distribution of Dark Matter

The actual distribution of DM in the universe, or rather in our galaxy is a difficult question to answer. The DM density is described in terms of a *local density* ρ_0, which corresponds to the average over a volume of few hundreds parcecs in the solar neighborhood. There are attempts to measure locally and globally the shape of the Milky Way DM halo. However,

[9] Note that Ω_b is associated with the electric charge inducing the radiation pressure [101, 102].

[10] There are investigations allowing for milli-charged DM as for instance dark photon models. However, the resulting upper limit on the electric charge of the DM candidate is rather strict.

the actual shape of the DM halo has to be extracted from simulations and yields rather large theoretical errors. For direct detection of DM, an attempt to measure the interaction of DM in a laboratory experiment (*see* next section), it is crucial to know the kinematical distribution of DM in the solar system. We will use the *Standard Halo Model* (SHM) for the DM halo description. It assumes an isotropic, isothermal sphere of DM particles with a density profile of $\rho(r) \sim r^{-2}$. The velocity distribution is assumed to be Maxwellian with a dispersion of $\sigma_v = {}^{v_c}/\sqrt{2}$. The local circular speed v_c is of the order $(218 - 246)\,{}^{km}/_{s}$ [100]. The velocity distribution is cut at the escape velocity $v_{esc} = 528^{+24}_{-25}{}^{km}/_{s}$ [100]. An improved model setup of the SHM is discussed in [104] including the data obtained by *Gaia*. They estimate the systematic error to be of the order $\mathcal{O}(30\%)$ for the local DM density. Due to the large uncertainties in the DM distribution, it is important that observables are isolated from these possible errors. As we will see in the next section, the prediction for the direct detection of DM on the Earth is separated into a kinematical part involving the velocity distribution and one part, which allows us to compare different experiments independent of the local DM distribution.

4.2.2. Direct Detection

In the following, we assume that the DM consists of WIMPs. WIMPs do not interact electromagnetically and yield a *weak* interaction with the SM. Furthermore, we consider thermally produced WIMPs. The relic density is calculated with the standard freeze-out mechanism as sketched in Eq. (4.56). The *weak* interaction with the SM particle content is achieved through a *Higgs portal*. Higgs portal models usually extend the Higgs sector and simultaneously introduce a DM candidate. In the context of this thesis, the models PNGDM and VDM are considered. The Higgs-DM coupling is introduced through a new *dark* gauge coupling in the VDM, whereas the PNGDM introduces a DM candidate in the complex singlet.
The basic idea of direct detection is simple and was proposed first in [21]. Since the DM candidate is coupled to a mediator (in our case the Higgs bosons) and the corresponding mediator to SM particles, there exists an effective DM-SM particle interaction *e.g.* also a DM-nucleus interaction.
If we assume the SHM, there is a local non-zero DM density ρ_0 in which the Earth is traveling. This implies that DM particles steam through the Earth every second. This DM stream might interact with some nuclei and transfer a small amount of energy, in the following referred to as *recoil energy*. If this recoil energy is measured, we would have an evidence for the existence of *weakly-interacting* DM. So far, no clear signal could be observed in direct detection experiments. However, the absence of such events can be used to set exclusion limits on the DM-nucleus interaction strength, allowing us to constrain DM models.
The differential scattering rate R as a function of the nuclear recoil energy E_R is given as [100]

$$\frac{dR(E_R,t)}{dE_R} = N_T \frac{\rho_0}{m_\chi} \int_{v>v_{\min}} v f(\mathbf{v}+\mathbf{v}_E(t)) \frac{d\sigma(E_R,v)}{dE_R} d^3v \ , \tag{4.58}$$

with the number of target nuclei N_T, the DM mass m_χ, $v = |\mathbf{v}|$ as the speed of the particle in the rest frame of the experiment, the DM velocity distribution function $f(\mathbf{v}+\mathbf{v}_E(t))$ depending on the Earth's frame, $v_{\min}$ as the minimum speed of the DM causing a recoil energy and σ as the scattering cross-section on the nucleus [105,106]. The minimum velocity can be expressed as $v_{\min} = \left(m_N E_R/2\mu^2\right)^{1/2}$ for elastic scattering with the reduced mass $\mu = \dfrac{m_N m_\chi}{m_N + m_\chi}$. The mass of the nucleus is denoted as m_N.
If the DM-nucleus interaction of the DM-nuclei is split into spin-independent (SI) and spin-dependent (SD) interactions, the corresponding differential cross-section obeys ${}^{d\sigma}/_{d_{E_R}} \sim v^{-2}$ allowing us to rewrite the velocity distribution as [106, 107]

$$g(v_{\min},t) = \int_{v>v_{\min}} \frac{f(\mathbf{v}+\mathbf{v}_E(t))}{v} d^3v \ . \tag{4.59}$$

Eq. (4.59) enables the comparison of various experimental results independently of the underlying velocity distribution [107]. This allows us to separate the uncertainty due to the velocity distribution from SI/SD interactions. The time-integrated differential cross-section reads [100]

$$\frac{d\sigma(E_R, v)}{dE_R} = \frac{m_N}{2\mu^2 v^2} \left(\sigma^{\mathrm{SI}} F^2_{\mathrm{SI}}(E_R) + \sigma^{\mathrm{SD}} F^2_{\mathrm{SD}}(E_R)\right) \tag{4.60}$$

with m_N as the nucleon mass, the SI/SD cross-section in the limit of zero momentum transfer and the nuclear form factors $F^2(E_R)$. The DM velocity is non-relativistic $v/c \sim 10^{-3}$, hence the expected recoil energies are quite low ($\mathcal{O}$(keV)) and the momentum transfer $q = (2m_N E_R)^{1/2} \sim \mathcal{O}\,(10 - 100\mathrm{GeV})$. This implies that the nuclei cannot be treated as point-like objects in the scattering process with DM and necessitates the inclusion of non-trivial form factors. These form factors have to be calculated for all different target materials, respectively. The SI-cxn for a target nucleus i can be expressed as

$$\sigma^{\mathrm{SI}}_i = \frac{\mu_i}{\pi} \left|Z_i g^{\mathrm{SI}}_p + (A_i - Z_i)\, g^{\mathrm{SI}}_n\right|^2 |F_i(q)|^2 \ , \tag{4.61}$$

with i indicating the detector material and the proton number Z_i and mass number A_i of the target material. However, to compare results from different experiments and target materials, it is convenient to express the SI/SD cross-sections for a single nucleon. The derivation of the theoretically predicted SI-cxn on a single nucleon n, either a proton or neutron, will be discussed in the next section.

4.3. Spin-Independent Cross Section

The goal of this section is to derive an *efficient* and *sufficient* approach to describe the interaction between DM and nuclei. As already stated, the DM velocity is expected to be small in the SHM yielding small momentum transfers. Hence, the interaction of DM particles with the nuclei can be described within a non-relativistic effective field theory (NREFT). The operator basis is built of operators obeying Galilean-invariance, T-symmetry and are Hermitian [108]. The corresponding nuclear response, required to determine the recoil energy, is evaluated in shell-model calculations regarding the target material of the detector, respectively. The kinematics are defined by the two in- and out-coming momenta of the WIMP candidate χ and the nucleon N

$$N(\mathbf{p}) + \chi(\mathbf{k}) \to N(\mathbf{p}') + \chi(\mathbf{k}') \ , \tag{4.62}$$

where the momentum transfer is given as

$$\mathbf{q} = \mathbf{k}' - \mathbf{k} = \mathbf{p}' - \mathbf{p} \ . \tag{4.63}$$

The perpendicular velocity is defined as

$$\mathbf{v}^{\perp} = \frac{\mathbf{k} + \mathbf{k}'}{2m_\chi} - \frac{\mathbf{p} + \mathbf{p}'}{2m_N} \ , \tag{4.64}$$

which implies $\mathbf{v}^{\perp} \cdot \mathbf{q} = 0$. The operator basis is then given by [108–111]

$$\begin{aligned}
&\mathcal{O}_1 = \mathbb{1} \ , && \mathcal{O}_2 = \left(\mathbf{v}^{\perp}\right)^2 \ , \\
&\mathcal{O}_3 = i\mathbf{S}_N \cdot \left(\mathbf{q} \times \mathbf{v}^{\perp}\right) \ , && \mathcal{O}_4 = \mathbf{S}_{\boldsymbol{\chi}} \cdot \mathbf{S}_N \ , \\
&\mathcal{O}_5 = i\mathbf{S}_\chi \cdot \left(\mathbf{q} \times \mathbf{v}^{\perp}\right) \ , && \mathcal{O}_6 = \mathbf{S}_\chi \cdot \mathbf{q}\mathbf{S}_N \cdot \mathbf{q} \ , \\
&\mathcal{O}_7 = \mathbf{S}_N \cdot \mathbf{v}^{\perp} \ , && \mathcal{O}_8 = \mathbf{S}_\chi \cdot \mathbf{v}^{\perp} \ ,
\end{aligned} \tag{4.65}$$

$$\mathcal{O}_9 = i\mathbf{S}_\chi \cdot (\mathbf{S}_N \times \mathbf{q}) \ , \qquad \mathcal{O}_{10} = i\mathbf{S}_N \cdot \mathbf{q} \ ,$$
$$\mathcal{O}_{11} = i\mathbf{S}_\chi \cdot \mathbf{q} \ , \qquad \mathcal{O}_{12} = \mathbf{S}_\chi \cdot \left(\mathbf{S}_N \times \mathbf{v}^\perp\right) \ ,$$

with the spin-operators of the DM candidate $\mathbf{S}_\chi$ and of the nucleon $\mathbf{S}_N$. Indeed there are operators depending on the spin configurations of the DM candidate and the nucleon, hence these operators contribute to the spin-dependent interactions. Note that these operators would vanish for scalar DM. Furthermore, there are operators depending on the momentum transfer $\mathbf{q}$ or the perpendicular velocity $\mathbf{v}^\perp$. These operators are suppressed compared to the spin-dependent contributions due to the small velocity expected in the SHM. However, the operator $\mathcal{O}_1$ yields an unsuppressed operator and a spin-independent interaction. This operator $\mathcal{O}_1$ induces the dominant contribution to the SI-cxn.
Apart from the NREFT approach, a low-energy effective theory of QCD, based on chiral effective field theory (ChEFT), determines the WIMP-nuclei interaction [112–114]. By mapping the operator basis of the ChEFT in the NREFT basis, it is possible to identify which operators in ChEFT[11] contributes to the SI-interaction required for the SI-cxn.
ChEFT requires the knowledge of the nuclear matrix elements of the parton operators. They are defined for on-shell nucleons n as

$$\langle n| \, m_q \bar{q} q \, |n\rangle \equiv m_n f_q^n \ , \tag{4.66a}$$
$$\langle n| -\frac{\alpha_s}{12\pi} G^a_{\mu\nu} G^{a\mu\nu} \, |n\rangle \equiv \frac{2}{27} m_n f_g^n \ , \tag{4.66b}$$
$$\langle n(p)| \, \mathcal{O}^q_{\mu\nu} \, |n(p)\rangle = \frac{1}{m_n} \left(p_\mu p_\nu - \frac{1}{4} m_n^2 g_{\mu\nu} \right) (q^n(2) + \bar{q}^n(2)) \ , \tag{4.66c}$$

with the quark spinor q, the respective quark mass m_q, the nucleon mass m_n. The expectation value of the gluon field strength tensor $G^a_{\mu\nu} G^{a\mu\nu}$ is rescaled with the strong coupling α_s. The twist-2 operator [115, 116]

$$\mathcal{O}^q_{\mu\nu} = \frac{1}{2} \bar{q} i \left(\partial_\mu \gamma_\nu + \partial_\nu \gamma_\mu - \frac{1}{2} \partial\!\!\!/ \right) q \ , \tag{4.67}$$

requires the second momenta of the quarks $q^n(2)$. The numerical values for the nuclear matrix elements f_q^n $(n = P, N)$ are determined on the lattice, where we use the values from [117],

$$f_u^P = 0.01513 \, , \quad f_d^P = 0.0.0191 \, , \quad f_s^P = 0.0447 \, , \tag{4.68a}$$
$$f_u^N = 0.0110 \, , \quad f_d^N = 0.0273 \, , \quad f_{9s}^N = 0.0447 \, , \tag{4.68b}$$

where P indicates the value for a proton and N for a neutron, respectively. The nuclear matrix elements for the gluon interactions can be related to the quark interaction as

$$f_g^p = 1 - \sum_{q=u,d,s} f_q^p \, , \qquad f_g^N = 1 - \sum_{q=u,d,s} f_q^N \, . \tag{4.69}$$

The second momenta of the quarks are given as [118]

$$u^P(2) = 0.22 \, , \qquad \bar{u}^P(2) = 0.034 \, , \tag{4.70a}$$
$$d^P(2) = 0.11 \, , \qquad \bar{d}^P(2) = 0.036 \, , \tag{4.70b}$$
$$s^P(2) = 0.026 \, , \qquad \bar{s}^P(2) = 0.026 \, , \tag{4.70c}$$
$$c^P(2) = 0.019 \, , \qquad \bar{c}^P(2) = 0.019 \, , \tag{4.70d}$$

[11] The operators in the ChEFT are expressed in terms of parton operators, hence can be directly identified with the corresponding fields in the underlying model.

$$b^P(2) = 0.012\,, \qquad \bar{b}^P(2) = 0.012\,. \tag{4.70e}$$

The identification of the corresponding contributions of the operators and the relation to the SI operator $\mathcal{O}_1$ in Eq. (4.65) has to be discussed for different spin configurations of the DM candidate. In the following, we will introduce the identification for scalar and vector-like DM candidates.

4.3.1. Scalar Dark Matter

Scalar DM as present in the PNGDM cannot produce spin-dependent interactions with the nuclei[12], thus only the SI contributions are unsuppressed by the perpendicular velocity or the momentum transfer. The effective Lagrangian with the parton operators is given as [116, 119, 120]

$$\mathcal{L}_{\text{eff}} = \sum_q C_S^q \mathcal{O}_S^q + C_S^g \mathcal{O}_S^g + \sum_q C_T^q \mathcal{O}_T^q\,, \tag{4.71}$$

with the Wilson coefficients C_S^q, C_S^g, C_T^q and the parton operators, respectively,

$$\mathcal{O}_S^q = m_q \chi^2 \bar{q} q\,, \tag{4.72a}$$

$$\mathcal{O}_S^g = \frac{\alpha_s}{\pi} \chi^2 G^a_{\mu\nu} G^{a\mu\nu}\,, \tag{4.72b}$$

$$\mathcal{O}_T^q = \frac{1}{m_\chi^2} \chi i\partial^\mu i\partial^\nu \chi \mathcal{O}^q_{\mu\nu}\,. \tag{4.72c}$$

The sum runs over all contributing quarks. The SI-cxn on a single nucleon n is then given by

$$\sigma_n = \frac{1}{\pi}\left(\frac{m_n}{m_\chi + m_n}\right)^2 \left| \sum_{q\,=\,u,\,d,\,s} m_n f_q^n C_S^q - \frac{8}{9} m_n f_g^n C_S^g + \frac{3}{4} m_n \sum_{q\,=\,u,\,d,\,s,\,c,\,b} \left(q^n(2) + \bar{q}^n(2)\right) C_T^q \right|^2\,, \tag{4.73}$$

with m_n either the proton or neutron mass, the Wilson coefficients in accordance to Eq. (4.71) and the nuclear matrix elements as in Eqs. (4.68) and (4.70). Note that the first sum runs solely over the light quarks $q = u, d, s$, whereas the second sum runs over all quarks, except for the top quark.

4.3.2. Vector Dark Matter

Analogous to the previous subsection, the SI-cxn on a single nucleon can be determined for vector-like DM. The VDM introduces a vector-like DM candidate, which is coupled to the Higgs sector. The effective Lagrangian with the contributing parton operators reads [121]

$$\mathcal{L}^{\text{eff}} = \sum_{q=u,d,s} \mathcal{L}_q^{\text{eff}} + \mathcal{L}_G^{\text{eff}}\,, \tag{4.74}$$

with

$$\mathcal{L}_q^{\text{eff}} = f_q \chi_\mu \chi^\mu m_q \bar{q} q + \frac{g_q}{m_\chi^2} \chi^\rho i\partial^\mu i\partial^\nu \chi_\rho \mathcal{O}^q_{\mu\nu}\,, \tag{4.75a}$$

$$\mathcal{L}_G^{\text{eff}} = f_G \chi_\rho \chi^\rho G^a_{\mu\nu} G^{a\,\mu\nu}\,. \tag{4.75b}$$

[12] Even though there are operators in Eq. (4.65) depending on the spin of the nucleon, the corresponding operators are suppressed by the perpendicular velocity or momentum transfer. These operators are neglected in our analysis.

The operator structure reflects Eq. (4.72), however, we have a vector-like state χ_μ in the parton operators. The SI-cxn on a single nucleon, either a proton ($n = P$) or a neutron ($n = N$) reads

$$\sigma_n = \frac{1}{\pi}\left(\frac{m_n}{m_\chi + m_n}\right)^2 \left|f_n\right|^2 , \tag{4.76}$$

with the effective nucleon coupling

$$f_n/m_n = \sum_{q=u,d,s} f_q f_q^n + \sum_{q=u,d,s,c,b} \frac{3}{4}\left(q^n(2) + \bar{q}^n(2)\right) g_q - \frac{8\pi}{9\alpha_S} f_G^N f_G \, . \tag{4.77}$$

Again the prefactors f_q, g_q and f_G are the Wilson coefficients of the parton operators, respectively. The corresponding nuclear matrix elements are given in Eqs. (4.68) and (4.70).

4.3.3. Extracting the Wilson Coefficients

The only missing piece required for the determination of the SI-cxn of an underlying model is the matching of the Wilson coefficients in front of the ChEFT operators in Eqs. (4.72) and (4.75). The procedure applied in this thesis will be discussed in the following section, followed by a separate discussion on the inclusion of NLO EW corrections in Chapter 5 and 6. Comparing the contributing operators in Eqs. (4.72) and (4.75), we have two different kinds of DM interactions with the nuclei. The first one is induced through an effective DM-quark interaction, whereas the latter is induced through an effective DM-gluon interaction. Even though there is no direct coupling between the DM candidate and quarks neither to gluons in PNGDM and VDM, there exist Feynman diagrams generating this interaction.

Quark Contributions:

The t-channel interaction between the DM and a quark mediated through a Higgs boson can be generically described as

$$\mathcal{A}_{\text{gen}} = \sum_i C_{\chi\chi h_i} C_{qqh_i} \frac{1}{q^2 - m_{h_i}^2} \bar{u}(\mathbf{p}) u(\mathbf{p}+\mathbf{q}) \xrightarrow{q^2 \to 0} -\sum_i C_{\chi\chi h_i} C_{qqh_i} \frac{1}{m_{h_i}^2} \bar{u}(\mathbf{p}) u(\mathbf{p}) \ , \tag{4.78}$$

with the generic trilinear coupling $C_{\chi\chi h_i}$ between two χ's and the i-th Higgs boson and the generic trilinear coupling C_{qqh_i} between two quarks and the i-th Higgs boson, respectively. The sum runs over all involved Higgs bosons of the underlying model. The quark spinor with its corresponding momentum p is described as $u(p)$. The explicit zero momentum transfer limit ($q^2 \to 0$) is taken to extract the SI-cxn, since we neglect the velocity or momentum transfer suppressed operator contributions. For simplicity let us assume scalar DM implying scalar-like couplings. Such a diagram would be produced by the EFT operators

$$\mathcal{L}_{\text{eff}} \supset -\sum_i \frac{C_{\chi\chi h_i} C_{qqh_i}}{2m_{h_i}^2} \chi\chi\bar{q}q \ , \tag{4.79}$$

with the scalar fields χ and the quark spinor q. Note the additional factor $1/2$ to account for the symmetry factor due to the scalar fields. The comparison with Eq. (4.72) allows us to extract the contribution to the Wilson coefficient for the quark operator $\chi\chi m_q \bar{q}q$ to be

$$C_S^q \supset -\sum_i \frac{C_{\chi\chi h_i} C_{qqh_i}}{2m_q m_{h_i}^2} \ . \tag{4.80}$$

Furthermore, there can be additional contributions to the quark operators generated through other diagrams, even though at tree level the t-channel exchange is the only topology contributing to this operator in the models under investigation. This method can be applied to

both models PNGDM and VDM. In addition, it can be generalized to NLO. The application to the specific model will be discussed in Chapter 5 for the PNGDM and in Chapter 6 for the VDM, respectively.

Gluon Contributions:

In the following, we discuss the extraction of the gluon interaction. The effective DM-gluon

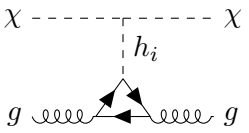

Figure 4.4.: Interaction of a DM particle and a gluon via a Higgs boson mediator and a quark loop.

interaction arises at one-loop level. One example of such a diagram is depicted in Fig. 4.4, where the quark triangle induces the coupling to the Higgs mediator. This triangle can be expanded for heavy quark masses and for vanishing momentum transfer, however there is also the possibility to extract this coupling from the effective Higgs-nuclei interaction [122]. The derivation is based on the *QCD trace anomaly* allowing us to determine the trace of the energy-momentum tensor of the nuclei to be [122, 123]

$$\Theta^{\mu}_{\ \mu} = \sum_{q \leq N_f} m_q \left(1-\gamma\right) \bar{q}q + \frac{\beta_{N_f}(\alpha_s)}{4\alpha_s} G^a_{\mu\nu} G^{a\mu\nu} \ , \tag{4.81}$$

with N_f being the number of active quark flavors, the anomalous dimension γ and β_{N_f} as the β-function. In the leading-order approximation, the three lightest quarks $q = u, d, s$ yield the mass of the nucleon n

$$m_n = \langle n| \Theta^{\mu}_{\ \mu} |n\rangle = \langle n| \sum_{q=u,d,s} m_q \left(1-\gamma\right) \bar{q}q + \frac{\beta_3(\alpha_s)}{4\alpha_s} G^a_{\mu\nu} G^{a\mu\nu} |n\rangle \ . \tag{4.82}$$

Eq. (4.82) implies that the heavy quarks $Q = c, b, t$ do not contribute to the nucleon mass (at leading order). By going from $N_f \to N_f + 1$ it is possible to determine the expectation value for the heavy quark operator

$$\langle n| m_Q \bar{Q}Q |n\rangle = -\frac{\Delta\beta(\alpha_s)}{4\alpha_s(1-\gamma)} \langle n| G^a_{\mu\nu} G^{a\mu\nu} |n\rangle = -\frac{\alpha_s}{12\pi} \langle n| G^a_{\mu\nu} G^{a\mu\nu} |n\rangle + \mathcal{O}\left(\alpha_s^2\right) \ , \tag{4.83}$$

with $\Delta\beta \equiv \beta_4 - \beta_3 = \alpha_s^2/(3\pi)^2$ indicating the difference of the β-function between $N_f + 1$ and N_f. This coincides with the result for the effective $hG^a_{\mu\nu}G^{a\mu\nu}$ vertex for small q^2 at the order of α_s [124].

Thus, in order to derive the effective DM-gluon interaction, one can calculate the corresponding diagram with a heavy quark line and replace

$$m_Q \bar{Q}Q \to -\frac{\alpha_s}{12\pi} G^a_{\mu\nu} G^{a\mu\nu} \ . \tag{4.84}$$

This replacement yields the Wilson coefficient of the effective gluon contributions to the SI-cxn as depicted in Fig. 4.4. This method implies subtle problems when including NLO EW corrections. We will discuss the implications of this problem and possible solutions in the specific part of the calculation.

Besides the triangle quark loop, also a fermion box-like topology can induce an effective DM-gluon interaction. However, these contributions are of two-loop order. Nevertheless, we want to investigate their overall effect on the SI-cxn in suitable approximations.

The corresponding topology is shown in Fig. 4.5. The upper gray blob indicates possible

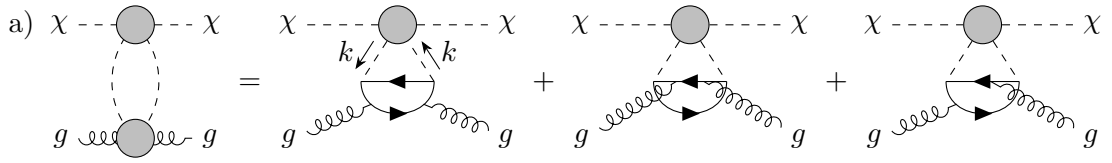

Figure 4.5.: Effective DM-gluon interactions induced by a quark box. The lower gray blob indicates the quark loops contributing to the effective Higgs-gluon vertex, whereas the upper vertex corresponds to the quartic vertex of two Higgs bosons and the external DM particles. The upper vertex will be discussed separately in both models.

couplings of the quartic vertex between two χ and two Higgs bosons. The upper part will be discussed in the respective chapters. The lower gray blob indicates the effective quartic coupling of two Higgs boson mediators and two external gluons. The naive approach to use Eq. (4.84) in the box topology to derive the Wilson coefficient would yield large errors [115, 125]. However, it is possible to derive an effective $h_i h_j G^a_{\mu\nu} G^{a\mu\nu}$ vertex in the Fock-Schwinger gauge for heavy top quark masses m_t [125],

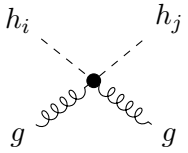

$$\approx \frac{ig_s^2}{48\pi^2 m_t^2} a_i a_j \,, \tag{4.85}$$

where $a_{i,j}$ are the Higgs-quark couplings, which depend on the underlying model and g_s is the strong gauge coupling. The vertex is produced by the effective Lagrangian

$$\mathcal{L} \supset \frac{1}{2} \frac{g_s^2}{48\pi^2 m_t^2} a_i a_j \, h_i h_j G^a_{\mu\nu} \, G^{a\mu\nu} \,. \tag{4.86}$$

We will include this effective quartic vertex $h_i h_j G^a_{\mu\nu} G^{a\mu\nu}$ to derive additional gluon contributions to the SI-cxn. We will discuss the overall size of the corrections induced by this quartic coupling and the corresponding complications in the models, respectively.

CHAPTER 5

SI-cxn in the Pseudo-Nambu Goldstone Dark Matter Model

In this following chapter, we discuss the calculation of the EW NLO corrections to the SI-cxn in the PNGDM. The PNGDM features an interesting consequence of the $U(1)$ symmetry of the potential. The resulting tree-level SI-cxn vanishes in the limit of vanishing momentum transfer [80], which is taken to extract the SI-cxn. Thus, there is no possibility to derive any exclusion limits based on the tree-level predictions for the direct detection experiments in the PNGDM. There are already calculations concerning EW one-loop corrections for this specific model [119, 126]. In [126], they utilize the $U(1)$ symmetry of the potential yielding a crucial cancellation of diagrams. These cancellations allow them to drop specific types of diagrams. However, we provide a systematic full on-shell calculation including all contributions, allowing for a consistency check.
Even though we follow the calculation of [119], we will pin down conceptional problems in their calculation concerning the calculation of the EW NLO corrections of the lower vertex. Our proposed solution restores the *Goldstone nature of the DM candidate*, which is not observable in the approach of [119].
We start the discussion with the determination of the tree-level SI-cxn, followed by the calculation of the EW NLO corrections to the SI-cxn. We will separately discuss the different topologies of the $2 \to 2$ DM-nuclei scattering process.

5.1. Tree-Level Matching

There are no direct couplings between the DM weakly interacting massive particle (WIMP) candidate and quarks or gluons. As already discussed in Sec. 4.3.3, the contributing diagrams generating the effective interaction have to be identified and the respective Wilson coefficient has to be matched. At tree-level, there are two contributing diagrams. The required vertices for the calculation between two quarks q and the Higgs boson h_i as well as the vertex between two DM fields χ and the respective Higgs boson h_i read

$$V_{qqh_i} = i\frac{m_q}{v}R_{1,i} \ , \qquad V_{\chi\chi h_i} = -i\frac{m_{h_i}^2}{v_s} \ . \tag{5.1}$$

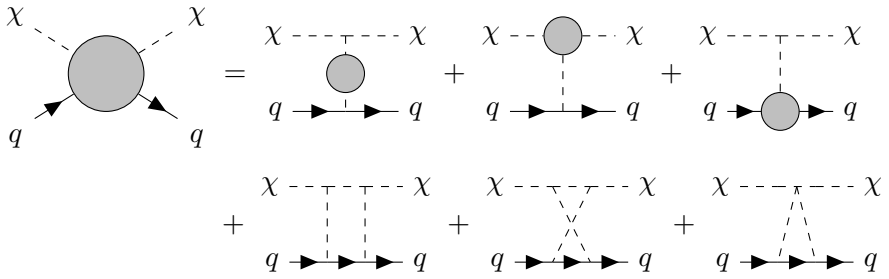

Figure 5.1.: One-loop EW corrections to DM-quark scattering. They are given by propagator corrections, vertex corrections, box and triangle diagrams.

Both Higgs bosons h_i $(i = 1, 2)$ of the PNGDM act as mediator between the DM candidate χ and the quark q. The tree-level diagram for a quark q is then given by

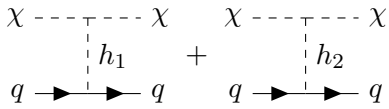

$$= -i\frac{(m_{h_1}^2 - m_{h_2}^2)\cos\alpha\sin\alpha}{(t - m_{h_1}^2)(t - m_{h_2}^2)vv_S} m_q t\,\bar{u}(p_2)u(p_1)\,, \tag{5.2}$$

with the masses m_{h_1} and m_{h_2} of the two mass eigenstates h_1 and h_2, respectively, the singlet VEV v_s, the mixing angle α and the quark mass m_q. The Mandelstam variable is indicated as $t = (p_\chi - p_q)$. The amplitude in Eq. (5.2) allows us to read off the required Wilson coefficient C_S^q in Eq. (4.71). Further, Eq. (4.84) allows us to replace $m_q\bar{q}q$ in Eq. (5.2), hence the extraction of the Wilson coefficient C_S^g in Eq. (4.71) is possible. However, both, the amplitude and thus the Wilson coefficients are proportional to t and vanish in the limit of vanishing momentum transfer, resulting in a vanishing tree-level predicted SI-cxn. This behavior of vanishing SI-cxn can be linked with the softly-broken $U(1)$ symmetry of the Lagrangian [80].
In conclusion, the tree-level SI-cxn is expected to be highly suppressed and to avoid naturally the direct detection limits. Even though, the velocity and momentum transfer suppressed operators could yield a non-zero cross-section in a direct detection experiment, we explore the possibility that EW NLO corrections generate a non-zero SI-cxn. The calculation of the NLO EW corrections will be discussed in the following section.

5.2. Electroweak Next-to-leading Order Corrections

The EW NLO corrections of the SI-cxn can be categorized in quark and gluon contributions. Subsequently, they can be separated in the respective topologies. We start the discussion with the quark contributions. The EW NLO corrections to the gluon interactions is discussed afterwards in detail. The effective one-loop quark interaction is depicted in Fig. 5.1 denoted as the gray blobb on the left side of the equation. The one-loop coupling can be split into mediator, upper and lower vertex, triangle and box-like corrections indicated as generic gray blobs, respectively. All gray blobbs on the right-hand side of the equation correspond to EW one-loop corrections. The triangle- and box-type diagrams are generated through two scalar mediators. To simplify the bookkeeping, we discuss each topology separately.

5.2.1. Mediator Corrections

The calculation of the one-loop corrections to the mediator requires the evaluation of the genuine virtual one-loop diagrams depicted in Fig. 5.2. The genuine one-loop diagrams in

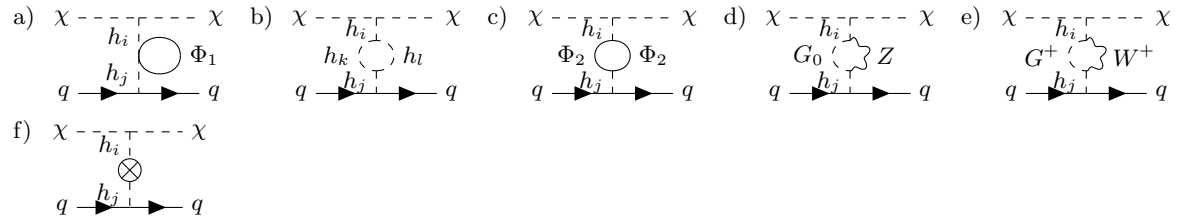

Figure 5.2.: The one-loop EW corrections to the mediator. They can be split into the genuine one-loop diagrams diagrams a)-e)) and the respective counterterm amplitude (diagram f)). The indices $i, j, k, l = 1, 2$ indicate the respective Higgs mediator h_1, h_2. The possible field insertions are given by $\Phi_1 = \{h_i, \chi, G^{(0,\pm)}, Z, W^\pm\}$ and $\Phi_2 = \{\chi, G^{(0,\pm)}, Z, W^\pm, \eta_Z, \eta_W, f\}$, where f stands for all SM fermions, $G^{(0,\pm)}$ for the neutral and charged Goldstone bosons, respectively, and $\eta_{Z,W}$ for the ghost fields.

Fig. 5.2 a)-e) are calculated in the general R_ξ gauge in order to be able to check for gauge parameter cancellation in the final result. The last diagram f) indicates the corresponding counterterm of the mediator corrections. We express the sum of all one-loop contributions in terms of the renormalized one-loop propagator ($i, j = 1, 2$)

$$\Delta_{h_i h_j} = -\frac{\hat{\Sigma}_{h_i h_j}(p^2 = 0)}{m^2_{h_i} m^2_{h_j}} \,, \tag{5.3}$$

with the renormalized self-energy matrix

$$\begin{pmatrix} \hat{\Sigma}_{h_1 h_1} & \hat{\Sigma}_{h_1 h_2} \\ \hat{\Sigma}_{h_2 h_1} & \hat{\Sigma}_{h_2 h_2} \end{pmatrix} \equiv \hat{\Sigma}(p^2) = \Sigma(p^2) - \delta m^2 - \delta T + \frac{\delta Z}{2}\left(p^2 - \mathcal{M}^2\right) + \left(p^2 - \mathcal{M}^2\right)\frac{\delta Z}{2} \,. \tag{5.4}$$

The genuine one-loop self-energy is denoted by Σ, with the tadpole and mass counterterm and the Z-factors as defined in Eq. (4.14). The scalar mass matrix of the two Higgs bosons is denoted as $\mathcal{M}$. Some remarks about the treatment of δZ counterterm: the Higgs boson mediators correspond to an internal degree of freedom, hence the introduction of the δZ part in Eq. (5.3) is artificially. However, if the WFRCs are included in all different topologies (upper, lower vertex and mediator), they cancel each other exactly in the sum. Even though the introduction of these δZ parts is artificially, it allows us to check for UV finiteness in each topology separately and simplifies the bookkeeping, or rather enables the comparison of the size of the corrections induced by the different topologies. The actual cancellation is checked analytically and numerically in our calculation.

5.2.2. Upper Vertex Corrections

The genuine one-loop upper vertex corrections are depicted in Fig. 5.3 a)-f), the diagram g) indicates the respective vertex counterterm. The virtual corrections are calculated in the limit of vanishing momentum transfer, where we assume $p_{\text{in}} = p_{\text{out}}$. We emphasize that this limit is stricter than taking $q^2 = (p_\chi - p_q)^2 = 0$, since *e.g.* the Gram determinant is vanishing implying a complication in the reduction of the standard one-loop scalar integrals [127–133]. We used `FeynArts` [134] to generate the respective Feynman diagrams and `FeynCalc v9.2` [135] to reduce the corresponding amplitudes. Since the expressions of the genuine one-loop corrections are rather lengthy, we do not list them explicitly.
The vertex counterterm in Fig. 5.3 g) is derived from the tree-level coupling of the upper vertex ($i = 1, 2$)

$$C_{\chi\chi h_i} = -\frac{m^2_{h_i}}{v_s} R_{i2} \,, \tag{5.5}$$

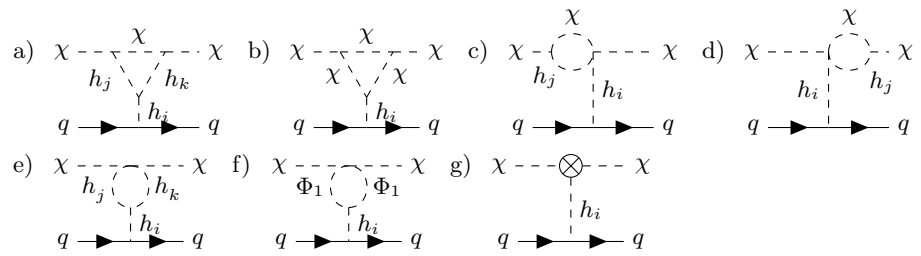

Figure 5.3.: The EW NLO corrections to the upper vertex. The indices $i, j, k = 1, 2$ indicate the respective Higgs mediator h_1, h_2. The field insertion is given by $\Phi_1 = \{\chi, G^{(0,\pm)}\}$.

yielding

$$\delta C_{\chi\chi h_i} = -\frac{R_{i2}}{v_s}\delta m^2_{h_i} - \frac{\delta R_{i2} m^2_{h_i}}{v_s} = -\frac{R_{i2}}{v_s}\delta m^2_{h_i} - \frac{R_{i1} m^2_{h_i}}{v_s}\delta\alpha\,. \tag{5.6}$$

The rotation matrix R_{ij} is given in Eq. (3.18). This allows us to construct the counterterm amplitudes for the upper vertex topology (referred to as upV)

$$iA^{\mathrm{CT}}_{\mathrm{upV},h_1} = \frac{-C_{qqh_1}}{m^2_{h_1}}\left[\delta C_{\chi\chi h_1} + \frac{1}{2}\left(C_{\chi\chi h_1}\delta Z_{h_1h_1} + C_{\chi\chi h_2}\delta Z_{h_2h_1}\right) + C_{\chi\chi h_1}\delta Z_{\chi\chi}\right]\bar{u}(p_q)u(p_q)\,, \tag{5.7a}$$

$$iA^{\mathrm{CT}}_{\mathrm{upV},h_2} = \frac{-C_{qqh_2}}{m^2_{h_2}}\left[\delta C_{\chi\chi h_2} + \frac{1}{2}\left(C_{\chi\chi h_2}\delta Z_{h_2h_2} + C_{\chi\chi h_1}\delta Z_{h_1h_2}\right) + C_{\chi\chi h_2}\delta Z_{\chi\chi}\right]\bar{u}(p_q)u(p_q)\,, \tag{5.7b}$$

where we again include the artificially introduced δZ parts for the internal degree of freedom, the Higgs boson. The quark couplings are given by ($i = 1, 2$)

$$C_{qqh_i} = -\frac{g m_q}{2m_W}R_{i1}\,. \tag{5.8}$$

5.2.3. Lower Vertex Corrections

The EW NLO corrections of the lower vertex can be determined analogously to the upper vertex. The genuine one-loop diagrams are depicted in Fig. 5.4, where we again impose the limit of vanishing momentum transfer, $p_{\mathrm{in}} = p_{\mathrm{out}}$. Again we use `FeynArts` and `FeynCalc` to calculate the reduced amplitudes. The vertex counterterm is derived from the tree-level coupling in Eq. (5.8)

$$\delta C_{qqh_i} = \frac{-g m_q}{2m_W}\left(R_{i1}\left(-\frac{\delta m^2_W}{2m^2_W} + \frac{\delta g}{g} + \frac{\delta m_q}{m_q}\right) - R_{i2}\delta\alpha\right)\,, \tag{5.9}$$

hence the counterterm amplitudes read for the lower vertex topology (referred to as loV)

$$i\mathcal{A}^{CT}_{\mathrm{loV},h_1} = \frac{-C_{\chi\chi h_1}}{m^2_{h_1}}\left(\delta C_{qqh_1} + \frac{1}{2}\delta^{\mathrm{Leg}}_{h_1}\right)\bar{u}(p_q)u(p_q)\,, \tag{5.10a}$$

$$i\mathcal{A}^{CT}_{\mathrm{loV},h_2} = \frac{-C_{\chi\chi h_2}}{m^2_{h_2}}\left(\delta C_{qqh_2} + \frac{1}{2}\delta^{\mathrm{Leg}}_{h_2}\right)\bar{u}(p_q)u(p_q)\,, \tag{5.10b}$$

with the external leg corrections

$$\delta^{\mathrm{Leg}}_{h_1} = \left(C_{qqh_1}\delta Z_{h_1h_1} + C_{qqh_2}\delta Z_{h_2h_1} + C_{qqh_1}\delta Z^L_{qq} + C_{qqh_1}\delta Z^R_{qq}\right)\,, \tag{5.11a}$$

$$\delta^{\mathrm{Leg}}_{h_2} = \left(C_{qqh_2}\delta Z_{h_2h_2} + C_{qqh_1}\delta Z_{h_1h_2} + C_{qqh_2}\delta Z^L_{qq} + C_{qqh_2}\delta Z^R_{qq}\right)\,. \tag{5.11b}$$

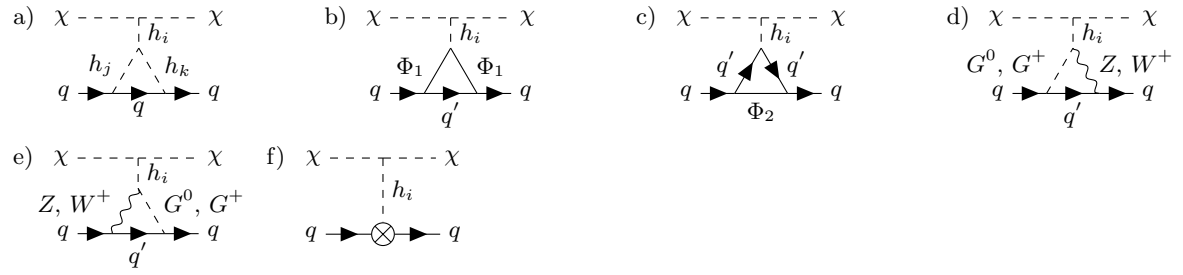

Figure 5.4.: The EW NLO corrections to the lower vertex. The indices $i, j, k = 1, 2$ indicate the respective Higgs mediator h_1, h_2. The possible field insertions are given by $\Phi_1 = \{G^{(0,\pm)}, Z, W^\pm\}$, $\Phi_2 = \{h_i, G^{(0,\pm)}, \gamma, Z, W^\pm\}$. The quark q' corresponds to the up- or down-type quark depending on the field insertion, respectively. Note that for simplicity a diagonal CKM matrix is assumed.

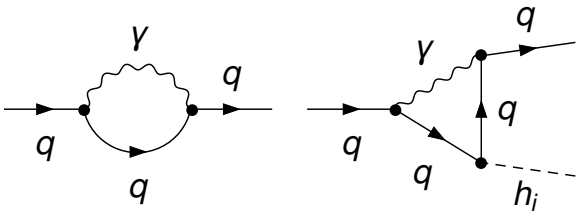

Figure 5.5.: The QED subset. Left: The quark self-energy containing an internal photon line. Right: The vertex correction with an internal photon line.

Again, we artificially introduce the δZ WFRCs for the internal Higgs boson mediator to ensure the proper cancellation in the sum of all topologies. There is one subtle problem in the EW NLO corrections of the lower vertex. The presence of charged external particles, the quarks, implies infrared (IR) divergencies arising in the corrections. They are related to the diagrams including the massless propagators of the photon. The IR divergent diagrams form a UV-finite closed subset depicted in Fig. 5.5, which we refer to as QED subset. The self-energy correction enters through the counterterms (*see* Sec. 4.1) and the other diagram corresponds to a genuine one-loop virtual correction to the quark-Higgs boson vertex. However, due to the softly-broken $U(1)$ symmetry of the Lagrangian, the QED subset cancels out in the sum of all contributing diagrams. So no IR divergent diagrams contribute to the Wilson coefficient and thus to the SI-cxn. Hence, a regularization of the IR divergencies is not required in the PNGDM. This conclusion does not generalize to other models. The QED subset does contribute in the VDM. We will discuss the relating problems in Chapter 6.

5.2.4. Box Corrections

The box corrections, which contribute to the SI-cxn, are depicted in Fig. 5.6. They can be separated in the pure box diagrams and the triangle topology. For simplicity, we show the calculation for diagrams with only Higgs boson mediators, the respective diagrams with Goldstone mediators are calculated analogously.
The extraction of the SI-cxn requires the limit of vanishing momentum transfer. To account for this, we expand the box diagrams for small momentum transfer and follow [125,136]. The

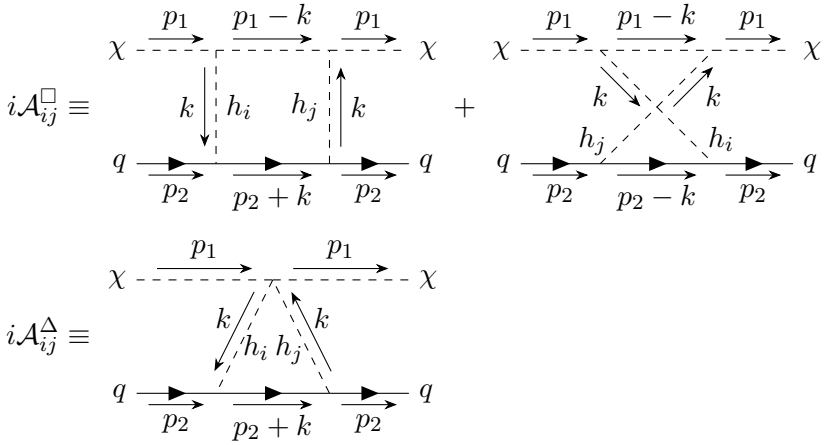

Figure 5.6.: Box topologies contributing to the DM-quark scattering referred to as $\mathcal{A}^{\square}$ and the triangle topologies denoted by $\mathcal{A}^{\Delta}$. The indices i, j denote the Higgs mediators h_1, h_2.

conventions of the momenta are defined in Fig. 5.6, where the incoming and outgoing quark momentum is the same. The corresponding amplitudes read

$$\begin{aligned} i\mathcal{A}_{ij}^{\square} = i^4 A_{ij}\, \bar{u}(p_2) \int \frac{d^4k}{(2\pi)^4} \frac{1}{k^2 - m_i^2} \frac{1}{(p_1 - k)^2 - m_\chi^2} \frac{1}{k^2 - m_j^2} \\ \cdot \left(\frac{\not{p}_2 + \not{k} + m_q}{(p_2 + k)^2 - m_q^2} + \frac{\not{p}_2 - \not{k} + m_q}{(p_2 - k)^2 - m_q^2} \right) u(p_2)\,, \end{aligned} \tag{5.12a}$$

$$i\mathcal{A}_{ij}^{\Delta} = i^4 B_{ij}\, \bar{u}(p_2) \int \frac{d^4k}{(2\pi)^4} \frac{1}{k^2 - m_i^2} \frac{1}{k^2 - m_j^2} \frac{\not{p}_2 + \not{k} + m_q}{(p_2 + k)^2 - m_q^2} u(p_2)\,, \tag{5.12b}$$

with the generic couplings defined as $A_{ij} = a_i a_j b_i b_j$ and $B_{ij} = a_i a_j b_{ij}$, where $a_{i,j}$ and $b_{i,j}$ are the coefficients of the $h_{i,j}\bar{q}q$ and $h_{i,j}\chi\chi$ vertices, respectively, and b_{ij} is the coefficient of the $h_i h_j \chi\chi$ vertex. The coefficients are explicitly given by

$$\begin{aligned} a_1 &= -i\frac{m_q \cos\alpha}{v}\,, \quad a_2 = -i\frac{m_q \sin\alpha}{v}\,, \quad b_1 = -i\frac{m_{h_1}^2 \sin\alpha}{v_s}\,, \quad b_2 = -i\frac{m_{h_2}^2 \cos\alpha}{v_s}\,, \\ b_{11} &= \frac{\sin\alpha}{4vv_s^2}\left(v_s\left(m_{h_2}^2 - m_{h_1}^2\right)\cos^3\alpha + vm_{h_2}^2 \cos^2\alpha \sin\alpha + vm_{h_1}^2 \sin^3\alpha\right), \\ b_{22} &= \frac{\cos\alpha}{4vv_s^2}\left(vm_{h_2}^2 \cos^3\alpha + vm_{h_1}^2 \cos\alpha \sin^2\alpha + v_s\left(m_{h_2}^2 - m_{h_1}^2\right)\sin^3\alpha\right), \\ b_{12} &= \frac{\cos\alpha \sin\alpha}{4vv_s^2}\left(2vm_{h_2}^2 \cos^2\alpha + 2vm_{h_1}^2 \sin^2\alpha - v_s\left(m_{h_2}^2 - m_{h_1}^2\right)\sin 3\alpha\right). \end{aligned} \tag{5.13}$$

The dominant contributions of the propagators to the integrals in Eq. (5.12) are coming from the regions close to the poles, *i.e.* $k^2 \approx m_{h_i}^2$ $(i = 1, 2)$. In the same time, the target nucleus is assumed to be at rest, hence its energy can be approximated by the Fermi energy, which is of the order of few MeV. This might allow us to expect $p_2 \ll k$ [125, 136], where p_2 is the momentum of the quark. Furthermore, we want to achieve that all momentum dependence is removed in the amplitude, since these parts would contribute to the momentum transfer, velocity suppressed operators nevertheless. They are neglected in this study. This yields the following expansion of the propagators in Eq. (5.12)

$$\frac{1}{(p_2 \pm k)^2 - m_q^2} = \frac{1}{k^2 \pm 2p_2 \cdot k} = \frac{1}{k^2} \mp \frac{2p_2 \cdot k}{k^4} + \mathcal{O}\left(\left(\frac{p_2 \cdot k}{k^2}\right)^2\right)\,. \tag{5.14}$$

Using the expansion and utilizing the Dirac equation $\not{p}u(p) = m_q u(p)$ we obtain

$$i\mathcal{A}_{ij}^{\square} = i^4 A_{ij}\,\bar{u}(p_2)\int \frac{d^4k}{(2\pi)^4}\frac{1}{k^2-m_i^2}\frac{1}{(p_1-k)^2-m_\chi^2}\frac{1}{k^2-m_j^2}\left(\frac{4m_q}{k^2}+\frac{-4p_2\cdot k}{k^4}\not{k}\right)u(p_2), \tag{5.15a}$$

$$i\mathcal{A}_{ij}^{\triangle} = i^4 B_{ij}\,\bar{u}(p_2)\int \frac{d^4k}{(2\pi)^4}\frac{1}{k^2-m_i^2}\frac{1}{k^2-m_j^2}\left(\frac{1}{k^2}-\frac{2p_2\cdot k}{k^4}\right)(2m_q+\not{k})\,u(p_2). \tag{5.15b}$$

These amplitudes in Eq. (5.15) are then reduced to the Passarino-Veltmann integral basis.

5.2.5. Gluon Contributions

The effective gluon-DM interaction is shown in Fig. 5.7. The first two diagrams correspond to the mediator and upper vertex corrections in combination with the lower effective gluon-Higgs interaction induced through the quark triangle. Strictly speaking, these diagrams correspond to a mixed QCD-EW two-loop order correction. However, as discussed in Sec. 4.3.3, we treat the Higgs-gluon vertex as an effective vertex by integrating out the heavy quarks. We first evaluate the upper vertex and mediator corrections as discussed in the previous sections and use Eq. (4.84) to derive the effective gluon-Higgs interaction.

Even though, this approach is used in several publications (*e.g.* [119]), we want to discuss several problems arising if these contributions are taken into account.
The naive approach to calculate the EW NLO corrections of the lower vertex in accordance with Sec. 5.2.3 and using Eq. (4.84) would ensure the proper cancellation of the artificially introduced δZ part of the internal Higgs boson mediator. Furthermore, this would ensure the numerical stability of the KOSY renormalization scheme for the mixing angle α. Note that there is an explicit mass pole $1/(m_{h_2}^2 - m_{h_1}^2)$ in the definition of $\delta\alpha$ in Eq. (4.20). In [89], it is discussed that the KOSY scheme provides numerical stable predictions in the sense that there are no pole structures induced by degenerate Higgs boson masses, if either $\delta\alpha$ and $\delta Z_{h_i h_j}$ occur in a specific combination or only the combination of $(m_{h_2}^2 - m_{h_1}^2)\delta\alpha$ occurs in the final result. The former is present in $1 \to 2$ on-shell decays, the latter for instance in the full $2 \to 2$ process, since the upper and lower vertex contribute $\delta\alpha$. Both contributions add up to the required combination $(m_{h_2}^2 - m_{h_1}^2)\delta\alpha$.
However, it is unclear if the matching in Eq. (4.84) holds if EW corrections are taken into account. A proper calculation would require a two-loop matching of the QCD trace anomaly in this specific model. This is beyond the scope of this thesis. We circumvent this uncertainty, by dropping the EW corrections of the lower vertex in the context of the gluon contributions. Though, this immediately implies that both, the upper and mediator corrections, cannot be included either, since we would miss the proper cancellation of the $\delta Z_{h_i h_j}$ (or rather UV poles in the full $2 \to 2$ process). To compare with [119], we nevertheless include both (upper vertex and mediator) corrections while using Eq. (4.84) and compare to our approach, where we drop them completely. We refer to this approach including the first two diagrams in Fig. 5.7 as *additional gluon contributions*.
Furthermore, we take the effective quartic Higgs-gluon vertex in Eq. (4.85) into account corresponding to the last diagram in Fig. 5.7. This vertex generates diagrams depicted in Fig. 4.5b) which show in detail in the upper gray blob. They are discussed in the literature to be crucial to have the dominant gluon contributions to the SI-cxn [115, 125]. We include them and investigate their overall impact on the SI-cxn.

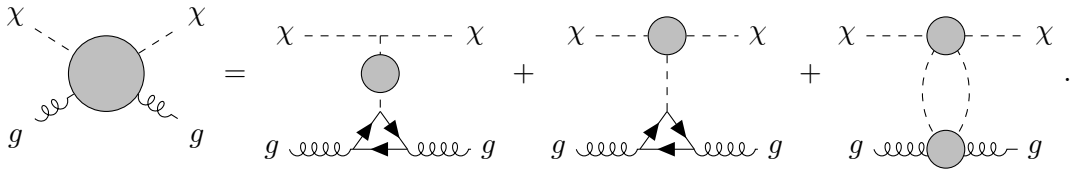

Figure 5.7.: Generic one-loop correction of the DM-gluon interaction. The contributions can be split in mediator, vertex corrections and the effective two-loop contributions. The gray blob indicates the genuine one-loop corrections and the respective counterterm insertion. The upper vertex is shown explicitly in Fig. 4.5 b).

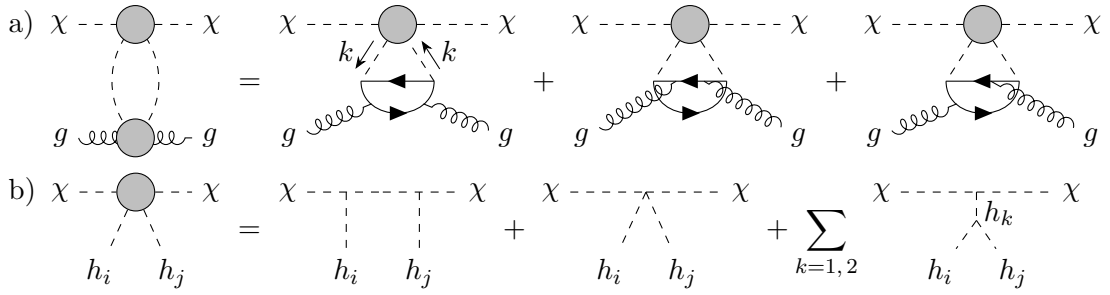

Figure 5.8.: Triangle and box diagrams with external gluons. a) shows the different contributions of the lower gray blobb; b) indicates the contributing coupling structures of the upper vertex.

5.2.6. Contributing Tensor Structures

All NLO corrections generate in the limit of vanishing momentum transfer two independent spinor structures, $\bar{u}(p_2)u(p_2)$ (with the remainder of the amplitude being independent of the momenta) and terms proportional to $(p_1 \cdot p_2)\,\bar{u}(p_2)\not{p}_1 u(p_2)$. This allows us to cast the full amplitude into the form

$$i\mathcal{A} = i\left(A\bar{u}(p_2)u(p_2) + B\,(p_1 \cdot p_2)\,\bar{u}(p_2)\not{p}_1 u(p_2)\right) \tag{5.16}$$

with some momentum-independent constants A and B. The twist-2 operator $\mathcal{O}^q_{\mu\nu}$ can be rewritten as

$$\bar{q}i\partial_\mu\gamma_\nu q = \mathcal{O}^q_{\mu\nu} + i\bar{q}\left(\frac{\partial_\mu\gamma_\nu - \partial_\nu\gamma_\mu}{2} + \frac{1}{4}g_{\mu\nu}\not{\partial}\right)q\,, \tag{5.17}$$

where the asymmetric part is not relevant for the SI-cxn, thus it can be dropped. This amplitude can be produced by the following effective Lagrangian

$$\mathcal{L}_{eff} = \left(\frac{1}{2m_q}A + \frac{1}{8}m_\chi^2 B\right)m_q\chi\chi\bar{q}q + \frac{1}{2}B\,(\chi i\partial^\mu i\partial^\nu\chi)\,\mathcal{O}^q_{\mu\nu}\,. \tag{5.18}$$

Comparing the coefficients in Eq. (5.18) with the Wilson coefficients of Eq. (4.72) yields

$$C_S^q = \frac{1}{2m_q}A + \frac{m_\chi^2}{8}B\,, \tag{5.19a}$$

$$C_T^q = \frac{m_\chi^2}{2}B\,. \tag{5.19b}$$

The identification in Eq. (5.19) allows us to extract the NLO corrections to the Wilson coefficients, hence allows for the determination of the SI-cxn at EW NLO.

5.3. Results

Before we discuss the results of [3], we list the numerical values used in the analysis and the respective tools. Furthermore, we only discuss the SI-cxn for the proton in the following

$$\sigma \equiv \sigma_P \ . \tag{5.20}$$

The SI-cxn for a neutron is slightly different due to the different nuclear matrix elements and respective mass. The proton mass is taken as

$$m_P = 0.938\,\text{GeV} \ . \tag{5.21}$$

The SM input parameters are taken as [137]

$$\begin{aligned}
m_u &= 0.19\,\text{GeV}\,, & m_c &= 1.4\,\text{GeV}\,, & m_t &= 172.5\,\text{GeV}\,, \\
m_d &= 0.19\,\text{GeV}\,, & m_s &= 0.19\,\text{GeV}\,, & m_b &= 4.75\,\text{GeV}\,, \\
m_e &= 0.511\,\text{MeV}\,, & m_\mu &= 105.658\,\text{MeV}\,, & m_\tau &= 1.777\,\text{GeV}\,, \\
m_W &= 80.398\,\text{GeV}\,, & v &= 246\,\text{GeV}\,, & & \\
m_Z &= 91.188\,\text{GeV}\,. & & & &
\end{aligned} \tag{5.22}$$

The electroweak gauge input parameters are chosen to be

$$g = 2m_W/v = 0.653\,, \qquad \sin\theta_W = m_W/m_Z = 0.472\,. \tag{5.23}$$

One of the two neutral Higgs bosons h_i $(i = 1, 2)$ is identified with the SM-like Higgs boson with a mass of [18]

$$m_h = 125.09\,\text{GeV} \ , \tag{5.24}$$

which we refer to as h in the following. The other remaining non-SM like Higgs boson is referred to as ϕ with its mass m_ϕ. The nuclear matrix elements and second momenta are given in Eqs. (4.68) and (4.70). The parameter sample used for this analysis is generated by `ScannerS` [60, 61]. Thus the generated parameter points obey theoretical and experimental constraints as discussed in Sec. 3.1. The DM relic abundance is calculated with `MicrOMEGAS` [138] and required to be below the Planck measurement of $\left(\Omega h^2\right)^{\text{obs}}_{\text{DM}} = 0.1186 \pm 0.002$ [103]. The Feynman diagrams are generated with `FeynArts` [134], where the required model file is created with the help of `SARAH` [139]. The reduction to the standard Passarino-Veltmann basis is done with `FeynCalc v9.2.0` [135]. For the numerical evaluation of the scalar one-loop integrals, we use `Collier` [140].

In our analysis, we do not demand that the DM candidate accounts for the full relic abundance. This requires that the expected SI-cxn in a direct detection experiment has to be corrected to take into account the reduced flux of DM particles. The ratio of the produced DM relic abundance of the WIMP particle $\left(\Omega h^2\right)_\chi$ normalized to the measured DM density $\left(\Omega h^2\right)_{\text{DM}}$

$$f_{\chi\chi} \equiv \frac{\left(\Omega h^2\right)_\chi}{\left(\Omega h^2\right)_{\text{DM}}} \tag{5.25}$$

allows us to rescale the SI-cxn expected for a single nucleon to the expected SI-cxn in a direct detection experiment. This effective SI-cxn is shown as function of the DM mass in Fig. 5.9. The color code indicates the mass of the non-SM like Higgs boson. The solid and dashed lines indicates the derived upper limits on the SI-cxn from the Xenon1T and Xenon10T experiments, respectively. The red vertical line corresponds to $m_\chi = {}^{m_h}/_2$.
The gray background shows the *neutrino floor*, which puts the natural limit on the sensitivity of direct detection. The neutrino floor is the result of coherent neutral neutrino-nucleus

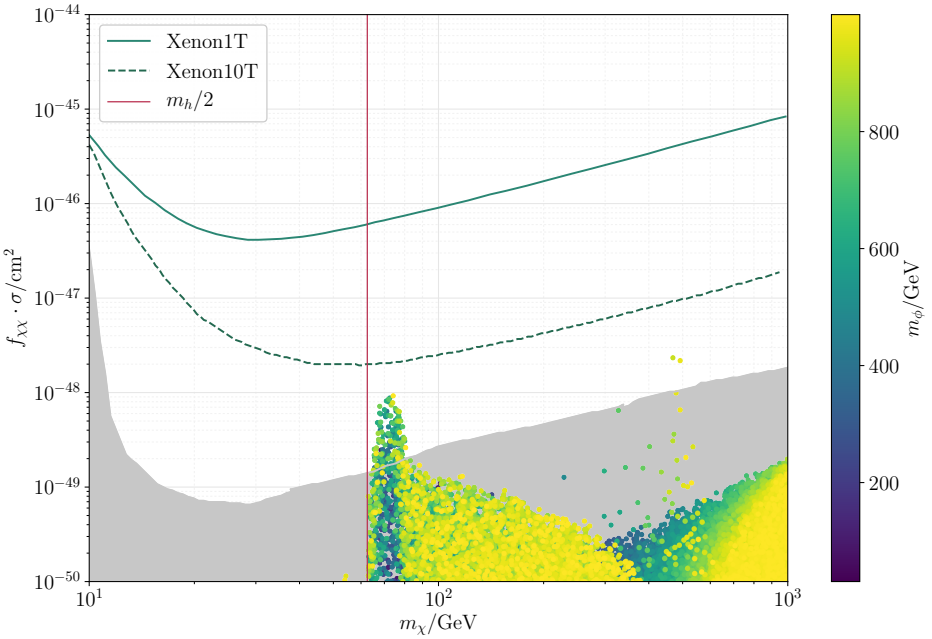

Figure 5.9.: The effective SI-DM nucleon cross-section versus the DM mass m_χ is shown. The gray background corresponds to the neutrino floor. The color code indicates the mass of the non-SM like Higgs boson and the red vertical lines indicates the half of the SM-like Higgs boson mass, $m_\chi = m_h/2$. The curves denote the corresponding limits derived from Xenon1T and Xenon10T. *The figure is takem from [3].*

elastic scattering [141, 142], hence yields an irreducible background for DM direct detection. Concluding, DM parameter points below the neutrino floor predict signals that are not distinguishable from neutrino scattering.
The color points in Fig. 5.9 correspond to the generated sample used in this analysis. The DM masses lie in the range of roughly 40 GeV up to 1 TeV, which is also true for the non-SM like Higgs boson masses. Almost all of the benchmark scenarios are below the neutrino floor and in this way cannot be probed in direct detection. However, there are two specific mass regions $m_\chi \gtrsim m_h/2$ and $m_\chi \simeq m_\phi/2$, which allow for SI-cxns above the neutrino floor. Both regions correspond to the resonant region, in which the decay $\{h, \phi\} \to \chi\chi$ is kinematically possible. This enhancement can compensate for the suppression of the corresponding couplings, which is required to remain below the relic abundance.
The absence of valid parameter points with $m_\chi \lesssim m_h/2$ is induced through the Higgs-to-invisible searches. The decay channel $h \to \chi\chi$ is open in this specific mass region.
We emphasize again, that the leading-order (LO) prediction of the SI-cxn is zero in the PNGDM. By including the EW NLO corrections in the ChEFT and the NREFT framework, it is possible to produce SI-cxns above the neutrino floor and even almost in reach of the Xenon10T experiment. The XENONnT projection [143] suggests that some of the benchmark scenarios could even be probed. Therefore, higher-order corrections for SI-cxns might play an important role to discuss the sensitivity of future DM direct detection experiments and thus also for the derivation of exclusion limits for DM models.

The discussion of Fig. 5.10 requires some comments about the expectations. The potential of the PNGDM in Eq. (3.30) has a softly-broken $U(1)$ symmetry, which is induced by the parameter m_χ^2. As it turns out, this parameter is also the mass of the DM candidate, the imaginary part of the singlet field χ in Eq. (3.35). The $U(1)$ gives rise to the (pseudo-) Goldstone nature of the dark matter candidate [80] resulting in the cancellation mechanism, so

$m\phi$ [GeV]	m_χ [GeV]	v_s [GeV]	α	$f_{\chi\chi}$	$\sigma^{(\mathrm{SI})}$ [cm^2]
546.93	72.53	152.05	0.224	0.40	$8.63 \cdot 10^{-49}$

Table 5.1.: Benchmark point of the PNGDM: The benchmark point is used to illustrate the parameter dependencies in the following. This parameter point provides an SI-cxn above the neutrino floor.

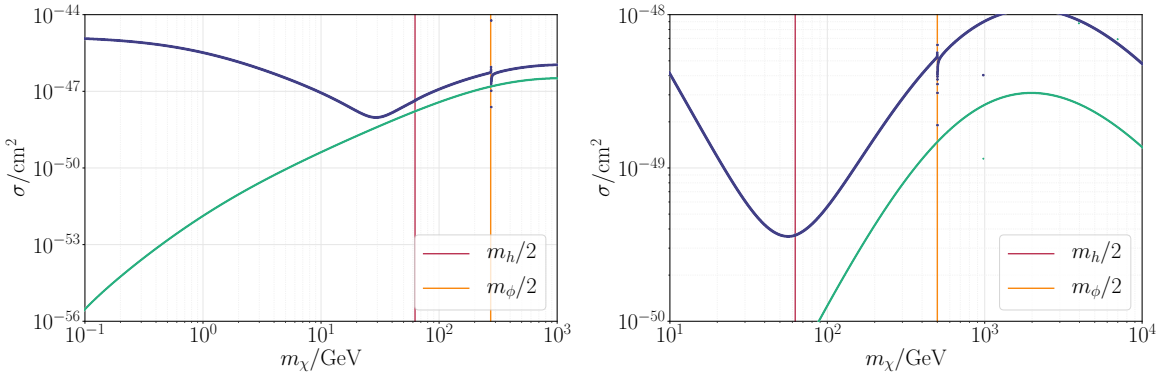

Figure 5.10.: In both figures the SI-cxn is shown as a function of the DM mass m_χ. The green curve corresponds to our proposed approach to treat the gluon contributions, whereas the blue line is the result including the *addition gluon contributions*. For both plots, we used one single parameter point and varied the DM mass m_χ. The left plot is obtained by using the benchmark scenario presented in Tab. 5.1. For the right plot, we use the presented benchmark scenario from [119] with $m_\phi = 1\mathrm{TeV}, v_s = 2v$ and $\sin\alpha = 0.2$. *The figures are taken from [3].*

that the limit of vanishing momentum transfer yield a vanishing LO SI-cxn. There are additional $U(1)$ breaking terms generated at one-loop, however, these vanish if the soft-breaking parameter vanishes [80]. Consequently, if the DM mass m_χ is zero, the $U(1)$ symmetry of the potential is explicit and thus, the (pseudo-) Goldstone nature of the DM candidate has to be restored. The one-loop SI-cxn is expected to be zero in the limit of vanishing momentum transfer and simultaneously vanishing DM mass.
In Fig. 5.10, we investigate the SI-cxn as a function of the DM mass while keeping the remaining input parameters of the benchmark scenario fixed. The left plot corresponds to the benchmark point presented in Tab. 5.1, while the right plot is obtained by using the benchmark point from [119]. The parameter point in Tab. 5.1 provides a SI-cxn above the neutrino floor, while the latter one enables a direct comparison of our results with [119]. In both plots, the green line corresponds to the calculation of the SI-cxn as we proposed in Sec. 4.3. The blue line is taking the *additional gluon contributions* into account. The vertical lines show $m_h/2$ and $m_\phi/2$, respectively. The small kinks at these masses are due to the crossing of thresholds in the loop-integrals. In principle, these numerical instabilities due to the thresholds could be cured by a proper resummation or introduction of a finite decay width in the respective propagators. Since these effects are due to special kinematic configurations, we left out the proper treatment in our calculation.
Both green lines show the expected behavior. The SI-cxn vanishes if the DM mass approaches zero. However, by including the additional gluon contributions, the SI-cxn does not reflect the proper limit. As already pointed out in Sec. 4.3.3, the inclusion of the additional gluon contributions without a proper matching of the $h_i G^a_{\mu\nu} G^{a\mu\nu}$ vertex, implies several problems. In addition, the expected limit for vanishing DM masses cannot be reproduced in this ap-

proach as shown in Fig. 5.10.
Furthermore, both approaches differ around by a factor of nine for large DM masses, which can be explained by the additional gluon contributions, which roughly scales with the squared color factor. We can reproduce the scaling behavior of the SI-cxn as showed in [119], however, only if the additional gluon contributions are included.

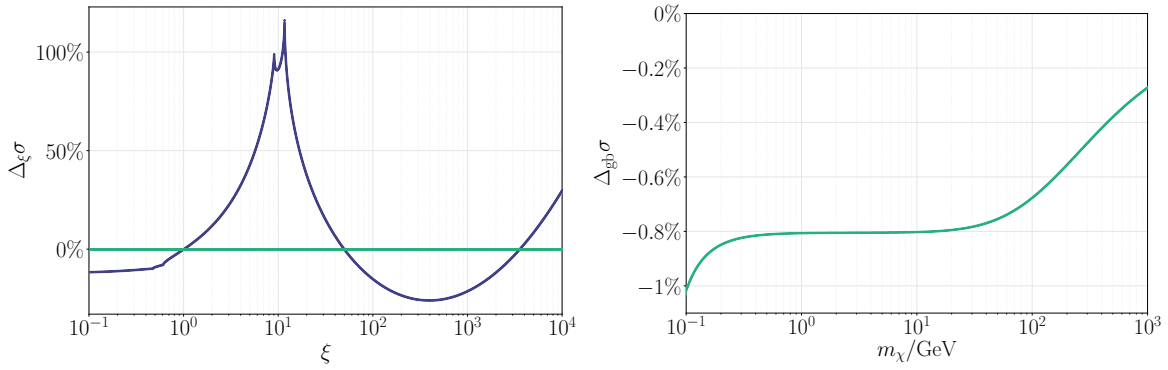

Figure 5.11.: Left: The relative change of the SI cross-section as defined in Eq. (5.26) is shown as a function of the gauge parameter ξ. The green line indicates the result calculated in our presented approach and the blue line corresponds to the approach including the additional gluon contributions.; Right: The relative change of the SI cross-section as defined in Eq. (5.27) as a function of the DM mass m_χ. *The figures are taken from [3].*

In addition, for a consistency check, we investigate the gauge parameter dependence of the SI-cxn. We define the relative change of the SI-cxn as follows

$$\Delta_\xi\sigma \equiv \frac{\sigma - \sigma|_{\xi=1}}{\sigma|_{\xi=1}}\,, \tag{5.26}$$

with $\sigma|_{\xi=1}$ as the SI-cxn in the Feynman gauge (all gauge parameters set to 1). In Fig. 5.11(a), the relative change of the SI-cxn is shown as a function of the gauge parameter ξ[13]. The benchmark point presented in Tab. 5.1 is used for the variation of the gauge parameter ξ. The green line indicates again our proposed approach to calculate the SI-cxn. As can be seen, we do not have a gauge parameter dependence in the SI-cxn, indicating a proper cancellation of all gauge dependent pieces[14]. We emphasize that the inclusion of the triangle diagrams in Fig. 5.6 with Goldstone bosons as mediator, is crucial in order to obtain a gauge-independent result. These contributions are usually not discussed or dropped in the literature.

The inclusion of the additional gluon contributions yield a strong dependence on the gauge parameter ξ up to 100%. This does not allow us to rely on the prediction, since the dependence and hence the uncertainty on the gauge parameter (a nonphysical parameter) is of the same order as the prediction.

[13] For simplicity, we set all gauge parameter to $\xi_W = \xi_Z = \xi_\gamma = \xi$.
[14] Note that the KOSY scheme as presented and used here for the renormalization of the mixing angle introduces an explicit gauge-dependent counterterm. This can be circumvented by using the *pinched scheme* as proposed in [85, 87]

In Fig. 5.11(b), we investigate the overall impact of the effective two-loop contributions induced by the quartic $h_i h_j G^a_{\mu\nu} G^{a\mu\nu}$ vertex in Eq. (4.85). For this, we define

$$\Delta_{\mathrm{gb}\sigma} \equiv \frac{\sigma - \sigma|_{\mathrm{nogb}}}{\sigma|_{\mathrm{nogb}}}\,, \tag{5.27}$$

where $\sigma|_{\mathrm{nogb}}$ indicates the SI-cxn without the effective two-loop diagrams depicted in the last diagram in Fig. 5.7. We show the relative change $\Delta_{\mathrm{gb}\sigma}$ as a function of the DM mass. The benchmark scenario in Tab. 5.1 is used for this variation. The most dominant impact on the SI-cxn is obtained for small and large DM masses. Despite that, the overall effect is in the sub-percentage region.

5.4. Conclusion

We extended the calculation of [126] to an approach taking into account a full on-shell renormalization scheme of the $2 \to 2$ process. By utilizing the ChEFT framework, it is possible to derive a SI-cxn depending on Wilson coefficients, which can be determined in a matching procedure. We compared our results with [119].
We discussed the problems related to the introduction of the additional gluon contributions depicted as the first two diagrams in Fig. 5.7. Including these contributions yield an explicit mass pole for degenerate Higgs boson masses, a gauge-dependent SI-cxn and furthermore the proper limit for vanishing DM masses cannot be reproduced. This leads to the conclusion that these contributions can only be taken into account if a proper matching of the $h_i G^a_{\mu\nu} G^{a\mu\nu}$ vertex with EW corrections, or a full two-loop mixed EW-QCD calculation is performed. In view of the plethora of different DM models and missing strong arguments for a specific DM model, it is questionable if such an involved calculation is promising. We showed, however, that indeed EW NLO correction might play an important role in the context of direct detection and especially in the discussion of the sensitivity of experimental constraints and the resulting derived limits for the parameter space of the underlying model. In addition, we discussed several technical subtleties in the renormalization of dark sectors.

CHAPTER 6

SI-cxn in the Vector Dark Matter Model

The VDM presented in Sec. 3.4 provides a vector-like DM candidate. The spin-nature of the DM candidate allows for an interesting and rich phenomenology in particular for spin-dependent interactions with nuclei [144–150]. The gauged $U(1)_\chi$ symmetry introduces a new gauge interaction which couples the singlet field with the respective gauge boson χ, the DM candidate. Through the mixing of the singlet field S and the Higgs doublet, the vector-like DM candidate is coupled to the Higgs bosons of VDM. Hence, the VDM corresponds to a Higgs portal model. Contrary to the PNGDM, the VDM model does not provide (naturally) suppressed SI-cxns at tree level. The tree-level matching yields a non-vanishing SI-cxn, however, as we will see in the next section, there are *blind spots*. These blind spots indicate parameter regions, or rather points, which yield a vanishing SI-cxn. The vanishing SI-cxn is due to the choice of parameters, unlike to the PNGDM, where a symmetry ensures the cancellation of the different mediator contributions. EW NLO corrections might shift or avoid blind spots, which is a crucial point in the derivation of constraints on the parameter space of the VDM in respect of direct detection experiments.
We present the tree-level matching required for the LO SI-cxn of the VDM in Sec. 6.1, followed by the discussion of the EW NLO corrections in Sec. 6.2. We again split the presentation in the different topology classes. We discuss each topology separately in Secs. 6.2.1 to 6.2.5. We conclude the calculation of the EW NLO corrections to the SI-cxn in Sec. 6.2.6. The results of the phenomenological analysis are presented in Sec. 6.3

6.1. Tree-Level Matching

As described in Sec. 4.3, the leading-order SI-cxn is built of two contributions: light quark and gluon contributions. By using Eq. (4.84), however, it is possible to relate the gluon interactions with the *heavy* quark contributions. This allows us to calculate the LO SI-cxn by first evaluating the diagrams in Fig. 6.1 and then identifying the corresponding dim-6 operators and reading off the Wilson coefficients, respectively. The required vertices between the two DM fields χ and the Higgs boson h_i as well as the vertex between two quarks q and the respective Higgs boson h_i read

$$V_{\chi\chi h_i} = i2g_\chi m_\chi R_{2,i} \ , \quad V_{qqh_i} = i\frac{m_q}{v} R_{1,i} \ . \tag{6.1}$$

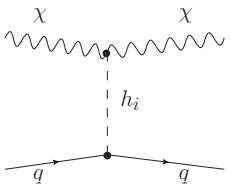

Figure 6.1.: Generic tree-level diagram contribution to the SI-cxn. The mediator h_i corresponds to the two Higgs bosons h_1 and h_2. The quark line q corresponds to all quarks $q = u, d, s, c, b, t$.

The Wilson coefficient of the operator $m_q \bar{q} q \chi_\mu \chi^\mu$ is then given by

$$f_q = \frac{1}{2} \frac{g g_\chi}{m_W} \frac{\sin(2\alpha)}{2} \frac{m_{h_1}^2 - m_{h_2}^2}{m_{h_1}^2 m_{h_2}^2} m_\chi \,, \quad q = u, d, s, c, b, t \,, \tag{6.2}$$

with the input parameters of the VDM and the SM parameters. Eq. (4.84) yields the Wilson coefficient required for the gluon contribution

$$f_G = \sum_{q=c,b,t} -\frac{\alpha_S}{12\pi} f_q \,. \tag{6.3}$$

Note that the LO Wilson coefficient of the gluon operator can be expressed in terms of the Wilson coefficient of the quark operator. Furthermore, the Wilson coefficients of the respective quark type are independent of the quark family. Thus, the resulting LO SI-cxn for a nucleon n ($n = N, P$) is given by

$$\sigma_n^{\mathrm{LO}} = \frac{\sin^2 2\alpha}{4\pi} \left(\frac{m_\chi m_n}{m_\chi + m_n} \right)^2 \frac{\left(m_{h_1}^2 - m_{h_2}^2 \right)^2}{m_{h_1}^4 m_{h_2}^4} \frac{m_\chi^2 m_n^2}{v^2 v_S^2} \left| \sum_{q=u,d,s} f_{T_q}^n + 3 \cdot \frac{2}{27} f_{T_G}^n \right|^2 \,, \tag{6.4}$$

where the Wilson coefficient of the quark operator f_q is factorized and where we used $g_\chi = {}^{m_\chi}/_{v_s}$. The LO SI-cxn is in agreement with [150]. The authors of [150] use an effective coupling constant $f_N \approx 0.3$ between the Higgs boson and a nucleon, which allows us to derive the SI-cxn in a similar manner. The quark line in Fig. 6.1 has to be replaced by an effective *nucleon* spinor line with the corresponding coupling f_N. The effective nucleon-Higgs boson coupling approximately coincides with the factor $\left| \sum_{q=u,d,s} f_{T_q}^N + 3 \cdot \frac{2}{27} f_{T_G}^N \right| \approx 0.3$, where we used the nuclear matrix elements in Eq. (4.68). Even though the LO predictions are approximately the same, the approach of the effective Higgs-nucleon coupling f_N does not allow for a consistent generalization to NLO corrections.

Eq. (6.4) indicates three different blind spots: $\alpha = 0$, degenerate Higgs boson masses $m_{h_1} = m_{h_2}$ and $g_\chi = 0$. The case of vanishing mixing $\alpha = 0$ implies a complete singlet-like Higgs boson $h_2 = \Phi_S$ and a doublet-like $h_1 = \Phi_H$ (*c.f.* Eq. (3.44)). Due to the missing mixing, the singlet field is solely coupled to the DM candidate and cannot interact with the SM particle content. From a phenomenological point of view, this is not an appealing situation.

The blind spot with degenerate Higgs boson masses is a specific kinematical parameter point. In particular, the renormalization and virtual corrections introduce severe numerical problems related with this specific kinematical configuration. Mass poles $\sim {}^1/\left(m_{h_1}^2 - m_{h_2}^2\right)$ are explicitly present, which requires a proper treatment, or resummation of higher-order corrections. This is beyond the scope of this thesis. However, as we will see in the discussion of the EW NLO corrections, the blind spots at degenerate Higgs boson masses remain at NLO and show similar behavior.

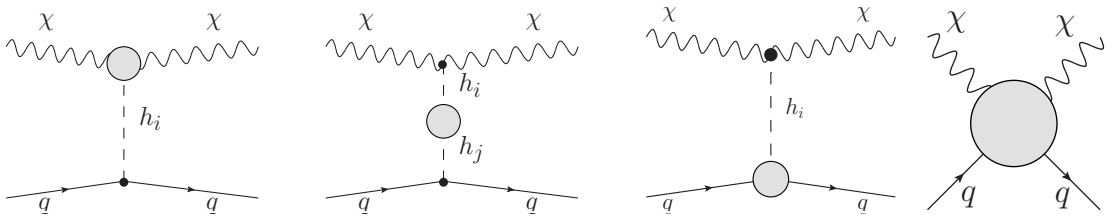

(a) UpV Corrections (b) Mediator Corrections (c) LoV Corrections (d) Box Corrections

Figure 6.2.: Generic one-loop corrections to the scattering of VDM with the nucleon. The gray blob indicates the renormalized one-loop corrections. The corrections can be separated into upper vertex (a), mediator (b), lower vertex (c) and box (d) corrections.

The last blind spot $g_\chi = 0$ can be achieved through two conditions. Note that the dark gauge coupling is related to the DM mass and the singlet vacuum expectation value (VEV), $g_\chi = {}^{m_\chi}/_{v_S}$. Vanishing DM masses m_χ are phenomenologically not of interest and tiny DM masses m_χ are strictly constrained by indirect searches [150]. In addition, we *expect* DM masses of the order of the EW scale due to the *WIMP miracle* as indicated in Eq. (4.56). To account for large v_S, we included a wide range of possible values in our parameter scan.

6.2. Electroweak Next-to-Leading Order Corrections

Analogous to Sec. 5.2, we separate the discussion of the EW NLO corrections in all different topology classes. This allows us to discuss the different sizes of corrections induced by the different topologies and hereby the importance of the corrections, respectively. The four topology classes for the quark contributions are shown in Fig. 6.2. Again we have two vertices, the upper and lower vertex, the mediator and box-type corrections. The gray blobs indicate the fully renormalized EW one-loop diagrams *i.e.* the sum of the virtual genuine one-loop diagrams and the respective counterterm amplitude.

6.2.1. Mediator Corrections

The mediator corrections in Fig. 6.2(b) are calculated analogous to Sec. 5.2.1 by evaluating the renormalized one-loop propagator at zero momentum transfer ($i, j = 1, 2$)

$$\Delta_{h_i h_j} = -\frac{\hat{\Sigma}_{h_i h_j}(p^2 = 0)}{m_{h_i}^2 m_{h_j}^2} \ , \tag{6.5}$$

with the renormalized self-energy matrix

$$\begin{pmatrix} \hat{\Sigma}_{h_1 h_1} & \hat{\Sigma}_{h_1 h_2} \\ \hat{\Sigma}_{h_2 h_1} & \hat{\Sigma}_{h_2 h_2} \end{pmatrix} \equiv \hat{\Sigma}(p^2) = \Sigma(p^2) - \delta m^2 - \delta T + \frac{\delta Z}{2}\left(p^2 - \mathcal{M}^2\right) + \left(p^2 - \mathcal{M}^2\right)\frac{\delta Z}{2} \ . \tag{6.6}$$

Note that $\Sigma(p^2)$ indicates here the 2×2 matrix with the genuine one-loop self-energies of $h_i h_j$, respectively. Similarly, the mass counterterm matrix $\delta m^2 = \text{diag}\left(\delta m_{h_1}^2, \delta m_{h_1}^2\right)$ (*c.f.* Eq. (4.13)), the tadpole counterterm matrix δT, the WFRC matrix δZ (*c.f.* Eq. (4.14c)) and the mass scalar mass matrix $\mathcal{M}$ (*c.f.* Eq. (3.45)) of the VDM have the 2×2 matrix structure. The renormalized one-loop propagator at zero momentum transfer yields the following Wilson coefficient for the quark operator $m_q \bar{q} q \chi_\mu \chi^\mu$

$$f_q^{\text{med}} = \frac{g g_\chi m_\chi}{2 m_W} \sum_{i,j} R_{\alpha,i2} R_{\alpha,j1} \Delta_{h_i h_j} \ , \tag{6.7}$$

with the rotation matrix $R_{\alpha,ij}$ defined in Eq. (3.18) and the one-loop propagator in Eq. (6.5).

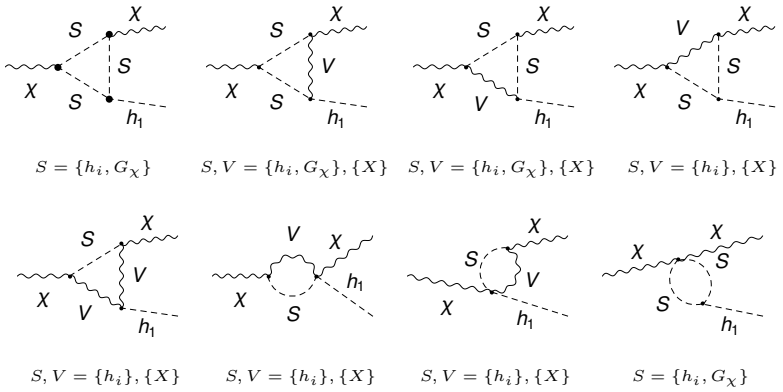

Figure 6.3.: Generic diagrams contributing to the virtual corrections to the vertex $\chi\chi h_i$. The generic symbols denote F fermions, S scalars and V gauge bosons.

6.2.2. Upper Vertex Corrections

We construct the full $2 \to 2$ process with the renormalized upper vertex by first evaluating the fully renormalized upper vertex and plugging the respective NLO coupling in the full process. To avoid double counting of the LO contributions, we calculate in the following only the pure NLO corrections of the upper vertex. They consist of the genuine one-loop diagrams $\mathcal{A}^{\text{VC}}_{\chi\chi h_i}$ and the vertex counterterm $\mathcal{A}^{\text{CT}}_{\chi\chi h_i}$, respectively,

$$i\mathcal{A}^{\text{NLO}}_{\chi\chi h_i} = i\mathcal{A}^{\text{VC}}_{\chi\chi h_i} + i\mathcal{A}^{\text{CT}}_{\chi\chi h_i} \,. \tag{6.8}$$

The LO amplitude is given in terms of the polarization vectors $\varepsilon^{(*)}$ of the in- and out-going χ_μ and the tree-level coupling $g_{\chi\chi h_i} = 2g_\chi m_\chi R_{\alpha,i2}$

$$i\mathcal{A}^{\text{LO}}_{\chi\chi h_i} = g_{\chi\chi h_i}\varepsilon(p)\cdot\varepsilon^*(p) = 2g_\chi m_\chi \varepsilon(p)\cdot\varepsilon^*(p) \begin{cases} \sin\alpha\,, & i=1 \\ \cos\alpha\,, & i=2 \end{cases} \,, \tag{6.9}$$

where p denotes the four-momenta of the DM particles. The counterterm amplitude is derived from the tree-level coupling to be

$$i\mathcal{A}^{\text{CT}}_{\chi\to\chi h_1} = \left[\frac{1}{2}\left(g_{\chi\chi h_2}\delta Z_{h_2h_1} + g_{\chi\chi h_1}\delta Z_{h_1h_1}\right) + g_{\chi\chi h_1}\delta Z_{\chi\chi} + \delta g_{\chi\chi h_1}\right]\varepsilon(p)\cdot\varepsilon^*(p) \tag{6.10a}$$

$$i\mathcal{A}^{\text{CT}}_{\chi\to\chi h_2} = \left[\frac{1}{2}\left(g_{\chi\chi h_1}\delta Z_{h_1h_2} + g_{\chi\chi h_2}\delta Z_{h_2h_2}\right) + g_{\chi\chi h_2}\delta Z_{\chi\chi} + \delta g_{\chi\chi h_2}\right]\varepsilon(p)\cdot\varepsilon^*(p)\,, \tag{6.10b}$$

where we take the $\delta Z_{h_ih_j}$ $(i,j=1,2)$ into account. The WFRCs of the Higgs bosons are introduced artificially, since the Higgs boson mediators are actually internal degrees of freedom in the full $2 \to 2$ process. However, if we include the δZ WFRCs for the Higgs mediators and in this way treat the Higgs to be on-shell, we can check for UV finiteness in each topology separately. The artificially introduced δZ contributions cancel each other in the sum of all topologies. The variation of the tree-level coupling yields the respective counterterm

$$\delta g_{\chi\chi h_i} = \sum_p \frac{\partial g_{\chi\chi h_i}}{\partial p}\delta p\,, \quad p \in \{m_\chi^2, g_\chi, \alpha\}\,. \tag{6.11}$$

The genuine one-loop diagrams are depicted in Fig. 6.3, where S indicates the involved scalars, F fermions and V vector bosons. An additional tensor structure arises at the NLO level, given by

$$i\mathcal{A}^{\text{NLO}} = (\ldots)\underbrace{\varepsilon(p_{\text{in}})\cdot\varepsilon^*(p_{\text{out}})}_{\sim\text{LO}} + (\ldots)\underbrace{\left(p_{\text{in}}\cdot\varepsilon^*(p_{\text{out}})\right)\left(p_{\text{out}}\cdot\varepsilon(p_{\text{in}})\right)}_{\sim\text{NLO}}\,, \tag{6.12}$$

with the in- and out-going momentum $p_{\text{in}}, p_{\text{out}}$ of the DM particle. We emphasize that we assume $p_{\text{in}} = p_{\text{out}}$, which yields a stricter assumption than solely $p_{\text{in}}^2 = p_{\text{out}}^2$. This allows us to drop the newly arising NLO tensor structure for freely propagating gauge bosons, since they obey $\varepsilon(p) \cdot p = 0$. The expressions for the one-loop corrected vertices are quite lengthy, hence we do not list them explicitly.
The counterterm amplitude in Eq. (6.10) cancels all UV divergences of the virtual corrections, which is checked numerically and analytically. Plugging the NLO vertex coupling in the full $2 \to 2$ process while taking symmetry factors into account allows us to extract the respective the Wilson coefficient f_q^{upV} of the upper vertex.

6.2.3. Lower Vertex Corrections

The calculation of the EW NLO corrections of the lower vertex is analogous to Sec. 5.2.3. The respective one-loop Feynman diagrams of the lower vertex can be taken over from Fig. 5.4 where the upper scalar line has to be replaced with a gauge boson line indicating the vector DM candidate χ_μ. The tree-level coupling in Eq. (5.8) can also be taken over. This allows us to derive the counterterm amplitude to be

$$i\mathcal{A}^{CT}_{\text{LV},h_1} = \left(\delta C_{qqh_1} + \frac{1}{2}\left(C_{qqh_1}\delta Z_{h_1h_1} + C_{qqh_2}\delta Z_{h_2h_1} + C_{qqh_1}\delta Z^L_{qq} + C_{qqh_1}\delta Z^R_{qq}\right)\right)\mathcal{R}_1\,, \tag{6.13a}$$

$$i\mathcal{A}^{CT}_{\text{LV},h_2} = \left(\delta C_{qqh_2} + \frac{1}{2}\left(C_{qqh_2}\delta Z_{h_2h_2} + C_{qqh_1}\delta Z_{h_1h_2} + C_{qqh_2}\delta Z^L_{qq} + C_{qqh_2}\delta Z^R_{qq}\right)\right)\mathcal{R}_2\,, \tag{6.13b}$$

with the tree-level like remainder

$$\mathcal{R}_i \equiv -\frac{C_{\chi\chi h_i}}{m^2_{h_i}}\bar{u}(p_q)u(p_q)\varepsilon(p_\chi)\cdot\varepsilon(p_\chi)^*\,. \tag{6.14}$$

We indicate the momentum of the quark (DM candidate) as p_q (p_χ) and the corresponding tree-level trilinear couplings between the particles ijk as C_{ijk}. The quark-quark-Higgs vertex counterterm is defined in Eq. (5.9) with the counterterms and WFRCs defined in Eqs. (4.14), (4.28), (4.29) and (4.36).
The crucial difference compared to the PNGDM is that the different contributions of the QED subset do not cancel each other and hence require a proper treatment to regularize the IR divergences. These IR divergences arise due to the presence of charged particles in the final state. The two generic diagrams are depicted in Fig. 5.5. The *usual* approach of including real radiation in order to regulate the IR divergences in the cross-section does not apply here. First of all, the cancellation is taking place on the cross-section level and hence requires the squared amplitude and integration over the phase space. However, the matching of the Wilson coefficients happens on the amplitude level. Furthermore, real radiation introduces an additional polarization vector in the final state introducing new tensor structures which are not taken into account in the non-relativistic operator basis. We use the approach of *strictly vanishing external momentum* for the quark propagator. This allows us to isolate the IR divergences and in addition we can show that these IR divergences cancel each other in the expansion. The detailed discussion and derivation of the virtual one-loop corrections and the respective counterterm of the QED subset is presented in Appendix A. The QED subset contributions are dropped in the virtual one-loop diagrams and the corresponding counterterms in Eq. (6.13). They are included by the expanded expressions presented in Appendix A. By doing so, we can ensure a UV and simultaneously IR safe amplitude and thus Wilson coefficient. We refer to this Wilson coefficient as f_q^{LV}.

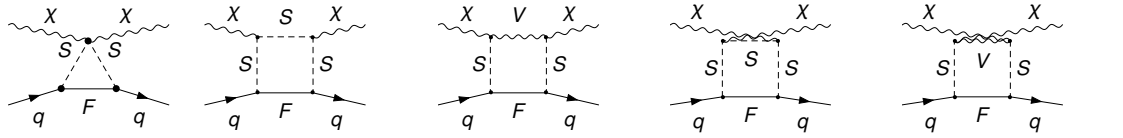

$F, S = \{q\}, \{h_i\}$ $F, S = \{q\}, \{h_i, G_\chi\}$ $F, S, V = \{q\}, \{h_i, G_\chi\}, \{X\}$ $F, S = \{q\}, \{h_i\}$ $F, S, V = \{q\}, \{h_i, G_\chi\}, \{X\}$

Figure 6.4.: Generic diagrams of the box topology contributing to the SI-cxn. The symbol S denotes scalars, F fermions and V vector bosons. The flavor of the fermion F and the external quark q are the same as we set the CKM matrix equal to the unit matrix.

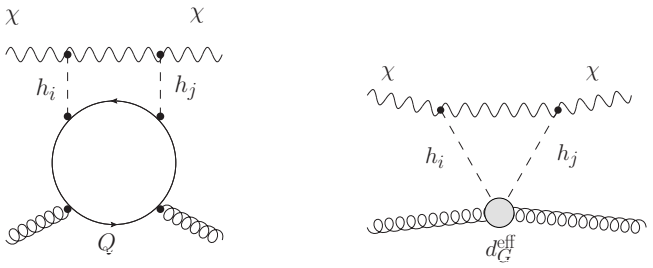

Figure 6.5.: The full two-loop gluon interaction with the DM candidate (left) and the effective two-loop interaction after integration out the heavy quarks (right).

6.2.4. Box Corrections

We now present the box corrections. The generic diagrams are depicted in Fig. 6.4, where S indicates scalars, F fermions and V gauge bosons, respectively. Again, we assume the strict assumption $p_{\text{in}} = p_{\text{out}}$ for the quark and DM momenta. To be consistent with the strict vanishing momentum expansion in Sec. 6.2.3, we expand the quark propagator as follows

$$\frac{1}{(l \pm p_q)^2 - m_q^2} = \frac{1}{l^2 - m_q^2}\left[1 \mp \frac{2p_q \cdot l}{l^2 - m_q^2}\right] + \mathcal{O}\left(p_q^2\right) \ , \tag{6.15}$$

with the respective quark mass m_q, the quark four-momentum p_q and the loop momentum l. The expansion in Eq. (6.15) allows us to extract Wilson coefficient corresponding to the unsuppressed operators. Note that without this expansion, the amplitude and thus the Wilson coefficient is dependent on the Mandelstam variables and in this way on the kinematics. These kinematically dependent pieces would contribute to the velocity and momentum transfer suppressed non-relativistic operators.
With the expansion at hands, the one-loop diagrams can be reduced to the standard Passarino-Veltmann integral basis. The corresponding Wilson coefficient can be read off, which we refer to as f_q^{box} and g_q^{box}. Note that Eq. (5.17) enables to rewrite $\bar{q} i \partial_\mu \gamma_\nu q$, so that additional contributions to the twist-2 operator arise in the box topology.

6.2.5. Gluon Contributions

As already discussed in Chapter 5, the EW NLO corrections of the gluon contributions are a non-trivial task. Using Eq. (4.84) in an EW one-loop diagram would require a proper mixed QCD-EW matching of the QCD trace anomaly. This is beyond the scope of this thesis. We emphasize again, that the neglection of the EW corrections of the lower vertex would induce a missing cancellation of the artificially introduced δZ parts of the internal Higgs bosons[15].

[15] If the artificially introduced δZ parts are dropped in the first place, the overall result would not be UV finite, if the lower vertex is neglected.

This immediately implies that we cannot use Eq. (4.84) while considering EW corrections. As shown in [120], the naive usage of the replacement in Eq. (4.84) in the box topologies would yield rather large theoretical errors. However, the VDM allows for the usage of Eq. (4.84) in combination with the tree-level amplitude[16]. These gluon contributions are already taken into account in Eqs. (6.3) and (6.4), respectively.
We investigate the gluon contribution induced by a fermion box depicted in Fig. 6.5. Q denotes heavy quarks, which are integrated out. If the mediator masses are assumed to be small compared to the *heavy* quark (in the following only the top quark), it is possible to derive an effective quartic coupling between two Higgs bosons $h_i h_j$ and external gluons. The effective Lagrangian reads [125]

$$\mathcal{L}^{hhGG} = \frac{1}{2} d_G^{\text{eff}} h_i h_j \frac{\alpha_S}{12\pi} G^a_{\mu\nu} G^{a\,\mu\nu} \,, \tag{6.16}$$

with

$$\left(d_G^{\text{eff}}\right)_{ij} = (R_\alpha)_{i1} (R_\alpha)_{j1} \frac{1}{v^2} \,. \tag{6.17}$$

Including this effective quartic vertex allows us to calculate the triangle diagram in Fig. 6.5 (right) and read off the resulting Wilson coefficient for the gluon operators

$$f_G^{\text{top}} = \left(d_G^{\text{eff}}\right)_{ij} C_\triangle^{ij} \frac{-\alpha_S}{12\pi} \,, \tag{6.18}$$

where $C_\triangle^{ij}$ accounts for the one-loop pre-factor required for the matching of the Wilson coefficient. These NLO gluon contributions have to be taken with a grain of salt. One the one hand, the effective quartic coupling induces vertex corrections in the lower vertex $h_i G^a_{\mu\nu} G^{a\mu\nu}$, which introduces UV-divergences. This would require a corresponding vertex counterterm. However, the effective quartic operator is not renormalizable, indicating the need of the introduction of counterterms order-by-order. It was argued in [119], that these additionally induced gluon interactions are small compared to the dominant contribution depicted in Fig. 6.5 (right). This hierarchy could not be reproduced in our calculation and so these effective two-loop contributions might be of the same order.
On the other hand, the approximation used in [125] assumes that the mediator masses are small compared to the heavy quarks and compared their result to a full two-loop calculation. It showed good agreement between the approximate and the exact result for mediator masses below m_t. Even though there is this good agreement, not all parameter points used in this analysis obey this condition.
In summary, a consistent inclusion of the EW NLO gluon contributions is not possible. Therefore, we investigate the overall effect of the effective two-loop order gluon contributions given in Eq. (6.16) (right) by considering the SI-cxn with and without these additional contributions. We refer to this contribution as f_G^{top}. We observed that the contribution by f_G^{top} is of the same order or below the box induced contributions. As it will turn out, the box contributions to the SI-cxn are suppressed compared to the vertex, mediator and LO corrections, hence also the f_G^{top}.

6.2.6. Building the Cross Section

In the following, we summarize the inclusion of the EW NLO corrections in the SI-cxn. To avoid double counting of the LO contributions, we divide the SI-cxn in purely NLO and LO contributions. The NLO nuclear factor of a nucleon n, where $n = N$ for a Neutron and $n = P$ for a proton, respectively, is given by

$$\frac{f_n^{\text{NLO}}}{m_n} = \sum_{q=u,d,s} f_q^{\text{NLO}} f_{T_q}^N + \sum_{q=u,d,s,c,b} \frac{3}{4} \left(q(2) + \bar{q}(2)\right) g_q^{\text{NLO}} - \frac{8\pi}{9\alpha_S} f_{T_G}^N f_G^{\text{NLO}} \,, \tag{6.19}$$

[16] This corresponds to one-loop QCD corrections.

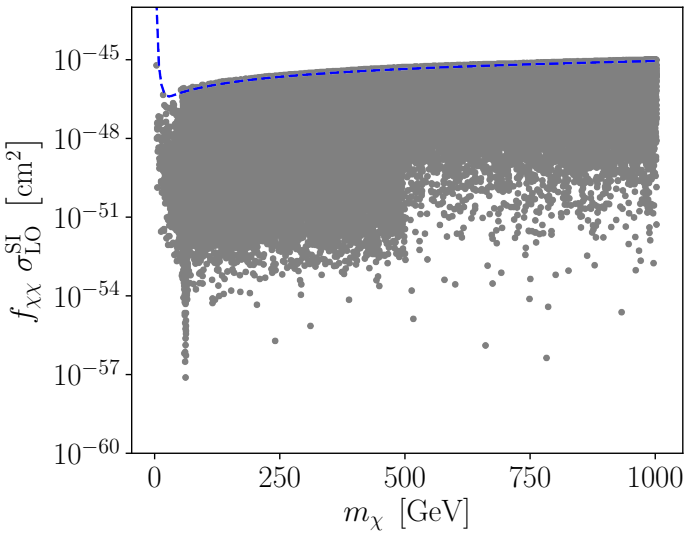

Figure 6.6.: The effective SI-cxn as expected in a direct detection experiment is shown as a function of the DM mass m_χ. The dashed line indicates the current expected Xenon-1T limit.

where we introduced the (purely) NLO Wilson coefficients

$$f_q^{\mathrm{NLO}} = f_q^{\mathrm{upV}} + f_q^{\mathrm{LV}} + f_q^{\mathrm{med}} + f_q^{\mathrm{box}} \tag{6.20}$$

$$g_q^{\mathrm{NLO}} = g_q^{\mathrm{box}} \tag{6.21}$$

$$f_G^{\mathrm{NLO}} = f_G^{\mathrm{top}} \ . \tag{6.22}$$

The LO Wilson coefficients are given in Eqs. (6.2) and (6.3). The strictly one-loop expanded SI-cxn for a nucleon n ($n = P, N$) is then given by

$$\sigma_n = \frac{1}{\pi}\left(\frac{m_n}{m_\chi + m_n}\right)^2 \left[|f_n^{\mathrm{LO}}|^2 + 2\mathrm{Re}\left(f_n^{\mathrm{LO}*} f_n^{\mathrm{NLO}}\right)\right] \ . \tag{6.23}$$

Note that this is a different treatment as in the PNGDM. The LO Wilson coefficients in the PNGDM are zero, hence the first non-vanishing terms are the squared f_n^{NLO}, which are dropped here.

6.3. Results

The parameter sample of roughly $2.3 \cdot 10^5$ points used in this analysis is taken from [150]. The generation of the parameter sample was performed with an early version of `ScannerS` [61,151], which checked for theoretical constraints as described in Sec. 3.1 as well as experimental constraints. The used tools conincide with those described in Sec. 3.1. We refer to [150] for further details. We show the results of the SI-cxn for a proton in the following and use the same input values of the nuclear matrix elements as well as the SM input parameter as those presented in Sec. 5.3.

We start the discussion with Fig. 6.6. The rescaled LO SI-cxn is shown as a function of the DM mass m_χ. Note that if the DM candidate does not account for the full relic density, the expected SI-cxn has to be corrected by the factor $f_{\chi\chi}$ defined in Eq. (5.25). The gray points denote the benchmark scenarios used in the analysis, where the blue dashed line indicates the central value of the current Xenon-1T limit. The DM mass m_χ ranges from roughly 30 GeV up to 1 TeV which coincides with the scan ranges used in the parameter scan. There is no strong correlation between the effective SI-cxn and the DM mass. We can observe a wide

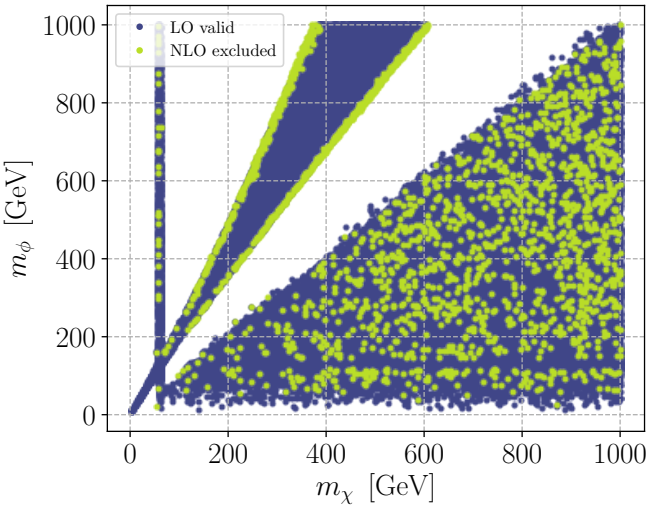

Figure 6.7.: The mass plane of the DM m_χ and the non-SM like Higgs boson mass m_ϕ is shown. The blue points denote all parameter points fulfilling theoretical and experimental constraints and that are compatible with the Xenon-1T limits if the LO predictions are considered. Green points indicate benchmark scenarios where the NLO prediction of the SI-cxn is above the current Xenon-1T limit. *The figure is taken from [2].*

range of possible effective SI-cxns near the Xenon-limit as well far below the sensitivity of the direct detection experiment. We emphasize that the Xenon limit is already applied in the parameter scan, hence there are no benchmark scenarios above the Xenon limit. As an additionally applied parameter cut, we demand $g_\chi^2 < 4\pi$ to account for the usual unitarity bounds of gauge couplings.

We show the mass plane of (m_χ, m_ϕ) in Fig. 6.7. The blue points indicate all parameter points of the analysis, where the green points are shifted above the Xenon limit if the EW NLO corrections, as described in the above sections, are included. We observe the same mass range for the non-SM like Higgs boson mass from roughly 30 GeV up to 1 TeV. Consequently, both mass hierarchies are possible, $m_h < m_\phi$ and $m_h > m_\phi$. There are three distinct mass regions present. The widest range is the mass configuration $m_\chi > m_\phi$. The narrow region around $m_\chi \simeq {}^{m_h}/_2$ and the triangle-shaped narrow region centered around $m_\phi \simeq 2{\cdot}m_\chi$ indicate special mass configurations. As soon as the DM mass obeys $2 \cdot m_\chi < \max(m_h, m_\phi)$, the decay channel $h_i \to \chi\chi$ is kinematically open and the possibility of invisible searches of the LHC, or indirect detection will become significant contraints. Furthermore, the thermal average annihilation cross-section required for the relic density calculation is significantly enhanced near the resonances (*c.f.* [99]). To account for the correct relic density, the corresponding couplings have to be suppressed to compensate the kinematic resonance. These suppressed couplings result in less severe constraints by direct detection near the two resonances $2 \cdot m_\chi \simeq m_h, m_\phi$.

The exclusion of benchmark scenarios due to the inclusion of EW NLO corrections does not show a significant pattern in the mass regions $m_\chi > m_\phi$ and $m_\chi \simeq {}^{m_h}/_2$. However, in the remaining narrow region, which is centered around the mass configurations $m_\phi \simeq 2 \cdot m_\chi$, only the edges are excluded due to the EW NLO corrections. In particular in this region, the direct detection constraint is dominant as discussed above, hence, the sensitivity to NLO corrections is strengthened.

We show the ratio of the NLO SI-cxn and the LO SI-cxn in Fig. 6.8 as a function of the LO SI-cxn (Fig. 6.8(a)) and the non-SM like Higgs boson mass m_ϕ (Fig. 6.8(b)). The ratio allows for an estimate of the significance of the EW NLO corrections. Overall, the size of

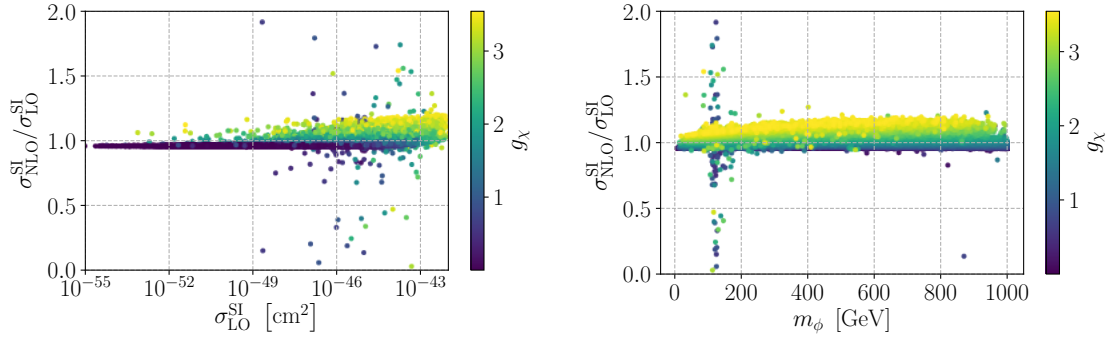

(a) (b)

Figure 6.8.: The ratio of the NLO and LO SI-cxn is shown as a function of the LO SI-cxn (left) and of the non-SM like Higgs boson mass m_ϕ (right). All points of the analysis are shown. The color code indicates the size of the dark gauge coupling g_χ. *The figures are taken from [2].*

the EW NLO corrections is of $\sim 30\%$ of the LO SI-cxn, except for few outliers. These outliers, however, are all centered around $m_\phi \simeq m_h$[17]. Degenerate neutral Higgs boson masses introduce severe numerical issues related with the introduction of $1/(m_\phi^2 - m_h^2)$ poles in the WFRCs and counterterms as well as in the virtual corrections. To achieve a smoothly behaving NLO SI-cxn, a proper treatment of the degenerate mass limit has to be taken into account or rather a proper resummation of higher order corrections. Since we are only interested in the overall possible parameter space of the VDM, we skip this specific mass configuration and emphasize that these predictions have to be taken with some grain of salt. Besides this specific mass configuration the ratio of NLO and LO SI-cxn yields a stable prediction.

The ratio scales with the dark gauge coupling g_χ as one can infer from both plots in Fig. 6.8. On the one hand the LO SI-cxn is proportional to g_χ^2 (*c.f.* Eq. (6.4) and note $g_\chi = m_\chi/v_s$), on the other hand the virtual corrections of the upper vertex contribute g_χ^2 due to the squared $\chi\chi h_i$ coupling. It turns out that the upper vertex corrections are the most dominant NLO corrections contributing to the SI-cxn. Thus the NLO SI-cxn scales as $\mathrm{Re}\left(f_q^{\mathrm{LO}*} f_q^{\mathrm{NLO}}\right) \sim g_\chi^3$. In Fig. 6.8(a), it becomes clear that the blind spots of the SI-cxn in the VDM remain at NLO. The ratio of NLO and LO SI-cxn decreases with decreasing LO SI-cxn. One obvious argument for this behavior is the different scaling behavior of the NLO SI-cxn in terms of the dark gauge coupling g_χ. To achieve suppressed LO SI-cxn, the corresponding gauge coupling g_χ has to be sufficiently small, however, this pushes the NLO corrections to even lower values.

We compare the sizes of the different contributions of the topologies in Fig. 6.9. We restrict ourself to the Wilson coefficients of the quark contributions. Each Wilson coefficient of the different topologies is normalized to the LO Wilson coefficient defined in Eq. (6.2). We see no significant dependence of the Wilson coefficient on the mass m_ϕ of the non-SM like Higgs boson, except near the SM Higgs boson mass, $m_\phi \simeq m_h$. There, we can observe a clear peak in the vertex and mediator corrections, while the box contributions significantly drop. This can be explained with the related numerical issues of degenerate neutral Higgs boson masses. Furthermore, a clear hierarchy between the vertex/mediator and the box topology can be observed. The box contributions are several orders of magnitude below the vertex corrections, indicating that also the effective two-loop top gluon interactions (referred to as f_G^{top}) are

[17] One specific benchmark scenario at $m_\phi \simeq 850\,\mathrm{GeV}$ predicts a highly suppressed NLO SI-cxn. This specific benchmark points yields $m_\phi \simeq m_\chi$ indicating as well numerical instabilities.

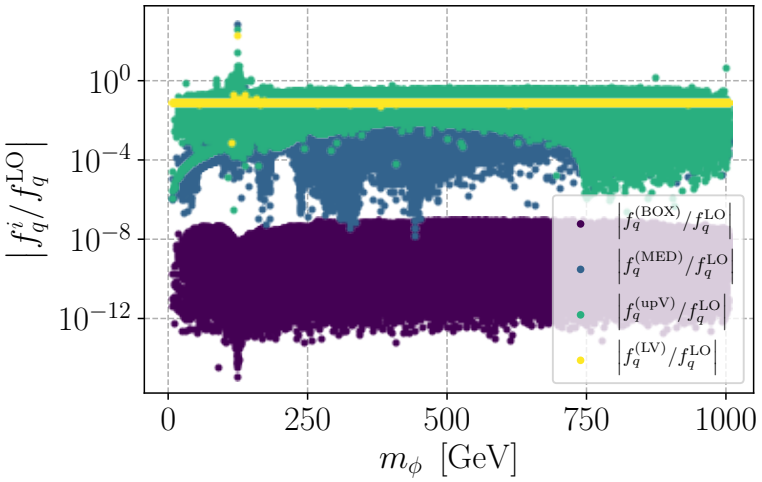

Figure 6.9.: The normalized absolute values of the Wilson coefficients of the different topologies are shown as a function of the non-SM like Higgs boson mass m_ϕ. The NLO Wilson coefficients are normalized to the LO Wilson coefficient defined in Eq. (6.2). *The figure is taken from [2].*

subleading[18]. The upper vertex and mediator corrections show a wide variation of the order of their size, whereas the lower vertex corrections remains stable in its order. Note that the corrections of the lower vertex include almost exclusively SM-like particles, which explains the independence of the non-SM like input parameters of the VDM. The strong hierarchy between the box contributions and the remaining topologies might justify the argument of [126] to drop box-like contributions in the first place. However, we emphasize that the relative sizes of the contributions are not clear a priori, yielding possible large theoretical errors in the prediction.

We conclude the discussion of the EW NLO corrections in the VDM with the comparison of the different renormalization schemes for the mixing angle α. In Fig. 6.10, the ratio of the NLO to the LO SI-cxn is shown as a function of the LO SI-cxn. The three different colors indicate three different renormalization schemes for the mixing angle α. The yellow points corresponds to the KOSY scheme defined in Eq. (4.20). The process-dependent (green points) counterterm $\delta\alpha$ is extracted from the decay $h_1 \to \tau\tau$ as described in Sec. 4.1.2. The respective $\overline{\mathrm{MS}}$ counterterm (purple points) is obtained by using the process-dependent counterterm and solely taking the UV pole into account. The renormalization scale is taken to be $\mu = 1\,\mathrm{GeV}$. The predictions of the process-dependent and $\overline{\mathrm{MS}}$ renormalization schemes are highly enhanced/suppressed compared to the KOSY scheme. There are differences of several orders of magnitude in the prediction. It was already shown that the scheme dependence induced by the mixing angle is rather large in non-minimal extended Higgs sectors [85, 87]. The NLO corrections obtained in the process-dependent and $\overline{\mathrm{MS}}$ scheme are unacceptably large, hence unsuitable for practical use. We recommend the usage of the KOSY scheme which yields mild EW NLO corrections and shows a numerically stable behavior.

6.4. Conclusion

We used the framework of ChEFT to extract the effective DM-nucleon interaction in terms of Wilson coefficients. These Wilson coefficients are matched to the physical $2 \to 2$ scattering

[18] It was explicitly checked that f_G^{top} is of the same order as the box contributions or even several orders below.

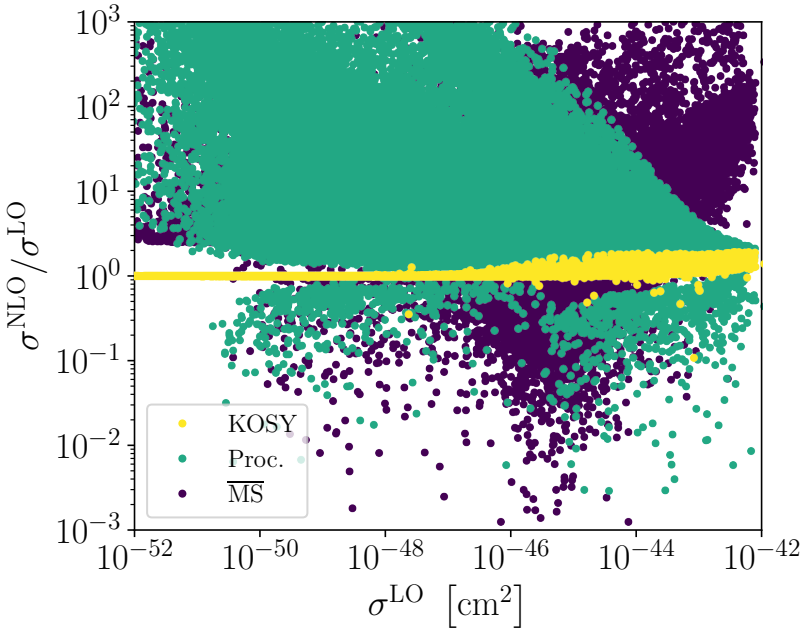

Figure 6.10.: The NLO SI-cxns are shown for different renomalization schemes for the mixing angle $\delta\alpha$ as a function of the LO SI-cxn. *The figure is taken from [1].*

process while including EW NLO corrections. This allows us to consistently include EW quantum corrections in the prediction of the SI-cxn. The VDM provides a vector-like DM candidate. The spin-nature of the DM candidate does not solely allow for spin-independent, velocity and momentum transfer suppressed interactions with the nucleon, but also for spin-dependent interactions. Contrary to the PNGDM, the VDM model does not provide a naturally suppressed LO SI-cxn, so that already tree-level calculations are able to derive significant model constraints from direct detection experiments (*cf.* [150]). However, there are still *blind spots* remaining which are caused by specific choice of parameters. We showed, that the blind spots remain at the EW NLO level.

Furthermore, we showed that the overall NLO corrections behave mildly and are of the order of $\sim 30\%$ of the LO SI-cxn. The size of the EW NLO corrections shows a scaling behavior in terms of the dark gauge coupling g_χ, which we could explain from the behavior of the virtual one-loop vertex corrections. The only unstable region for the NLO corrections are induced by the degenerate neutral Higgs boson masses $m_\phi \simeq m_h$, which requires a proper treatment in the renormalization. For instance a proper limit in the WFRCs, or a resummation of higher-order corrections might help to ensure a smooth behavior. This is beyond the scope of this thesis.

The renormalization of mixing angles is a non-trivial task [85, 87, 89, 152]. There are several suggestions to define a respective counterterm $\delta\alpha$. Each approach does have advantages as well as disadvantages. We compared three different approaches, namely the KOSY scheme, based on a rigid symmetry argument, a process-dependent and the $\overline{\mathrm{MS}}$ scheme. We found that only the KOSY provides reasonable EW NLO corrections of the order $\sim 30\%$, whereas the other two schemes predict highly suppressed/enhanced EW NLO SI-cxns.

We discussed the problem of the gluon contributions. Since we are not able to include EW NLO corrections in the effective $h_i G^a_{\mu\nu} G^{a\mu\nu}$ vertex in a self-consistent way, we cannot use Eq. (4.84) to derive the Wilson coefficient for the DM-gluon interactions. Otherwise, we would miss a proper cancellation of the UV-poles as well as the KOSY-scheme for the renormalization of the mixing angle would introduce numerical instabilities if the lower vertex is dropped. To avoid nonphysical enhancements/suppression in the SI-cxn, we left out com-

pletely the EW NLO corrections while deriving the DM-gluon interactions. Only the LO contributions while using Eq. (4.84) are taken into account.

Part III.

Strong First-order Electroweak Phase Transition

CHAPTER 7

Theoretical Foundations

7.1. One-loop Effective Potential at Finite Temperature

The description of the early universe during the electroweak phase transition (EWPT) is a demanding task. On the one hand, the system is in a non-equilibrium state. On the other hand, quantum corrections might also play an important role to describe the system properly. In the context of this thesis, the ansatz of the one-loop effective potential at finite temperature is chosen. This approach allows us to include next-to-leading-order (NLO) corrections and further finite temperature effects, needed to describe the Higgs potential in the early universe. In the following we will give a short introduction in the effective potential at zero temperature, followed by a discussion of finite temperature effects. We will comment on the resummation of the *hard thermal loops* and discuss different ansätze. We close the discussion with fixing our notation of the general Coleman-Weinberg potential and the temperature dependent potential for a generic extended Higgs sector and conclude with the discussion of the renormalization scheme used in this work.

7.1.1. One-loop Effective Potential at Zero Temperature

In a quantum field theory (QFT) in the presence of an external field, the *quantum effective action* allows us to determine propagators or vertices (including all-order quantum corrections). The effective action corresponds to the one-particle-irreducible connected vacuum-vacuum amplitude in the presence of an external field. Furthermore, it allows us to express the *effective potential* allowing us to define the true ground state of the theory including higher-order corrections. The effective action of a QFT theory is given by the Legendre transformation of the generating functional for the connected Greens functions $W[J]$ [153]

$$\Gamma\left[\bar{\phi}\right] = W[J] - \int d^d dx \bar{\phi}(x) J(x) \ , \tag{7.1}$$

with the corresponding source $J(x)$ and the field $\bar{\phi}$. For simplicity, a field theory with only one scalar field is considered in the following. The generalization to a theory with multiple scalar fields or fermions is discussed in [153].

Expanding the effective action in terms of the external momenta

$$\Gamma\left[\bar{\phi}\right] = \int d^4x \left[-V_{\text{eff}}(\bar{\phi}) + \frac{1}{2}\partial_\mu\bar{\phi}Z(\bar{\phi})\partial^\mu\bar{\phi} + \ldots\right] , \tag{7.2}$$

allows us to define the effective potential V_{eff} indicating the zeroth order in the external momentum expansion. For a translation invariant theory the field does not show a space-time dependence

$$\bar{\phi} = \phi_c = \text{const.} , \tag{7.3}$$

hence the effective potential can be expressed as

$$\Gamma\left[\phi_c\right] = -\Omega V_{\text{eff}}(\phi_c) , \tag{7.4}$$

with the overall space-time volume Ω. So far the effective action and potential includes all orders, however in a general QFT it is often not possible to calculate the full-order result. Nonetheless, it is possible to expand the effective action in the loop order parameter $\hbar$[19] in order to obtain a perturbative one-loop result [154]

$$\Gamma\left[\phi_c\right] = -\Omega V^{(0)}(\phi_c) + \frac{i\hbar}{2}\,\text{Tr}\ln\mathcal{D}^{-1} + \mathcal{O}(\hbar^2) , \tag{7.5}$$

with the tree-level potential $V^{(0)}$ and the inverse propagator $\mathcal{D}^{-1}$ in the presence of the constant background field. Identifying Eq. (7.4) with Eq. (7.5) allows us to express the pure one-loop effective potential as

$$V_{\text{eff}}^{(1)} = \frac{1}{2}\int \frac{d^4k_E}{(2\pi)^4}\ln\left(k_E^2 + m_{eff}^2\right) . \tag{7.6}$$

Several comments are needed for the last step. The Tr is resolved by writing the propagator in the momentum space, where the zero component k_0 is Wick-rotated to $k_0 \to ik_4$. The transformation to the Euclidean space will become clear while considering the finite temperature field theory. The effective mass term m_{eff}^2 is given as the eigenvalues of the mass matrix determined by the tree-level potential

$$\left(m_{eff}^2\right) = \left.\frac{\partial^2 V^{(0)}}{\partial\phi^2}\right|_{\phi=\langle\phi\rangle} , \tag{7.7}$$

with the VEV field configuration $\langle\phi\rangle$.

7.1.2. Intermezzo: Finite Temperature Field Theory

The description of quantum fields as a thermal system is an intricate problem. However, for systems in thermodynamical equilibrium or *near-equilibrium*, there are various, but equivalent, ways to describe the thermodynamical system. The oldest approach to describe quantum systems at finite temperature relies on the imaginary time formalism [155, 156].
The statistical ensemble of a thermodynamical system in equilibrium is described by its *partition function* [156]

$$Z(\beta) = \text{Tr}\,\rho(\beta) = \text{Tr}\exp(-\beta H) , \tag{7.8}$$

with the density matrix ρ and the inverse temperature $\beta = 1/T$. The Hamilton operator of the system is denoted as H. The following discussion is restricted to quantum mechanical

[19] To be consistent with the literature the order parameter $\hbar$ is taken. We emphasize that this parameter is not related with the Plank constant, but indicates the number of loops taking into account in the evaluation of the effective potential. Let L be the number of loops and P the power of $\hbar$, then $L = P + 1$.

operators, the generalization to QFTs will be discussed later on.
A physical observable $\mathcal{O}$ in a thermodynamical system can be measured as thermal ensemble average which is given by

$$\langle \mathcal{O} \rangle_\beta = \frac{1}{Z(\beta)} \operatorname{Tr} \rho(\beta) \mathcal{O} \ . \tag{7.9}$$

One important consequence of the cyclicity of the Tr in Eq. (7.9) is the so-called *Kubo-Martin-Schwinger* (KMS) relation [157, 158]

$$\begin{aligned} \left\langle \mathcal{O}_1(t) \mathcal{O}_2(t') \right\rangle_\beta &= \frac{1}{Z(\beta)} \operatorname{Tr} \mathrm{e}^{-\beta H} \, \mathcal{O}_1(t) \mathcal{O}_2(t') & \text{(7.10a)} \\ &= \frac{1}{Z(\beta)} \operatorname{Tr} \mathrm{e}^{-\beta H} \, \mathcal{O}_2(t') \, \mathrm{e}^{-\beta H} \, \mathcal{O}_1(t) \, \mathrm{e}^{\beta H} & \text{(7.10b)} \\ &= \frac{1}{Z(\beta)} \operatorname{Tr} e^{-\beta H} \mathcal{O}_2(t') \mathcal{O}_1(t + i\beta) & \text{(7.10c)} \\ &= \left\langle \mathcal{O}_2(t') \mathcal{O}_1(t + i\beta) \right\rangle_\beta \ , & \text{(7.10d)} \end{aligned}$$

which can be generalized to all statistical ensembles. Note that the KMS relation implies a periodicity in the complex time for the quantum operators, which can be generalized for quantum fields.
The crucial observation in the imaginary time formalism is that the operator $\mathrm{e}^{-\beta H}$ in Eq. (7.8) can be related to the time-evolution operator with imaginary time $\tau = -i\beta$, which was also used in Eq. (7.10b) for the time-evolution of the operator. Hence, the partition function of the thermodynamical system can be represented by the path integral

$$Z(\beta) = \int \mathcal{D}x \, \mathrm{e}^{-S_E[x]} \ , \tag{7.11}$$

with the Euclidean action $S_E[x]$. Note that the Euclidean action is defined over a finite time interval

$$S_E[x] = \int_0^\beta dt L_E(x, \dot{x}) \ . \tag{7.12}$$

The cyclicity of the trace immediately implies periodic boundary conditions $x(\beta) = x(0)$. Analogously, the partition function of a QFT at finite temperature can be formulated as

$$Z(\beta) = \int \mathcal{D}\bar{\psi} \mathcal{D}\psi \mathcal{D}\phi \, \mathrm{e}^{-S_E\left[\phi, \psi, \bar{\psi}\right]} \ , \tag{7.13}$$

with the spinor fields $\psi, \bar{\psi}$ and the scalar field ϕ. Again, the Euclidean action of the QFT is denoted by $S_E\left[\phi, \psi, \bar{\psi}\right]$. Similar to the periodic boundary conditions also the fields obey the (anti-) periodic boundary conditions

$$\phi(\beta, \mathbf{x}) = \phi(0, \mathbf{x}) \ , \quad \psi(\beta, \mathbf{x}) = -\psi(0, \mathbf{x}) \ . \tag{7.14}$$

Since the *complex time* interval is finite, the Fourier transformation of the time component results in discrete energies. Hence, the Greens functions defined by the QFT in Eq. (7.13) can be written in the following general form

$$G_\beta(\tau, \mathbf{x}) = \frac{1}{\beta} \sum_{n \in \mathbb{Z}} \mathrm{e}^{-i\omega_n \tau} \, G_\beta(\omega_n, \mathbf{x}) \ , \tag{7.15}$$

with the Fourier transformation $G_\beta(\omega_n, \mathbf{x})$ and the discrete energies $\omega_n = \dfrac{n\pi}{\beta}$ $(n \in \mathbb{Z})$. The KMS relation in Eq. (7.10) implies an important consequence for the fermionic and bosonic Greens functions for $\tau < 0$ [156]

$$G_\beta(\tau, \mathbf{x}) = \pm G_\beta(\tau + \beta, \mathbf{x}) \ , \tag{7.16}$$

with τ being the complex time and the $+(-)$ sign corresponds to the bosonic (fermionic) Greens functions. Using this periodicity (anti-periodicity) of the Greens function in Eq. (7.16) allows us to find the possible modes

$$G_\beta(\omega_n, \mathbf{x}) = \frac{1}{2}\int_{-\beta}^{\beta} d\tau\, \mathrm{e}^{-i\omega_n\tau}\, G_\beta(\tau, \mathbf{x}) \tag{7.17a}$$

$$= \frac{1}{2}\int_{0}^{\beta} d\tau\, \mathrm{e}^{-i\omega_n\tau}\, G_\beta(\tau, \mathbf{x}) + \frac{1}{2}\int_{-\beta}^{0} d\tau\, \mathrm{e}^{-i\omega_n\tau}\, G_\beta(\tau, \mathbf{x}) \tag{7.17b}$$

$$\overset{Eq.\ (7.16)}{=} \pm\frac{1}{2}\int_{0}^{\beta} d\tau\, \mathrm{e}^{-i\omega_n\tau}\, G_\beta(\tau+\beta, \mathbf{x}) + \frac{1}{2}\int_{-\beta}^{0} d\tau\, \mathrm{e}^{-i\omega_n\tau}\, G_\beta(\tau, \mathbf{x}) \tag{7.17c}$$

$$= \frac{1}{2}\left(1 \pm \mathrm{e}^{-i\omega_n\beta}\right)\int_{0}^{\beta} d\tau\, \mathrm{e}^{i\omega_n\tau}\, G_\beta(\tau) \tag{7.17d}$$

$$= \frac{1}{2}\left(1 \pm (-1)^n\right)\int_{0}^{\beta} d\tau\, \mathrm{e}^{i\omega_n\tau}\, G_\beta(\tau)\ , \tag{7.17e}$$

with $n \in \mathbb{Z}$. Depending on the spin of the particle, only even or odd $n \in \mathbb{Z}$ are possible. The possible frequencies are referred as *Matsubara modes* and are given by [155]

$$\omega_n = \begin{cases} \dfrac{2\pi n}{\beta} & \text{for bosons} \\ \dfrac{(2n+1)\,\pi}{\beta} & \text{for fermions.} \end{cases} \tag{7.18}$$

Contrary to a QFT at zero temperature, the quantum fields at finite temperatures do not have a continuous energy spectrum. Overall, the discrete energy spectrum of the QFT at finite temperatures is a consequence of the KMS relation and therefore also of the definition of the partition function of the QFT. By identifying the partition function with the path integral representation of the Euclidean action, it is possible to calculate all thermodynamical observables by the *usual* perturbative methods as in the zero-temperature field theory. Analogous to the QFT at zero temperature the respective Feynman rules can be derived for the QFT at finite temperature. The resulting propagators for the bosonic (G_β) and fermionic (S_β) fields in momentum space are then given by [156]

$$G_\beta(\omega, \mathbf{k}) = \frac{1}{\omega_n^2 + \mathbf{k^2} + m^2}\ , \tag{7.19}$$

$$S_\beta(\omega_n, \mathbf{k}) = \frac{\gamma_0\omega_n + \boldsymbol{\gamma}\cdot\mathbf{k} + m}{\omega_n^2 + \mathbf{k}^2 + m^2}\ , \tag{7.20}$$

with the Matsubara frequencies ω_n defined in Eq. (7.18) and the Dirac matrices γ_0 and the remaining three denoted as vector $\boldsymbol{\gamma}$. Note that the imaginary time formalism used the Euclidean action of the theory, hence the usual mass pole of the zero temperature propagators is not present. In addition, the integration over internal energies has to be replaced by

$$\int \frac{d^4k}{(2\pi)^4} \to \frac{1}{\beta}\not{\sum} \equiv \frac{1}{\beta}\sum_{n\in\mathbb{Z}}\int \frac{d^3k}{(2\pi)^3}\ , \tag{7.21}$$

to account for the periodicity of the complex time. With these tools at hand, it is possible to calculate observables perturbatively.

It is worth noting that the imaginary time formalism is well suited for physical systems in thermodynamical equilibrium, since the time variable is traded for the temperature. Consequently, the time-evolution of a thermodynamical system cannot be described within this formalism. However, especially the description of the Higgs potential in the early universe demands on the one hand a time evolution and on the other hand incorporates non-equilibrium

effects. Thus, the imaginary time formalism is not sufficient to describe the full picture.
A better suited approach is the so-called Closed-Time Path (CTP) formalism [159–161]. This formalism allows us to describe the thermal- and the time-evolution of a physical system by using the time evolution of the density matrix, allowing us to express the thermal expectation value in terms of time evolution operators on a *closed time path*. This closed time path is going back and forth on the real time branch and along the complex time branch, hence it is required to describe the quantum fields on both branches (real and complex) and the degrees of freedom have to be doubled. For instance, in a scalar field theory with the field ϕ, it is needed to introduce a field ϕ_+ propagating forward towards positive (real) times and a field ϕ_- propagating backwards in (real) time. The resulting propagator of the field becomes a 2×2 matrix. For a detailed introduction and discussion of the CTP formalism we refer to the literature.

7.1.3. One-loop Effective Potential at Finite Temperature

In the following we will present the one-loop effective potential at finite temperature. We start the discussion by showing a generic feature of the one-loop effective potential while considering finite temperatures, followed by the discussion of mass corrections induced by the so-called *hard thermal* loops resummation. Afterwards, we present a generic formalism to express the one-loop effective potential at finite temperature for arbitrary extended Higgs sectors.
Starting with the one-loop effective potential at zero temperature in Eq. (7.6), we can apply the replacement rules for finite temperature field theory discussed in Sec. 7.1.2,

$$V_{\text{eff}}^{(1)} = \frac{1}{2}\int \frac{d^4k_E}{(2\pi)^4} \ln\left(k_E^2 + m_{eff}^2\right) \xrightarrow{T\neq 0} \frac{T}{2} \sum\!\!\!\!\!\!\int \ln\left[\omega_n^2 + \mathbf{k^2} + m^2\right] \ , \tag{7.22}$$

with the Matsubara modes ω_n defined in Eq. (7.18) and the respective mass m of the scalar field. Note that this potential corresponds to a single scalar field. Defining $\omega_k^2 \equiv \mathbf{k}^2 + m^2$ allows us to express the *Bose* sum as

$$\sum_{n\in\mathbb{Z}} \ln\left(\omega_n^2 + \omega_k^2\right) = \sum_{n\in\mathbb{Z}} \ln\left(\omega_n^2 + {}^1\!/_{\beta^2}\right) + \int_{1/\beta}^{\omega_k} du \sum_{n\in\mathbb{Z}} \frac{2u}{u^2+\omega_n^2} \ . \tag{7.23}$$

Considering the sum identity

$$\sum_{n\in\mathbb{Z}} \frac{y}{y^2 + n^2\pi^2} = \coth(y) \ , \tag{7.24}$$

and identifying

$$\nu(u) = \sum_{n\in\mathbb{Z}} \ln(\omega_n^2 + u^2) \ , \quad \frac{\partial \nu}{\partial u} = \sum_{n\in\mathbb{Z}} \frac{2u}{\omega_n^2 + u^2} \ , \tag{7.25}$$

allows for a closed expression of the one-loop effective potential at finite temperatures

$$V_{\text{eff}}^{(1)} = \int \frac{d^3k}{(2\pi)^3} \frac{\omega_k}{2} + \int \frac{d^3k}{(2\pi)^3} \frac{1}{\beta} \ln\left(1 - \mathrm{e}^{-\beta\omega_k}\right) + (\omega_k\text{-independent const. }) \ . \tag{7.26}$$

The first term is temperature independent and UV divergent. This term incorporates the one-loop corrections present at zero temperature and is referred to as Coleman-Weinberg potential. By using an $\overline{\text{MS}}$ renormalization, the first term can be written as [154, 162]

$$V_{\text{CW}}|_{\overline{\text{MS}}} = \frac{m^4}{64\pi^2}\left(\ln\left(\frac{m^2}{\mu^2}\right) - \frac{3}{2}\right) \ , \tag{7.27}$$

with the renormalisation scale μ.
The second term in Eq. (7.26) represents the temperature dependent part of the one-loop effective potential and it is often expressed as [156]

$$V_T = \int \frac{d^3k}{(2\pi)^3} \frac{1}{\beta} \ln\left(1 - \mathrm{e}^{-\beta\omega_k}\right) \equiv \frac{1}{2\pi^2\beta^4} J_B\left[m^2\beta^2\right] \ , \tag{7.28}$$

with the thermal bosonic function J_B defined as

$$J_B\left[m^2\beta^2\right] = \int_0^\infty dx x^2 \ln\left[1 - \exp\left(x^2 + \beta^2 m^2\right)\right] \ . \tag{7.29}$$

Up to this point the effective potential describes only one single scalar field, but can be generalised including multiple scalar fields, fermions and gauge bosons. However, also in the general case the one-loop effective potential at finite temperature splits into a zero-temperature part containing the one-loop corrections present at zero temperatures and one temperature-dependent part. For the general case we will provide the corresponding formulas.
In the following the different treatments of including thermal mass corrections in the effective potential are discussed. For simplicity, we start the discussion with a simple scalar field theory with the Lagrangian

$$\mathcal{L} = \frac{1}{2}\left(\partial_\mu\phi\right)^2 + \frac{\mu^2}{2}\phi^2 + \frac{\lambda}{4}\phi^4 \ , \tag{7.30}$$

with the scalar field ϕ and the Lagrange parameters μ and λ. Expanding the field around its vacuum expectation value (VEV)

$$\phi \to \phi + \langle\phi\rangle \equiv \phi + v \ , \tag{7.31}$$

allows us to express the mass of the scalar field as

$$m_\phi^2 = 3\lambda v^2 - \mu^2 \ . \tag{7.32}$$

In addition to the UV divergences in the one-loop effective potential, also infrared (IR) divergences are present. The Matsubara zero-modes ($n = 0$) yield an IR divergence in the limit of vanishing momentum

$$V_{\text{eff}} \sim \ln\left(\mathcal{D}^{-1}\right)\big|_{n=0} \xrightarrow{\mathbf{k}\to 0} \infty \ . \tag{7.33}$$

It turns out that higher-order corrections to thermal masses are required to cure the IR divergences. However, finite temperature alters the usual perturbative expansion in the self-coupling λ. Eq. (7.32) implies that the mass scales with the self-coupling, $m_\phi \sim \lambda$, hence an expansion in terms of the mass corresponds to an expansion in the self-coupling simultaneously. The temperature dependent potential of a single scalar field in Eq. (7.28) in the *high-temperature limit* [163]

$$V_T(v) = T^4\left[-\frac{\pi^2}{90} + \frac{m^2(v)}{24T^2} - \frac{m^3(v)}{12\pi T^3} + \mathcal{O}\left({}^{m^4}/_{T^4}\right)\right] \ , \tag{7.34}$$

shows indeed that the next leading order correction is not of the order of λ^2 as expected, but of the order $m^3(v) \sim \lambda^{3/2}$. In [163] it was shown that the *ring corrections* (or Debye corrections) reproduce exactly this order in the self-coupling and hence have to be taken into account as they are the leading corrections. The Debye corrections correspond to the one-loop corrections to the polarisation tensor of the field. They are calculated in the soft-momentum limit ($\mathbf{k} \to 0$) and in the so-called *hard thermal loop approximation*, where ${}^m/_T \ll 1$. The

scalar field in Eq. (7.30) would produce the following one-loop correction with vanishing external momentum

$$\pi^{(1)}(0) = 3\lambda T \sum\!\!\!\!\!\!\int \frac{1}{\omega_n^2 + \omega_k^2} \tag{7.35a}$$

$$= 3\lambda T \int \frac{d^3k}{(2\pi)^3} \frac{1}{2\omega_k} \frac{d}{d\omega_k} \sum_{n\in\mathbb{Z}} \ln\left(\omega_n^2 + \omega_k^2\right) \tag{7.35b}$$

$$= 3\lambda \left[\int \frac{d^3k}{(2\pi)^3} \frac{1}{2\omega_k} + \int \frac{d^3k}{(2\pi)^3} \frac{1}{\omega_k \left(\mathrm{e}^{\beta\omega_k} - 1\right)} \right] , \tag{7.35c}$$

where in the last step the same trick was used as in Eq. (7.25) to perform the Bose sum. In the hard thermal loop limit ($m/T \ll 1$) the temperature dependent one-loop mass correction reads

$$\pi^{(1)}(0) = \lambda \frac{3T^2}{12} . \tag{7.36}$$

The approach of [164] suggests to resum the thermal mass corrections in the propagators of the theory by replacing the tree-level masses with the thermal masses

$$m_0 \to \overline{m} = m_0 + \pi^{(1)}(0) , \tag{7.37}$$

in the propagator. The non-zero thermal masses cure the IR-divergences depicted in Eq. (7.33). Indeed, this replacement yields cubic mass terms in the temperature dependent effective potential, hence they are of the correct order in the self-coupling [164]. Alternatively, Parwani [165] suggests to replace all masses by their thermal masses $\overline{m}$. However, this method admixes higher-order corrections which at one-loop level could lead to a non-consistent description, since effective one-loop masses are used.
Another approach is given by [166]. In this approach the different Matsubara modes, namely the heavy ($n \neq 0$) and zero ($n = 0$) modes are treated independently. To motivate the different treatments of the Matsubara modes a typical one-loop integral in $d = 4 - 2\varepsilon$ dimensions can be split into the zero and heavy modes by [166]

$$I(m) = I_0 + I_{n\neq 0} , \tag{7.38}$$

with the zero mode contribution

$$I_0 = \mu^{2\varepsilon} T \int \frac{d^{3-2\varepsilon}}{(2\pi)^{3-2\varepsilon}} \frac{1}{k^2 + m^2} = \frac{\Gamma\left(-1/2 + \epsilon\right)}{(4\pi)^{3/2}} \left[\frac{4\pi\mu^2}{m^2}\right]^{\varepsilon} mT \overset{\varepsilon\to 0}{\longrightarrow} \quad -\frac{1}{4\pi} mT \tag{7.39}$$

and the heavy modes

$$I_{n\neq 0} = 2\mu^{2\varepsilon} T \sum_{n=1}^{\infty} \int \frac{d^{3-2\varepsilon}}{(2\pi)^{3-2\varepsilon}} \frac{1}{(2\pi n T)^2 + k^2 + m^2} \tag{7.40}$$

$$= 2\mu^{2\varepsilon} T \sum_{n=1}^{\infty} \sum_{l=0}^{\infty} \int \frac{d^{3-2\varepsilon}}{(2\pi)^{3-2\varepsilon}} \frac{(-1)^l m^{2l}}{\left[(2\pi n T)^2 + k^2\right]^{l+1}}$$

$$= \frac{1}{12} T^2 - \frac{1}{16\pi^2} m^2 \left[\frac{1}{\varepsilon} + \ln(\frac{\mu^2}{T^2}) - 2c_b\right]$$

$$+ T^2 \sum_{l=2}^{\infty} \left(\frac{-m^2}{4\pi^2 T^2}\right)^l \frac{(2l-3)!!}{(2l)!!} \zeta(2l-1) + \mathcal{O}(\varepsilon) .$$

The crucial point is that the integral of the heavy modes can be treated as an expansion in m^2, while the zero mode gives rise to the only non-analytical term in m^2. So the Matsubara zero modes are the origin of the problematic term, hence it is sufficient to resum only the

static zero Matsubara modes. The resummation results in the following replacement in the bosonic (fermionic) thermal integral

$$J_{\pm}^{(k)} = \begin{cases} J_{-}(\frac{m_k^2}{T^2}) - \frac{\pi}{6}\left(\overline{m}_k^3/T^3 - m_k^3/T^3\right), & k = W_L, Z_L, \gamma_L, \Phi^0, \Phi^{\pm} \\ J_{-}(\frac{m_k^2}{T^2}) & k = W_T, Z_T, \gamma_T \\ J_{+}(\frac{m_k^2}{T^2}) & k = \text{fermion}\ , \end{cases} \tag{7.41}$$

where k denotes all particles present in the Standard Model (SM), or also in extended Higgs sectors. The bosonic (fermionic) thermal integral is given by

$$J_{\pm}(x^2) = \int_0^{\infty} dk k^2 \log\left(1 \pm \exp\left(-\sqrt{k^2 + x^2}\right)\right)\ , \tag{7.42}$$

where the + sign corresponds to fermions and − to bosons, respectively. The index L, T refers to the longitudinal and transversal polarisations of the respective particle. The mass m_k indicates the tree-level mass of the particle and $\overline{m}_k$ the respective thermal mass. The thermal mass for *e.g.* a scalar field is given by Eq. (7.37). Note that fermions do not require a resummation of thermal mass corrections, since there are no zero modes and in this way no IR divergences. We will provide a generic description in the following section. All results shown in this work use the resummation prescription for the static zero modes. We refer to this procedure as *Arnold Espinosa method*.

7.1.4. Generic Extended Higgs Sector Models

In the last section several aspects of the one-loop effective potential at finite temperature were shown, such as the splitting in a temperature dependent and independent part. Further, the different approaches to resum the thermal mass corrections were discussed. In this section, we show a possibility to write the Coleman-Weinberg and temperature dependent potential in terms of generic tensors describing an arbitrary extended Higgs sector. The approach is based on [167] and it is implemented in the `C++` code BSMPT [5, 168].
The scalar, fermion and gauge boson sector in an arbitrary extended Higgs sector[20] can be written in terms of the tensors describing the coupling structure

$$-\mathcal{L}_S = L^i\Phi_i + \frac{1}{2}L^{ij}\Phi_i\Phi_j + \frac{1}{3!}L^{ijk}\Phi_i\Phi_j\Phi_k + \frac{1}{4!}L^{ijkl}\Phi_i\Phi_j\Phi_k\Phi_l\,, \tag{7.43a}$$

$$-\mathcal{L}_F = \frac{1}{2}Y^{IJk}\Psi_I\Psi_J\Phi_k + c.c.\,, \tag{7.43b}$$

$$\mathcal{L}_G = \frac{1}{4}G^{abij}A_{a\mu}A_b^{\mu}\Phi_i\Phi_j\ , \tag{7.43c}$$

with the real scalar fields Φ_i introduced by the Higgs multiplets. The index i of the scalar fields runs up to the number of included real scalar field components n_{Higgs}. The fermion fields have to be expressed in terms of Weyl spinors Ψ_I with $I = 1 \ldots n_{\text{Fermions}}$ and the four-vector fields $A_{a\mu}$ correspond to the gauge field with the index $a = 1 \ldots n_{\text{gauge}}$. The tensors L^i, L^{ij}, L^{ijk} and L^{ijkl} indicate the Higgs self-interactions, whereas the Y^{IJk} correspond to the Yukawa interactions between the Ith and Jth fermion with the k-th real scalar field and G^{abij} to the gauge interaction between two gauge bosons with the indices a, b and the real scalar fields with the indices i, j, respectively. Note that the tensors in Eq. (7.43) are defined in the unbroken Higgs basis with all VEVs of the scalar fields set to zero. After electroweak symmetry breaking, the scalar fields are expanded around their VEV ω_i as

$$\Phi_i = \omega_i + \phi_i\ , \tag{7.44}$$

[20] At least for non-minimal extended Higgs sector models as presented in Chapter 3.

resulting in the following Lagrangians

$$-\mathcal{L}_S = \Lambda + \Lambda^i_{(S)}\phi_i + \frac{1}{2}\Lambda^{ij}_{(S)}\phi_i\phi_j + \frac{1}{3!}\Lambda^{ijk}_{(S)}\phi_i\phi_j\phi_k + \frac{1}{4!}\Lambda^{ijkl}_{(S)}\phi_i\phi_j\phi_k\phi_l\,, \tag{7.45a}$$

$$-\mathcal{L}_F = \frac{1}{2}M^{IJ}\Psi_I\Psi_J + \frac{1}{2}Y^{IJk}\Psi_I\Psi_J\phi_k\,, \tag{7.45b}$$

$$\mathcal{L}_G = \frac{1}{2}\Lambda^{ab}_{(G)}A_{a\mu}A^\mu_b + \frac{1}{2}\Lambda^{abi}_{(G)}A_{a\mu}A^\mu_b\phi_i + \frac{1}{4}\Lambda^{abij}_{(G)}A_{a\mu}A^\mu_b\phi_i\phi_j\,. \tag{7.45c}$$

The corresponding tensors in the broken phase read [167]

$$\Lambda = V^{(0)} = L^i\omega_i + \frac{1}{2}L^{ij}\omega_i\omega_j + \frac{1}{3!}L^{ijk}\omega_i\omega_j\omega_k + \frac{1}{4!}L^{ijkl}\omega_i\omega_j\omega_k\omega_l\,, \tag{7.46a}$$

$$\Lambda^i_{(S)} = L^i + L^{ij}\omega_j + \frac{1}{2}L^{ijk}\omega_j\omega_k + \frac{1}{6}L^{ijkl}\omega_j\omega_k\omega_l\,, \tag{7.46b}$$

$$\Lambda^{ij}_{(S)} = L^{ij} + L^{ijk}\omega_k + \frac{1}{2}L^{ijkl}\omega_k\omega_l\,, \tag{7.46c}$$

$$\Lambda^{ijk}_{(S)} = L^{ijk} + L^{ijkl}\omega_l\,, \tag{7.46d}$$

$$\Lambda^{ijkl}_{(S)} = L^{ijkl}\,, \tag{7.46e}$$

$$\Lambda^{ab}_{(G)} = \frac{1}{2}G^{abij}\omega_i\omega_j\,, \tag{7.46f}$$

$$\Lambda^{abi}_{(G)} = G^{abij}\omega_j\,, \tag{7.46g}$$

$$\Lambda^{abij}_{(G)} = G^{abij}\,, \tag{7.46h}$$

$$\Lambda^{IJ}_{(F)} = M^{*IL}M^J_L = Y^{*ILk}Y^{Jm}_L\omega_k\omega_m\,, \tag{7.46i}$$

$$M^{IJ} = Y^{IJk}\omega_k\,. \tag{7.46j}$$

Note that the tensors $\Lambda^{ij}_{(S)}$, $\Lambda^{ab}_{(G)}$ and M^{IJ} coincide with the respective mass matrices of the scalar, gauge and fermion fields, respectively. With the definition of the tensors, the Coleman-Weinberg potential can be written as [167]

$$V_{\mathrm{CW}} = \frac{1}{64\pi^2}\sum_{X=S,G,F}(-1)^{2s_X}(1+2s_X)\mathrm{Tr}\left[\left(\Lambda^{xy}_{(X)}\right)^2\left(\log\left(\frac{1}{\mu^2}\Lambda^{xy}_{(X)}\right) - k_X\right)\right]\,, \tag{7.47}$$

with the spin and $\overline{\mathrm{MS}}$ constants

$$s_X = \begin{cases} 0 & \text{scalars} \\ \frac{1}{2} & \text{fermion} \\ 1 & \text{gauge boson} \end{cases}\,, \quad \text{and} \quad k_X = \begin{cases} \frac{5}{6} & \text{gauge boson} \\ \frac{3}{2} & \text{scalar and fermions} \end{cases}\,. \tag{7.48}$$

The indices x, y reflect the respective indices depending on the type of the field ij, ab or $,IJ$ for $X = S, G$ or F. The temperature dependent potential is then given by [167]

$$V_T = \sum_{X=S,G,F}(-1)^{2s_X}(1+2s_X)\frac{T^4}{2\pi^2}J_\pm\left(\Lambda^{xy}_{(X)}/T^2\right)\,, \tag{7.49}$$

with the fermionic (bosonic) thermal integral defined as

$$J_\pm\left(\Lambda^{xy}_{(X)}/T^2\right) = \mathrm{Tr}\left[\int_0^\infty \mathrm{d}k k^2 \log\left[1 \pm \exp\left(-\sqrt{k^2 + \Lambda^{xy}_{(X)}/T^2}\right)\right]\right]\,. \tag{7.50}$$

The thermal mass corrections, or Debye corrections can also be expressed in terms of the tensor couplings. They are given by

$$\Pi^{ij}_{(S)} = \frac{T^2}{24}\left[(-1)^{2s_S}(1+2s_S)\sum_{k=1}^{n_{\text{Higgs}}} L^{ijkk} + (-1)^{2s_G}(1+2s_G)\sum_{a=1}^{n_{\text{gauge}}} G^{aaij} \right.$$
$$\left. -(-1)^{2s_F}(1+2s_F)\frac{1}{2}\sum_{I,J=1}^{n_{\text{fermion}}}\left(Y^{*IJj}Y^{i}_{IJ} + Y^{*IJi}Y^{j}_{IJ}\right)\right] , \tag{7.51}$$

$$\Pi^{ab}_{(G)} = T^2\frac{2}{3}\left(\frac{\tilde{n}_H}{8}+5\right)\frac{1}{\tilde{n}_H}\sum_{m=1}^{n_{\text{Higgs}}} G^{aamm}\delta_{ab} , \tag{7.52}$$

with $\tilde{n}_H$ being the number of real scalar fields coupled to gauge bosons. The presented formulas are only valid, if the model does not introduce additional fermions or gauge bosons compared to the SM. Since all models under investigation in the context of the electroweak phase transition in this thesis solely extend the Higgs sector and leave the fermion and gauge sector unchanged, the formulas do not need to be changed. The resummation of the static Matsubara zero modes is then equivalent to add the additional term to the temperature dependent potential

$$V_T(\omega,T) \to V_T(\omega,T) + V_{\text{Debye}}(\omega,T) , \tag{7.53}$$

$$V_{\text{Debye}}(\omega,T) = -\frac{T}{12\pi}\left[\sum_{i=1}^{n_{\text{Higgs}}}\left(\left(\overline{m}_i^2\right)^{3/2} - \left(m_i^2\right)^{3/2}\right) + \sum_{a=1}^{n_{\text{gauge}}}\left(\left(\overline{m}_a^2\right)^{3/2} - \left(m_a^2\right)^{3/2}\right)\right] . \tag{7.54}$$

The tree-level masses $m^2_{i/a}$ are the eigenvalues obtained from the mass matrices $\Lambda^{ij}_{(S)}$ and $\Lambda^{ab}_{(G)}$. The thermal masses $\overline{m}^2_{i,a}$ are the eigenvalues of the thermal mass corrected mass matrices respectively

$$\Lambda^{ij}_{(S)} \to \Lambda^{ij}_{(S)} + \Pi^{ij}_{(S)} , \tag{7.55a}$$

$$\Lambda^{ab}_{(G)} \to \Lambda^{ab}_{(G)} + \Pi^{ab}_{(G)} . \tag{7.55b}$$

The evaluation of the one-loop effective potential and the required mass eigenvalues is performed numerically within `BSMPT`.

7.1.5. Renormalisation

In what follows, we present the renormalisation prescription introduced in [169] and applied in [4, 72]. Up to this point, higher-order corrections in the Coleman-Weinberg potential are renormalised in the $\overline{\text{MS}}$-scheme (see Eqs. (7.27) and (7.47)) changing the input parameters, especially the masses and mixing angles of the theory, compared to their tree-level values. However, for large parameter scans it is convenient to use the tree-level parameters as direct input parameters. This can be achieved by absorbing the radiative corrections in *on-shell* counterterms. By identifying all Lagrange parameters in the tree-level Lagrangian to be *bare* parameters and expanding them in renormalised parameters and the respective counterterms

$$p_0 \to p + \delta p , \tag{7.56}$$

the additional counterterm potential can be split off as

$$V(\omega,T) = V^{(0)}(\omega) + V_{\text{CW}}(\omega) + V_{\text{CT}}(\omega) + V_T(\omega,T) . \tag{7.57}$$

The counterterm potential reads then

$$V_{\text{CT}} = \sum\frac{\partial V^{(0)}}{\partial p_i}\delta p_i + \sum \delta T_k\left(\phi_k + \omega_k\right) , \tag{7.58}$$

where the first sum runs over all Lagrange parameters present in the tree-level potential and the second sum runs over all fields getting a non-zero VEV at tree level. The tadpole counterterms δT_i are needed to ensure that the NLO vacuum ground state yields the same masses and mixing angles as the LO vacuum state.
Fixing the counterterms defined in Eq. (7.58) requires to impose several renormalisation conditions. To ensure that the NLO masses and mixing angles remain the same as the tree-level input parameters, the following conditions are imposed at zero temperature

$$0 = \partial_{\phi_i} \left(V_{\mathrm{CW}} + V_{\mathrm{CT}}\right)|_{\phi_k=\langle\phi_k\rangle(T=0)} \ , \tag{7.59}$$

$$0 = \partial_{\phi_i}\partial_{\phi_j} \left(V_{\mathrm{CW}} + V_{\mathrm{CT}}\right)|_{\phi_k=\langle\phi_k\rangle(T=0)} \ , \tag{7.60}$$

where ∂_{ϕ_i} indicates the derivatives with respect of the i-th scalar field component and the indices i, j, k indicate all different scalar field components introduced in the Higgs multiplets. Note that $\langle\phi_k\rangle\,(T=0)$ corresponds to the zero-temperature ground state of the scalar fields as defined *e.g.* in Eq. (3.14). The first condition ensures that the NLO vacuum state remains unchanged and the second one the NLO masses to be the same. To be precise, the renormalisation conditions ensure that the NLO vacuum is a local minimum of the potential, though it has to be checked numerically if it is still the global minimum of the effective potential. The first and second derivatives of the Coleman-Weinberg potential can be expressed in terms of the tensors defined in Eq. (7.43) and are given in [167].
In general, the system of equations defined in Eq. (7.60) is overconstrained, so that additional assumptions are needed in order to regularize the system. These assumptions have be found case by case in the different extensions of the SM.

7.2. Electroweak Phase Transition

As will be discussed in Chapter 9 the EWPT is one required condition for electroweak baryogenesis (EWBG) and needed to explain the baryon asymmetry of the universe. However, the EWPT is not only of interest concerning the EWBG, but can also give contributions to the gravitational wave spectrum [170–172].
We investigate the possibility of a strong first-order electroweak phase transition (SFOEWPT) in non-minimal Higgs sectors. In order to describe the Higgs potential in the early universe we chose the ansatz of the effective potential at finite temperature presented in Sec. 7.1.3. In the following we will first sketch the evolution of the universe starting in the Big Bang and ending in the today's present vacuum structure, followed by the discussion of the used method to quantify the strength of the phase transition.
In Secs. 7.1.1, 7.1.3 and 7.1.4 it was demonstrated that the effective potential of an arbitrary non-minimal extended Higgs sector can be found by including higher-order quantum corrections and at the same time finite temperature effects. The effective potential can be parametrized at high temperature as follows [173–175]

$$V(\phi, T) = D\left(T^2 - T_0^2\right)\phi^2 - ET\phi^3 + \frac{\lambda(T)}{4}\phi^4 \ , \tag{7.61}$$

with some coefficients $D, E, \lambda(T)$ and T_0. These coefficients are functions of the particle masses and the respective couplings of the theory at zero temperature. However, the exact dependence of the parameters is model dependent and not important for the following discussion. The coupling $\lambda(T)$ shows also a mild temperature dependence, but can be neglected compared to the other temperature dependencies.
The first crucial observation is, that at sufficiently high temperatures the global minimum of the effective potential is in the symmetric ground state $\langle\phi\rangle = 0$, regardless if the electroweak symmetry breaking takes place at zero temperature. Hence, a phase transition must take

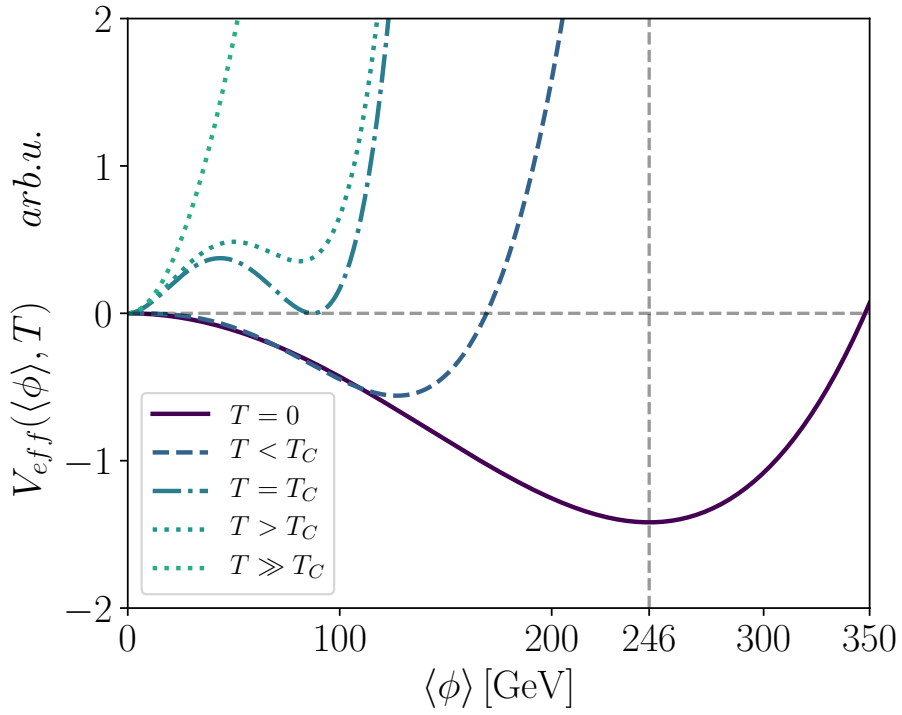

Figure 7.1.: The different vacuum structures of the one-loop effective potential at finite temperature are shown for different temperatures.

place between the Big Bang starting in the symmetric phase of the universe ($\langle\phi\rangle = 0$) and the broken phase ($\langle\phi\rangle \neq 0$) as present in our today's universe.
The so-called *smooth crossover* is the continuous phase transition between the two vacuum states without a barrier separating both vacua. The smooth crossover is obtained if the cubic mass term in Eq. (7.61) is dropped

$$V(\phi, T) = D\left(T^2 - T_0^2\right)\phi^2 + \frac{\lambda(T)}{4}\phi^4 \ . \tag{7.62}$$

The mass term or rather potential curvature is then given by

$$m^2(\phi, T) = 3\lambda(T)\phi^2 + 2D\left(T^2 - T_0^2\right) \ , \tag{7.63}$$

and the extrema of the potential can be expressed as

$$\phi_c = 0 \ , \quad \text{and} \quad \phi_c = \sqrt{\frac{2D\left(T^2 - T_0^2\right)}{\lambda(T)}} \ . \tag{7.64}$$

Eq. (7.64) indicates the critical temperature to be $T_c = T_0$ yielding two degenerate extrema at $\phi = 0$ with $m^2(0, T_c) = 0$. For temperatures above the critical temperature $T > T_0$ we have only one global minimum at $\phi = 0$, since $m^2(0, T) > 0$. For temperatures below the critical temperatures $T_c < T_0$, the second extrema in Eq. (7.64) is present which turns out to be new global minimum since $m^2(\phi_c, T) > 0$ and the extremum at $\phi = 0$ is a local maximum. Despite the smooth crossover, successful baryogenesis requires a first order phase transition. To enable a first order phase transition the cubic mass term is needed in Eq. (7.61). Note these exactly cubic mass terms arise by including the thermal mass corrections, the Debye corrections, in the effective potential. The evolution of the effective potential in Eq. (7.61) is shown in Fig. 7.1 For sufficiently high temperatures ($T \gg T_c$) the symmetric potential has

only one global minimum, namely $\langle\phi\rangle = 0$. For decreasing temperatures ($T < T_c$) a new local minimum arises at

$$\langle\phi\rangle = \frac{3E}{2\lambda}\frac{T_0^2}{1 - 9E^2/8\lambda D} \ , \tag{7.65}$$

still with one global minimum at $\langle\phi\rangle = 0$. The two minima are degenerate at the critical temperature ($T = T_c$), where the cubic mass term generates a barrier between both equivalent minima. At this point the vacuum state of the universe is metastable and quantum tunneling between both vacua is possible. For temperatures below the critical temperature only one global minimum is present in the potential, the broken minimum. At zero temperature the effective potential reflects the well-known Higgs potential with the VEV at $\langle\phi\rangle = 246.22\,\text{GeV}$. As an additional condition it is required to have a *strong* first-order EWPT in the context of electroweak baryogenesis as discussed in Chapter 9, but also for gravitational waves. The so-called baryon wash-out condition yields a requirement for the ratio of the critical temperature and the electroweak VEV configuration v_c at the critical temperature (see *e.g.* [31]),

$$\xi_c \equiv \frac{v_c}{T_c} \gtrsim 1 \ . \tag{7.66}$$

The exact numerical value of the required condition is model dependent, however for simplicity we take $\xi_c > 1$ as the SFOEWPT condition.
In general the coefficients in Eq. (7.61) cannot be calculated analytically and if at all, then only for rather simple models (*e.g.* see [176]) or under additional simplifications. Thus, we use a numerical approach to find the global minimum of the one-loop effective potential at finite temperature. All used numerical routines are implemented in `BSMPT` [5, 168].

CHAPTER 8

Phenomenological Study of the Electroweak Phase Transition

In this chapter we will present the results of the N2HDM. We start with the discussion of the general idea of the analysis, followed by the presentation of the used approach and numerical tools. We conclude with the phenomenological impact on the parameter region of the N2HDM by requiring an SFOEWPT.
For the numerical analysis we sample a parameter set of the N2HDM by using the program `ScannerS` [60] allowing us to generate benchmark points fulfilling all experimental and theoretical constraints discussed and presented in Sec. 3.1. The scan ranges used in this analysis are listed in Tab. 8.1 for the `Type I` N2HDM and in Tab. 8.2 for `Type II`, respectively. To account for the flavor constraints $B \to X + \gamma$ shown in Fig. 3.1 the scan range of the charged mass in the Type II N2HDM starts at 580 GeV [177]. The SM-input parameters are listed in Appendix B.
To check if a considered benchmark point also provides an SFOEWPT, we implemented the calculation of the one-loop effective potential at finite temperatures in the `C++` code `BSMPT`. `BSMPT` allows us to find the global minimum of the one-loop effective potential at finite temperature, in particular the vacuum structure of the N2HDM in Eq. (3.53) at a given temperature. Hence, it is possible to deduce the strength of the phase transition ξ_c defined in Eq. (7.66). Note that only the *electroweak* $SU(2)_L$ VEV components enter the definition of ξ_c in Eq. (7.66). Therefore, the critical VEV squared of the N2HDM is given by

$$\omega_c^2 = \omega_1^2 + \omega_2^2 + \omega_{\mathrm{CB}}^2 + \omega_{\mathrm{CP}}^2 \ , \tag{8.1}$$

where ω_i $(i = 1, 2, \mathrm{CP}, \mathrm{CB})$ correspond to the VEV configuration at finite temperatures. To calculate ω_c, `BSMPT` uses the following algorithm:

- Determine the NLO global minimum of the effective potential at zero temperature. If the NLO vacuum reflects the tree-level minimum, the parameter point provides an *NLO stable vacuum*.
- Determine the NLO global minimum of the effective potential at $T = 300\,\mathrm{GeV}$. Check if the resulting electroweak VEV ω_c vanishes. If not, the benchmark point cannot provide an SFOEWPT.[21]

[21] To provide an SFOEWPT, the electroweak VEV ω_c can be at most given by the electroweak VEV $v \approx 246\,\mathrm{GeV}$. To allow for some numerical fluctuations, $T = 300\,\mathrm{GeV}$ is chosen as starting point, since temperatures above the chosen limit do not yield an SFOEWPT.

m_h	$m_{H_\downarrow}$	$m_{H_\uparrow}$	m_A	$m_{H^\pm}$	m_{12}^2
		in GeV			in GeV^2
125.09	$[30, 1500]$	$[30, 1500]$	$[30, 1500]$	$[30, 1500]$	$\left[10^{-3}, 10^5\right]$
α_1	α_2	α_3	$\tan\beta$	v_S [GeV]	
$\left[-\frac{\pi}{2}, \frac{\pi}{2}\right)$	$\left[-\frac{\pi}{2}, \frac{\pi}{2}\right)$	$\left[-\frac{\pi}{2}, \frac{\pi}{2}\right)$	$[0.8, 20]$	$[1, 3000]$	

Table 8.1.: Parameter ranges for the N2HDM T1 input parameters used in `ScannerS`.

m_h	$m_{H_\downarrow}$	$m_{H_\uparrow}$	m_A	$m_{H^\pm}$	m_{12}^2
		in GeV			in GeV^2
125.09	$[30, 1500]$	$[30, 1500]$	$[30, 1500]$	$[580, 1500]$	$\left[10^{-3}, 10^5\right]$
α_1	α_2	α_3	$\tan\beta$	v_S [GeV]	
$\left[-\frac{\pi}{2}, \frac{\pi}{2}\right)$	$\left[-\frac{\pi}{2}, \frac{\pi}{2}\right)$	$\left[-\frac{\pi}{2}, \frac{\pi}{2}\right)$	$[0.8, 20]$	$[1, 3000]$	

Table 8.2.: Parameter ranges for the N2HDM T2 input parameters used in `ScannerS`.

- Following a bisection method in the temperature interval with the starting points $T_l = 0\,\text{GeV}$ and $T_r = 300\,\text{GeV}$, allows us to determine the electroweak VEV $\omega_c(\frac{T_l+T_r}{2})$. If the obtained VEV vanishes, the right side of the interval is set to $T_r = \frac{T_l+T_r}{2}$, otherwise the left side $T_l = \frac{T_l+T_r}{2}$, respectively. This procedure is repeated until a precision of $T_l - T_r \leq 10^{-2}$ GeV is achieved. The critical temperature is then set to $T_c = T_l$ and the critical VEV to $v_c = \omega_c(T_l)$.

Some additional remarks on the chosen approach are in order. By using a bisection in order to determine the critical temperature and thereby the critical VEV, it is not possible to track down possible two-step phase transitions. To discuss the full vacuum structure with possible multi-step phase transitions, it would be required to track the vacua at all temperatures. A possible ansatz is realized in the program package `PhaseTracer` [178], enabling to track all minima evolving with the temperature. However, since we are only interested in single SFOEWPT and not in multi-step EWPTs, the usage of the bisection method yields a significantly better run time performance allowing for a more efficient parameter scan.

8.1. Type I N2HDM

In the following, we present the results of the numerical analysis for both types of the N2HDM. We start with the discussion of the impact on the overall mass spectrum induced by the requirement of an SFOEWPT, followed by the trilinear Higgs self-couplings, in particular the trilinear self-coupling between three SM-like Higgs bosons.

8.1.1. Mass Spectrum of the N2HDM Type I

The N2HDM is a combination of a doublet and singlet extension of the SM. Hence, the resulting Higgs mass spectrum is enlarged compared to the SM. The model includes three CP-even neutral Higgs bosons, which we will refer to as h as the SM-like Higgs boson, $H_\downarrow$ as the non-SM-like Higgs boson with the lower mass $m_{H_\downarrow}$ and $H_\uparrow$ with higher mass $m_{H_\uparrow}$, respectively. Note that three mass hierarchies are possible within the neutral CP-even Higgs sector,

$$m_h < m_{H_\downarrow} < m_{H_\uparrow} \,, \tag{8.2}$$

the *semi-inverted mass hierarchy* with

$$m_{H_\downarrow} < m_h < m_{H_\uparrow} \,, \tag{8.3}$$

and the *inverted mass hierarchy*

$$m_{H_\downarrow} < m_{H_\uparrow} < m_h \,, \tag{8.4}$$

where the masses are identified with the masses in Eq. (3.62). Moreover, a charged Higgs H^+ and a pseudoscalar A are part of the Higgs particle spectrum of the N2HDM. For a detailed introduction of the N2HDM see Sec. 3.5 and references therein. Due to the additional singlet, all of the three CP-even neutral Higgs bosons acquire a contribution of the singlet field. Henceforth, we define the singlet admixture of the i-th CP-even neutral Higgs boson to be

$$\Sigma_{H_i} \equiv R_{i3}^2 \,, \tag{8.5}$$

where we identify H_i $(i = 1, 2, 3)$ with either $h, H_\downarrow$ or $H_\uparrow$ depending on the mass hierarchy. In Fig. 8.1 the two non-SM like Higgs bosons masses $m_{H_\downarrow}$ and $m_{H_\uparrow}$ versus the respective singlet admixture are shown. In both plots, the gray points denote all parameter points used in the analysis fulfilling all experimental and theoretical constraints presented in Sec. 3.1. The brown points additionally provide an NLO stable vacuum. The global minimum of the effective one-loop potential at zero temperature is equal to the tree-level potential defined in Eq. (3.54) for these points. The color code indicates the strength of the EWPT as defined in Eq. (7.66) and thus also the parameter points providing an SFOEWPT.
The strength of the EWPT is required to be at least $\xi_c > 1$, where the maximum value is given by $\xi_c^{\max} = 2.04$ for the Type I N2HDM. The theoretical and experimental constraints allow for a large mass range for the CP-even neutral Higgs bosons up to 1.5 TeV. For heavy $m_{H_\downarrow} \gtrsim 1250\,\text{GeV}$ configurations it is getting gradually more difficult to provide NLO stable vacua. However, the full parameter space up to 1.5 TeV[22] can be filled with valid parameter points if the parameter scan is extended in that regard. Though, the additional requirement of an SFOEWPT significantly pushes the overall mass spectrum to intermediate mass ranges,

$$m_{H_\downarrow} \in [53, 513]\,\text{GeV} \,, \quad m_{H_\uparrow} \in [136, 1479]\,\text{GeV} \,, \tag{8.6}$$

apart from the heavy masses $m_{H_\uparrow}$ above 800 GeV which are only possible for singlet-like Higgs bosons, where the singlet admixture is $\Sigma_{H_\uparrow} \gtrsim 80\%$. These heavy singlet-like Higgs bosons are especially interesting, since the large mass allows for Higgs to Higgs decays $H_\uparrow \to H_i H_j$. At the same time, the singlet nature of the heavy Higgs boson yields a suppression of the Higgs-to-Higgs coupling, so that the Higgs-to-Higgs decay branching ratios are suppressed.
As Eq. (8.6) implies, the normal and semi-inverted mass hierarchy is possible while requiring an SFOEWPT. Note that only a few parameter points with an inverted mass hierarchy were found in this analysis fulfilling all experimental and theoretical constraints, which might cause the missing SFOEWPT benchmark points. To summarize, the overall bulk of the

[22] Note that the upper limit of the scan range is chosen to be 1.5 TeV.

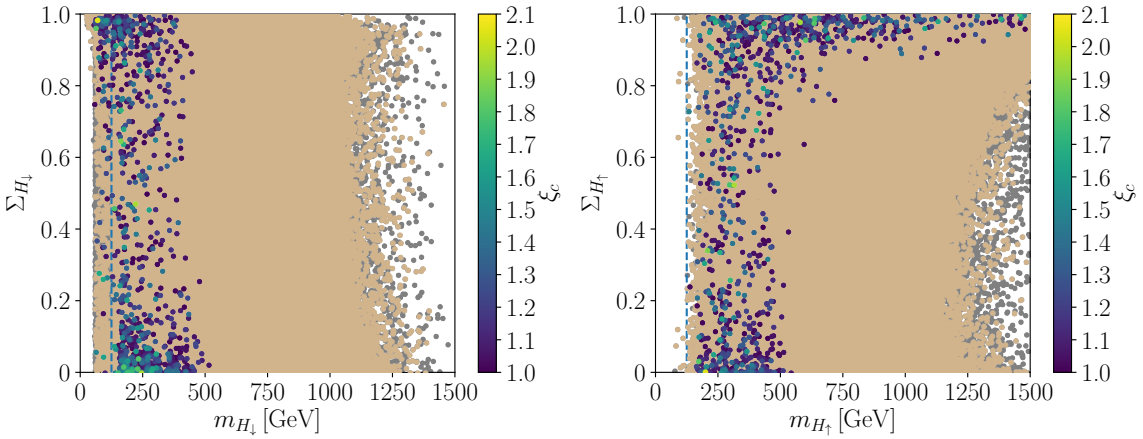

Figure 8.1.: N2HDM Type I The singlet-admixture is shown as a function of the non-SM like Higgs mass $m_{H_\downarrow}$ ($m_{H_\uparrow}$) on the left (right) side. The gray parameter points are all points fulfilling theoretical and experimental constraints, while the brown points additionally provide an NLO stable vacuum. The color code indicates the strength of the phase transition ξ_c and thus parameter points providing an SFOEWPT. The blue dashed line indicates the SM-like Higgs boson mass $m_h = 125\,\text{GeV}$. *The figures are taken from [4].*

CP-even neutral Higgs boson masses is pushed to intermediate mass ranges of the order $\mathcal{O}(200 - 500\ \text{GeV})$ by requiring an SFOEWPT. Nonetheless, the singlet admixture present in the N2HDM allows for significantly larger masses for $H_\uparrow$. This fact enables also stronger SFOEWPTs in the N2HDM as for instance for the C2HDM [4, 72]. A possible reason is discussed in the context of the trilinear self-couplings later on.

In Fig. 8.2 the charged mass $m_{H^\pm}$ (left) and the mass gap between the charged mass and the pseudoscalar mass $m_A - m_{H^\pm}$ (right) are shown as a function of $\tan\beta$. In both plots, the gray points denote all parameter points in the sample fulfilling all experimental and theoretical constraints, where the brown points additionally provide an NLO stable vacuum. The color code indicates the strength of the EWPT and thus all parameter points providing an SFOEWPT.

The strongest constraint in this parameter plane is given by the $B \to X_s + \gamma$ constraint discussed in Sec. 3.1.1. The exclusion limits for the 2HDM `Type I` are shown in Fig. 3.1 yielding the sharp cut-off on the left side of the viable parameter region in Fig. 8.2 (left). Note that the limits of the 2HDM can be taken over to the N2HDM [81]. This allows for charged Higgs boson masses from 150 GeV up to 1.5 TeV while fulfilling all experimental and theoretical constraints, where the lower bound on $\tan\beta$ depends on the charged mass (induced by the experimental flavor constraints) which is roughly $\tan\beta_{\text{min}} \approx 0.8$ for heavy charged masses and up to $\tan\beta_{\text{min}} \approx 2.5$ for light charged Higgs masses. Again by demanding an SFOEWPT the charged Higgs mass spectrum is pushed to intermediate mass ranges of the same order as observed in the CP-even neutral non-SM like Higgs bosons and hence $\tan\beta$ is above its minimal allowed value of 0.8.

In Fig. 8.2 (right) the mass gap between the pseudoscalar mass and the charged mass is shown. The requirement of an SFOEWPT allows for two distinct parameter regions. One in which the charged and pseudoscalar mass are degenerate and one parameter region in which the pseudoscalar mass is significantly heavier compared to the charged mass. Especially the T parameter of the oblique precision parameters discussed in Sec. 3.1.2 puts a stringent upper bound on the mass gap between the charged Higgs boson and the corresponding closest-in-mass neutral scalar. So either one of the CP-even neutral Higgs boson is mass degenerate with the charged Higgs boson, or the pseudoscalar Higgs boson. The requirement of an SFOEWPT

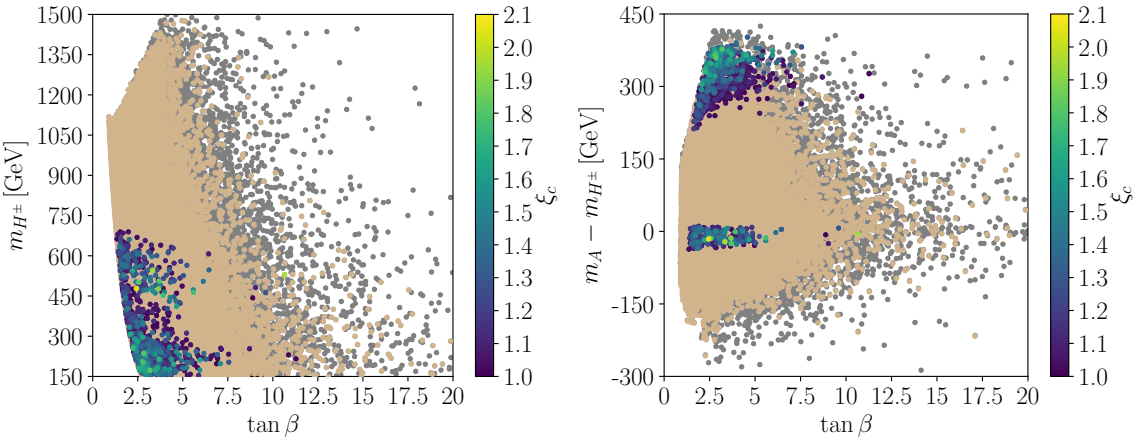

Figure 8.2.: Left: The charged Higgs mass $m_{H^\pm}$ is shown as a function of the mixing angle $\tan\beta$; Right: The mass gap between the pseudoscalar Higgs bosons A and the charged Higgs boson as a function of $\tan\beta$. In both plots, the gray parameter points are all points fulfilling theoretical and experimental constraints, while the brown points additionally provide an NLO stable vacuum. The color code indicates the strength of the phase transition ξ_c and thus parameter points providing an SFOEWPT. *The figures are takem from [4].*

strengthens this behavior [4]. We emphasize that especially the parameter region with a mass gap between A and H^+ is often neglected in the phenomenological discussion of EWBG and gravitational waves, since the additional assumption of $m_A \approx m_{H^\pm} \approx m_\Phi$ with the non-SM like neutral Higgs boson mass m_Φ is taken to simplify the calculation. In Fig. 8.2 (right) a slight tendency for stronger EWPTs for increasing mass gaps $m_A - m_{H^\pm}$ in the parameter region with large mass gaps in Fig. 8.2 (right) can be observed. In order to understand this, we recapitulate the findings in [72,179]. The strength of the EWPT scales with the size of the couplings of the light bosonic particles to the SM-like Higgs boson and is suppressed with the Higgs boson mass. Furthermore, non-SM like Higgs bosons contribute to the EWPT through their non-vanishing electroweak VEV[23]. Hence, for a stronger EWPT, the masses of the Higgs bosons have to be either light or their electroweak VEV contributions small, in the case of the N2HDM the corresponding singlet admixture high. Particles which do not get an electroweak VEV (A, H^+) and *singlet-like* CP-even neutral Higgs bosons ($\Sigma_i \approx 1$) are still allowed to be heavy without decreasing the strength of the EWPT. They can even enable a deeper potential barrier between the broken and symmetric vacuum state, which might enhance the strength of the EWPT [180]. Exactly this behavior can be observed in the parameter region with a large mass gap between the pseudoscalar and charged Higgs boson mass. The pseudoscalar mass is getting larger for increasing mass gap, while the charged Higgs mass remains mass degenerate with one of the CP-even neutral Higgs bosons. The neutral Higgs bosons remain light to enable an SFOEWPT, where the heavy degree of freedom A produces a higher potential barrier to strengthen the EWPT. However, there are additional interplays determining the size of the actual strength of the EWPT ξ_c. Hence, the actual effect is not significantly enhanced.

8.1.2. Trilinear Couplings of the N2HDM Type I

In the following we want to discuss the impact of the SFOEWPT on the effective one-loop trilinear Higgs self-coupling. The one-loop trilinear Higgs self-couplings are derived from

[23] Note that in the N2HDM the three CP-even neutral Higgs bosons have an electroweak VEV contribution, but also a singlet contribution due to the singlet admixture.

the one-loop effective potential by the respective third derivative with respect to the Higgs fields. Infrared divergencies related to the Goldstone bosons in the Landau gauge are treated analogously to the mass derivation from the effective potential, see [167] for details.
As SM reference values we take the values of [181] given as

$$\lambda_{hhh}^{\mathrm{LO,SM}} = -\frac{3m_h^2}{v} \ , \tag{8.7}$$

$$\lambda_{hhh}^{\mathrm{NLO,SM}} = -\frac{3m_h^2}{v}\left[1 - \frac{m_t^4}{\pi^2 m_h^2 v^2}\right] + \mathcal{O}\left(\frac{m_t^2}{v^2}, \frac{p_i^2 m_t^2}{m_h^2 v^2}\right) \ , \tag{8.8}$$

where the dominant top-loop contributions are taken into account with the top quark mass m_t. In Fig. 8.3 the NLO trilinear coupling between three SM-like Higgs bosons is shown as a function of the leading-order (LO) self-coupling, both are normalized to the respective SM reference value. The color code is the same as above. The strongest SFOEWPTs are obtained for the largest NLO/LO Higgs self-coupling, however the maximum values of the trilinear Higgs self-coupling remain significantly below the allowed values by the experiments. This can be explained by an interplay between the corresponding Higgs masses and quartic couplings. Besides the dominant top-loop corrections, also loop-corrections due to internal Higgs-loops are present in the extended Higgs-sector models as the N2HDM [88, 181]. The Higgs boson masses of the N2HDM can be cast in the following schematic form

$$m_\Phi^2 = M^2 + f_v(\lambda_i)v^2 + f_m(\lambda_i)vv_s + f_s(\lambda_i)v_s^2 + \mathcal{O}\left({}^{v^4}/_{M^2}, {}^{v_s^4}/_{M^2}\right) \ , \tag{8.9}$$

with M^2 being a mass scale independent of the VEV as well as quartic couplings and the functions f_i $(i = v, m, s)$ are linear combinations of the quartic couplings of the Higgs potential in Eq. (3.52). Fig. 8.3 shows that, the strongest EWPTs are obtained for the largest Higgs self-couplings, which are also a function of the quartic couplings. Hence, large quartic couplings are needed for SFOEWPTs. On the other hand, we observe that a sufficiently strong EWPT requires intermediate Higgs masses, thus limiting the maximum values for the quartic coupling due to Eq. (8.9). Henceforth, the strongest EWPTs are observed for the largest trilinear coupling, but the maximum enhancement of the trilinear Higgs self-coupling remains below the values compatible with the applied constraints.

8.2. `Type II` N2HDM

In this section, the results for the `Type II` N2HDM are shown. Beside the different couplings structure in the Yukawa sector as discussed in Sec. 3.1.1 both types do not show significant differences. The most impactful difference is induced by the flavor constraints $B \to X + \gamma$. This constraint requires the charged Higgs mass to be at least $\sim 580\,\mathrm{GeV}$. In combination with the S, T, U oblique parameter constraints, especially the T parameter, this forces the overall Higgs mass spectrum to be heavier. We start the discussion with the overall Higgs mass spectrum, followed by the trilinear one-loop coupling.

8.2.1. Mass Spectrum of the N2HDM `Type II`

In Fig. 8.4 the singlet admixture of the two non-SM like Higgs bosons is shown as a function of the respective mass. The gray points indicate the full parameter sample fulfilling all applied constraints, whereas the brown points additionally provide an NLO stable vacuum. The color code indicates the strength of the EWPT, thus all parameter points providing an SFOEWPT. The strength of the EWPT is weaker compared to the `Type II`. Furthermore, the normal and semi-inverted mass hierarchy is possible in the N2HDM in both scenarios with and without an SFOEWPT. However, the complete inverted mass hierarchy is already excluded by the

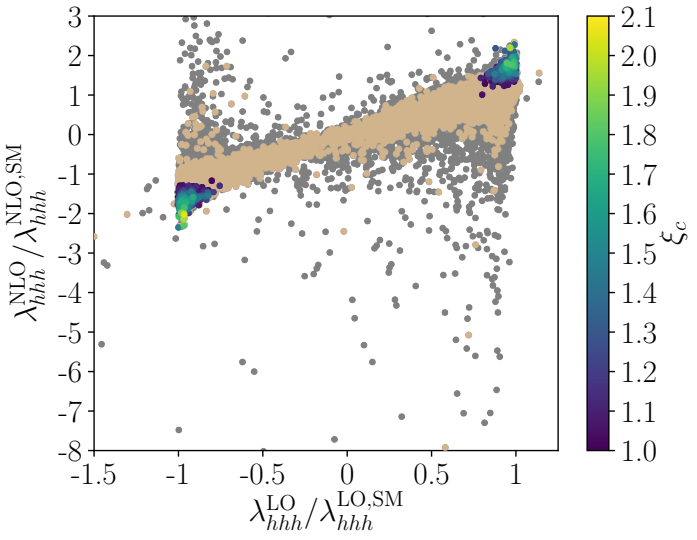

Figure 8.3.: N2HDM Type I: The NLO trilinear Higgs self-coupling between three SM-like Higgs bosons normalized to the SM reference value is shown as a function of the LO trilinear self-coupling between three SM-like Higgs bosons again normalized to the SM reference. The gray parameter points are all points fulfilling theoretical and experimental constraints, while the brown points additionally provide an NLO stable vacuum. The color code indicates the strength of the phase transition ξ_c and thus parameter points providing an SFOEWPT. *The figure is taken from [4].*

experimental constraints, as seen in Fig. 8.4 (right). The requirement of a heavy charged Higgs mass of at least 580 GeV in combination with the oblique parameters pushes the overall CP-even neutral Higgs bosons around or above 500 GeV. Note that the T parameter puts strict constraints on the upper bound on the mass difference between the charged Higgs boson and the neutral one, whereas the S parameter tighten the possible mass gaps between the mixing scalars. The semi-inverted mass hierarchy is also only possible for singlet-like $H_\downarrow$ as seen in left plot in Fig. 8.4. For all other points non-singlet-like Higgs bosons $H_\downarrow$ are of the order $\mathcal{O}(500\,\mathrm{GeV})$ or above. The requirement of an SFOEWPT yields the same results as observed in the `Type I` N2HDM. The overall Higgs mass spectrum is pushed significantly below its compatible upper mass ranges. Only singlet-like non-SM like Higgs bosons can be either light or heavy.
In Fig. 8.5 on the left hand side, the charged Higgs mass is shown as a function of $\tan\beta$ with the same color code as above. On the right hand side, the mass gap between the charged and pseudoscalar Higgs bosons is shown as a function of the mass gap between the two non-SM like CP-even neutral Higgs bosons. As in the `Type I` N2HDM the sharp cut-off in the $m_{H^\pm} - \tan\beta$ plane is induced by the flavor constraints $B \to X_s + \gamma$, where in `Type II` the depence on the minimal $\tan\beta$ does not depend on the corresponding charged Higgs mass. By demanding an SFOEWPT, again the charged Higgs mass is pushed significantly to lower masses and additionally also large $\tan\beta$ are unfavored by the SFOEWPT. An additional difference compared to `Type I` is that there is no parameter space providing an SFOEWPT with a large mass gap between A and H^+, which can be simply explained by the already large charged Higgs mass. Since the mass spectrum is overall heavier compared to `Type I`, also the strength of the EWPT is weaker, as discussed in Sec. 8.2.

To conclude the discussion of the N2HDM `Type II`, we show the normalized NLO and LO trilinear Higgs self-couplings between three SM-like Higgs bosons in Fig. 8.6. Again the dominant top-loop contributions are taken into account for the NLO SM reference value as defined in Eq. (8.8). The color code is the same as above. While all factors between ± 2 for

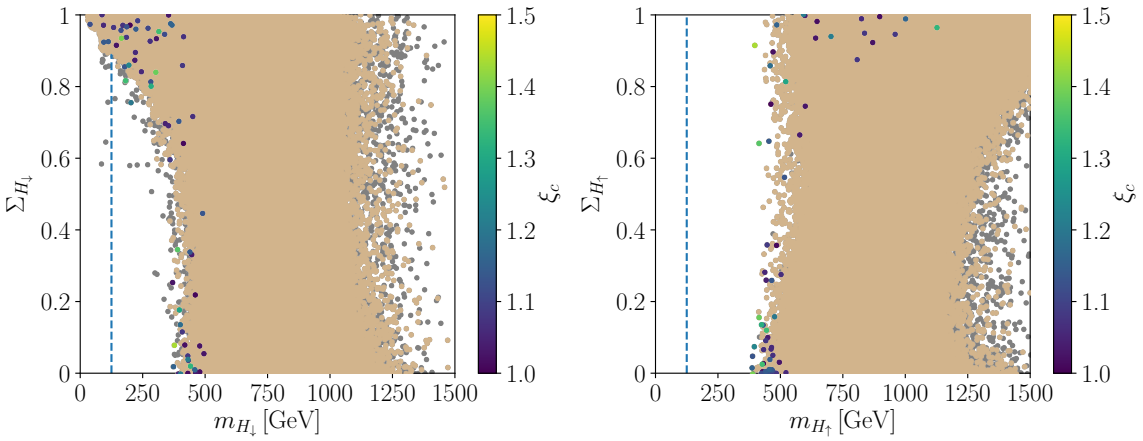

Figure 8.4.: N2HDM Type II: The singlet-admixture is shown as a function of the non-SM like Higgs mass $m_{H_\downarrow}$ ($m_{H_\uparrow}$) on the left (right) side. The gray parameter points are all points fulfilling theoretical and experimental constraints, while the brown points additionally provide an NLO stable vacuum. The color code indicates the strength of the phase transition ξ_c and thus parameter points providing an SFOEWPT. *The figures are taken from [4].*

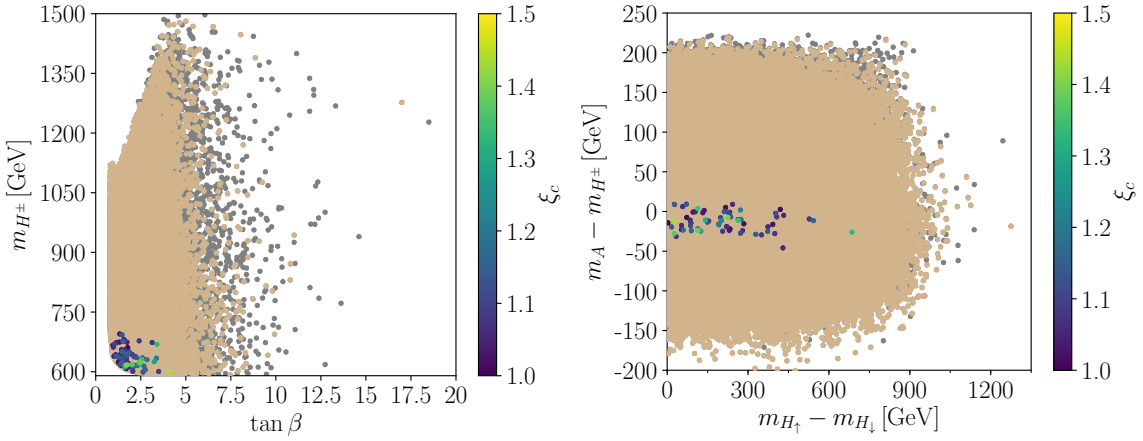

Figure 8.5.: N2HDM Type II: Left: The charged Higgs mass is shown as a function of the mixing angle $\tan\beta$; Right: The mass gap between the charged and pseudoscalar Higgs boson as a function of the mass gap between the two non-SM like CP-even neutral Higgs bosons. In both plots, the gray parameter points are all points fulfilling theoretical and experimental constraints, while the brown points additionally provide an NLO stable vacuum. The color code indicates the strength of the phase transition ξ_c and thus parameter points providing an SFOEWPT. The blue dashed line indicates the SM-like Higgs boson mass $m_h = 125\,\text{GeV}$. *The figures are taken from [4].*

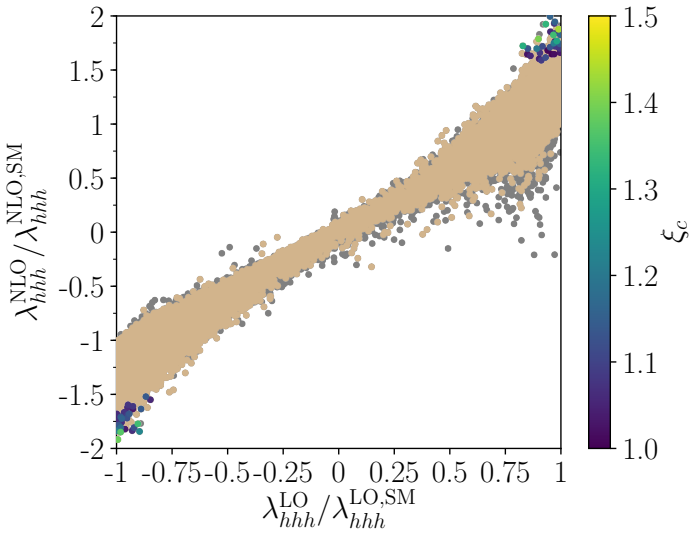

Figure 8.6.: N2HDM Type II: The NLO trilinear Higgs self-coupling between three SM-like Higgs bosons normalized to the SM reference value is shown as a function of the LO trilinear self-coupling between three SM-like Higgs bosons again normalized to the SM reference. The gray parameter points are all points fulfilling theoretical and experimental constraints, while the brown points additionally provide an NLO stable vacuum. The color code indicates the strength of the phase transition ξ_c and thus parameter points providing an SFOEWPT. *The figure is taken from [4].*

the NLO self-coupling and ± 1 for the LO one, respectively are compatible with the applied constraints, the parameter points providing an SFOEWPT lie on the maximum values. The behavior is analogous to the `Type I` N2HDM.

8.3. Conclusion

The N2HDM studied in this chapter provides a rich phenomenology due to the additional Higgs doublet and the singlet added to the Higgs sector. The applied theoretical and experimental constraints put strict limits on the viable model parameter space, however there is still a large amount of freedom involved. For instance, the CP-even neutral Higgs mass spectrum can vary from $\sim 30\,\mathrm{GeV}$ up to $\sim 1.5\,\mathrm{TeV}$. Where we again emphasize, that the chosen upper limit of our parameter scan is chosen to be $1.5\,\mathrm{TeV}$. By requiring an SFOEWPT as additional model requirement and in turn linking cosmological theoretical constraints with the LHC phenomenology, it is possible to reduce the possible parameter space significantly. We observed that with the required SFOEWPT the overall Higgs mass spectrum involving the neutral CP and CP-odd Higgs bosons $h, H_\downarrow, H_\uparrow$ and A and the charged Higgs boson H^+ is pushed to intermediate mass ranges of the order $\mathcal{O}\,(200 - 500\ \mathrm{GeV})$ remaining significantly below the compatible lower and upper bounds. Only singlet-like Higgs bosons with a singlet admixture above $\sim 80\%$ might have larger masses. In both types of the N2HDM the parameter points providing an SFOEWPT are on the edge on the valid $m_{H^\pm} - \tan\beta$ plane, so that future updates on the flavor constraints might have an important impact on the valid benchmark points with an SFOEWPT.
Furthermore, the trilinear one-loop self-couplings between three SM-like Higgs bosons are enhanced compared to the SM reference given by the interval

$$\texttt{Type I:} \quad \lambda_{hhh}^{\mathrm{NLO,N2HDM}}/\lambda_{hhh}^{\mathrm{NLO,SM}}\big|_{\xi_c>1} \in [-2.4, -1.2] \cup [1.0, 2.4] \tag{8.10a}$$

$$\texttt{Type I:} \quad \lambda_{hhh}^{\mathrm{NLO,N2HDM}}/\lambda_{hhh}^{\mathrm{NLO,SM}}\big|_{\xi_c>1} \in [-1.9, -1.5] \cup [1.6, 2.0] \tag{8.10b}$$

as long as an SFOEWPT is required. These kind of enhanced trilinear coupling might be in reach for future LHC searches.

Part IV.

Electroweak Baryogenesis

CHAPTER 9

Theoretical Foundations

In the following, we discuss the important theoretical foundations for electroweak baryogenesis (EWBG). For a detailed introduction and further discussions of other approaches we refer to the excellent reviews [30, 31, 33, 34, 182–184]. We start with the discussion of one of the Sakharov conditions: B-violating processes. This condition is already fulfilled in the Standard Model (SM) and allows us to produce a baryon asymmetry through a topological transition between different vacuum states of an $SU(2)$ gauge theory. Followed by a rough sketch of the actual calculation of the baryon asymmetry of the universe (BAU), we end our theoretical introduction with the presentation of the two used approaches to determine the quantum transport equations and the needed transport parameters.
One of the outstanding open problems in modern physics is to explain the BAU. As already mentioned in Sec. 2.3 the BAU can be measured in terms of the baryon-to-photon ratio by the CMB measurement and is given by

$$\eta \equiv \frac{n_B}{n_\gamma} = (6.2 \pm 0.4) \cdot 10^{-10} \ . \tag{9.1}$$

The ratio of the baryon asymmetry $n_B = n_b - n_{\bar{b}}$ and the photon number density n_γ is a crucial parameter for the prediction of the CMB, hence through its measurement, it is possible to deduce a strict limit on this quantity. Note that during the expansion of the universe the photon density is not a conserved quantity. It is more convenient to use the entropy density, s, of the universe to calculate the actual BAU. However, both quantities can be related to each other, which we will discuss shortly in order to compare the experimentally measured value in Eq. (9.1) and the calculated quantity n_B/s.
In the radiation dominated early universe the particle number density of the photons is a function of the temperature of the photons [26]

$$n_\gamma = \frac{2\zeta(3)}{\pi^2} T^3 \ , \tag{9.2}$$

with the numerical prefactor of $2\zeta(3)/\pi^2 \approx 0.2436$. Whereby, the entropy density of the universe at high temperatures is given as [26]

$$s = \left(\sum_B g_B + \frac{7}{8} \sum_F g_F \right) \frac{4}{3} \frac{\pi^2}{30} T^3 \ , \tag{9.3}$$

where the sum runs over all bosonic (B) and fermionic (F) degrees of freedom g_x $(x = F, B)$ with the respective masses $m_i \ll T$. Note that all other particles with $m \gtrsim T$ are effectively decoupled from the thermal system. The entropy density indeed obeys $d(sR^3)/dt = 0$ with R being the radius of the expanding universe, hence it is conserved in a co-moving frame.
Quantitatively, a particle i is in equilibrium with the thermal system if the respective rate Γ_i describing an interaction of the particle i with the plasma is larger than the expansion rate of the universe which is given by the Hubble rate H,

$$\Gamma_i > H \ . \tag{9.4}$$

The interaction rate of a specific process can be estimated by

$$\Gamma_i \sim n_i \langle v\sigma \rangle \ , \tag{9.5}$$

where n_i indicates the particle number density, v the velocity of the particle and σ the respective cross-section of the process. The $\langle \dots \rangle$ corresponds to the thermal average. With the minimal condition for thermal equilibrium in Eq. (9.4) and Eq. (9.5) it is possible to determine the temperature at which the particle specie decouples from the thermal system of the universe. The universe becomes transparent for this specific specie at this point. After the decoupling of the neutrinos at the freeze-out temperature, the photons are the only remaining particles in thermal equilibrium. If the temperature further falls below the electron mass $(T \lesssim m_e)$, the annihilation of electron-positron pairs heat the photon background relative to the neutrinos. It is possible to determine the relative temperature between photons and neutrinos to be [26]

$$T_\nu = \left(\frac{4}{11}\right)^{1/3} T_\gamma \approx 1.9\,\mathrm{K} \ . \tag{9.6}$$

The total entropy density including the photons and three neutrino flavors is then given by

$$s = \frac{4}{3}\frac{\pi^2}{30}\left(2 + \frac{21}{4}\left(T_\nu/T_\gamma\right)^3\right) T_\gamma^3 = 7.04\ n_\gamma \ , \tag{9.7}$$

allowing us to find a relation between the photon density and the entropy density.
The non-zero value of the BAU entails a problem: If the universe begins with the Big Bang and furthermore the CPT symmetry is not broken, we would expect a symmetric universe, where the baryon density is equal to the anti-baryon density. It might be the case that the BAU is just a *local* phenomenon: we just live in a local cluster of matter and the respective anti-matter is *somewhere else*. However, the matter domain must be of large size, roughly 10 Mpc [185, 186], since otherwise annihilation processes would be observed.
Another possibility is to produce the BAU dynamically starting with a symmetric universe. In this context Sakharov [22] proposed three required conditions a model needs to fulfill in order to be able to explain such a dynamical production of the BAU, namely C- and CP-violation, departure from thermal equilibrium and B-violating processes. The CP-violation has to be included through the beyond the Standard Model (BSM) model, since the CP-violation present in the SM through the CKM matrix is not sufficient to explain the BAU [53]. The departure from thermal equilibrium can be achieved through an strong first-order electroweak phase transition (SFOEWPT) as presented in Sec. 7.2. The requirement of B-violating processes will be discussed in the following section.

9.1. B-violating Processes (in the SM)

At the classical level, the number of each fermion species is separately conserved in all possible processes, which is related to the presence of exactly classical conserved global $U(1)$ currents.

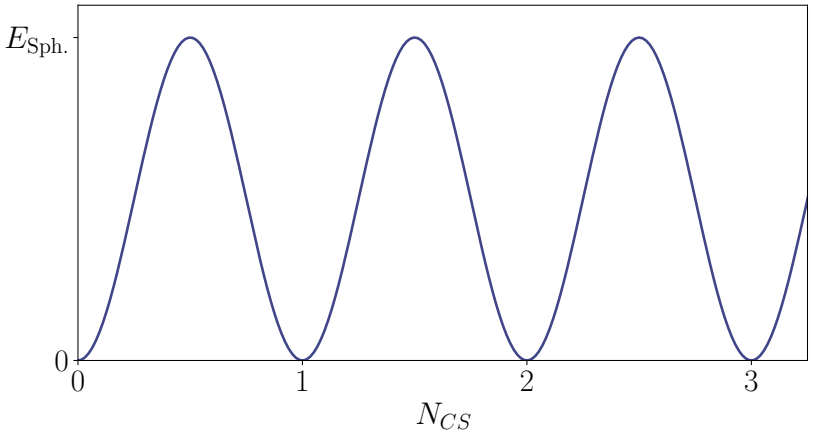

Figure 9.1.: The $SU(2)$ vacuum structure as a function of the Chern-Simons number.

For the SM particle content, there are 12 different fermion species, hence 12 conserved global currents, which can be written as

$$j_B^\mu = \frac{1}{2}\overline{Q}\gamma^\mu Q \ , \tag{9.8}$$

with the quark spinor Q and analogous for the leptons. However, any axial current of a gauge coupled Dirac fermion is anomalous [30,187] making it possible to write the divergence of the bosonic and leptonic current as

$$\partial_\mu j_B^\mu = \partial_\mu j_L^\mu = N_f \left(\frac{g^2}{32\pi^2} W_{\mu\nu}^a \tilde{W}^{a,\mu\nu} - \frac{g'^2}{32\pi^2} F_{\mu\nu}^a \tilde{F}^{a,\mu\nu} \right) \ , \tag{9.9}$$

with N_f as the family number or number of generations, g the $SU(2)$ gauge coupling and g' as the $U(1)$ gauge coupling. The field-strength tensors $W_{\mu\nu}^a$ ($F_{\mu\nu}^a$) correspond to the $SU(2)$ ($U(1)$) gauge fields. The tilde indicates the dual field strength tensor *e.g.*

$$\tilde{W}^{\mu\nu} = \frac{1}{2}\varepsilon^{\mu\nu\alpha\beta} W_{\alpha\beta} \ . \tag{9.10}$$

Note that Eq. (9.9) directly implies the conservation of $B - L$, while $B + L$ is anomalous. The crucial point is that the right-hand side of Eq. (9.9) can be written as a divergence of the non-invariant gauge currents K^μ and k^μ

$$\partial_\mu j_B^\mu = \partial_\mu j_L^\mu = N_f \left(\frac{g^2}{32\pi^2} \partial_\mu K^\mu - \frac{g'^2}{32\pi^2} \partial_\mu k^\mu \right) \ . \tag{9.11}$$

This relation allows us to relate the change of the baryon and lepton number with the vacuum structure of the gauge fields. Since the $U(1)$ as an abelian group does not contribute, it is sufficient to consider the $SU(2)$ vacuum structure. The Chern-Simons number

$$N_{\text{CS}} = \int d^3x K^0 \ , \tag{9.12}$$

corresponds to the *winding number* of the $SU(2)$ gauge field and allows us to label the infinite equivalent vacuum states for the gauge field, depicted in Fig. 9.1. Each minimum yields a valid physical vacuum state and classically these minima are degenerate. However, if it is possible to perform a transition from one vacuum to the next-closest, the Chern-Simons number changes by an integer

$$N_{\text{CS}}(t_1) - N_{\text{CS}}(t_0) = \int_{t_0}^{t_1} \int d^3x \ \partial_\mu K^\mu = n \in \mathbb{Z} \ . \tag{9.13}$$

The change of the Chern-Simons number and the bosonic/fermionic current can then be related with the help of Eq. (9.11) yielding the change of the baryon and lepton number in terms of the change in the Chern-Simon numbers in units of the family number

$$\Delta B = \Delta L = N_f \Delta N_{\mathrm{CS}} \ . \tag{9.14}$$

To summarize, nine left-handed quarks (three color states for each generation) and three left-handed leptons are generated, if it is possible to perform a transition from one $SU(2)$ vacuum state to the next-closest one.

9.1.1. Topological Transitions

In 1976, 't Hooft discovered that indeed there exists a classical non-perturbative solution to the equations of motion with a non-vanishing action, which tunnels between two adjacent vacua [188]. The field configuration is referred as an *instanton*. As it turns out, the transition rate per unit volume of instanton processes (at zero temperature) is approximately given by [188]

$$\Gamma(T=0) \sim 10^{-170} \ , \tag{9.15}$$

indicating that not even one event would have occurred within the present Hubble volume in the history of the universe. Hence, instantons are not able to explain the produced BAU. However, in the year 1985 Kuzmin, Rubakov and Shaposhnikov realized that at high temperature the possibility exists, that these transitions between two vacua become unsuppressed [189]. Instead of tunneling through the potential barrier separating two adjacent vacua, the solution at finite temperature *hops over the barrier* due to the availability of thermal energy. The resulting pseudo-particles are named *sphalerons* [190] (Greek: *"ready to fall"*) to refer to their meta-stability. The sphaleron is a non-perturbative saddle point solution of the energy functional. The determination of the thermal transition rates of the sphalerons requires the considerations of both Higgs phases. After the SFOEWPT the electroweak symmetry breaking has taken place and the universe is in its broken phase. The corresponding transition rate per unit volume is then suppressed by the (Euclidean) action[24] [189]

$$\Gamma_{\mathrm{Sph}}(T) = \kappa \left(\frac{m_W}{\alpha_w T}\right)^3 m_W^4 \exp\left(-\frac{E_{Sph}(T)}{T}\right) \ , \tag{9.16}$$

with the W-boson mass m_W, the $SU(2)$ gauge coupling α_w and some dimensionless parameter κ. The sphaleron energy in the broken phase is given as

$$E_{Sph}(T) = \frac{m_W(T)}{\alpha_w} \varepsilon \ , \tag{9.17}$$

with a dimensionless parameter ε of the order $\mathcal{O}(1)$ and thermal mass of the W-gauge boson. In the symmetric phase of the universe, before the electroweak symmetry breaking, the determination of the transition rate per unit volume requires a careful treatment of high temperature effects, which is in general an involved task. A rough estimate can be obtained by the following consideration. The only important length scale in the symmetric phase[25] is given by the magnetic screening length $\xi = (\alpha_w T)^{-1}$. The magnetic screening length reflects exactly the thermal mass corrections discussed in Sec. 7.1.2. Hence, on dimensional grounds, the transition rate per unit volume of the sphaleron is expected to be

$$\Gamma_{\mathrm{Sph}} = \kappa \alpha_w^4 T^4 \ , \tag{9.18}$$

[24] Here, the Euclidean action is denoted as the sphaleron energy E_{Sph}.

[25] Note that the Higgs vacuum expectation value (VEV) is zero, hence all particles are massless.

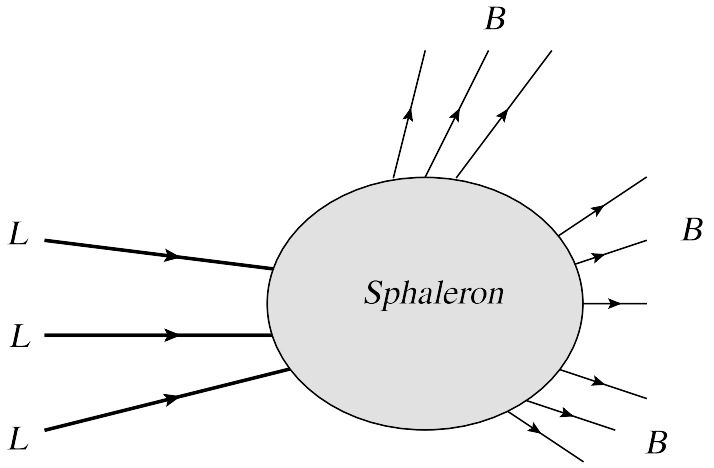

Figure 9.2.: The effective Feynman diagram for a sphaleron transition, where three left-handed leptons L and nine left-handed quarks (three baryons) are involved.

with a dimensionless factor κ of the order $\mathcal{O}(1)$. Arnold *et al.* criticized that the inclusion of hard thermal loop contributions would damp the transition further [191, 192]. The most precise calculation of the transition rate per unit volume is obtained on the lattice, where the additional hard thermal loop contributions as well as further improvements are taken into account. The lattice result is then given by [193, 194][26]

$$\Gamma_{\text{Sph}}\left(T \gg T_c\right) = \kappa' \alpha_w \left(\alpha_w T\right)^4 \ , \tag{9.19}$$

with

$$\kappa' = 29 \pm 6 \ . \tag{9.20}$$

In summary, in models with an $SU(2)$ gauge structure it is possible to generate B-violating processes at quantum level through sphaleron transitions. This process is a non-perturbative solution at finite temperatures, consequently there is no corresponding Feynman diagram. The large sphaleron transition rate in the symmetric phase yields a thermal equilibrium between three left-handed leptons and nine left-handed quarks, which can be schematically interpreted as an effective Feynman diagram, depicted in Fig. 9.2. However, the transition rate in the broken phase is exponentially suppressed, such that produced baryon asymmetries are conserved in the broken phase. As it turns out, this is a crucial point in order to produce the BAU through electroweak baryogenesis.

9.2. General Idea of the Electroweak Baryogenesis

So far we discussed the three required conditions Sakharov proposed in order to be able to explain the dynamical production of the BAU as well as the need for BSM physics to enable an SFOEWPT. In the following section we want to sketch the general idea of the actual calculation of the BAU in a non-local approach of electroweak baryogenesis. For a more detailed discussion, see *e.g.* [31].
The departure from thermal equilibrium requires that an SFOEWPT is present. The electroweak phase transition (EWPT) is taking place at the critical temperature T_c as discussed in Sec. 7.2. Both vacua are degenerate and quantum tunneling is possible. At this point, a *bubble* with the broken phase (the Higgs VEV is non-zero) inside and the symmetric phase outside starts to evolve. However, the interplay between surface tension and internal pressure

[26] For simplicity, we dropped the discussion of the leading log contributions present in the sphaleron transition rate, since this is beyond the scope of this thesis.

does not allow the bubble to nucleate. At the nucleation temperature $T_N < T_c$, the probability of a bubble to nucleate is of the same order as the Hubble expansion. Hence, the bubble can grow and does not collapse until the whole universe is filled with the broken phase[27].
At some point the growing bubble is *large* enough to be approximated as a planar wall neglecting curvature terms. By doing so the problem reduces to an effective $1+1$ dimensional problem with only one spatial coordinate z indicating the perpendicular distance to the bubble wall. The bubble wall separating the symmetric phase (positive z) from the broken phase inside the bubble (negative z), is set at the origin $z = 0$.
The actual production of the BAU can be divided in three steps. As a first step the (pseudo-) particles in the plasma scatter with the bubble wall. The CP-violation, which is required to be provided by the underlying BSM model, generates an asymmetry in the particle number densities during the interaction with the propagating bubble wall. We end up with a net non-zero excess of left-handed fermions in front of the bubble wall, biasing the electroweak sphaleron transition discussed in Sec. 9.1.1 to produce more baryons than anti-baryons in a second step.
In the final step, the net baryon charge is then swept up by the expanding wall inside the bubble. Since the electroweak sphaleron transition rate is exponentially suppressed in the broken phase, the produced BAU is conserved and a *wash out* is avoided. This step also makes clear why we have to demand an SFOEWPT. The criterion in Eq. (7.66) ensures to avoid the baryon washout. In this way all three Sakharov conditions can be fulfilled in a CP-violating model. In this work we calculate the BAU within the C2HDM, presented in Sec. 3.2.

The BAU can be calculated for small bubble wall velocity as follows

$$\frac{n_B}{s} = \frac{-3\tilde{\Gamma}_{ws}}{2v_w s} \int_0^\infty \exp\left(-\frac{\tilde{\Gamma}_{ws}\mathcal{R}}{v_w} z'\right) n_L^0(z') dz' \ , \tag{9.21}$$

where $\tilde{\Gamma}_{ws}$ is the (rescaled) sphaleron transition rate of the symmetric phase, v_w is the bubble wall velocity[28], $\mathcal{R} = 15/4$ the SM relaxation constant and $n_L^0(z)$ is the left-handed fermion number density profile in front of the bubble wall. The left-handed fermion particle number density profile $n_L^0(z)$ is obtained by solving the quantum transport equations describing the diffusion process in front of the propagating bubble wall. A detailed motivation of Eq. (9.21) is described in Appendix C.

9.3. Bubble Wall Profile

The left-handed asymmetry in front of the bubble wall is produced through a CP-violating interaction between the propagating wall and the plasma. Hence, a description of the bubble dynamics is needed, which requires the solution of the equations of motions for the scalar fields. However, this is an involved task in non-minimal extended Higgs sectors and in general not analytically solvable without approximations. In this work, we choose a rather simple approach to approximate the wall profile, which we will discuss in the following. We start the discussion with one single real scalar field.
The decay rate of a meta-stable vacuum state is given as an exponential decay law

$$\mathcal{P} \simeq A(T) \exp\left(-S_3/T\right) \ , \tag{9.22}$$

[27] The nucleation and possible collisions of the growing bubbles might also contribute to the stochastic spectrum of gravitational waves. For simplicity, we assume that only one bubble nucleates and fills the whole universe at some point.
[28] Note, that we treat the bubble wall velocity as direct input parameter in our calculation.

with some temperature dependent prefactor $A(T)$ and the three-dimensional euclidean action S_3. The corresponding equation of motion for the scalar field derived from the 3-D Euclidean action reads

$$\frac{d^2\phi}{dr^2} + \frac{2}{r}\frac{d\phi}{dr} = \frac{\partial}{\partial\phi} V_{\text{eff}}(\phi, T) \ . \tag{9.23}$$

In Eq. (9.23) it is already assumed that the field obeys a spherical symmetry, allowing us to describe the field with the radial distance r. If the *bubble* described by the scalar field is large enough, we can neglect curvature terms and drop the first derivative $\left(\frac{1}{r}\frac{\partial\phi}{\partial r} \xrightarrow{R>>L_w} 0\right)$ in Eq. (9.23). This reduces on the one hand the dimensionality of the problem from a $3+1$ to an effective $1+1$ dimensional one with the spatial coordinate z and further simplifies the equations of motion significantly to

$$\frac{d^2\phi}{dz^2} = \frac{\partial}{\partial\phi} V_{\text{eff}}(\phi, T) \ . \tag{9.24}$$

Suppose the following example for a potential reflecting the vacuum structure at the critical phase transition point

$$V_{\text{eff}}(\phi) = \frac{\lambda}{4}\left(\phi^2 \left(\phi - v_c\right)^2\right) \ , \tag{9.25}$$

with some quartic coupling λ and the critical VEV v_c. The potential in Eq. (9.25) has two degenerate global minima, one at $\langle\phi\rangle = 0$ and one at $\langle\phi\rangle = v_c$. Both minima are separated by a potential barrier with the height V_b. Solving the equation of motion in Eq. (9.23) for the potential in Eq. (9.25) yields the following *Kink* wall profile and barrier height

$$\phi(z) = \frac{v_c}{2}\left(1 - \tan\left(\frac{z}{L_w}\right)\right) \ , \qquad V_b = V_{\text{eff}}(\phi = {}^{v_c}/_2) = \frac{\lambda}{64} v_c^4 \ . \tag{9.26}$$

The wall profile $\phi(z)$ is then described with the critical VEV v_c and the *wall thickness* L_w given by

$$L_w^2 = \frac{8}{\lambda v_c^2} = \frac{v_c^2}{8 V_b} \ . \tag{9.27}$$

For simplicity, we assume for a non-minimal extended Higgs sector, that all scalar fields can be independently described by the *Kink* profile in Eq. (9.26). Hence, for the description of the field configuration as a function of the perpendicular distance to the bubble wall, we need to determine the critical field configuration at the SFOEWPT and the wall thickness L_w. In what follows, we describe the numerical approach to determine the wall thickness in a non-trivial scalar sector.

In the first step, we determine the critical temperature and the critical VEV by using the routines as implemented in `BSMPT`. The numerical minimization of the effective potential allows us to find the VEV configuration of the broken phase denoted as $\boldsymbol{\omega}_b$. The vector $\boldsymbol{\omega}$ contains all scalar degrees of freedom which have to be taken into account in the minimization. The VEV configuration of the C2HDM is given in Eq. (3.13) implying $\boldsymbol{\omega} = (\omega_1, \omega_2, \omega_{\text{CP}}, \omega_{\text{CB}})$. We parametrize the straight line connecting both vacua as

$$\boldsymbol{\omega}(t) = \boldsymbol{\omega}_s + t\mathbf{n} \ , \qquad \text{with} \qquad \mathbf{n} = \boldsymbol{\omega}_b - \boldsymbol{\omega}_s \ , \tag{9.28}$$

with $\boldsymbol{\omega}_s$ being the symmetric VEV configuration, $\mathbf{n}$ as the direction of the straight path connecting both vacua and $t \in [0, 1]$. Now we subsequently go step wise with steps $t_i = \dfrac{i}{N}$ and N as the number of steps. We perform a minimization of the effective potential in the orthogonal plane at $\boldsymbol{\omega}(t_i)$

$$\boldsymbol{\omega} \in \{\boldsymbol{\omega} \big| \ (\boldsymbol{\omega} - \boldsymbol{\omega}(t_i)) \cdot \mathbf{n} = 0\} \ . \tag{9.29}$$

The value of the minimum in the orthogonal plane at $\boldsymbol{\omega}(t_i)$ is referred to as V_i. Once all V_i are determined, the tunnel path can be approximated with a spline of the points $(t_i|V_i)$ denoted as $V_m(t)$. Note that the broken and symmetric minima are degenerate, hence $V_{\text{eff}}(\boldsymbol{\omega}_s, T_c) = V_{\text{eff}}(\boldsymbol{\omega}_\mathbf{b}, T_c)$. For the determination of the barrier height, we calculate the maximum $V_{\max}$ of $V_m(t)$ and find

$$V_b = V_{\max} - V(\boldsymbol{\omega}_\mathbf{b}, T_c) \ . \tag{9.30}$$

Eq. (9.27) allows us then to evaluate the wall thickness and thus the parametrization of the wall profile in Eq. (9.26).
Some final remarks concerning the wall profile: Both approaches to derive the quantum transport equations are based on the fact, that the particles in front of the bubble wall acquire a space-dependent mass and a respective space-dependent complex phase

$$\hat{m}_i(z) = m_i(z)\, \mathrm{e}^{i\theta(z)} \ , \tag{9.31}$$

with the absolute value m_i and the phase factor $\theta(z)$. The absolute mass at a given z is calculated by determining numerically the eigenvalues of the mass matrix, where the Higgs fields are parametrized as in Eq. (9.26). The evolution of the phase factor is obtained as follows. First, we determine the phase of the broken minimum by calculating the argument of the complex mass obtained by the mass matrix, referred to as θ_{brk}. The determination of the symmetric phase θ_{sym} is a bit more involved. In a completely symmetric VEV configuration, the phase is arbitrary, however we want to achieve a smooth function for $\theta(z)$ along the tunnelpath. For that reason, we determine the complex phase of the mass matrix *shortly* before the symmetric phase by searching the global minimum in the orthogonal VEV plane in

$$\mathbf{p}_\varepsilon = \omega_s + \varepsilon \mathbf{n} \ , \tag{9.32}$$

with some small number $\varepsilon = 10^{-2}$. Since we use a bisection method to obtain the critical temperature and set the critical temperature to be the lower bound of the bisection interval, we are slightly below the *true* critical temperature, where both minima are exactly degenerate. To compensate this, we furthermore extract the symmetric phase at the temperature $T = T_c + \delta T$ to ensure that the global minimization finds the symmetric minimum. The default value for this temperature shift is chosen to be $\delta T = 1\,\text{GeV}$ in `BSMPT v2`. It was explicitly checked that both numerical parameters ε and δT do not show any significant impact on the overall predicted BAU.
Finally, the phase factor is then parametrized as [35]

$$\theta(z) = \left(\theta_{\text{brk}} - \frac{\theta_{\text{brk}} - \theta_{\text{sym}}}{2}\left(1 + \tanh\frac{z}{L_w}\right)\right) \ . \tag{9.33}$$

9.4. Quantum Transport Equations

In the following, we present the two approaches used in this thesis to formulate the quantum transport equations. These systems of equations are required to describe the thermal system of the early universe and to determine the profile of the left-handed chemical potential in front of the bubble wall, needed in the Eq. (9.21). It is an ongoing discussion in the literature how to extract the corresponding source terms, which enables the generation of the asymmetries in the first place. A first systematical comparison of both approaches was done in [195]. They parametrized the CP-violation in a generic way by including a space-dependent phase factor $\theta(z)$ in the top quark mass

$$\mathcal{L}_{\text{Yuk}} \supset m_t(z)\left(\bar{t}_L\, \mathrm{e}^{i\theta(z)}\, t_R + \bar{t}_R\, \mathrm{e}^{-i\theta(z)}\, t_L\right) \ . \tag{9.34}$$

Such structures also occur in the C2HDM, since the corresponding Yukawa terms in the Lagrangian include the coupling of the Higgs doublets and the left- and right-handed top quark spinors. The complex nature of λ_5 and m_{12}^2 in Eq. (3.11) introduces a complex phase $\theta(z)$ analogous to Eq. (9.34). The space-dependence of the mass terms is due to the space-dependent Higgs background, parametrized as in Eq. (9.26).
We investigate two approaches taking the full model-dependence into account. We start the discussion of the approach based on the *top transport* referred as `FH` ansatz and afterwards we introduce the concepts of the VEV insertion approximation (VIA). We conclude the theoretical introduction with the discussion of the thermal interactions present in the plasma of the early universe.

9.4.1. Top Transport Equations

The introduction of the quantum transport equations based on the top transport closely follows [195] based on the work of Fromme and Huber in [35] which has been applied to the 2HDM in [36]. However, we emphasize that the derivation of the quantum transport equations is also possible from first principles by considering the Kadanoff-Baym equations as presented in [37–39]. A good overview of both derivations can be found in [196].
In principle, the thermodynamical system of the early universe is in a non-equilibrium state. However, for small wall velocities[29] we can treat the system to be *near equilibrium* and consider a small perturbation around the equilibrium. As follows, we consider a single top quark interacting with the thermal system and the bubble wall. The thermodynamical evolution of the particle distribution function f is given by the Boltzmann equation

$$\left(v_g \partial_z + F \partial_{p_z}\right) f = \mathcal{C}\left[f\right] \ , \tag{9.35}$$

with the group velocity v_g, the force F acting on the respective particle and the collision integral $\mathcal{C}\left[f\right]$. Note, that the equation is formulated in the rest-frame of the bubble wall, hence there is only one spatial coordinate z and the respective momentum p_z. The complex top quark mass is parametrized as

$$\hat{m}(z) = m(z)\, \mathrm{e}^{i\gamma_5 \theta(z)} \ , \tag{9.36}$$

with the Dirac gamma matrix γ_5 and the absolute space-dependent mass value $m(z)$ and phase factor $\theta(z)$. Note, that this parametrization is equivalent to Eq. (9.34) and hence induces CP-violation in top quark interactions.
Expanding the Dirac equation with the complex mass in Eq. (9.36) with a WKB ansatz for the spinor in terms of the gradient, allows us to find the group velocity and the semi-classical force acting on the top quark [35, 195, 199]

$$v_g = \frac{p_z}{E} + s_h s_{k_0} \frac{m^2 \theta'}{2E^2 E_z} \ , \tag{9.37}$$

$$F = -\frac{\left(m^2\right)'}{2E} + s_h s_{k_0} \left(\frac{\left(m^2 \theta'\right)'}{2E E_z} - \frac{m^2 \left(m^2\right)' \theta'}{4E^3 E_z} \right) \ . \tag{9.38}$$

The energy of the Dirac fermion is given by $E \equiv \sqrt{\mathbf{p}^{\,2} + m^2}$ and $E_z \equiv \sqrt{p_z^2 + m^2}$. The mass m and phase factor θ are defined in Eq. (9.36) and $(\ldots)'$ denotes the derivative with respect to the perpendicular distance to the bubble wall z. The helicity factor is given by

[29] The typical bubble wall velocities are assumed to be of the order $\mathcal{O}\left(10^{-1}\right)$ for the SM(see *e.g.* [197, 198]). This might be not the case for an arbitrary extended Higgs sector model. Since we treat the bubble wall speed as direct input parameter, we emphasize that the following approaches are only valid for small wall velocities.

$s_h = h\ \mathrm{sgn}\,(p_z)$, where $h = \pm 1$ corresponds to the helicity of the particle. The sign s_{k_0} is $+1$ for particles and -1 for anti-particles, respectively. Thus, the second term in Eq. (9.38) is acting differently on particles and anti-particles. Hence the second term is CP-odd. The first term is CP-even and corresponds to the classical force term present for a varying mass.
The particle number density is assumed to be near equilibrium, which allows us to parametrize the distribution function as follows

$$f = \frac{1}{\mathrm{e}^{\beta[\gamma_w(E_w + v_w p_z) - \mu]}} + \delta f \ , \tag{9.39}$$

with β as the inverse temperature, γ_w the Lorentz boost factor $\gamma_w = 1/\sqrt{1-v_w^2}$ and the conserved wall frame energy

$$E_w \simeq E - s_h s_{k_0} \frac{m^2 \theta'}{2 E E_z} \equiv E + s_h s_{k_0} \Delta E \ . \tag{9.40}$$

Here μ stands for the pseudo-chemical potential defining the particle asymmetry and δf describes kinematical perturbations in the distribution function. To ensure that δf does not affect the local particle density, the following normalization is chosen

$$\int d^3 p \delta f = 0 \ . \tag{9.41}$$

The CP-even part of Eq. (9.38) is of first order in gradient, while the CP-odd (second term) is of second order in the gradient expansion. This means that there exists a hierarchy between both parts, hence the CP-even and CP-odd equations can be solved separately. Starting with the expansion of the (pseudo) chemical potential and kinematical perturbation in a CP-even/odd part[30]

$$\mu \equiv \mu_e + s_{k_0} \mu_o \tag{9.42}$$
$$\delta f \equiv \delta f_e + s_{k_0} \delta f_o \tag{9.43}$$

allows us to expand the distribution function as

$$f \approx f_{0w} + \Delta f_e + s_{k_0} \Delta f_o \ , \tag{9.44}$$

with the definitions

$$f_{0w} = \frac{1}{\mathrm{e}^{\beta[\gamma_w(E_w + v_w p_z)]} \pm 1} \ , \tag{9.45a}$$
$$\Delta f_e = -\mu_e f'_{0w} + \delta f_e \ , \tag{9.45b}$$
$$\Delta f_o = (-\mu_o + s_h \gamma_w \Delta E)\, f'_{0w} - s_h \gamma_w \Delta E f''_{0w} \mu_e + \delta f_o \ . \tag{9.45c}$$

The CP-even equation then reads

$$L\,[\mu_e, \delta f_e] = \mathcal{S}_e + \delta \mathcal{C}_e \ , \tag{9.46}$$

with the Liouville operator

$$L\,[\mu, \delta f] \equiv -\frac{p_z}{E} f'_{0w} \partial_z \mu + v_w \gamma_w \frac{\left(m^2\right)'}{2E} f''_{0w} \mu + \frac{p_z}{E} \partial_z \delta f - \frac{\left(m^2\right)'}{2E} \partial_{p_z} \delta f \ , \tag{9.47}$$

and the respective CP-even source term

$$\mathcal{S}_e = v_w \gamma_w \frac{\left(m^2\right)'}{2E} f'_{0w} \ . \tag{9.48}$$

[30] In [35] the chemical potential and kinematical perturbation of a particle specie i are expanded as $\mu_i = \mu_{i,1e} + \mu_{i,2o} + \mu_{i,2e}$ and $\delta f_i = \delta f_{i,1e} + \delta f_{i,2o} + \delta f_{i,2e}$. The index $1, 2$ indicates the order of the gradient expansion.

The collision integral $\delta\mathcal{C}_e$ incorporates all interactions present in the plasma. The inclusion or rather the impact on the interactions depends on the relevant time-scale of the respective process. For instance, if a process $A \rightleftharpoons B$ has a large interaction rate $\Gamma_{A\rightleftharpoons B}$, *i.e.* the process happens *fast* on a small time-scale $t_{A\rightleftharpoons B} = (\Gamma_{A\rightleftharpoons B})^{-1}$, the participating particles A, B are in equilibrium and the respective chemical potentials μ_A, μ_B can be related to each other. However, a slow process can be decoupled in the description of the thermal system, since the process is not taking place on the relevant time-scale. In this way, the question which process has to be taken into account in the collision integral requires a careful analysis of the relevant time-scale for the corresponding processes, which is a model dependent decision. Since the same question arises in the second approach to determine the quantum transport equations, we postpone the discussion of the relevant interactions to Sec. 9.5.
Analogous to Eq. (9.46) the CP-odd equation can be formulated with the following source term

$$\mathcal{S}_o = - v_w\gamma_w s_p \frac{\left(m^2\theta'\right)'}{2EE_z} f'_{0w} + v_w\gamma_w s_p \frac{m^2\left(m^2\right)'\theta'}{4E^2E_z}\left(\frac{f'_{0w}}{E} - \gamma_w f''_{0w}\right) , \tag{9.49}$$

with $s_p = \mathrm{sgn}\,(p_z)$.
The goal is to find a closed set of equations for the (pseudo) chemical potentials. The two lowest moments of the CP-even and CP-odd equations are considered. In doing so, we integrate over the momentum, weighting the equations with $(p_z/E)^l$ and normalize it to

$$N_1 \equiv \int d^3p f'_{0w,FD} = \gamma_w \int d^3p f'_{0,FD} \equiv \gamma \hat{N}_1 = -\gamma_w \frac{2\pi^3}{3} T^2 . \tag{9.50}$$

The distribution function $f_{0w,FD}$ corresponds to the distribution function of a massless fermion in the fluid frame. The average over the phase space is of the form

$$\langle X \rangle \equiv \frac{1}{N_1}\int d^3p X . \tag{9.51}$$

The l-th moment of the velocity perturbations is defined through the kinematical perturbation

$$u_l \equiv \left\langle \left(\frac{p_z}{E}\right)^l \delta f \right\rangle , \tag{9.52}$$

and similar the l-th moment of the evolution equation as

$$\left\langle \left(\frac{p_z}{E}\right)^l L \right\rangle = \left\langle \left(\frac{p_z}{E}\right)^l (\mathcal{S} + \delta\mathcal{C}) \right\rangle . \tag{9.53}$$

The results for the zero and first moment of the Liouville operator are then given by

$$\langle L \rangle = -D_1\mu' + u'_1 + v_w\gamma_w \left(m^2\right)' Q_1\mu , \tag{9.54a}$$

$$\left\langle \frac{p_z}{E} L \right\rangle = -D_2\mu' - v_w u'_1 + v_w\gamma_w \left(m^2\right)' Q_2\mu + \left(m^2\right)' \left\langle \frac{1}{2E^2}\delta f \right\rangle , \tag{9.54b}$$

where $(\ldots)'$ corresponds to the derivative with respect of the spatial coordinate z. The thermal transport coefficients are given as

$$D_l \equiv \left\langle \left(\frac{p_z}{E}\right)^l f'_{0w} \right\rangle , \tag{9.55a}$$

$$Q_l \equiv \left\langle \left(\frac{p_z^{l-1}}{2E^l}\right) f''_{0w} \right\rangle , \tag{9.55b}$$

where $(\dots)'$ indicates the derivative $\partial_{(\gamma_w E)}$. So far the full dependence of the bubble wall velocity is kept in Eq. (9.55). In [35, 36] an additional expansion for small wall velocities is performed, such that the thermal coefficients in Eq. (9.55) become [35]

$$K_{1,i} = -\left\langle \frac{p_z^2}{E_0}\partial_E^2 f_{i,0} \right\rangle , \tag{9.56a}$$

$$K_{2,i} = \left\langle \frac{\partial_E^2 f_{i,0}}{2E_0} \right\rangle , \tag{9.56b}$$

$$K_{4,i} = \left\langle \frac{p_z^2}{E_0^2}\partial_E f_{i,0} \right\rangle , \tag{9.56c}$$

$$\tilde{K}_{5,i} = \left[\frac{p_z^2}{E_0}\partial_E f_{i,0} \right] , \tag{9.56d}$$

$$\tilde{K}_{6,i} = \left[\frac{E_0^2 - p_z^2}{2E_0^3}\partial_E f_{i,0} \right] , \tag{9.56e}$$

$$K_{8,i} = \left\langle \frac{|p_z|\partial_E f_{i,0}}{2E_0^2 E_{0z}} \right\rangle , \tag{9.56f}$$

$$K_{9,i} = \left\langle \frac{|p_z|}{4E_0^3 E_{0z}} \left(\frac{\partial_E f_{i,0}}{E_0} - \partial_E^2 f_{i,0} \right) \right\rangle . \tag{9.56g}$$

In the above equations we wrote the explicit partial derivatives with respect to the energy, since the corresponding Lorentz boost factor γ_w is expanded to be 1. The thermal averages are defined in accordance with [35]

$$\langle X \rangle = \frac{\int d^3p X(p)}{\int d^3p \partial_E f_{0+}(m=0)} , \tag{9.57}$$

$$[X] = \frac{\int d^3p X(p)}{\int d^3p f_{i,0}|_{v_w=0}} , \tag{9.58}$$

with the corresponding distributions functions of particle i

$$f_{i,0} = f_i|_{\mu_i=0,\delta f_i=0,v_w=0} , \tag{9.59}$$

$$f_{0+} = f_i|_{i=\text{Fermion},\mu_i=0,\delta f_i=0,v_w=0} . \tag{9.60}$$

Furthermore, we introduced an index i indicating the respective particle. The momentum integrals in Eq. (9.56) require a numerical integration. These numerical integrations are in general time consuming. Hence, we created a bi-cubic spline over the equidistant plane $\left(m^2, T\right)$ over the interval $m^2 \in \left[0, (200)^2\right] \text{GeV}^2$ and $T \in [10, 250]\,\text{GeV}$. This bi-cubic spline allows for a fast evaluation of the respective thermal transport coefficients in `BSMPT` [5, 168]. The interaction of fermions with the bubble wall scales with their respective masses. Thus, the dominant contributions are obtained from the heaviest particles. In this way, the top quark is expected to dominate the production mechanism. The thermodynamical system is then described by the chemical potential of the left-handed top quark $\mu_{t,2}$, its right-handed counterpart μ_{t^c} described as the charged conjugated field and the left-handed bottom quark chemical potential $\mu_{b,2}$. Further, a chemical potential for the Higgs boson fields is introduced through $\mu_{h,2}$. Note, that we follow the notation of [35, 36], where the index 2 in $\mu_{i,2}$ indicates the order of the gradient expansion and further corresponds to the net-chemical potential, meaning the difference between the particle and anti-particle chemical potential. The corresponding transport equations are then given by [36]

$$\begin{aligned} 0 = {} & 3v_w K_{1,t}\left(\partial_z \mu_{t,2}\right) + 3v_w K_{2,t}\left(\partial_z m_t^2\right)\mu_{t,2} + 3\left(\partial_z u_{t,2}\right) \\ & - 3\Gamma_y\left(\mu_{t,2} + \mu_{t^c,2} + \mu_{h,2}\right) - 6\Gamma_m\left(\mu_{t,2} + \mu_{t^c,2}\right) - 3\Gamma_W\left(\mu_{t,2} - \mu_{b,2}\right) \end{aligned}$$

$$
\begin{aligned}
&- 3\Gamma_{ss}\left[(1+9K_{1,t})\,\mu_{t,2} + (1+9K_{1,b})\,\mu_{b,2} + (1-9K_{1,t})\,\mu_{t^c,2}\right]\,, && \text{(9.61a)}\\
0 = {}& 3v_w K_{1,b}\left(\partial_z \mu_{b,2}\right) + 3\left(\partial_z u_{b,2}\right) - 3\Gamma_y\left(\mu_{b,2} + \mu_{t^c,2} + \mu_{h,2}\right) - 3\Gamma_W\left(\mu_{b,2} - \mu_{t,2}\right)\\
&- 3\Gamma_{ss}\left[(1+9K_{1,t})\,\mu_{t,2} + (1+9K_{1,b})\mu_{b,2} + (1-9K_{1,t})\mu_{t^c,2}\right]\,, && \text{(9.61b)}\\
0 = {}& 3v_w K_{1,t}\left(\partial_z \mu_{t^c,2}\right) + 3v_w K_{2,t}\left(\partial_z m_t^2\right)\mu_{t^c,2} + 3\left(\partial_z u_{t^c,2}\right)\\
&- 3\Gamma_y\left(\mu_{t,2} + \mu_{b,2} + 2\mu_{t^c,2} + 2\mu_{h,2}\right) - 6\Gamma_m\left(\mu_{t,2} + \mu_{t^c,2}\right)\\
&- 3\Gamma_{ss}\left[(1+9K_{1,t})\,\mu_{t,2} + (1+9K_{1,b})\,\mu_{b,2} + (1-9K_{1,t})\,\mu_{t^c,2}\right]\,, && \text{(9.61c)}\\
0 = {}& 4v_w K_{1,h}\left(\partial_z \mu_{h,2}\right) + 4\left(\partial_z u_{h,2}\right) - 3\Gamma_y\left(\mu_{t,2} + \mu_{b,2} + 2\mu_{t^c,2} + 2\mu_{h,2}\right) - 4\Gamma_h \mu_{h,2}\,, && \text{(9.61d)}\\
S_t = {}& - 3K_{4,t}\left(\partial_z \mu_{t,2}\right) + 3v_w \tilde{K}_{5,t}\left(\partial_z u_{t,2}\right) + 3v_w \tilde{K}_{6,t}\left(\partial_z m_t^2\right) u_{t,2} + 3\Gamma_t^{\text{tot}} u_{t,2}\,, && \text{(9.61e)}\\
0 = {}& - 3K_{4,b}\left(\partial_z \mu_{b,2}\right) + 3v_w \tilde{K}_{5,b}\left(\partial_z u_{b,2}\right) + 3\Gamma_b^{\text{tot}} u_{b,2}\,, && \text{(9.61f)}\\
S_t = {}& - 3K_{4,t}\left(\partial_z \mu_{t^c,2}\right) + 3v_w \tilde{K}_{5,t}\left(\partial u_{t^c,2}\right) + 3v_w \tilde{K}_{6,t}\left(\partial_z m_t^2\right) u_{t^c,2} + 3\Gamma_t^{\text{tot}} u_{t^c,2}\,, && \text{(9.61g)}\\
0 = {}& - 4K_{4,h}\left(\partial_z \mu_{h,2}\right) + 4v_w \tilde{K}_{5,h}\left(\partial_z u_{h,2}\right) + 4\Gamma_h^{\text{tot}} u_{h,2}\,, && \text{(9.61h)}
\end{aligned}
$$

with the source term for the top quarks

$$
S_t = - v_w K_{8,t}\partial_z\left(m_t^2 \partial_z \theta\right) + v_w K_{9,t}\left(\partial_z \theta\right) m_t^2\left(\partial_z m_t^2\right)\,. \tag{9.62}
$$

Some additional comments are required. As already mentioned, all interactions which are present on the relevant time-scale have to be included in the collision integrals $\delta\mathcal{C}_e$. This will be discussed in detail in Sec. 9.5. There are two major contributions, the elastic and inelastic scatterings in the hot plasma. As shown in [200], the zeroth and first moment of the collision integral in Eq. (9.53) are related through

$$
\langle C[f]\rangle \simeq \Gamma^{\text{inel}} \sum_j \mu_{j,2}\,, \tag{9.63}
$$

$$
\left\langle \left(\frac{p_z}{E_0}\right) C[f] \right\rangle \simeq -u_2 \Gamma^{\text{tot}}\,, \tag{9.64}
$$

with the inelastic and total interactions rates, respectively. The sum of the chemical potentials depends on the specific inelastic process.
The following processes are included in the transport equations in Eq. (9.61). First, the W-scattering is included coupling left-handed top and bottom quarks to each other. This interaction is described by the rate Γ_W. Further, the Yukawa interaction of the top quark is included described with the rate Γ_y[31]. The strong sphaleron rate corresponds to the $SU(3)$ sphaleron transitions. We refer to this rate as Γ_{ss} and it is discussed in Sec. 9.5.2. The top helicity flipping rate is referred to as

$$
\Gamma_m = \frac{m_t^2(z,T)}{63T}\,, \tag{9.65}
$$

describing the helicity flip of a top quark through the interaction with the Higgs background field. The space-dependent mass of the top quark is determined at the critical temperature. Furthermore, Higgs boson interactions are included through the rate

$$
\Gamma_h = \frac{m_W^2(z,T)}{50T}\,. \tag{9.66}
$$

The space-dependent W-mass is determined analogously to the top quark mass. Using the Kink profile for the Higgs field in Eq. (9.26) allows us to express the mass matrix of the gauge boson as a function of z and by finding the eigenvalues the respective masses of the gauge

[31] To be consistent with the notation in Sec. 9.5.3: $\Gamma_y^{(t)} \equiv \Gamma_y$

bosons. The total interaction rates (corresponding to the inelastic scatterings) can be related with the diffusion constants of the quarks D_t, D_b and Higgs bosons D_h, respectively,

$$D_t = \frac{K_{4,t}}{K_{1,t}\Gamma_t^{\text{tot}}}\,, \tag{9.67}$$

$$D_b = \frac{K_{4,b}}{K_{1,b}\Gamma_b^{\text{tot}}}\,, \tag{9.68}$$

$$D_h = \frac{K_{4,h}}{K_{1,t}\Gamma_h^{\text{tot}}}\,. \tag{9.69}$$

Eq. (9.61) yields a closed set of differential equations for the chemical potentials and the respective plasma velocities of the particles u_i. Assuming, that the thermal system is in equilibrium far from the bubble wall allows us to choose the boundary conditions for the chemical potential and plasma velocities to vanish for $z \to \infty$. Note that we use net chemical potentials and plasma speed perturbations. With this association at hand, it is possible to solve the transport equations for $\{\boldsymbol{\mu}, \mathbf{u}\}$ and evaluate the left-handed chemical potential triggering the electroweak sphaleron transition in Eq. (9.21) [36]

$$\mu_L = \frac{1}{2}\left(1 + 4K_{1,t}\right)\mu_{t,2} + \frac{1}{2}\left(1 + 4K_{1,b}\right)\mu_{b,2} - 2K_{1,t}\mu_{t^c,2}\,, \tag{9.70}$$

since the left-handed chemical potential μ_L and particle distribution function n_L^0 are related through the high-temperature expansion.

9.4.2. VEV Insertion Approximation

In the following, an alternative way to derive the quantum transport equations will be introduced and the relevant notation is fixed. The `FH` approach uses a WKB ansatz for the fermion spinor to derive the semi-classical force. The corresponding WKB ansatz is valid, if the respective typical length-scale of the particles, the de Broglie wave-length λ_B, is smaller than the length-scale of the bubble profile, given by the wall thickness L_w

$$\lambda_B \sim {}^1\!/_T \ll L_w\ . \tag{9.71}$$

Since, the typical length-scale of the particles in a plasma is given by the inverse temperature, the validity condition for the `FH` approach is given by $L_w T_c \gg 1$. Hence, this approach is valid in the *thick wall regime*. The VEV insertion approximation (VIA) can be understood as an expansion in ${}^{v(z)}\!/_T$, where $v(z)$ is the VEV of the Higgs profile at a given space-point. Thus, the resulting space-dependent masses can be treated perturbatively.
For the following discussion and derivation of the quantum transport equations within the `VIA` approximation we closely follow [201–203], where the general idea of the approximation is based on the work of [204, 205].
The characterization of the thermal system of the universe right after the EWPT requires a description of non-equilibrium. As indicated in Sec. 7.1.2, this can be accomplished within the Closed-Time-Path formalism (CTP) [159–161]. The number current of a fermion(*e.g.* top quark) is then given by the Schwinger-Dyson transport equation

$$\begin{aligned}\partial_\mu j_i^\mu(x) = -\int d^3z \int_{-\infty}^{x_0} dz_0\, \mathrm{Tr}\left[\Sigma_i^>(x,z)S_i^<(z,x) - S_i^>(x,z)\Sigma_i^<(z,x)\right. \\ \left. + S_i^<(x,z)\Sigma_i^>(z,x) - \Sigma_i^<(x,z)S_i^>(z,x)\right]\,,\end{aligned} \tag{9.72}$$

where we have to distinguish between both chiralities ($i = L, R$). The fermionic Wightman function $S_i^\lambda(x,y)$ corresponds to the thermal (massless) propagators

$$S^>(x,y) = \left\langle \psi(x)\overline{\psi}(y)\right\rangle\ , \quad S^<(x,y) = \left\langle \overline{\psi}(x)\psi(y)\right\rangle\ . \tag{9.73}$$

The explicit form of the fermionic Wightman functions is given by [206] ($\lambda = <, >$)

$$S^{\lambda}(x,y) = \int \frac{d^4k}{(2\pi)^4}\, \mathrm{e}^{-ik\cdot(x-y)}\, g_f^{\lambda}(k_0,\mu)\rho(k_0,\mathbf{k})\,(\not{k} + m_T) \ , \tag{9.74}$$

with the spectral density ρ, as function of the particle energy k_0 and its momentum $\mathbf{k}$, the thermal mass of the fermion m_T and the thermal distribution function g_f^{λ} for fermions as a function of the chemical potential μ and the particle energy k_0. Near-equilibrium these thermal distribution function can be related with the distribution function in equilibrium *e.g.*

$$g_f^{>}(k_0,\mu) = 1 - n(k_0) + \mu\frac{h(k_0)}{T} + \mathcal{O}(\mu^2) \ ,$$

with the equilibrium distribution function for a fermion and its derivative

$$n(x) = (\mathrm{e}^x + 1)^{-1} \ , \qquad h(x) = \mathrm{e}^x\,(\mathrm{e}^x + 1)^{-2} \ . \tag{9.75}$$

We refer to [201] for more details. The thermal self-energies Σ_i^{λ} will be discussed in a moment. The left-hand side of Eq. (9.72) can be simplified by using Fick's law

$$j_i^{\mu} = (n_i, -D_i\boldsymbol{\nabla} n_i) \ , \tag{9.76}$$

relating the particle current with the scalar distribution function n_i and the respective diffusion constant D_i, to

$$\partial_\mu j_i^{\mu}(x) \simeq v_w n_i' - D_i\boldsymbol{\nabla}^2 n_i \simeq v_w n_i' - D_i n_i'' \ . \tag{9.77}$$

In Eq. (9.77) it was further used, that we perform the calculation in the wall frame, hence the problem reduces to a one dimensional problem.
The Higgs field background $\phi_b(z)$ in front of the bubble wall yields space-dependent masses for the fermions. Hence, the actual determination of the propagator is a sophisticated problem. The `VIA` proposes an approach to calculate the fermionic propagator [207–210]. In this approximation the field dependent part of the fermion mass is treated as perturbation. The idea is to split the mass of the respective fermion in a Higgs field dependent and independent part (in the following for the top quark)

$$\mathcal{L}_{\text{free}} \supset \sum_{i=L,R} \bar{t}_i \left(i\not{\partial} - \delta m_i^{\text{Re}}(T)\right) t_i \ , \tag{9.78}$$

$$\mathcal{L}_{\text{int}} \supset -\left[m_t^{\text{Re}}(\phi_b)) + i m_t^{\text{Im}}(\phi_b\right] \bar{t}_L t_R + \text{h.c.} \equiv -\frac{f(T,\phi_b)}{\sqrt{2}}\bar{t}_L t_R + \text{h.c.} \ , \tag{9.79}$$

where $\delta m_i^{\text{Re}}\,(T)$ are the one-loop thermal masses and $m_t(\phi_b)$ corresponds to the field dependent complex top quark mass (split in its real and imaginary part). The thermal masses can be interpreted as the resummed thermal one-loop corrections to the massless propagator and are given for right-(left-) handed quarks $q_{R,(L)}$ and leptons $l_{R,(L)}$ as

$$\left(\delta m_{q_L}^{\text{Re}}\right)^2 = \left(\frac{1}{6}g_s^2 + \frac{3}{32}g_2^2 + \frac{1}{288}g_1 + \frac{1}{16}y_t^2\right)T^2 \ , \quad \left(\delta m_{q_R}^{\text{Re}}\right)^2 = \left(\frac{1}{6}g_s^2 + \frac{1}{18}g_1^2 + \frac{1}{8}y_t^2\right)T^2 \tag{9.80a}$$

$$\left(\delta m_{l_L}^{\text{Re}}\right)^2 = \left(\frac{1}{32}g_1 + \frac{3}{32}g_2 + \frac{1}{16}y_t^2\right)T^2 \ , \qquad \left(\delta m_{l_R}^{\text{Re}}\right)^2 = \left(\frac{1}{8}g_1^2 + \frac{1}{8}y_t^2\right) \ , \tag{9.80b}$$

with the SM gauge couplings g_s, g_2 , g_1 and the top-Yukawa coupling y_t.

The interaction strength $f(T,\phi_b) \in \mathbb{C}$ is implicitely defined In Eq. (9.79). The interaction Lagrangian implies that for each VEV insertion (interaction with Higgs background field) a

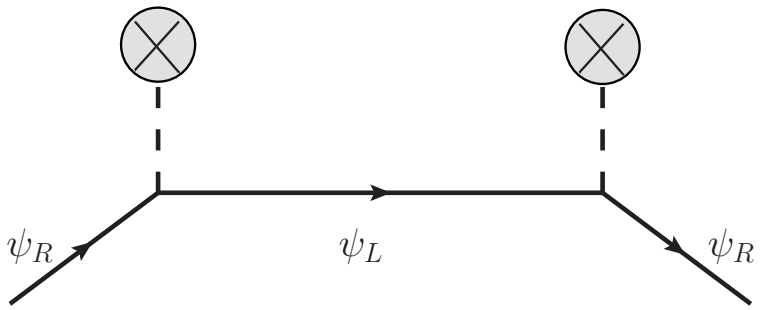

Figure 9.3.: The fermionic propagator of a right-handed fermion is shown with two VEV insertions indicated by the gray blobs. This diagram corresponds to the leading-order of the transport equations.

factor $f(x) \equiv f_x$ in the specific space-point x has to be multiplied in the respective amplitude. Thus, the right-hand self-energy in Fig. 9.3 reads

$$\Sigma_R^{\lambda}(x,y) = -f(x)f^*(y)P_R S_L^{\lambda}(x-y)P_L \ , \tag{9.81}$$

with the left- and right-handed projectors $P_{L,R}$. Using Eq. (9.81) in Eq. (9.72) allows us to recast the right-hand side in the form

$$\begin{aligned}\partial_\mu j_R^\mu(x) = \frac{1}{2}\int d^3z \int_{-\infty}^{x_0} [f_x f_z^* + f_x^* f_z]\,\mathrm{Re}\ \mathrm{Tr}\left[S_L^{>}(x,z)S_R^{<}(z,x) - S_L^{<}(x,z)S_R^{>}(z,x)\right]_{\mathrm{Tr}(m)=0} \\ + \frac{1}{2}\int d^3z \int_{-\infty}^{x_0} i\,[f_x f_z^* - f_x^* f_z]\,\mathrm{Im}\ \mathrm{Tr}\left[S_L^{>}(x,z)S_R^{<}(z,x) - S_L^{<}(x,z)S_R^{>}(z,x)\right]_{\mathrm{Tr}(m)=0} \\ = S_R^{\mathrm{CP}}(x) + S_R^{\not{\mathrm{CP}}}(x)\ .\end{aligned} \tag{9.82}$$

The subscript $\mathrm{Tr}(m) = 0$ indicates that the mass can be set to zero in the respective propagators. Hence, the transport equations split into a CP-conserving and CP-violating part. The CP-violating part is crucial to generate particle asymmetries in the first place. The corresponding transport equations for the left-handed top quark can be determined analogously. It turns out that $S_L^{\mathrm{CP}}(x) = -S_R^{\mathrm{CP}}(x)$ and $S_L^{\not{\mathrm{CP}}}(x) = -S_R^{\not{\mathrm{CP}}}(x)$.
The thermalization of the particles in front of the bubble is assumed to happen on a faster time-scale compared to the bubble dynamics, hence the prefactors can be simplified further

$$\lim_{z\to x}[f_x f_z^* + f_x^* f_z] \simeq 2\,|f(x)|^2\ , \quad \lim_{z\to x}[f_x f_z^* - f_x^* f_z] \simeq 2iv_w \mathrm{Im}\ \left(f'(x)f^*(x)\right)\left(x^0 - y^0\right)\ , \tag{9.83}$$

allowing us to express the CP-conserving interactions as

$$S_R^{\mathrm{CP}} = \Gamma_M^{+}\left(\mu_L + \mu_R\right) + \Gamma_M^{-}\left(\mu_L - \mu_R\right)\ , \tag{9.84}$$

with the relaxation rates

$$\Gamma_M^{\pm} = \frac{6}{T^2}\cdot\frac{N_c}{2\pi^2 T}\,|f|^2 \int \frac{k^2 dk}{\omega_L \omega_R}\mathrm{Im}\ \left[-\frac{(h(\varepsilon_L \mp h(\varepsilon_R^*)))}{\varepsilon_R^* - \varepsilon_L}\left(\varepsilon_L \varepsilon_R^* - k^2\right)\right. \tag{9.85}$$

$$\left. + \frac{(h(\varepsilon_L) \mp h(\varepsilon_R))}{\varepsilon_L + \varepsilon_R}\left(\varepsilon_L\varepsilon_R + k^2\right)\right]\ , \tag{9.86}$$

and the corresponding left- and right-handed chemical potentials of the top quark. Some remarks about the relaxation rate in Eq. (9.86): we already included the factor $6/T^2$ in the definition of the relaxation rate. This factor will be explained as we discuss the corresponding

chemical potentials. The color factor N_c is 3 for quarks and 1 for leptons, respectively. Due to the CP-violation (complex nature of the top quark mass) the dispersion of the left- and right-handed particles is different, hence we have to distinguish between the left- and right-handed energies

$$\varepsilon_i = \omega_i - i\Gamma_t = \sqrt{k^2 + \left(\delta m_i^{\mathrm{Re}}\right)^2} - i\Gamma_t \ , \tag{9.87}$$

with the thermal masses defined in Eq. (9.80) and the thermal decay width Γ_t. The thermal width is different for quarks and leptons and they are given by

$$\Gamma_t = \frac{4}{3}\alpha_s T \simeq 0.16T \ , \qquad \Gamma_l = \alpha_w T \simeq \frac{1}{30}T \ . \tag{9.88}$$

The derivative of the distribution function h is defined in Eq. (9.75).
For the evaluation of the relaxation rate, we further expand the rate for small mass differences for left- and right-handed particles (thus also the dispersion can be expanded)

$$(\delta m_p)^2 = \left(\delta m_{p_R}^{\mathrm{Re}}\right)^2 - \left(\delta m_{p_L}^{\mathrm{Re}}\right)^2 \ , \tag{9.89}$$

$$\delta\omega = \frac{(\delta m_p)^2}{2\sqrt{k^2 + \left(\delta m_{p_R}^{\mathrm{Re}}\right)^2}} \ , \tag{9.90}$$

where p indicates either the quark (q) or lepton (l). For simplicity we drop the index in ω. The approximation for degenerate thermal masses is an excellent approximation for quarks, however this does not hold for leptons in the same way. Furthermore, we assume that the thermal widths of the left- and right-handed quarks and leptons are the same and given by Eq. (9.88). This allows us to expand the relaxation rate to

$$\Gamma_M^- = \frac{6}{T^2}\cdot\frac{N_c}{2\pi^2 T}|f|^2 \int \frac{dkk^2}{\omega^2}\left(-\frac{k^2}{\Gamma_T} + \frac{\omega^2}{\Gamma_T} + \frac{k^2\Gamma_T}{\omega^2} + \left(\frac{k^2}{\omega\Gamma_T} - \frac{2k^2\Gamma_T}{\omega^3}\right)\delta\omega\right) h_f(\omega) \tag{9.91}$$
$$+\mathcal{O}\left(\delta\omega^2; \left(\frac{\Gamma_T}{T}\right)^2; h_f'\right) \ ,$$

and

$$\Gamma_M^+ \sim (\ldots)\,\delta\omega\cdot h'(\omega) + \mathcal{O}\left(\delta\omega^2; \left(\frac{\Gamma_T}{T}\right)^2; h_f'\right) \ . \tag{9.92}$$

Eq. (9.92) indicates that the positive rate Γ_M^+ is directly proportional to the small difference $\delta\omega$ and does not have any other (dominant) contributions. For that reason, we drop in the following the contribution Γ_M^+ and only take into account $\Gamma_M^- \equiv \Gamma_M$, which is compatible with the literature [203].
Analogously, the right-handed CP-violating source term can be found

$$S_R^{\not{CP}} = \frac{v_w N_c}{\pi^2}\mathrm{Im}\ \left(f' f^*\right)\int \frac{k^2 dk}{\omega_L\omega_R}\mathrm{Im}\ \left[\frac{(n(\varepsilon_L) - n(\varepsilon_R^*))}{\left(\varepsilon_L - \varepsilon_R^*\right)^2}\left(\varepsilon_L\varepsilon_R^* - k^2\right)\right. \tag{9.93}$$
$$\left. + \frac{(n(\varepsilon_L) + n(\varepsilon_R) - 1)}{\left(\varepsilon_L + \varepsilon_R\right)^2}\left(\varepsilon_L\varepsilon_R + k^2\right)\right] \ ,$$

with the same definition as in Eq. (9.86), v_w as the bubble wall velocity and the (equilibrium) distribution function $n(k_0)$ as defined in Eq. (9.75). The derivative acting on the interaction strength f' is the derivative with respect to the bubble wall distance z. The same arguments as above allow us to expand the CP-violating source term for the particle i, which enters the quantum transport equations[32] to

$$S_{\not{CP}}^{(i)} = \frac{N_c v_w}{\pi^2}\mathrm{Im}\ \left(f_i' f_i^*\right)\int dk\frac{k^4}{\omega^4}\left[-\frac{\Gamma_T}{2\omega} + \frac{5\Gamma_T}{4\omega^2}\delta\omega + \left(\frac{\Gamma_T}{\omega} - \frac{5\Gamma_T\delta\omega}{2\omega^2}\right)n(\omega)\right. \tag{9.94}$$

[32] Note that we use net-chemical potentials in the transport equations, hence we have to use also the difference of right- and left-hand source terms in the transport equations.

$$+\left(\frac{-\omega^2}{2\Gamma_T}+\frac{\omega^4}{2k^2\Gamma_T}-\frac{\Gamma_T}{2}+\left(\frac{\omega}{2\Gamma_T}+\frac{3\Gamma_T}{2\omega}\right)\delta\omega\right)n'(\omega)\Bigg] \\ +\mathcal{O}\left(\delta\omega^2;\left(\frac{\Gamma_T}{T}\right)^2;n''\right) \ .$$

Both expansions in Eqs. (9.91) and (9.94) are implemented in `BSMPT` v2.0 [5], where the integration is performed numerically with the `C++` library `Boost` [211]. The interaction strength in Eq. (9.79) can be identified with the complex mass parametrized as in Eq. (9.31), allowing us to write

$$|f|^2 = 2\,|m(z)|^2 \ , \quad \text{and} \quad \mathrm{Im}\left(f' f^*\right) = 2\theta'(z)m^2(z) \ . \tag{9.95}$$

The masses are determined by evaluating numerically the eigenvalues of the mass matrix obtained with the Higgs field configuration at the given distance z by using the parametrization of Eq. (9.26). Analogously, the evolution of the phase factor $\theta(z)$ is governed by the described approach in Sec. 9.3 while using Eq. (9.33).
At sufficiently high temperatures, the chemical potential and the particle number density can be related to each other by

$$n_p = \kappa_p \frac{T^2}{6}\mu_p + \mathcal{O}\left(\mu_p^3\right) \ , \tag{9.96}$$

for a particle specie p and the statistical factor

$$\kappa_p(x) = \kappa_p(0)\frac{c_{F,B}}{\pi^2}\int_{m/T}^{\infty} dx \frac{x\,\mathrm{e}^x}{\left(\mathrm{e}^x \pm 1\right)^2}\sqrt{x^2 - {}^{m^2}/_{T^2}} \ . \tag{9.97}$$

The factor ${}^{T^2}/_6$ is absorbed in the interaction rates (see *e.g.* in Eq. (9.86)) and the normalizations are given by $c_{F,(B)} = 6(3)$. The statistical factors at zero temperature for right-and left-handed quarks, leptons and a Higgs boson are given by

$$\kappa_{q_L}(0) = 6 \ , \quad \kappa_{q_R}(0) = 3 \ , \quad k_H(0) = 4 \ , \quad \kappa_{l_L}(0) = 2 \ , \quad \text{and} \quad \kappa_{l_R}(0) = 1 \ . \tag{9.98}$$

Up to this point, the transport equation for one single particle was discussed. However, we want to describe the complete thermal system of the early universe at the EWPT. For simplicity, we assume the top and bottom quarks to be massive, while the remaining quarks are assumed to be massless. Furthermore, we include massive τ leptons in the transport equations allowing us to investigate if a leptonic degree of freedom enhances the overall BAU production.
At a first glance, the CP-violating source term in Eq. (9.93) is proportional to the respective mass of the particle, hence the τ-leptons might suffer from a large suppression in the production for *e.g.* for the C2HDM

$$\frac{S^{\not{CP}}_{\tau_R}}{S^{\not{CP}}_{t_R}} \sim \frac{m_\tau(\phi_b,T)}{m_t(\phi_b,T)} = \begin{cases} \dfrac{m_\tau(0)}{m_t(0)}\dfrac{\omega_2(T)}{\omega_2(T)} \simeq 0.1 \ , & \text{for } \texttt{Type I} \\ \dfrac{m_\tau(0)}{m_t(0)}\dfrac{\omega_1(T)}{\omega_2(T)} \simeq \dfrac{0.1}{\tan\beta} \ , & \text{for } \texttt{Type II} \ , \end{cases} \tag{9.99}$$

with the thermal VEVs ω_1, ω_2 and the mixing angle $\tan\beta \gtrsim 1$. However, leptons do provide advantages compared to quarks. For instance, the diffusion constants (as discussed in the next chapter) are larger for leptons compared to quarks, allowing for a more efficient diffusion and production of asymmetries. Moreover, leptons do not suffer from strong sphaleron washout (also discussed in the next chapter), which allows us to *keep* produced asymmetries [203].
In the following we refer to the particle distribution functions of the left-and right-handed

top,bottom and τ, the τ-neutrino ν, the light quark contributions u and the scalar degrees of freedom h_k (k denotes the k-th Higgs doublet) as follows

$$n_q = n_{t_L} + n_{b_L}\,, \qquad n_t = n_{t_R}\,, \qquad n_b = n_{b_R}\,, \tag{9.100a}$$

$$n_u = n_{u_R} \qquad n_l = n_{\nu_L} + n_{\tau_L}\,, \qquad n_\tau = n_{\tau_R}\,, \tag{9.100b}$$

$$n_\nu = n_{\nu_R} \qquad n_{h_k} = n_{h_k^0} + n_{h_k^\pm}\,, \tag{9.100c}$$

where we use Eq. (9.96) to relate the chemical potentials with the particle distribution functions. Note, that we explicitly separate the left- from the right-handed densities. Furthermore, we identify these distributions functions to describe the net densities, meaning the distribution of the particle density minus the anti-particle distribution.
As discussed in the next section, gauge interactions and Higgs self-interaction rates are fast compared to the time-scale of the diffusion process, hence particles corresponding to the up- and down-components of $SU(2)_L$ doublets are assumed to be in thermal equilibrium (as well as the Higgs boson components), implying *e.g.* $n_{t_L} = n_{b_L}$. This is also the reason, why only one distribution function for the left-handed densities is required to describe the system.
Due to the small mass of the remaining quarks (u,d,c,s), or rather the small Yukawa interactions, the light quarks effectively decouple from the thermal system. However, they participate in strong sphaleron transitions, hence their respective chemical potentials (particle distribution functions) are related to each other through

$$n_{q_1} = n_{q_2} = -2n_u = -2n_d = -2n_s = -2n_c\,. \tag{9.101}$$

Eq. (9.101) allows us to choose the particle distribution function of the right-handed up-type quark to describe the light quark sector completely. Including the strong sphaleron transition and further Yukawa interactions in the transport equations, allows us to formulate the (quantum) transport equations for massive top, bottom and τ as follows [203]

$$\partial_\mu j_q^\mu = +\Gamma_M^{(t)}\mu_M^{(t)} + \Gamma_M^{(b)}\mu_M^{(b)} + \Gamma_y^{(t)}\mu_Y^{(t)} + \Gamma_y^{(b)}\mu_Y^{(b)} - 2\Gamma_{ss}\mu_{ss} - \cancel{S_{CP}^{(t)}} - \cancel{S_{CP}^{(b)}}, \tag{9.102a}$$

$$\partial_\mu j_t^\mu = -\Gamma_M^{(t)}\mu_M^{(t)} - \Gamma_y^{(t)}\mu_Y^{(t)} + \Gamma_{ss}\mu_{ss} + \cancel{S_{CP}^{(t)}}, \tag{9.102b}$$

$$\partial_\mu j_b^\mu = -\Gamma_M^{(b)}\mu_M^{(b)} - \Gamma_y^{(b)}\mu_Y^{(b)} + \Gamma_{ss}\mu_{ss} + \cancel{S_{CP}^{(b)}}, \tag{9.102c}$$

$$\partial_\mu j_l^\mu = +\Gamma_M^{(\tau)}\mu_M^{(\tau)} + \Gamma_y^{(\tau)}\mu_Y^{(\tau)} - \cancel{S_{CP}^{(\tau)}}, \tag{9.102d}$$

$$\partial_\mu j_\nu^\mu = 0\,, \tag{9.102e}$$

$$\partial_\mu j_\nu^\mu = -\Gamma_M^{(\tau)}\mu_M^{(\tau)} - \Gamma_y^{(\tau)}\mu_Y^{(\tau)} + \cancel{S_{CP}^{(\tau)}}, \tag{9.102f}$$

$$\partial_\mu j_{h_k}^\mu = +\Gamma_y^{(t)}\mu_Y^{(t)} - \Gamma_y^{(b)}\mu_Y^{(b)} + \Gamma_y^{(u)}\mu_Y^{(u)} - \Gamma_y^{(\tau)}\mu_Y^{(\tau)}\,, \tag{9.102g}$$

$$\partial_\mu j_u^\mu = +\Gamma_{ss}\mu_{ss}\,, \tag{9.102h}$$

with the (rescaled) chemical potentials

$$\mu_M^{(t)} = \left(\frac{n_t}{\kappa_t} - \frac{n_q}{\kappa_q}\right)\,, \qquad \mu_Y^{(t)} = \left(\frac{n_t}{\kappa_t} - \frac{n_q}{\kappa_q} - \sum_k \frac{h_k}{\kappa_{h_k}}\right)\,, \tag{9.103a}$$

$$\mu_M^{(b)} = \left(\frac{n_b}{\kappa_b} - \frac{n_q}{\kappa_q}\right)\,, \qquad \mu_Y^{(b)} = \left(\frac{n_b}{\kappa_b} - \frac{n_q}{\kappa_q} + \sum_k \frac{h_k}{\kappa_{h_k}}\right)\,, \tag{9.103b}$$

$$\mu_M^{(\tau)} = \left(\frac{n_\tau}{\kappa_\tau} - \frac{n_l}{\kappa_l}\right)\,, \qquad \mu_Y^{(\tau)} = \left(\frac{n_\tau}{\kappa_\tau} - \frac{n_l}{\kappa_l} + \sum_k \frac{n_{h_k}}{\kappa_{h_k}}\right)\,, \tag{9.103c}$$

$$\mu_{ss} = \left(\frac{2n_q}{\kappa_q} - \frac{n_t}{\kappa_t} - \frac{n_b}{\kappa_b} - \frac{8n_u}{\kappa_L} - \frac{4n_u}{\kappa_R}\right)\,. \tag{9.103d}$$

The index p of the statistical factor κ_p indicates the respective particle. The index L, R corresponds to the massless left- or right-handed particle, respectively. It is required to define an effective statistical factor for the left-handed density n_q.
Eq. (9.77) defines the left-hand side of the coupled differential system of equations with the diffusion constants for quarks and leptons, respectively. Assuming equilibrium far from the bubble wall in the symmetric phase, allows us to formulate boundary conditions for all particles p as $n_p(z) \xrightarrow{z\to\infty} 0$. Note, that we are considering net distribution functions.
This coupled system of differential equations can be solved for all particle distribution functions as a function of the bubble wall distance z. Finally, the left-handed density required for Eq. (9.21) can be written as

$$n_L^0(z) = \sum_{\text{fam.}} (n_q + n_l) \overset{Eq.\ (9.101)}{=} n_q + n_l - 4n_u \ . \tag{9.104}$$

The transport equations in Eq. (9.102) can also be formulated for massless τ leptons or b quarks. The corresponding Yukawa, relaxation rates and source terms have to be set to zero accordingly. Furthermore, massless b quarks have to be taken into account in the strong sphaleron interactions as an effective *light quark* degree of freedom (*i.e.* $n_u = n_b$). This allows us to investigate the following three different cases for the transport equations

- Taking massive t, b and τ into account: The transport equations are given by Eq. (9.102). We refer to this scenario as $\texttt{VIA} - \tau$.
- Neglecting the τ masses, where the b and t quarks are assumed to be massive. The respective Yukawa, relaxation rates and source terms for the τ lepton have to be dropped in Eq. (9.102). This scenario is referred to as $\texttt{VIA} - b$.
- Only the t quark is taken into account as massive degree of freedom. All remaining quark degrees of freedom are assumed to contribute to the light quarks. Furthermore, all leptons are neglected. This scenario is referred to as $\texttt{VIA} - t$.

9.5. Plasma Interactions and Thermal Rates

The thermal system of the early universe incorporates many interactions. In the following, we want to discuss which processes have to be taken into account in the quantum transport equations to describe the system in a consistent way.
As indicated in Sec. 9.2, the calculation of the BAU is performed in a two-step approach. First, the left-handed excess in front of the bubble wall is generated. In a second step, the baryon asymmetry is calculated by considering the electroweak sphaleron transitions. This requires that the corresponding interaction rate of the electroweak sphaleron Γ_{ws} and the interaction rate of the diffusion process Γ_D obey

$$\Gamma_{ws} \ll \Gamma_D \ . \tag{9.105}$$

By demanding Eq. (9.105), it can be ensured that these two processes can be treated separately. A rough estimate of the diffusion rate can be obtained by considering the distance of a particle diffusing

$$d_D \sim \sqrt{D\tau_D} \ , \tag{9.106}$$

with the respective diffusion constant D and relate it with the distance the bubble wall has traveled in the same time

$$d_w = v_w \tau_w \ . \tag{9.107}$$

Hence, the resulting time-scale of the diffusion process (and diffusion rate) is given as

$$\tau_w \overset{!}{=} \tau_D = (\Gamma_D)^{-1} = \frac{D}{v_w^2} \ . \tag{9.108}$$

Note, that Eq. (9.108) and Eq. (9.105) imply a lower bound on the wall velocity. However, the typical order of wall speeds $\left(\mathcal{O}\left(v_w\right) = 10^{-1}\right)$ required for the EWBG is above this lower limit.
If an interaction rate, describing a process $A \leftrightharpoons B$, is (much) larger compared to the process under investigation (in our case Γ_D defines the relevant time-scale of the diffusion process), the chemical potentials involved in the process $A \leftrightharpoons B$ can be equated $\mu_A = \mu_B$, since the fast process yields equilibrium between both particles A and B. We assume, that the gauge interactions ($\Gamma_{\text{gauge}} \sim \alpha_i T$ [200]) are fast on the relevant diffusion time-scale, hence the chemical potentials of the components of the $SU(2)_L$ doublets can be set equal, implying *e.g.*

$$n_{t_L} = n_{b_L} \ , \quad n_{h^\pm} = n_{h^0} \ . \tag{9.109}$$

These two interaction rates, the EW sphaleron and Yukawa rate, dictate the relevant time-scale and thus the relevant processes, which have to be taken into account in the description of the quantum transport system. The lower bound is given by $\Gamma_{ws} \sim \alpha_w^4 T$ in terms of the electroweak coupling $\alpha_w = g_2/4\pi$ and the upper bound by the gauge interactions $\Gamma_{\text{gauge}} \sim \alpha_i T$ with either the strong gauge coupling $\alpha_s = g_s/4\pi$ or the electroweak coupling α_w.
We start the discussion of the diffusion constants of quarks and leptons in a hot plasma. The diffusion constants describe the mean free path of the respective particle in the hot plasma. Followed by the discussion of the strong sphaleron transitions and the Yukawa interactions.

9.5.1. Diffusion Constants

In this section, the diffusion constants D_i for quarks and leptons are motivated. The sketch of the derivation closely follows [32].
The diffusion constant of a particle in a hot plasma gives a measure of the mean free path of the respective particle. It relates the particle current to the corresponding distribution function n

$$\mathbf{J}_D = -D\boldsymbol{\nabla} n \ . \tag{9.110}$$

Since the equilibrium distribution function does not provide a current, we allow for a small perturbation δf in the equilibrium distribution f_0 (*see* Eq. (9.39)). The determination of the δf by solving the Boltzmann equations, allows then to calculate the resulting current by

$$\mathbf{J}_D = \int_p \delta f \frac{\mathbf{p}}{E} \ , \tag{9.111}$$

and read off the resulting diffusion constant. The static Boltzmann equations read

$$L[f] = -\mathcal{C}[f] \tag{9.112}$$

with the Liouville operator on the left side and the respective collision integral $\mathcal{C}[f]$. The collision integral for two incoming $\{p, k\}$ and outgoing $\{p', k'\}$ momenta is given by

$$\mathcal{C}[f] = \frac{1}{2p_0} \int_{\{p'k,k'\}} \delta^{(4)}(\sum_l p_l) \left|\mathcal{M}\right|^2 \mathcal{P}[f] \tag{9.113}$$

with the delta function ensuring momentum conservation and the respective matrix element $\mathcal{M}$. As mentioned in the last section, the gauge interactions are assumed to be dominant in the hot plasma, limiting the mean free path of quarks and leptons. Hence, $\mathcal{M}$ corresponds to the t-channel vector boson exchange diagrams. The statistical factor is defined as

$$\mathcal{P}[f] = f_p f_k \left(1 - f_{p'}\right)\left(1 - f_{k'}\right) - f_{p'} f_{k'} \left(1 - f_p\right)\left(1 - f_k\right) \ . \tag{9.114}$$

Note, that the electroweak symmetry breaking is restored at high temperatures. Therefore, the corresponding diagrams have to be evaluated with the gauge interactions states

B_μ, W_μ^i $(i = 1, 2, 3)$ (*c.f.* Eq. (2.13)) and the masses of the external legs are zero. The regularization of the divergences related to the massless propagators is achieved by including the one-loop thermal masses of the longitudinal vector bosons:

$$m_B^2 = \frac{4\pi}{3}\alpha_w \tan^2\theta_w T^2 \simeq 0.04\ T^2\ , \tag{9.115a}$$

$$m_{W_i}^2 = \frac{20\pi}{3}\alpha_w T^2 \simeq 0.69\ T^2\ , \tag{9.115b}$$

$$m_g^2 = 8\pi\alpha_s T^2 \simeq 3.6\ T^2\ , \tag{9.115c}$$

with the electroweak vector bosons B, W_i associated to the $U(1)_Y$ and $SU(2)_L$ and the gluon g. The Weinberg angle is denoted as θ_w. Expanding the Boltzmann equations in terms of δf and considering small momentum transfers in the elastic scattering processes, allows us to find the diffusion constants for left- and right-handed leptons ($l_{L,R}$) and left- and right-handed quarks ($q_{L,R}$) [32]

$$D_{l_R}^{-1} \simeq \frac{T}{380}\ , \qquad D_{l_L}^{-1} \simeq \frac{T}{100}\ , \qquad D_{q_{L,R}}^{-1} \simeq \frac{T}{6}\ . \tag{9.116}$$

9.5.2. Strong sphaleron Transition

The strong sphaleron is the correspondence of the electroweak sphaleron discussed in Sec. 9.1.1 for the $SU(3)_c$ gauge group. The strong sphaleron yields an equilibrium between the left- and right-handed up- and down-type quarks for each generation i

$$u_L^{(i)} + d_L^{(i)} \leftrightharpoons u_R^{(i)} + d_R^{(i)}\ . \tag{9.117}$$

The corresponding transition rate was calculated on the lattice and is given by [212, 213]

$$\Gamma_{ss} \simeq 14\alpha_s^4 T\ , \tag{9.118}$$

where it is assumed that the strong coupling $\alpha_s \sim 0.1$ and $N_f = 6$ as the number of active quarks. However, due to the large QCD gauge coupling, the theoretical error on the strong sphaleron transition rate might be huge and of the order $\mathcal{O}(50\%)$ [213].

9.5.3. Yukawa Interactions

The last contributing interaction, which is included in the transport equations, is the Yukawa-like interaction. Since the corresponding t-channel diagrams have the same form as the gauge interactions, we expect that the thermal decay width is proportional to the respective gauge coupling α_i ($i = w$ for leptons and $i = s$ for quarks, respectively). However, as it turns out the thermal decay widths induced through fermion exchanges are proportional to the squared zero-temperature Yukawa coupling y_i. Hence, they are suppressed compared to the gauge-interactions.
The starting point is the thermal rate per unit time, which can be evaluated by using the real time formalism [32]

$$\Gamma = \frac{12}{T^3}\int_{\{p,p',k,k'\}} f_p f_k \left(1 + f_{p'}\right)\left(1 - f_{k'}\right)\delta^{(4)}\left(p + k - p' - k'\right)|\mathcal{M}|^2\ , \tag{9.119}$$

with the in-coming $\{p, k\}$ and out-going $\{p', k'\}$ momenta. The delta distribution ensures the conservation of the 4-momentum and the matrix element $\mathcal{M}$ denotes the scattering of an incoming left- (right-)handed quark/lepton with either a Higgs boson or a gauge boson. The

distribution functions f_i are taken in accordance with the spin-nature of the particles. All diagrams yield a similar structure. Thus, the rate can be cast in the following form

$$\Gamma = \frac{12}{T^3} \int_{p,k} f_p f_k \mathcal{I} \ , \tag{9.120}$$

with the integral

$$\mathcal{I} = \int_{p',k'} \delta^{(4)}(p + k - p' - k') A \frac{-ts}{\left(t - m_T^2\right)^2} \ . \tag{9.121}$$

The variable A indicates the couplings of the involved particles and t, s are the usual Mandelstam variables. The mass in the propagator is the respective thermal mass of the quark/lepton $m_T^2 = g_i^2 C_R T^2/8$ with the Casimir constant C_R of the representation R.
The remaining integrals over the momenta in Eq. (9.120) can be performed approximately (for details we refer to [32]), allowing us to find the thermal decay rates for the left- (right-) handed leptons and quarks, respectively,

$$\Gamma_y^{(l_R)} = 2\Gamma_y^{(l_L)} \simeq 0.28 \alpha_w y_l^2 T \ , \tag{9.122}$$

$$\Gamma_y^{(q_R)} = \Gamma_y^{(q_L)} \equiv \Gamma_y^{(q)} \simeq 0.19 \alpha_s y_q^2 T \ , \tag{9.123}$$

with the corresponding zero-temperature Yukawa couplings.

CHAPTER 10

Phenomenological Study of the Electroweak Baryogenesis

The phenomenological study of the impact of the additional requirement of EWBG on the valid parameter space of the C2HDM concerning the LHC measurements, requires valid benchmark scenarios. The parameter points under investigation have to fulfill experimental and theoretical constraints. The constraints are presented and discussed in Sec. 3.1.
In a first step, we produce parameter points compatible with the experimental and theoretical constraints by using `ScannerS` [60, 61, 81, 214][33]. The corresponding scan ranges of the input parameter of the C2HDM are given in Tabs. 10.1 and 10.2 for the `Type I` and `Type II` C2HDM, respectively. Note that the flavor constraints $B \to X_s\gamma$ requires the charged Higgs boson mass to be heavier than 580 GeV in the `Type II` C2HDM (see for details Sec. 3.1.1).
In a second step, we check for the benchmark scenarios if the global minimum of the effective potential is NLO stable in the sense, that the NLO global minimum is the same as the tree-level one. Subsequently, we check if the benchmark points provides an SFOEWPT with `BSMPTv2.1` [5, 168]. The impact of the SFOEWPT on the valid parameter space of the C2HDM is discussed in [72] and updated in [4]. However, here we want to focus on the discussion of the EWBG.
Overall, 186 benchmark points were produced for the C2HDM providing an SFOEWPT, where 166 are of `Type I` and 20 of `Type II`, respectively. This required a large amount of valid benchmark scenarios, which had to be neglected due to too weak EWPT. Hence, we do not perform the direct comparison of the experimentally allowed parameter space of the C2HDM and the parameter space providing an SFOEWPT due to too less statistics.
We start the discussion with two single benchmark scenarios of `Type I` C2HDM and investigate the impact of the input parameters and the renormalization scale μ, followed by the full scan results of the C2HDM. The differences between both types of the C2HDM are not that significant concerning EWBG. Hence, we do not separate the discussion of both types of the C2HDM.

10.1. Parameter Dependence

We start with the discussion of two benchmark points of `Type I` C2HDM. The input parameters are given Tab. 10.3. The SM parameters are listed in Appendix B. The non-SM like

[33] The linked HiggsBound and HiggsSignal versions are `HiggsBounds5.7.1` and `HiggsSignal2.4.0`.

m_h	$m_{H_\downarrow}$	$m_{H_\uparrow}$	$m_{H^\pm}$	Re m_{12}^2
		in GeV		in GeV^2
125.09	$[30, 1500]$	$[30, 1500]$	$[30, 1500]$	$\left[10^{-3}, 10^5\right]$
α_1	α_2	α_3	$\tan\beta$	
$\left[-\frac{\pi}{2}, \frac{\pi}{2}\right)$	$\left[-\frac{\pi}{2}, \frac{\pi}{2}\right)$	$\left[-\frac{\pi}{2}, \frac{\pi}{2}\right)$	$[0.8, 20]$	

Table 10.1.: Parameter ranges for the C2HDM T1 input parameters used in `ScannerS`.

m_h	$m_{H_\downarrow}$	$m_{H_\uparrow}$	$m_{H^\pm}$	Re m_{12}^2
		in GeV		in GeV^2
125.09	$[30, 1500]$	$[30, 1500]$	$[580, 1500]$	$\left[10^{-3}, 10^5\right]$
α_1	α_2	α_3	$\tan\beta$	
$\left[-\frac{\pi}{2}, \frac{\pi}{2}\right)$	$\left[-\frac{\pi}{2}, \frac{\pi}{2}\right)$	$\left[-\frac{\pi}{2}, \frac{\pi}{2}\right)$	$[0.8, 20]$	

Table 10.2.: Parameter ranges for the C2HDM T2 input parameters used in `ScannerS`.

Higgs boson masses are all in intermediate mass ranges of the order $\mathcal{O}(450\,\text{GeV})$ and rather large $\tan\beta$. The corresponding strengths of the EWPT are given by

$$\xi_C|_{\texttt{BMP I}} = 1.17\,, \qquad (T_c = 191.62\text{GeV}, v_c = 163.20\text{GeV})\,, \tag{10.1a}$$
$$\xi_C|_{\texttt{BMP II}} = 1.05\,, \qquad (T_c = 166.02\text{GeV}, v_c = 174.61\text{GeV})\,. \tag{10.1b}$$

The `BMP I` yields a rather strong EWPT(compared to the overall sample), whereas `BMP II` is almost dropped by the *washout condition*.
The wall thicknesses as defined in Eq. (9.27) and calculated as described in Sec. 9.3 is obtained from

$$T_c L_w|_{\texttt{BMP I}} = 10.77\,, \tag{10.2a}$$
$$T_c L_w|_{\texttt{BMP II}} = 17.89\,. \tag{10.2b}$$

These wall thicknesses indicate that both benchmark scenarios yield a proper scenario in which the WKB expansion used in the `FH` approach is valid, $T_c L_w > 1$. The different predicted BAUs are derived as described in Secs. 9.4.1 and 9.4.2, where the different approaches of the quantum transport equations result in

$$\eta^{(\text{FH})}\Big|_{\texttt{BMP I}} = 2.469 \cdot 10^{-13}\,, \qquad \eta^{(\text{FH})}\Big|_{\texttt{BMP II}} = 1.990 \cdot 10^{-13}\,, \tag{10.3a}$$
$$\eta^{(\text{VIA}-\tau)}\Big|_{\texttt{BMP I}} = 9.482 \cdot 10^{-11}\,, \qquad \eta^{(\text{VIA}-\tau)}\Big|_{\texttt{BMP II}} = 3.250 \cdot 10^{-10}\,, \tag{10.3b}$$
$$\eta^{(\text{VIA}-b)}\Big|_{\texttt{BMP I}} = 9.482 \cdot 10^{-11}\,, \qquad \eta^{(\text{VIA}-b)}\Big|_{\texttt{BMP II}} = 3.250 \cdot 10^{-10}\,, \tag{10.3c}$$
$$\eta^{(\text{VIA}-t)}\Big|_{\texttt{BMP I}} = 9.354 \cdot 10^{-11}\,, \qquad \eta^{(\text{VIA}-t)}\Big|_{\texttt{BMP II}} = 3.138 \cdot 10^{-10}\,, \tag{10.3d}$$

	$m_{H_\downarrow}$ [GeV]	$m_{H_\uparrow}$ [GeV]	$m_{H^\pm}$ [GeV]	$\tan\beta$	α_1	α_2	α_3
BMP I	400.96	430.86	461.46	14.34	-1.5229	-0.0012	1.2023
BMP II	436.37	485.68	515.92	10.83	-1.5341	0.0055	-0.5623
	λ_1	λ_2	λ_3	λ_4	Re λ_5	Im λ_5	Re m_{12}^2 $[\text{GeV}^2]$
BMP I	1.8807	0.2517	5.9276	-1.3312	0.3029	0.2758	12570.8
BMP II	1.0828	0.2360	6.6691	-1.7342	-0.3084	-0.6776	18702.5

Table 10.3.: The input parameters of the two benchmark points discussed in Sec. 10.1 are given together with the corresponding quartic couplings and the softly $\mathbb{Z}_2$ breaking term m_{12}^2. The remaining neutral Higgs boson mass m_h is set to the SM reference of 125.09 GeV.

where we used for the bubble wall velocity $v_w = 0.1$. The mean measured value of the BAU used for the normalization in the following, is given by $\eta_{\text{obs.}} = 8.81 \cdot 10^{-11}$.

The dependence of the produced BAU as a function of the bubble wall velocity is shown in Fig. 10.1. The BMP I is used for the numerical evaluation. The left Fig. 10.1(a) shows the normalized BAU obtained in the FH approach, whereas the right Fig. 10.1(b) corresponds to the different VIA approaches. The differences of the VIA approaches are introduced at the end of Sec. 9.4.2.

The FH approach shows a mild dependence on the wall velocity for small wall velocities (up to $v_w \simeq 0.2$). This mild dependence is expected, since the FH approach uses an explicit expansion for small wall velocities. Note, that the FH approach is only valid for small wall velocities. This mild dependence ensures, that the choice of the input value for v_w does not alter the resulting BAU significantly. However, if the bubble wall velocity approaches the plasma sound speed ($v_w \simeq 1/\sqrt{3}$), the predicted BAU diverges. This divergent behavior can be explained, since the corresponding diffusion lengths (see Eq. (9.108)) is expected to diminish for large v_w. Though, if the full wall velocity dependence is taken into account in the thermal transport coefficients in Eq. (9.55), the divergent behavior might be cured [195]. As long as we are only considering small wall velocities, which is also an assumption used in the VIA approach, we do not need to take the full dependence into account.

The normalized BAUs in the different VIA approaches are shown in Fig. 10.1(b). For this specific benchmark point the difference between the inclusion of massive b, τ in the transport equations is not significant. The overall behavior or rather the impact of the inclusion will be discussed in the next section.

The gray band in Fig. 10.1(b) indicates the upper and lower limit on the observed BAU, hence all points inside this band would be compatible with the CMB measurement. The predicted BAU falls drastically if the wall velocity approaches zero. Note, that the movement of the bubble induces the diffusion process in the first place, since the corresponding source terms are proportional to the wall velocity (see Eq. (9.93)). However, the dependence of η on the wall velocity for the EWBG *relevant* wall velocities ($v_w \simeq 0.1 - 0.2$) is rather mild, so that a large range of wall velocity would produce the correct amount of BAU predicted by the experiment.

A similar behavior can be obtained for different benchmark scenarios: The divergence at the plasma sound speed in the FH approach and the maximal predicted BAU is obtained at roughly $v_w \simeq 0.1$ in the VIA approach, regardless of the chosen ansatz.

The Coleman-Weinberg potential incorporating one-loop effects at zero temperature is renormalized in the $\overline{\text{MS}}$ scheme. This procedure requires the introduction of a renormalization scale

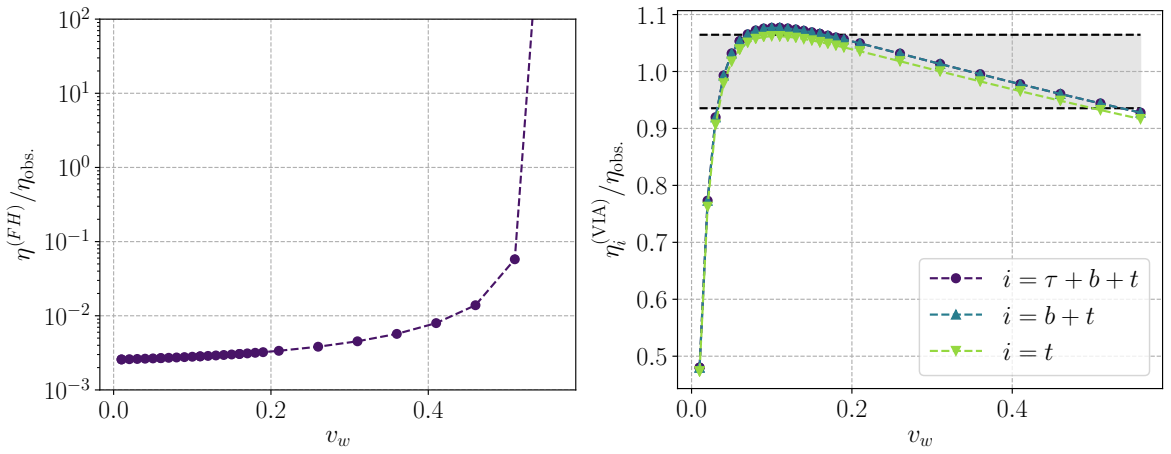

(a) (b)

Figure 10.1.: Left: The BAU normalized to observed value obtained by solving the top transport equations (*see Sec. 9.4.1*) is shown versus the wall velocity v_w. The divergence is approximately at the plasma sound speed. Right: The BAU calculated in the VIA method is shown as a function of the wall velocity. All three different mass scenarios are shown, where *e.g.* $i = \tau + b + t$ indicates, that massive τ, b and t are taken into account in the transport equations. The benchmark scenario `BMP I` presented in Tab. 10.3 is used for the numerical evaluation. *The figures are taken from [6].*

μ in Eq. (7.27). In principle, the input parameters used in the calculations are dependent on the renormalization scale and thus have to be chosen in accordance with the given scale. However, as discussed in Sec. 7.1.5, the additional counterterm potential has been chosen such that it allows us to treat the input masses as direct one-loop masses. Since the renormalization conditions applied on the counterterms in Eq. (7.60) do not correspond to a true on-shell scheme (see *e.g.* Sec. 4.1), a μ dependence remains in the final result. But precisely this remaining μ dependence can be used to estimate the theoretical uncertainty. For this purpose, we vary the default renormalization scale $\mu_0 \equiv v = 246.22\,\text{GeV}$ at which the input parameters are defined. We emphasize, that the variation is done without taking *renormalization-group-equations* (RGE) effects into account. Hence, we vary the renormalization scale only between $v/2$ to $1.5v$. It is possible to change the variation range in `BSMPT`.
In Fig. 10.2(a) the critical VEV and temperature are shown as a function of the normalized renormalization scale μ/v. The benchmark point `BMP I` is taken for the numerical evaluation. We see, that the critical temperature shows only a small variation ($\sim 10\%$), while the critical VEV breaks down for $\mu/v \lesssim 0.95$. For the remaining stable region ($\mu/v \gtrsim 0.95\%$), the critical VEV shows a similar behavior as the critical temperature. The resulting BAUs in the different approaches are shown in Fig. 10.2(b) as a function of the renormalization scale. The values are normalized to the value obtained for the default settings, respectively. Since the critical VEV breaks down for small μ, the predicted BAUs show a large derivation. However, this might indicate numerical problems, rather than a physical effect. The dependence in the stable region indicates a rather mild variation in the predicted BAU of the order of 10%, where the `VIA` approaches tend to depend more on the renormalization scale.
To conclude the discussion of the renormalization scale dependence, we observed overall in all benchmark points, that the dependence on the renormalization scale is of similar size as for `BMP I`, if the corresponding benchmark point provides a numerically stable minimum. There are parameter points with a vacuum structure that are quite sensitive to the renormalization scale. As observed in Fig. 10.2(a) the global minimum of the effective potential at finite

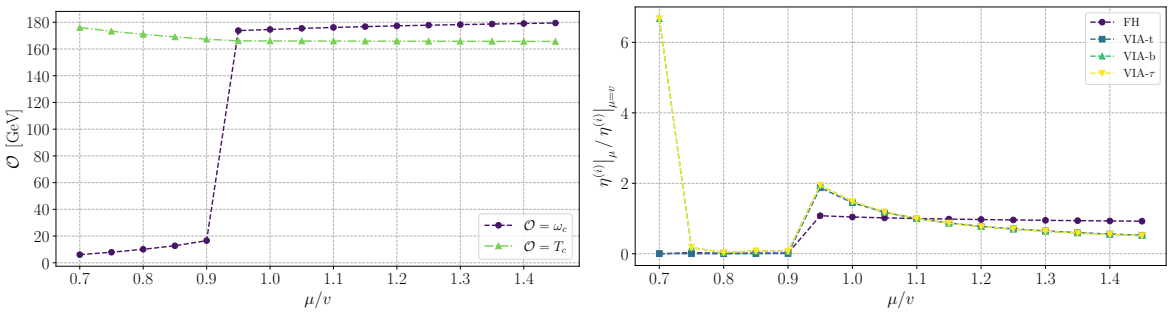

(a) (b)

Figure 10.2.: Left: The critical VEV and temperature are shown as a function of the renormalization scale μ normalized to the default value v indicating the SM VEV. Right: The different BAUs obtained by the several approaches to solve the quantum transport equations are shown as function of the renormalization scale. The benchmark scenario `BMP I` presented in Tab. 10.3 is used for the numerical evaluation. *The figures are taken from [6].*

temperature drops significantly for $\mu < v$. The inclusion of RGE effects might cure these effects, but it is beyond the scope of this thesis.

The complex top quark mass induces a phase factor (see Eq. (9.31)), which is a crucial tuning parameter for the quantum transport equations in Eqs. (9.61) and (9.102). If the corresponding complex phase of the top quark (and other quarks and leptons) vanishes, the source terms vanishes too. Thus, EWBG is not possible. Hence, we investigate the scaling behavior of the produced BAU as a function of the complex phase in Fig. 10.3. We use the benchmark point `BMP II` and vary the input parameter Im $\left(m_{12}^2\right)$ to achieve a variation of the top quark phase. All other input parameters are kept fixed. To see the scaling behavior of the BAU, we normalize the results to the minimum obtained in the variation. The `FH` approach (green points) shows a clear dependence on the phase factor implying that a large complex phase is required in order to produce sufficient BAU. However, the gray shaded region indicates the parameter space excluded by the EDM constraints, which shows the problematic situation in the `FH` approach: on the one hand, a large complex phase factor is favored, but on the other hand the complex phase is strictly constrained by the EDM measurements, requiring the phase factor to be small.

The `VIA` approach also shows a dependence on the complex phase θ_t, but it is rather mild compared to the `FH` ansatz. Note that the jumps in the `VIA` approach are due to numerical uncertainties in the evaluation of the complex phase and the respective solution of the transport equations, resulting in the unstable scaling behavior. However, only the overall scaling behavior is important, indicating a major difference in both approaches.

10.2. Parameter Space for Electroweak Baryogenesis

In the following, we will discuss the overall parameter space of the C2HDM in the context of EWBG. We emphasize again, that all points in this sections obey theoretical and experimental constraints as discussed in Sec. 3.1, provide an NLO stable vacuum and an SFOEWPT. In this way all required conditions for a successful EWBG are fulfilled and the calculation of the expected produced BAU can be performed. The bubble wall velocity is taken as $v_w = 0.1$ for all points.

In Fig. 10.4, the normalized produced BAUs in the `FH` and `VIA` approach are shown. The `VIA` results are only shown for the case where massive τ, b and t are taken into account in the transport equations. The impact of the different inclusions will be discussed later on. The results for `Type I` C2HDM are indicated with blue points, while the `Type II` points

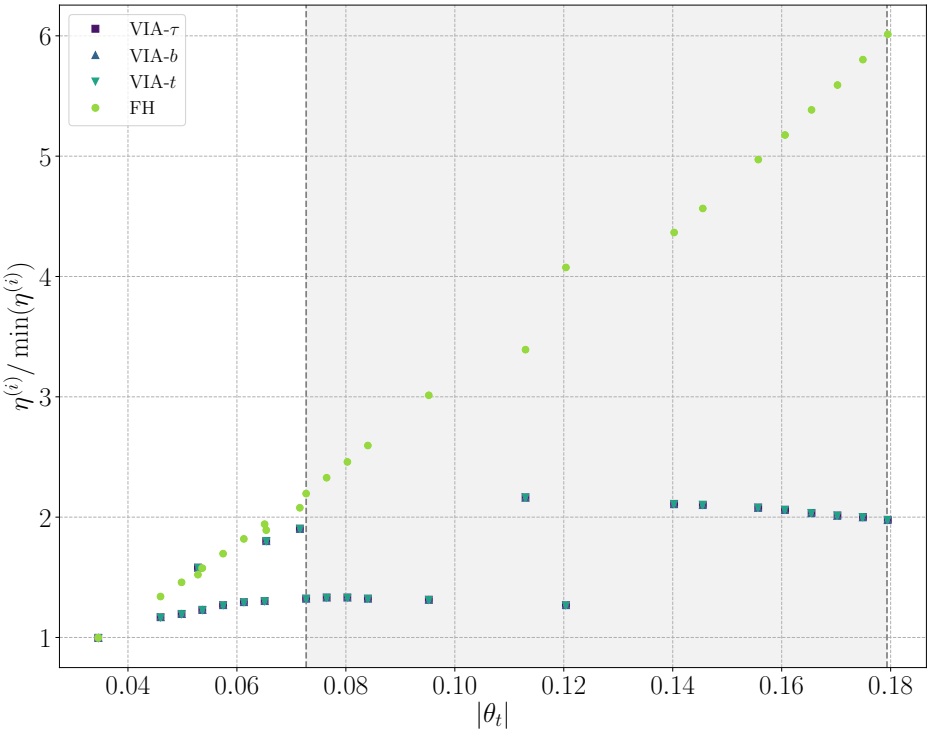

Figure 10.3.: The produced BAUs in the different approaches are shown as a function of the phase factor of the top quark θ_t. The different approaches of the quantum transport equations are introduced in Secs. 9.4.1 and 9.4.2. The phase factor is varied, while all other input parameters are kept fixed of the benchmark point `BMP II`. The gray shaded region indicates the parameter space excluded by the EDM constraints. *The figure is taken from [6].*

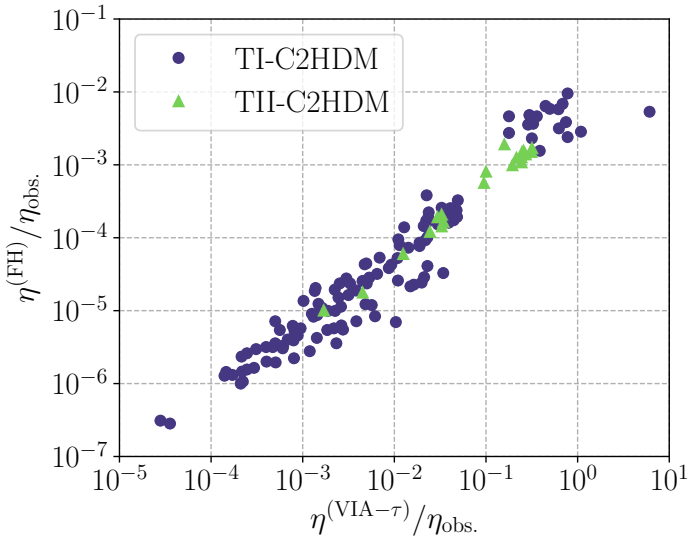

Figure 10.4.: The BAUs in both approaches for the quantum transport equations are shown, both normalized to the measured value. The blue dots correspond to the `Type I` C2HDM and the green triangles to the `Type II C2HDM`, respectively. *The figure is taken from [6].*

are shown as green triangles. First of all, both approaches to derive the quantum transport equations are correlated in the sense, that both approaches predict largest BAUs for the same benchmark points. However, the `FH` ansatz tends to produce significantly less BAU compared to the `VIA` method, around two to three orders of magnitudes. This is a known issue in the literature [195] and lead to some criticism about the validity of the approximations in the `VIA`. The expansion used in the derivation of the source term for the top quark might break down due to the large top quark mass [195, 206]. This might explain why it is possible to generate benchmark scenarios with such enhanced BAU. In this way, parameter points obeying all required conditions (experimental and theoretical constraints, NLO stable vacuum and an SFOEWPT) can be found which predict the correct amount of BAU in the `VIA`. However, the `FH` ansatz predicts less BAU and we could not find a benchmark scenario providing sufficient BAU with a small bubble wall velocity simultaneously in the `FH` ansatz. We try to give an explanation for this at the end of the section.
Furthermore, both types of the C2HDM predict similar BAU. For this reason, we discuss both types of the C2HDM simultaneously in the following.

In Fig. 10.5 the charged Higgs boson mass is shown as a function of the mass gap between h_3 and h_2. Note, that h_i $(i = 1, 2, 3)$ corresponds to mass ordered mass eigenstates of the neutral Higgs bosons. The color code indicates the normalized produced BAUs in the `FH` (`VIA`) approach on the left (right) side. As a starting the point, we want to discuss the overall mass spectrum of the C2HDM. We emphasize, that all shown points are compatible with recent measurements and provide an SFOEWPT. The upper bound of the scan ranges of the random sampling of the parameter space is given by 1.5 TeV. However, the heaviest charged and neutral masses with an SFOEWPT are of the order $\mathcal{O}(700\,\mathrm{GeV})$ and remain significantly below the experimentally possible masses. The SFOEWPT pushes the overall mass spectrum to intermediate mass ranges [4,169], which can be also observed in the N2HDM in Sec. 8.2. Furthermore, the mass gaps between the neutral Higgs bosons are rather small. Only a few parameter points provide a mass gap of the order $\mathcal{O}(100\,\mathrm{GeV})$. The electroweak oblique parameters S, T, U (see Sec. 3.1.2) put strict constraints on the mass spectrum of doublet extensions. The T parameter limits the upper bound on the mass difference between the charged Higgs bosons and the corresponding closest-in-mass neutral Higgs boson, whereas the S parameter constrains large mass-gaps between mixing Higgs bosons (in the C2HDM h_i).

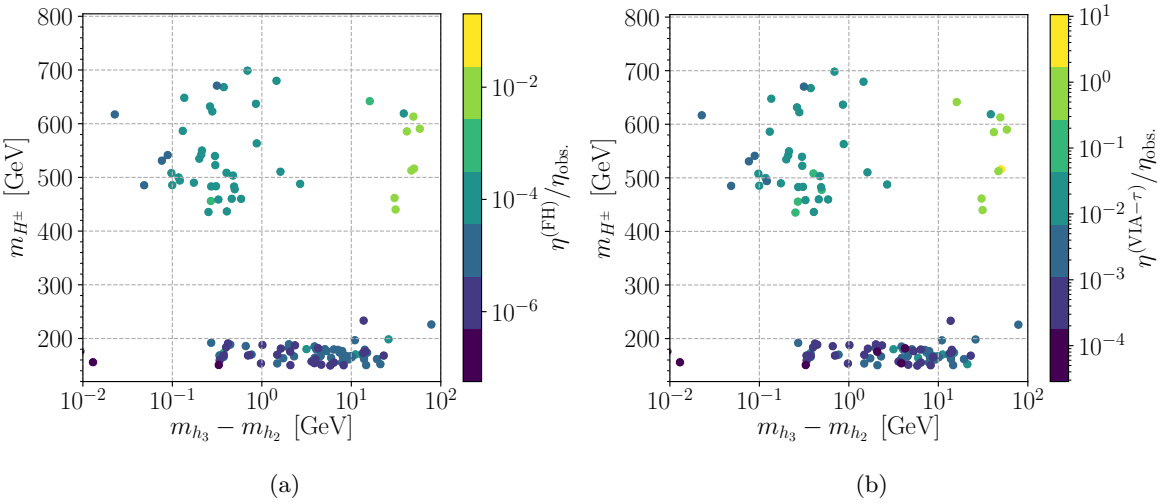

Figure 10.5.: The charged Higgs boson mass $m_{H^\pm}$ is shown versus the mass gap between the two heaviest neutral Higgs bosons h_3 and h_2. The color code indicates the normalized BAU predicted in the `FH` approach (left) and `VIA` (right). *The figures are taken from [6].*

So, already the experimental constraints influence the mass spectrum significantly. However, the additional requirement of an SFOEWPT enforces the degenerate mass spectrum even more [4, 169]. The largest produced BAU in both approaches are obtained in the heaviest mass scenarios, meaning for the largest charged Higgs boson masses and largest mass gaps.

In the following we want to investigate how we can enhance the produced BAU, or at least try to answer the question "Why is it so difficult to find valid benchmark scenarios in the C2HDM?". In Fig. 10.6 we plot the normalized BAU as a function of the product of $\theta_t \xi_c L_w T_c$. The color code indicates the average mass scale of the Higgs bosons

$$\overline{m} = \frac{1}{4}\left(\sum_{i=1}^{3} m_{h_i} + m_{H^\pm}\right) . \tag{10.4}$$

As already discussed in Sec. 10.1, we expect that the produced BAU scales with the phase factor of the complex top quark mass θ_t, since this parameter indicates the amount of CP-violation present in the benchmark point. Furthermore, the source terms in the transport equations are proportional to the phase factor. The strength of the phase transition ξ_c is also discussed in the literature to be a crucial tuning parameter for the EWBG (see *e.g.* [36]). It is expected to produce more BAU for stronger EWPT. The strength of the phase transition can be understood as a parameter describing the dynamics of the phase transition. The bubble wall thickness times the critical temperature $L_w T_c$ corresponds to the expansion factor used in the WKB ansatz in the `FH` method allowing us to estimate the validity of the expansion or approximations used in the `FH` ansatz. Moreover, L_w is used to parametrize the bubble wall profile in Eq. (9.26), thus can be understood as a parameter describing the state of the bubble. The parameter for the bubble dynamics, the wall velocity v_w, is fixed at 0.1 for all parameter points. The impact of the bubble wall velocity is shown in Fig. 10.1.

Both approaches (`FH` and `VIA`) show a clear scaling behavior with the product of all *tuning parameters* of the EWBG. For the `FH` approach this was already shown in [36][34]. Additionally, we observe that also the average mass scale of the Higgs bosons turns out to be a crucial tuning parameter for EWBG. For a fixed factor $\theta_t \xi_c L_w T_c$, the BAU can be enhanced by increasing the overall Higgs boson mass spectrum.

This might already answer the question. Large values for the phase factor of the top quarks are

[34] The authors assumed additionally that the non-SM like neutral and charged Higgs boson masses are degenerate.

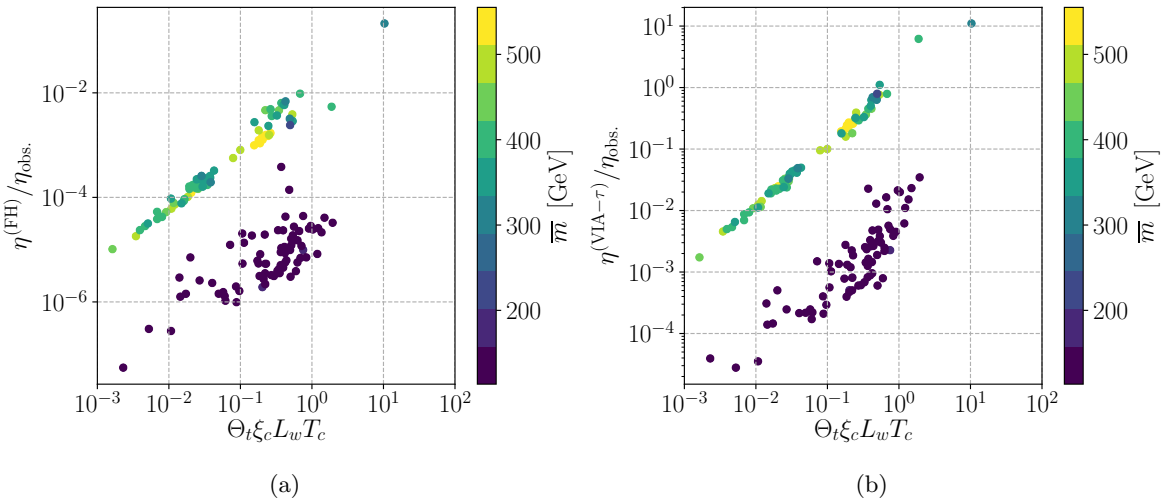

Figure 10.6.: The predicted normalized BAUs in the `FH`(left) and `VIA`(right) approach are shown as a function of the product of all *tuning parameters* in the electroweak baryogenesis. The color code indicates the average mass of all neutral and charged Higgs bosons. *The figures are taken from [6].*

limited through the EDM constraints, hence θ_t is pushed to tiny values. So the enhancement induced by the top quark phase is limited significantly. Furthermore, on the one hand side, strong EWPTs are favored, requiring the overall Higgs boson mass spectrum to be in the intermediate mass range [4, 72] and on the other hand, large BAU favors heavy Higgs boson mass scenarios. In combination with the bias induced by the oblique parameters S, T, U enforcing the charged mass to be mass degenerate with one of the neutral Higgs bosons and the mixing neutral Higgs boson masses to be *near* to each other in the masses, it is not possible to realize scenarios with large mass gaps. This contradictory requirements on the overall Higgs boson mass spectrum also limit the possibility for enhanced BAU. In this way, the crucial tuning parameters of the EWBG are separately constrained or rather the interplay between the constraints requires the tuning parameters to be small, resulting in suppressed produced BAU.

The last remaining tuning parameter $L_w T_c$ is discussed in the following. If both figures in Fig. 10.6 are directly compared to each other, the `VIA` approach tends to depend stronger on the scaling factor $\theta_t \xi_c L_w T_c$. However, the `FH` approach scales stronger with the top quark phase factor (see Fig. 10.3) and the dependence on the strength of the phase transition is not sufficient to explain the difference. Consequently, both approaches scale differently with $L_w T_c$. In Fig. 10.7, the ratio of the `FH` and `VIA` approach is shown as a function of the WKB expansion parameter $1/\epsilon_w \equiv L_w T_c$. The color code indicates again the average mass scale of the Higgs bosons. Note, that the ratio is shown on a log scale, hence there is a power law between the ratio and the expansion parameter ϵ_w, where the off-set of the ratio is determined by the average mass scale of the Higgs bosons.

The source terms in the `FH` approach are derived by using a systematic expansion in ϵ_w. The corresponding WKB ansatz is valid if the typical length scale of the particles, the de Broglie wavelength, is smaller than the length scale of the bubble wall profile, L_w. This requirement translates to $1 \ll L_w T_c$ and indicates that the `FH` approach can be trusted for *thick* wall scenarios, or small ϵ_w. But exactly for small ϵ_w (thick bubble walls), the largest discrepancies between both approaches are observed.

In the end, it is not possible to decide which approach predicts the most precise BAU, however it is remarkable, that especially the region in which the expansion used in the `FH` approach is valid, the `VIA` method predicts significantly more BAU. The different scaling behavior in

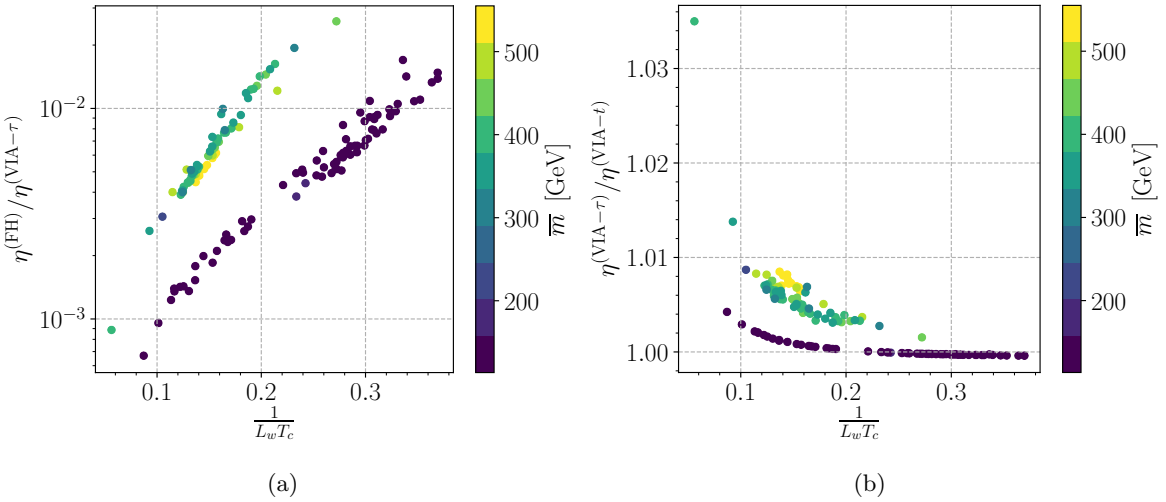

(a) (b)

Figure 10.7.: Left: The ratio of the BAU in the `FH` and `VIA` approach as a function of the expansion parameter $1/L_w T_c$; Right: The ratio of the predicted BAU in `VIA` while including massive τ, b and t and the result while solely including massive t. The color code indicates the average mass scale of the neutral and charged Higgs bosons in both figures. *The figures are taken from [6].*

terms of ϵ_w might indicate, that the `VIA` method is more sensitive to the bubble wall profile, which is not surprising. The `VIA` method derives the source term by considering the thermal fermionic propagator in the Higgs background, hence an expansion in $v(z)/T$, with the Higgs VEV at given space point z corresponding to the Higgs bubble wall profile. The wall thickness determines the Higgs bubble wall profile completely (see Eq. (9.26)).
To conclude the investigation of the impact of the EWBG, the comparison of the different `VIA` approaches is discussed. The ratio of the produced BAU in the `VIA` approach while including massive τ, b and t in the transport equations with their respective source terms and the BAU predicted by solely including a massive top quark in the transport equations, while assuming all other remaining quarks and leptons to be massless, is shown as a function of ϵ_w. The color code indicates the average mass scale of the Higgs bosons. The differences between the predicted BAUs is small for *thin* bubble walls. The largest differences are obtained for thick walls and heavy Higgs boson spectra. Since the bubble wall velocity is fixed for all parameter points, the corresponding diffusion time scale or rather the diffusion length scale is fixed. The only changing length scale in the system between two parameter points is given by the wall thickness, which indicates the length where the Higgs bubble profile is changing. In particular in this region the diffusion process is taking place, simply because the varying Higgs profile is triggering non-zero source terms. So the additional massive particles (τ and b) with their respective source terms can produce more efficiently a left-handed asymmetry for thick bubble walls. This results in the enhanced BAU compared to the approach solely taking the top quark as massive quark into account. This effect can be enhanced if the corresponding Higgs boson mass spectrum is heavy.
However, the overall effect on the enhancement of the BAU by including the τ lepton lies in the percentage range. Compared to other theoretical uncertainties as for instance the electroweak and strong sphaleron transition rates or systematical errors induced through the numerical integrations, the enhancements are almost negligible. There are attempts to further enhance the BAU through additional lepton-quark interactions [203]. This requires the introduction of dimension six operators, or including additional thermal interactions, which then are added to the transport equations. These considerations are beyond the scope of this thesis.

10.3. Conclusion

We investigated the C2HDM for the possibility of a sufficient production of BAU. We linked the theoretical and experimental collider constraints with the additional requirements of an SFOEWPT and a sufficiently large generation of BAU. To be able to calculate the BAU we first discussed the three required Sakharov conditions for a successful generation of BAU and how they can be realized in non-minimal extended Higgs sector models. After the brief sketch of the EWBG, we introduced our approach to calculate the Higgs bubble wall profile as well as both approaches to formulate the quantum transport equations. We found that both approaches `FH` and `VIA` show a mild dependence on the bubble wall velocity v_w in the *relevant* velocity range $10^{-2} \lesssim v_w \lesssim 0.2$. For the remaining wall velocities the `FH` diverges for wall velocities approaching the plasma sound speed, which is a known result in the literature. Taking into account the full wall velocity dependence in the thermal transport coefficients might cure this problem [195]. The `VIA` approach yields vanishing BAU for vanishing wall velocities as expected.
We showed that both types of the C2HDM yield similar predicted BAU and demonstrated that the respective BAU scales with the *tuning parameters of the EWBG*, namely the strength of the phase transition ξ_c, the complex phase of the top quark mass θ_t, the expansion parameter $L_w T_c$ with the bubble wall thickness L_w and the overall mass scale of the Higgs boson masses $\overline{m}$. Exactly the interplay of the electric dipole moments requiring the complex phase factor to be small and simultaneously having a strong first-order electroweak phase transition pushing the overall Higgs boson mass spectrum to intermediate ranges and the scaling with the overall mass spectrum of the Higgs bosons, complicates the search for valid benchmark scenarios in the C2HDM. This results in that we could not find any valid benchmark scenario for the `FH` approach (while using $v_w = 0.1$). However, the `VIA` approach yields valid benchmark scenarios with a sufficiently large produced BAU, while fulfilling all other remaining applied constraints.

CHAPTER 11

Final Conclusion and Outlook

The Standard Model (SM) of particle physics is confirmed to a remarkable precision and provides with the discovery of the SM-like Higgs boson in 2012 a self-consistent quantum field theory describing the properties and interactions between all observed fundamental particles. Despite its tremendous success, the SM does not provide an answer to all open questions of modern physics. In this thesis we discussed four different non-minimal extended Higgs sector models. Each of these models addresses one open issue of the SM. By linking the collider phenomenology and the investigation of the validity of the benchmark scenarios to provide a proper solution to (some of) the open questions of the SM, the parameter space of the respective model can be narrowed down significantly. This allows for more definite model predictions and a more reliable deduction of further constraints on the exclusion bounds.
In part I we briefly introduced the SM and discussed its short-comings. We reviewed the theoretical and experimental constraints, which we require for all four non-minimal extended Higgs sector models. The respective parameter scans used in this thesis are performed with the help of `ScannerS`, which applies the discussed theoretical and experimental constraints in its scans. Afterwards, we subsequently introduced the four non-minimal extended Higgs sector models: the Complex Two-Higgs Doublet model (C2HDM), which extends the SM-Higgs sector by an additional $SU(2)$ doublet, the Pseudo-Nambu-Goldstone Dark Matter model (PNGDM) extending the SM with a complex singlet, the Vector Dark Matter (VDM) model utilizing a gauged U(1) symmetry to include an additional gauge boson and finally the Next-to-Minimal Two-Higgs Doublet model (N2HDM) extending the SM by an additional $SU(2)$ doublet and singlet.
In part II we presented the calculation of the electroweak next-to leading order corrections to the spin-independent cross-section (SI-cxn). The SI-cxn is an observable to detect possible weakly-interacting massive Dark Matter (DM) candidates by measuring the recoil energy of DM-nucleon scattering processes. The inclusion of higher-order corrections gives rise to UV-divergences which have to be canceled systematically. For this purpose, we briefly discussed the on-shell renormalization of extended Higgs sectors, followed by a description of the calculation of the SI-cxn while including electroweak higher-order corrections. The detailed calculations and results of both models are shown subsequently in Chapter 5 and 6. We discussed the impact of the electroweak corrections on the *blind spots* of the respective models, hence also the sensitivity on the model constraints derived from the direct detection experiments.

In part III, we investigated the interplay between the additional requirement of a strong first-order electroweak phase transition (SFOEWPT) and the collider phenomenology of the N2HDM. The dynamics of the Higgs fields in the early universe is described within the one-loop effective potential at finite temperatures approach. A brief introduction of the one-loop effective potential was given, followed by the explanation of the numerical approach used in this thesis. We observed that the additional requirement of an SFOEWPT pushes the overall Higgs boson mass spectrum to the intermediate mass ranges of the order $\mathcal{O}(600\,\text{GeV})$ in both types of the N2HDM. Furthermore, the one-loop trilinear couplings between three SM-like Higgs bosons derived from the effective potential are enhanced compared to the SM-reference value, while significantly remaining below the maximal allowed value by the experimental constraints.
The final part IV of this thesis dealt with the calculation of the additional requirement of a sufficiently large produced baryon asymmetry of the universe (BAU) in combination with the collider phenomenology within the C2HDM. The C2HDM provides an extended Higgs sector enabling an SFOEWPT on the one hand and on the other hand also CP-violation. CP-violation is one of three required conditions a model needs to fulfill for successful baryogenesis. We used a two-step approach to calculate the BAU, where we first introduced two different approaches to derive the quantum transport equations, the top transport based on the semi-classical force as well as the VEV-insertion approximation. Both approaches yield a set of coupled quantum transport equations for the particle densities in front of the Higgs bubble wall. The solution allows for the determination of the BAU by solving the thermalization through electroweak sphaleron processes in a second step. We extended the `C++` code `BSMPT` to be able to solve the transport equations numerically and to provide the predicted BAU. We used several parametrizations of the quantum transport equations in order to compare the different impacts of the approximations. In all approaches we observed that the predicted BAU is enhanced for heavy Higgs boson mass scenarios and scales with the complex phase factor of the top quark, a measure for the CP-violation in the model. However, the electric dipole moment constraints put a severe constraint on the C2HDM parameter space requiring the complex phase of the top quark to be small. In addition, the requirement of an SFOEWPT pushes the overall Higgs boson mass spectrum to intermediate range limiting indirectly the sufficient production of the BAU. This interplay of the collider and cosmological constraints made it so problematic to find valid benchmark scenarios.
In the absence of new physics signatures at the LHC, and at the same time the demanding task to explain the outstanding open problems of modern physics such as the generation of the BAU or DM, it is important to explore a wide range of avenues beyond the measurements at the LHC to answer questions about the nature of DM or the BAU. The electroweak phase transition is not only required in the context of electroweak baryogenesis, but could also gives rise to a contribution to the gravitational waves spectrum. With the upcoming LISA experiment and the detection of the gravitational waves, a new window is opened to the exploration of the universe. These insights may give further additional constraints on the respective model parameter space. Furthermore, a closer look in the phase structure of the effective potential at finite temperature in non-minimal extended Higgs sector models may allow us to find more complex phase transitions. Temperature effects may allow for spontaneous generation of CP-violation in otherwise CP-conserving models or even CP-violation in dark sectors could be transferred to the visible sector. These effects could enhance the amount of CP-violation and hence the production of the BAU. With the development of `BSMPT v2`, we have a generic tool at hands allowing us to investigate the phase structures at finite temperatures in an arbitrary extended Higgs sector.
Next to the solution of conceptional problems and new approaches, also precision in the experiment as well as in the theoretical predictions enables to derive more appropriate constraints. Especially in DM studies, often higher-order corrections are missing due to the

plethora of different DM models, or even conceptional problems. Automatized calculations of electroweak higher-order corrections are a challenging task, but might be possible in the near future. This might allow for a systematic investigation of the impacts of higher-order corrections on the DM phenomenology in different models. In addition to the spin-independent interactions, also the velocity and momentum transfer suppressed operators contribute to the effective DM-nucleus interactions. A priori it is unclear if these operator contributions are of the same order as the electroweak corrections. A proper treatment of these operators and corresponding higher-order corrections are required.

APPENDIX A

Appendix A

A.1. Strict Vanishing Momentum Expansion

The regularization of the IR divergences in the QED subset requires a different approach than the usual inclusion of real radiation. In the following, we show the detailed derivation of the virtual one-loop vertex corrections and the required counterterms in the *strict vanishing momentum expansion*. The expansion allows us to regulate and cancel the IR divergences in the QED subset. The corresponding virtual one-loop correction is depicted in Fig. A.1(a). The one-loop tensor integral C_μ arises in the reduction of the amplitude in Fig. A.1(a), which can be expanded as follows

$$C_\mu = \int_k \frac{k_\mu}{k^2 \left[(k+p_1)^2 - m^2\right] \left[(k+p_2)^2 - m^2\right]} \tag{A.1a}$$

$$= \int_k \frac{k_\mu}{k^2} \frac{1}{(k^2-m^2)^2} \left[\frac{1}{1+\frac{p_1^2+2p_1\cdot k}{k^2-m^2}}\right] \left[\frac{1}{1+\frac{p_2^2+2p_2\cdot k}{k^2-m^2}}\right] \tag{A.1b}$$

$$= \int_k \frac{k_\mu}{k^2} \frac{1}{(k^2-m^2)^2} \left[1 - \frac{2k\cdot p_1}{k^2-m^2}\right] \left[1 - \frac{2k\cdot p_2}{k^2-m^2}\right] + \mathcal{O}\left(p_i^2\right) \tag{A.1c}$$

$$\underbrace{=}_{\text{uneven}} -2 \int_k \frac{k_\mu k_\nu (p_1+p_2)^\nu}{k^2 \left(k^2-m^2\right)^3} + \mathcal{O}\left(p_i^2\right) \tag{A.1d}$$

$$= -\frac{2g_{\mu\nu}}{D} \int_k \frac{k^2 (p_1+p_2)^\nu}{k^2 \left(k^2-m^2\right)^3} + \mathcal{O}\left(p_i^2\right) \tag{A.1e}$$

$$= -\frac{2}{D} \int_k (p_1+p_2)_\mu C_0(0,0,0,m,m,m) \ , + \mathcal{O}\left(p_i^2\right) \tag{A.1f}$$

where we used the symmetry of loop integrals

$$\int_k k_\mu k_\nu f(k^2) = \frac{g_{\mu\nu}}{D} \int_k k^2 f(k^2) \ , \tag{A.2}$$

in Eq. (A.1e). For better readability, we use m as the quark mass m_q here and in the following. D indicates the dimension and it is treated in DimReg, $D = 4 - 2\varepsilon$. Furthermore, we use

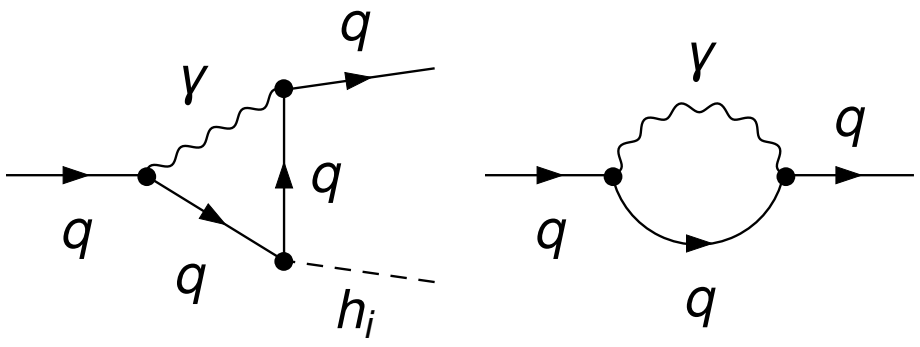

(a) (b)

Figure A.1.: Both diagrams of the QED subsets. Left: the virtual one-loop vertex corrections; Right: one-loop self-energy contribution required for the derivation of the WFRC and mass counterterm.

the shorthand notation $\int_k = \mu^{D-4} \int \frac{d^D k}{(2\pi)^D}$. In the last step in Eq. (A.1f), the three-point scalar integral was identified with the standard Passarino-Veltmann integral C_0. The vertex correction in Fig. A.1(a) is given as

$$\mathcal{M}_{VC} = \int_k \bar{u}(p_1)\,(-ie\gamma_\alpha)\,\frac{i\,(\not{k}+\not{p}_1+m)}{(k+p_1)^2-m^2}\,(-iC_{h_i})\,\frac{i\,(\not{k}+\not{p}_2+m)}{(k+p_2)^2-m^2}\,(-ie\gamma_\beta)\,\frac{-ig^{\alpha\beta}}{k^2}u(p_2) \tag{A.3a}$$

$$= -e^2 C_{h_i}\bar{u}(p_1)\int_k \frac{\gamma_\alpha\,(\not{k}+\not{p}_1+m)\,(\not{k}+\not{p}_2+m)\,\gamma^\alpha}{D_0 D_1 D_2}\,, \tag{A.3b}$$

with the denominators

$$D_0 = k^2\,, \tag{A.4a}$$
$$D_1 = (k+p_1)^2 - m^2 \tag{A.4b}$$
$$D_2 = (k+p_2)^2 - m^2\,. \tag{A.4c}$$

C_{h_i} indicates the quark-quark-Higgs boson coupling.

Applying the equations of motion and using the slash identities in DimReg

$$\gamma_\alpha \not{a}\not{b}\gamma^\alpha = 4ab + (D-4)\not{a}\not{b} \tag{A.5a}$$
$$\gamma_\alpha \not{a}\gamma^\alpha = -(D-2)\not{a} \tag{A.5b}$$

allows us to reduce the vertex corrections further

$$\mathcal{M}_{VC}^{(\mathrm{QED})} = -e^2 C_{h_i}\bar{u}(p_1)\int_k \frac{1}{D_0 D_1 D_2}\left[2\,(D_1+D_2) - p_1^2 - p_2^2 + p_1\cdot p_2 - 2\epsilon D_0 - 4m\not{k} + 4m^2\right]u(p_2)$$

$$= -e^2 C_{h_i}\bar{u}(p_1)\left[\int_k \frac{1}{D_0 D_1 D_2}\left[2\,(D_1+D_2) - 2\epsilon D_0 + 4m^2\right] - 4mC_\mu\gamma^\mu\right]u(p_2) \tag{A.6a}$$

$$= -e^2 C_{h_i} \bar{u}(p_1)\{4B_0(0,0,m) - 2\epsilon B_0(0,m,m) + 4m^2 C_0(0,0,0,0,m,m) \\ -4mC_\mu \gamma^\mu\} u(p_2) \tag{A.6b}$$

$$= -ie^2 \mathcal{M}_{\text{LO}}\{4B_0(0,0,m) - 2\epsilon B_0(0,m,m) + 4m^2 C_0(0,0,0,0,m,m) \\ + \frac{16m^2}{D} C_0(0,0,0,m,m,m)\}\,. \tag{A.6c}$$

In the last step, the LO amplitude is factorized. In conclusion, the one-loop vertex correction can be expressed in terms of the one-loop standard integrals of the Passarino-Veltmann basis. All contributing integrals are IR-safe. The UV poles can be identified by further reduction to A_0 and B_0

$$C_0(0,0,0,0,m,m) = \int_k \frac{1}{k^2\left(k^2-m^2\right)^2} = \underbrace{\frac{B_0(0,m,m)}{m^2}}_{\frac{1}{m^2}(\ln(\mu^2/m^2)+\Delta_\epsilon)} + \frac{A_0(0)-A_0(m)}{m^4} \tag{A.7}$$

and

$$B_0(0,0,m) = 1 + \ln\left(\frac{\mu^2}{m^2}\right) + \Delta_\epsilon\,. \tag{A.8}$$

The calculation of the counterterm requires the self-energy diagram in Fig. A.1(b). We use the following reduction of the tensor integral B_μ,

$$B_\mu = p_\mu B_1(p,0,m) = p_\mu \left[\frac{1}{2p^2}\left(A_0(0) - A_0(m) - \left(p^2-m^2\right)B_0(p,0,m)\right)\right]\,. \tag{A.9}$$

This allows us to calculate the one-loop self-energy

$$\Sigma(\not{p}) = \int_k (-ie\gamma_\nu)\frac{i\left(\not{k}+\not{p}+m\right)}{(k+p)^2-m^2}(-i\gamma_\mu)\frac{-ig^{\mu\nu}}{k^2} \tag{A.10a}$$

$$\underbrace{=}_{\text{Eq. (A.5b)}} -e^2\left[\int_k \frac{(2-D)\not{k}}{k^2[(k+p)^2-m^2]} + \int_k \frac{(2-D)\not{p}}{k^2[(k+p)^2-m^2]} + \int_k \frac{Dm}{k^2[(k+p)^2-m^2]}\right] \tag{A.10b}$$

$$= -e^2\left[DmB_0(p,0,m) + (2-D)\not{p}\underbrace{\left(\frac{A_0(0)-A_0(m)+\left(p^2+m^2\right)B_0(p,0,m)}{2p^2}\right)}_{F(p^2)}\right]\,. \tag{A.10c}$$

We refer to the brackets as $F(p^2)$. The self-energy can be separated in left-, right-handed and scalar parts in accordance to [83]

$$i\Sigma(p^2) = i\left[\not{p}\omega_-\Sigma^L(p^2) + \not{p}\omega_+\Sigma^R(p^2) + m\Sigma^S(p^2)\right]\,, \tag{A.11}$$

with the corresponding left-/right-handed projectors $\omega_\mp$. This allows us to identify and expanding for strict vanishing momentum

$$\Sigma^L(p^2) = \Sigma^R(p^2) = -e^2(2-D)F(p^2) = -e^2(2-D)F(0) + \mathcal{O}(p^2) \tag{A.12}$$

$$= -e^2\frac{2-D}{2}\left[B_0(0,0,m) + m^2 B_0'(0,0,m)\right] + \mathcal{O}(p^2) \tag{A.13}$$

and

$$\Sigma^S(p^2) = -e^2 D B_0(p,0,m) = -e^2 D B_0(0,0,m) + \mathcal{O}(p^2) \tag{A.14}$$

With this at hand, the required mass counterterm for the quark q is given by

$$\delta m_q^{(\mathrm{QED})} = -me^2 \left[\frac{D+2}{2} B_0(0,0,m) - \frac{D-2}{2} m^2 B_0'(0,0,m) \right] + \mathcal{O}(p^2) \ . \tag{A.15}$$

The WFRCs of the quark requires the derivatives of the self-energies with respect to the external momentum

$$\frac{\partial \Sigma^S}{\partial p^2} = \frac{\partial}{\partial p^2} \left[-e^2 D B_0(p,0,m) \right] = -De^2 B_0'(p,0,m) = -De^2 B_0'(0,0,m) + \mathcal{O}(p^2) \,, \tag{A.16}$$

$$\frac{\partial \Sigma^{(L/R)}}{\partial p^2} = -e^2 (2-D) \underbrace{\frac{\partial F(p^2)}{\partial p^2}}_{\sim p^2} = \mathcal{O}(p^2) \ , \tag{A.17}$$

which allows us to formulate the WFRCs as

$$\delta Z^{(L/R),(\mathrm{QED})} = \mathrm{Re} \left[e^2 \frac{2-D}{2} B_0(0,0,m) + e^2 m^2 \frac{2+3D}{2} B_0'(0,0,m) \right] + \mathcal{O}(p^2) \ . \tag{A.18}$$

Using the presented results for the virtual one-loop correction and the respective counterterms of the QED subset in the same way as presented in Sec. 6.2.3, the QED subset yields a UV and IR safe result, allowing for a consistent extraction of the Wilson coefficient.

APPENDIX B

SM Input Parameters for BSMPT

We list the SM input parameters used in BSMPT. The fine structure constant is taken at the Z boson mass scale [215],

$$\alpha_{\rm EM}^{-1}(M_Z^2) = 128.962\,, \tag{B.1}$$

and the respective masses for the gauge bosons are

$$m_W = 80.385\,\text{GeV} \quad \text{and} \quad m_Z = 91.1876\,\text{GeV}\,. \tag{B.2}$$

The lepton and quark masses are taken as

$$m_e = 0.511\ \text{MeV}, \quad m_\mu = 105.658\ \text{MeV}, \quad m_\tau = 1.777\,\text{GeV}\,, \tag{B.3}$$

and

$$m_u = m_d = m_s = 100\ \text{MeV}\,. \tag{B.4}$$

For consistency, the on-shell top quark mass is used as input parameter [137]

$$m_t = 172.5\,\text{GeV} \tag{B.5}$$

and the recommended charm and bottom quark on-shell masses

$$m_c = 1.51\ \text{GeV} \quad \text{and} \quad m_b = 4.92\ \text{GeV}\,. \tag{B.6}$$

To account for the CP-violation in the CKM matrix, we parametrize the CKM matrix by three mixing angles and the CP-violating phase δ [100]

$$V_{\rm CKM} = \begin{pmatrix} c_{12}c_{13} & s_{12}c_{13} & s_{13}\,\mathrm{e}^{-i\delta} \\ -s_{12}c_{23} - c_{12}s_{23}s_{13}\,\mathrm{e}^{i\delta} & c_{12}c_{23} - s_{12}s_{23}s_{13}\,\mathrm{e}^{i\delta} & s_{23}c_{13} \\ s_{12}s_{23} - c_{12}c_{23}s_{13}\,\mathrm{e}^{i\delta} & -c_{12}s_{23} - s_{12}c_{23}c_{13}\,\mathrm{e}^{i\delta} & c_{23}c_{13} \end{pmatrix}\,, \tag{B.7}$$

where $s_{ij} = \sin\theta_{ij}$ and $c_{ij} = \cos\theta_{ij}$. The EW VEV is taken as

$$v = 1/\sqrt{\sqrt{2}G_F} = 246.22\,\text{GeV}\,. \tag{B.8}$$

APPENDIX C

Calculation of the Baryon Asymmetry

In this appendix we present the derivation of the *master equation*

$$\frac{n_B}{s} = \frac{-3\tilde{\Gamma}_{ws}}{2v_w s}\int_0^\infty \exp\left(-\frac{\tilde{\Gamma}_{ws}\mathcal{R}}{v_w}z'\right) n_L^0(z')dz' \ , \tag{C.1}$$

in detail. The equation allows us to determine the BAU as a function of the rescaled sphaleron transition rate (per unit volume) $\tilde{\Gamma}_{ws} = 6\kappa\alpha_w^5 T$, the bubble wall velocity and the initial profile of the left-handed fermion density.
There are several time-scales involved in the description of the thermal system of the early universe. The time-scale of the sphaleron transition is given by the inverse of the transition rate

$$\tau_{ws} \equiv (\Gamma_{ws})^{-1} \ . \tag{C.2}$$

In addition, there are interactions present in the plasma. However, it turns out that the interaction rates as *e.g.* the Yukawa interactions, relaxations and the strong sphaleron transitions are much larger than the electroweak sphaleron rate. Hence, the actual calculation of the BAU can be separated in two distinct steps: First determine the net left-handed fermion excess in front of the bubble wall by solving the quantum transport equations. As a second step consider the actual transition of the left-handed fermion density to the baryon-asymmetry through sphaleron transitions.
In this way, the diffusion process of the left-handed fermions equilibrating through sphaleron transitions on a time-scale τ_{ws} can be considered completely decoupled from the other interaction present in the hot thermal system. This means that the net left-handed quark and lepton densities $n_{(q/l)_L}$ are in a chemical balance in the symmetric phase

$$3\ n_{q_L} + n_{l_L} \rightleftharpoons 0 \ . \tag{C.3}$$

If the bias is small (the densities correspond *almost* to the equilibrium values), detailed balance arguments with the usage of Fick's Law allow us to find an equation for the baryon asymmetry n_B (*e.g.* [189])

$$\dot{n}_B - D\boldsymbol{\nabla}^2 n_B = -N_f\frac{\Gamma_{ws}}{T}(\mu_{ws} + \mu_{ws}^0) \ , \tag{C.4}$$

with the diffusion constant D of the baryons in the symmetric phase, the family number N_f, the electroweak sphaleron rate Γ_{ws} and the chemical potentials trigger the baryon-asymmetry production. In the wall rest-frame, which corresponds to a co-moving frame with bubble-wall velocity v_w, we are interested in a static solution obeying $n_B(z,t) = n_B(z - v_w t)$. Hence, the left-hand side of Eq. (C.4) can be formulated as

$$\partial n_B \equiv -v_w n_B' - D\, n_B'' \ , \tag{C.5}$$

with $(\ldots)'$ denotes the derivative with respect to the only spatial coordinate z. The chemical potentials thriving the baryon production consist of two parts, the first term describes the *dynamically* produced chemical potentials, which are produced during τ_{ws}. The initial condition μ_{ws}^0 corresponds to the bias left-handed density produced by the CP-violation at the bubble wall beforehand. The chemical potential μ_p of a particle specie p can be linked with its particle number density n_p through the high-temperature expansion

$$n_p = \kappa_p \left(\frac{T^2}{6}\right) \mu_p + \mathcal{O}\left(\mu_p^3\right) \ , \tag{C.6}$$

with the statistical factor κ_p, which is 6 for quarks and 2 for leptons at zero temperature. Eq. (C.3) implies that the contributing chemical potentials are given by

$$\begin{aligned} \mu_{ws} &= \sum_{\text{fam.}} \left(3\mu_{q_L} + \mu_{l_L}\right) = \sum_{\text{fam.}} \left(\frac{6}{T^2}\right) \left(3\, \frac{n_{q_L}}{\kappa_q} + \frac{n_{l_L}}{\kappa_l}\right) \simeq \frac{1}{2} \left(\frac{6}{T^2}\right) \sum_{\text{fam.}} \left(n_{q_L} + n_{l_L}\right) \\ &\equiv \frac{1}{2} \left(\frac{6}{T^2}\right) n_L \ , \end{aligned} \tag{C.7}$$

where we used the high-temperature expansion and the zero temperature statistical factors to define the left-handed particle density.
The strong sphaleron rate is fast on the relevant time-scale, hence the involved particles are in equilibrium and the respective chemical potential is zero

$$0 = \mu_{ss} \sim \sum_{\text{fam.}} \left(n_{q_L} - n_{u_R} - n_{d_R}\right) \ , \tag{C.8}$$

with the left- and right-handed quark particle number densities. This implies that any net number of left-/right-handed particles are immediately divided into left- and right-handed quarks of the same generation through a strong sphaleron transition. Since the strong sphaleron ensures the balance between left- and right-handed quarks, the baryon number can be expressed in terms of the quark number density

$$n_B = n_B|_L + n_B|_R = 2\, n_B|_L = \frac{2}{3} \sum_{\text{fam.}} n_{q_L} \ . \tag{C.9}$$

The electroweak sphaleron conserves $B - L$ and thus all produced leptons on the time-scale τ_{ws} are directly related with the baryon asymmetry

$$n_B = \sum_{\text{fam.}} n_{l_L} \ . \tag{C.10}$$

Eqs. (C.9) and (C.10) allow us to express the first relaxing term in Eq. (C.4) as

$$\mu_{ws} = \frac{1}{2} \left(\frac{6}{T^2}\right) \left(\frac{3}{2} + 1\right) n_B \equiv \frac{1}{3} \left(\frac{6}{T^2}\right) \mathcal{R} n_B \ . \tag{C.11}$$

The SM relaxation term $\mathcal{R}$ is given by $15/4$. Finally, we can write down the differential equation for the baryon number density

$$-v_w n_B' - D n_B'' = -\tilde{\Gamma}_{ws} \left(\frac{3}{2} n_L^0 + \mathcal{R} n_B\right) \ , \tag{C.12}$$

where the family number is already taken to be $N_f = 3$ and the electroweak sphaleron rate is rescaled by

$$\tilde{\Gamma}_{ws} = \frac{6}{T^3}\Gamma_{ws} \ . \tag{C.13}$$

Solving the harmonic oscillator equation yields the following result (see next section for details)

$$\frac{n_B}{s} = \frac{-3\tilde{\Gamma}_{ws}}{2\Omega s}\int_0^\infty \exp\left(\frac{v_w - \Omega}{2D}z'\right) n_L^0(z')dz' \ , \tag{C.14}$$

with

$$\Omega = \sqrt{v_w^2 + 4\tilde{\Gamma}_{ws}D\mathcal{R}} \ , \tag{C.15}$$

and the entropy density

$$s = \frac{2\pi^2}{45}g_* T^3 \, . \tag{C.16}$$

The entropy density is given in terms of the effective degrees of freedom of the universe at electroweak temperatures, $g_* \simeq 106.75$, and the temperature T. The exponent can be simplified further to the result in Eq. (C.1) by using $4D\tilde{\Gamma}_{ws}\mathcal{R} \ll v_w^2$, which is true for typical wall speeds of $\mathcal{O}(v_w) \gtrsim 10^{-2}$.

C.1. Intermezzo: Solving the HO Equation

In this section, we want to present the solution of the differential equation defined in Eq. (C.12) to fix all sign conventions. Simplifying and writing the equation in Eq. (C.12) in the canonical form of a harmonic oscillator yields

$$n_B''(z) + 2\gamma n_B'(z) - \omega_0^2 n_B(z) = \tilde{n}_L(z) \ , \tag{C.17}$$

where we implicit defined

$$\gamma = \frac{v_w}{2D} \, , \quad \omega_0^2 = \frac{\Gamma_{ws}\mathcal{R}}{D} \, , \quad \tilde{n}_L(z) = \frac{3\Gamma_{ws}}{2D}n_L^0 \, , \quad \sqrt{\gamma^2 + \omega_0^2} = \frac{1}{2D}\sqrt{v_w^2 + 4\Gamma_{ws}D\mathcal{R}} \, . \tag{C.18}$$

Note that the initial left-handed fermion density is z dependent. We are interested in the particular solution. Hence, we need to solve for the Green's function

$$\left[\partial_z^2 + 2\gamma\partial_z - \omega_0^2\right] G(z, z') = \delta(z - z') \, . \tag{C.19}$$

Using the following conventions for the Fourier transformation

$$G(z, z') = \int_{\mathbb{R}} \frac{d\omega}{2\pi} e^{-i\omega z} G(\omega, z') \, , \quad G(\omega, z') = \int_{\mathbb{R}} e^{i\omega z} G(z, z') \ , \tag{C.20}$$

allows us to find the solution of the Fourier transformed function

$$G(\omega, z') = \frac{-e^{i\omega z'}}{\omega^2 + 2i\gamma\omega + \omega_0^2} \ , \tag{C.21}$$

and finally the Green's function in coordinate space

$$G(z, z') = \int_{\mathbb{R}} \frac{d\omega}{2\pi} \frac{-e^{-i\omega(z-z')}}{\omega^2 + 2i\gamma\omega + \omega_0^2} = \int_{\mathbb{R}} \frac{d\omega}{2\pi} \frac{-e^{-i\omega(z-z')}}{(\omega - \omega_-)(\omega - \omega_+)} \ , \tag{C.22}$$

with two purely imaginary poles at

$$\omega_\pm = i\left(-\gamma \pm \sqrt{\gamma^2 + \omega_0^2}\right) \, . \tag{C.23}$$

The Cauchy theorem allows us to perform the integration over ω by closing the integral path in the complex plane. However, we have to distinguish between to cases: for $z > z'$ we have to close the integration contour below the real axis, where the Cauchy theorem yields

$$G(z, z') = \theta\left(z - z'\right) \frac{2\pi i}{2\pi}(-1) \lim_{z \to \omega_-} \frac{-e^{-i\omega(z-z')}}{\omega - \omega_+} \,. \tag{C.24}$$

Note the additional sign due to the index of the path. Analogously for $z < z'$ we find

$$G(z, z') = \theta(z' - z) i(+1) \frac{-e^{-\omega_+(z-z')}}{\omega_+ - \omega_-} \,. \tag{C.25}$$

Combining both results and using the definition of $\omega_\pm$

$$G(z, z') = \frac{-1}{2\sqrt{\gamma^2 + \omega_0^2}} e^{-\gamma(z-z')} \left(\theta(z - z') e^{-\sqrt{\gamma^2+\omega_0^2}(z-z')} + \theta(z' - z) e^{\sqrt{\gamma^2+\omega_0^2}(z-z')}\right) \,, \tag{C.26}$$

allows us to calculate the particular solution by

$$n_B(z) = \int_{\mathbb{R}} dz' G(z, z') \tilde{n}_L(z') \,. \tag{C.27}$$

We want to find the produced BAU at the origin of the bubble wall ($z = 0$) and further need to account for the exponentially suppressed sphaleron transition rate in the broken phase ($z < 0$). Hence, the baryon number in the broken phase remains constant and we only need to integrate over the symmetric phase ($z' > 0$) yielding

$$n_B(0) = \frac{-1}{2\sqrt{\gamma^2 + \omega_0^2}} \int_0^\infty e^{+\gamma z'} e^{-\sqrt{\gamma^2+\omega_0^2} z'} \tilde{n}_L(z') dz' \,. \tag{C.28}$$

By plugging in the definitions in Eq. (C.18) we reproduce the solution given in Eq. (C.14).

Acknowledgements (Danksagungen)

Mein besonderer Dank gilt meiner Doktormutter Frau Prof. Dr. M. Margarete Mühlleitner. Sie hat mir die Möglichkeit gegeben vier Jahre während meiner Master Arbeit als auch bei der Doktorarbeit an einer der spannendsten Forschungsfelder mitzuwirken und mich stets unterstützt. Ich danke ihr für die vielen Diskussionen, die mich stets weiter gebracht haben. Weiterhin möchte ich mich für die von ihr angeleiteten internationalen Kollaboration und die Forschungsaufenthalte in Lissabon bedanken. Die Ausflüge waren stets ein Jahreshighlight.

Ich möchte mich bei PD Dr. Stefan Gieseke bedanken, der sich bereit erklärt hat den Zweitkorrektor zu übernehmen, aber auch für die Jam Sessions in der ITP Band "The Unharmonic Perturbations".

I want to express my gratitude to Prof. Dr. Rui Santos for his hospitality during several of my stays in Portugal, but also for the countless interesting discussions about physics.

Ich bedanke mich bei Philipp Basler für die Zusammenarbeit, aber auch für die spannende Reise während der letzten vier Jahre. Ohne ihn wären die zahlreichenden frustrierende Momente wohl nicht einfach vorbei gegangen.

Weiterhin möchte ich mich bei Martin Gabelmann bedanken. Ich habe die zahlreichen Diskussionen über Physik (oder ähnliches) genossen, auch wenn er mich nicht von VIM überzeugen konnte.

Ich bedanke mich bei Marcel Krause für die unzählbaren Hilfestellungen und Beantwortung von noch mehr Fragen während meiner Anfangszeit, aber auch im Verlauf meiner Doktorzeit.

Bedanken möchte ich mich auch bei Jonas Wittbrodt für seine Unterstützung bei Fragen über `ScannerS`.

Ich möchte mich ebenfalls bei Tizian Römer für die klasse Zusammenarbeit während seiner Masterarbeit bedanken.

I want to thank our DM working group consisting of Seraina Glaus, M. M. Mühlleitner, Tizian Römer, Shruti Patel and Rui Santos. Even though, this project was meant to be a *three month project* I enjoyed the countless discussions and I cannot believe how much I learned during this journey.

I thank Shruti Patel for several very helpful discussions about various aspects of my thesis and for being a kind of remote home office buddy during these strange times.

I express my gratitude to Niklas Arnold, Philipp Basler, Martin Gabelmann, Shruti Patel, Sabine Schork and Sophie Williamson for proofreading parts of my thesis and for providing helpful feedback.

Special thanks go to Stefan Liebler and Marcel Krause for taking care of the ITP coffee machine.

I would like to thank all members of the Institute of Theoretical Physics for the inspiring

time at the institute and for the countless discussions.

Ich möchte ich mich bei all meinen Freunden, die mich bei dieser Reise begleitet und unterstützt haben, bedanken.

Zu guter Letzt bedanke ich mich bei meiner Freundin und meinen Eltern. Ohne Euch wäre ich heute nicht da wo ich bin. Ihr habt es mir ermöglicht mich stets auf mein Studium zu konzentrieren und in schwierigen Zeiten zur Seite gestanden, danke!

Auch wenn ich ihr nicht mehr persönlich danken kann, möchte ich mich bei meiner Großmutter bedanken, die mich von klein auf motiviert hat meinen Weg zu gehen.

References

[1] S. Glaus, M. Mühlleitner, J. Müller, S. Patel, and R. Santos, "Electroweak Corrections to Dark Matter Direct Detection in a Vector Dark Matter Model," *JHEP* **10** (2019) 152, arXiv:1908.09249 [hep-ph].

[2] S. Glaus, M. Mühlleitner, J. Müller, S. Patel, and R. Santos, "NLO corrections to Vector Dark Matter Direct Detection – An update," *PoS* **CORFU2019** (2020) 046, arXiv:2005.11540 [hep-ph].

[3] S. Glaus, M. Mühlleitner, J. Müller, S. Patel, T. Römer, and R. Santos, "Electroweak Corrections in a Pseudo-Nambu Goldstone Dark Matter Model Revisited," arXiv:2008.12985 [hep-ph].

[4] P. Basler, M. Mühlleitner, and J. Müller, "Electroweak Phase Transition in Non-Minimal Higgs Sectors," *JHEP* **05** (2020) 016, arXiv:1912.10477 [hep-ph].

[5] P. Basler, M. Muhlleitner, and J. Müller, "BSMPT v2 A Tool for the Electroweak Phase Transition and the Baryon Asymmetry of the Universe in Extended Higgs Sectors," arXiv:2007.01725 [hep-ph].

[6] P. Basler, M. Mühlleitner, and J. Müller, "Electroweak Baryogenesis Revisited in the Complex Two-Higgs Doublet Models," arXiv:tba.

[7] S. L. Glashow, "Partial-symmetries of weak interactions," *Nuclear Physics* **22** no. 4, (1961) 579 – 588. http://www.sciencedirect.com/science/article/pii/0029558261904692.

[8] F. Englert and R. Brout, "Broken symmetry and the mass of gauge vector mesons," *Phys. Rev. Lett.* **13** (Aug, 1964) 321–323. https://link.aps.org/doi/10.1103/PhysRevLett.13.321.

[9] P. W. Higgs, "Broken symmetries and the masses of gauge bosons," *Phys. Rev. Lett.* **13** (Oct, 1964) 508–509. https://link.aps.org/doi/10.1103/PhysRevLett.13.508.

[10] G. S. Guralnik, C. R. Hagen, and T. W. B. Kibble, "Global conservation laws and massless particles," *Phys. Rev. Lett.* **13** (Nov, 1964) 585–587. https://link.aps.org/doi/10.1103/PhysRevLett.13.585.

[11] P. Higgs, "Broken symmetries, massless particles and gauge fields," *Physics Letters* **12** no. 2, (1964) 132 – 133. http://www.sciencedirect.com/science/article/pii/0031916364911369.

[12] T. W. B. Kibble, "Symmetry breaking in non-abelian gauge theories," *Phys. Rev.* **155** (Mar, 1967) 1554–1561. https://link.aps.org/doi/10.1103/PhysRev.155.1554.

[13] S. Weinberg, "A model of leptons," *Phys. Rev. Lett.* **19** (Nov, 1967) 1264–1266. https://link.aps.org/doi/10.1103/PhysRevLett.19.1264.

[14] A. Salam and J. C. Ward, "Weak and electromagnetic interactions," *Nuovo Cim.* **11** (1959) 568–577.

[15] **ATLAS** Collaboration, G. Aad *et al.*, "Observation of a new particle in the search for the Standard Model Higgs boson with the ATLAS detector at the LHC," *Phys. Lett. B* **716** (2012) 1–29, arXiv:1207.7214 [hep-ex].

[16] **CMS** Collaboration, S. Chatrchyan *et al.*, "Observation of a New Boson at a Mass of 125 GeV with the CMS Experiment at the LHC," *Phys. Lett. B* **716** (2012) 30–61, arXiv:1207.7235 [hep-ex].

[17] M. Baak, M. Goebel, J. Haller, A. Hoecker, D. Kennedy, R. Kogler, K. Moenig, M. Schott, and J. Stelzer, "The Electroweak Fit of the Standard Model after the Discovery of a New Boson at the LHC," *Eur. Phys. J. C* **72** (2012) 2205, arXiv:1209.2716 [hep-ph].

[18] **ATLAS, CMS** Collaboration, G. Aad *et al.*, "Combined Measurement of the Higgs Boson Mass in *pp* Collisions at $\sqrt{s} = 7$ and 8 TeV with the ATLAS and CMS Experiments," *Phys. Rev. Lett.* **114** (2015) 191803, arXiv:1503.07589 [hep-ex].

[19] **ATLAS, CMS** Collaboration, G. Aad *et al.*, "Measurements of the Higgs boson production and decay rates and constraints on its couplings from a combined ATLAS and CMS analysis of the LHC pp collision data at $\sqrt{s} = 7$ and 8 TeV," *JHEP* **08** (2016) 045, arXiv:1606.02266 [hep-ex].

[20] **Planck** Collaboration, N. Aghanim *et al.*, "Planck 2018 results. VI. Cosmological parameters," arXiv:1807.06209 [astro-ph.CO].

[21] M. W. Goodman and E. Witten, "Detectability of certain dark-matter candidates," *Phys. Rev. D* **31** (Jun, 1985) 3059–3063. https://link.aps.org/doi/10.1103/PhysRevD.31.3059.

[22] A. Sakharov, "Violation of CP Invariance, C asymmetry, and baryon asymmetry of the universe," *Sov. Phys. Usp.* **34** no. 5, (1991) 392–393.

[23] Z. Fodor, J. Hein, K. Jansen, A. Jaster, and I. Montvay, "Simulating the electroweak phase transition in the SU(2) Higgs model," *Nucl. Phys. B* **439** (1995) 147–186, arXiv:hep-lat/9409017.

[24] M. Shaposhnikov, "Baryon asymmetry of the universe in standard electroweak theory," *Nuclear Physics B* **287** (1987) 757 – 775. http://www.sciencedirect.com/science/article/pii/0550321387901271.

[25] K. Kajantie, M. Laine, K. Rummukainen, and M. E. Shaposhnikov, "The Electroweak phase transition: A Nonperturbative analysis," *Nucl. Phys. B* **466** (1996) 189–258, arXiv:hep-lat/9510020.

[26] **Particle Data Group** Collaboration, e. a. Tanabashi, "Review of particle physics," *Phys. Rev. D* **98** (Aug, 2018) 030001. https://link.aps.org/doi/10.1103/PhysRevD.98.030001.

[27] C.-Y. Chen, M. Freid, and M. Sher, "Next-to-minimal two Higgs doublet model," *Phys. Rev. D* **89** no. 7, (2014) 075009, arXiv:1312.3949 [hep-ph].

[28] M. Fukugita and T. Yanagida, "Barygenesis without grand unification," *Physics Letters B* **174** no. 1, (1986) 45 – 47. http://www.sciencedirect.com/science/article/pii/0370269386911263.

[29] W. Buchmuller, P. Di Bari, and M. Plumacher, "Leptogenesis for pedestrians," *Annals Phys.* **315** (2005) 305–351, arXiv:hep-ph/0401240.

[30] M. Trodden, "Electroweak baryogenesis," *Rev. Mod. Phys.* **71** (1999) 1463–1500, arXiv:hep-ph/9803479.

[31] D. E. Morrissey and M. J. Ramsey-Musolf, "Electroweak baryogenesis," *New J. Phys.* **14** (2012) 125003, arXiv:1206.2942 [hep-ph].

[32] M. Joyce, T. Prokopec, and N. Turok, "Nonlocal electroweak baryogenesis. Part 1: Thin wall regime," *Phys. Rev. D* **53** (1996) 2930–2957, arXiv:hep-ph/9410281.

[33] A. Riotto and M. Trodden, "Recent progress in baryogenesis," *Ann. Rev. Nucl. Part. Sci.* **49** (1999) 35–75, arXiv:hep-ph/9901362.

[34] A. Riotto, "Theories of baryogenesis," in *ICTP Summer School in High-Energy Physics and Cosmology*, pp. 326–436. 7, 1998. arXiv:hep-ph/9807454.

[35] L. Fromme and S. J. Huber, "Top transport in electroweak baryogenesis," *JHEP* **03** (2007) 049, arXiv:hep-ph/0604159.

[36] L. Fromme, S. J. Huber, and M. Seniuch, "Baryogenesis in the two-Higgs doublet model," *JHEP* **11** (2006) 038, arXiv:hep-ph/0605242.

[37] K. Kainulainen, T. Prokopec, M. G. Schmidt, and S. Weinstock, "First principle derivation of semiclassical force for electroweak baryogenesis," *JHEP* **06** (2001) 031, arXiv:hep-ph/0105295.

[38] T. Prokopec, M. G. Schmidt, and S. Weinstock, "Transport equations for chiral fermions to order h bar and electroweak baryogenesis. Part 1," *Annals Phys.* **314** (2004) 208–265, arXiv:hep-ph/0312110.

[39] T. Prokopec, M. G. Schmidt, and S. Weinstock, "Transport equations for chiral fermions to order h-bar and electroweak baryogenesis. Part II," *Annals Phys.* **314** (2004) 267–320, arXiv:hep-ph/0406140.

[40] Y. Ne'eman, "Derivation of strong interactions from a gauge invariance," *Nucl. Phys.* **26** (1961) 222–229.

[41] G. Zweig, *An SU(3) model for strong interaction symmetry and its breaking. Version 2*, pp. 22–101. 2, 1964.

[42] M. Gell-Mann, "A Schematic Model of Baryons and Mesons," *Phys. Lett.* **8** (1964) 214–215.

[43] S. L. Glashow, "The renormalizability of vector meson interactions," *Nucl. Phys.* **10** (1959) 107–117.

[44] S. Glashow, "Partial Symmetries of Weak Interactions," *Nucl. Phys.* **22** (1961) 579–588.

[45] Y. Nambu, "Quasi-particles and gauge invariance in the theory of superconductivity," *Phys. Rev.* **117** (Feb, 1960) 648–663. https://link.aps.org/doi/10.1103/PhysRev.117.648.

[46] J. Goldstone, "Field Theories with Superconductor Solutions," *Nuovo Cim.* **19** (1961) 154–164.

[47] J. Goldstone, A. Salam, and S. Weinberg, "Broken symmetries," *Phys. Rev.* **127** (Aug, 1962) 965–970. https://link.aps.org/doi/10.1103/PhysRev.127.965.

[48] F. Zwicky, "Die Rotverschiebung von extragalaktischen Nebeln," *Helv. Phys. Acta* **6** (1933) 110–127.

[49] F. Zwicky, "On the Masses of Nebulae and of Clusters of Nebulae," *Astrophys. J.* **86** (1937) 217–246.

[50] B. Famaey and J. Binney, "Modified Newtonian dynamics in the Milky Way," *Mon. Not. Roy. Astron. Soc.* **363** (2005) 603–608, arXiv:astro-ph/0506723.

[51] B. Famaey and S. McGaugh, "Modified Newtonian Dynamics (MOND): Observational Phenomenology and Relativistic Extensions," *Living Rev. Rel.* **15** (2012) 10, arXiv:1112.3960 [astro-ph.CO].

[52] S. Nojiri, S. Odintsov, and V. Oikonomou, "Modified Gravity Theories on a Nutshell: Inflation, Bounce and Late-time Evolution," *Phys. Rept.* **692** (2017) 1–104, arXiv:1705.11098 [gr-qc].

[53] M. Gavela, P. Hernandez, J. Orloff, and O. Pene, "Standard model CP violation and baryon asymmetry," *Mod. Phys. Lett. A* **9** (1994) 795–810, arXiv:hep-ph/9312215.

[54] J. F. Gunion, H. E. Haber, G. L. Kane, and S. Dawson, *The Higgs Hunter's Guide*, vol. 80. 2000.

[55] F. Jegerlehner, M. Y. Kalmykov, and B. A. Kniehl, "Self-consistence of the Standard Model via the renormalization group analysis," *J. Phys. Conf. Ser.* **608** no. 1, (2015) 012074, arXiv:1412.4215 [hep-ph].

[56] D. Buttazzo, G. Degrassi, P. P. Giardino, G. F. Giudice, F. Sala, A. Salvio, and A. Strumia, "Investigating the near-criticality of the Higgs boson," *JHEP* **12** (2013) 089, arXiv:1307.3536 [hep-ph].

[57] G. Degrassi, S. Di Vita, J. Elias-Miro, J. R. Espinosa, G. F. Giudice, G. Isidori, and A. Strumia, "Higgs mass and vacuum stability in the Standard Model at NNLO," *JHEP* **08** (2012) 098, arXiv:1205.6497 [hep-ph].

[58] I. P. Ivanov, M. Köpke, and M. Mühlleitner, "Algorithmic Boundedness-From-Below Conditions for Generic Scalar Potentials," *Eur. Phys. J. C* **78** no. 5, (2018) 413, arXiv:1802.07976 [hep-ph].

[59] J. Haller, A. Hoecker, R. Kogler, K. Mönig, T. Peiffer, and J. Stelzer, "Update of the global electroweak fit and constraints on two-Higgs-doublet models," *Eur. Phys. J. C* **78** no. 8, (2018) 675, arXiv:1803.01853 [hep-ph].

[60] M. Mühlleitner, M. O. Sampaio, R. Santos, and J. Wittbrodt, "ScannerS: Parameter Scans in Extended Scalar Sectors," arXiv:2007.02985 [hep-ph].

[61] R. Coimbra, M. O. Sampaio, and R. Santos, "ScannerS: Constraining the phase diagram of a complex scalar singlet at the LHC," *Eur. Phys. J. C* **73** (2013) 2428, arXiv:1301.2599 [hep-ph].

[62] **ACME** Collaboration, V. Andreev *et al.*, "Improved limit on the electric dipole moment of the electron," *Nature* **562** no. 7727, (2018) 355–360.

[63] P. Bechtle, O. Brein, S. Heinemeyer, G. Weiglein, and K. E. Williams, "HiggsBounds: Confronting Arbitrary Higgs Sectors with Exclusion Bounds from LEP and the Tevatron," *Comput. Phys. Commun.* **181** (2010) 138–167, arXiv:0811.4169 [hep-ph].

[64] P. Bechtle, O. Brein, S. Heinemeyer, G. Weiglein, and K. E. Williams, "HiggsBounds 2.0.0: Confronting Neutral and Charged Higgs Sector Predictions with Exclusion Bounds from LEP and the Tevatron," *Comput. Phys. Commun.* **182** (2011) 2605–2631, arXiv:1102.1898 [hep-ph].

[65] P. Bechtle, O. Brein, S. Heinemeyer, O. Stal, T. Stefaniak, G. Weiglein, and K. Williams, "Recent Developments in HiggsBounds and a Preview of HiggsSignals," *PoS* **CHARGED2012** (2012) 024, arXiv:1301.2345 [hep-ph].

[66] P. Bechtle, O. Brein, S. Heinemeyer, O. Stål, T. Stefaniak, G. Weiglein, and K. E. Williams, "HiggsBounds – 4: Improved Tests of Extended Higgs Sectors against Exclusion Bounds from LEP, the Tevatron and the LHC," *Eur. Phys. J. C* **74** no. 3, (2014) 2693, arXiv:1311.0055 [hep-ph].

[67] P. Bechtle, S. Heinemeyer, O. Stal, T. Stefaniak, and G. Weiglein, "Applying Exclusion Likelihoods from LHC Searches to Extended Higgs Sectors," *Eur. Phys. J. C* **75** no. 9, (2015) 421, arXiv:1507.06706 [hep-ph].

[68] P. Bechtle, S. Heinemeyer, O. Stål, T. Stefaniak, and G. Weiglein, "*HiggsSignals*: Confronting arbitrary Higgs sectors with measurements at the Tevatron and the LHC," *Eur. Phys. J. C* **74** no. 2, (2014) 2711, arXiv:1305.1933 [hep-ph].

[69] P. Bechtle, S. Heinemeyer, O. Stål, T. Stefaniak, and G. Weiglein, "Probing the Standard Model with Higgs signal rates from the Tevatron, the LHC and a future ILC," *JHEP* **11** (2014) 039, arXiv:1403.1582 [hep-ph].

[70] O. Stål and T. Stefaniak, "Constraining extended Higgs sectors with HiggsSignals," *PoS* **EPS-HEP2013** (2013) 314, arXiv:1310.4039 [hep-ph].

[71] D. Fontes, M. Mühlleitner, J. C. Romão, R. Santos, J. P. Silva, and J. Wittbrodt, "The C2HDM revisited," *JHEP* **02** (2018) 073, arXiv:1711.09419 [hep-ph].

[72] P. Basler, M. Mühlleitner, and J. Wittbrodt, "The CP-Violating 2HDM in Light of a Strong First Order Electroweak Phase Transition and Implications for Higgs Pair Production," *JHEP* **03** (2018) 061, arXiv:1711.04097 [hep-ph].

[73] R. Santos and A. Barroso, "On the renormalization of two Higgs doublet models," *Phys. Rev. D* **56** (1997) 5366–5385, arXiv:hep-ph/9701257.

[74] I. P. Ivanov, "Minkowski space structure of the Higgs potential in 2HDM. II. Minima, symmetries, and topology," *Phys. Rev. D* **77** (2008) 015017, arXiv:0710.3490 [hep-ph].

[75] A. Barroso, P. Ferreira, and R. Santos, "Neutral minima in two-Higgs doublet models," *Phys. Lett. B* **652** (2007) 181–193, arXiv:hep-ph/0702098.

[76] P. Ferreira, R. Santos, and A. Barroso, "Stability of the tree-level vacuum in two Higgs doublet models against charge or CP spontaneous violation," *Phys. Lett. B* **603** (2004) 219–229, arXiv:hep-ph/0406231. [Erratum: Phys.Lett.B 629, 114–114 (2005)].

[77] G. Branco, P. Ferreira, L. Lavoura, M. Rebelo, M. Sher, and J. P. Silva, "Theory and phenomenology of two-Higgs-doublet models," *Phys. Rept.* **516** (2012) 1–102, arXiv:1106.0034 [hep-ph].

[78] T. D. Lee, "A theory of spontaneous t violation," *Phys. Rev. D* **8** (Aug, 1973) 1226–1239. https://link.aps.org/doi/10.1103/PhysRevD.8.1226.

[79] I. F. Ginzburg, M. Krawczyk, and P. Osland, "Two Higgs doublet models with CP violation," in *International Workshop on Linear Colliders (LCWS 2002)*, pp. 703–706. 11, 2002. arXiv:hep-ph/0211371.

[80] C. Gross, O. Lebedev, and T. Toma, "Cancellation Mechanism for Dark-Matter–Nucleon Interaction," *Phys. Rev. Lett.* **119** no. 19, (2017) 191801, arXiv:1708.02253 [hep-ph].

[81] M. Muhlleitner, M. O. P. Sampaio, R. Santos, and J. Wittbrodt, "The N2HDM under Theoretical and Experimental Scrutiny," *JHEP* **03** (2017) 094, arXiv:1612.01309 [hep-ph].

[82] P. Ferreira, M. Mühlleitner, R. Santos, G. Weiglein, and J. Wittbrodt, "Vacuum Instabilities in the N2HDM," *JHEP* **09** (2019) 006, arXiv:1905.10234 [hep-ph].

[83] A. Denner and S. Dittmaier, "Electroweak Radiative Corrections for Collider Physics," *Phys. Rept.* **864** (2020) 1–163, arXiv:1912.06823 [hep-ph].

[84] S. Kanemura, Y. Okada, E. Senaha, and C.-P. Yuan, "Higgs coupling constants as a probe of new physics," *Phys. Rev. D* **70** (2004) 115002, arXiv:hep-ph/0408364.

[85] M. Krause, R. Lorenz, M. Muhlleitner, R. Santos, and H. Ziesche, "Gauge-independent Renormalization of the 2-Higgs-Doublet Model," *JHEP* **09** (2016) 143, arXiv:1605.04853 [hep-ph].

[86] M. Krause, M. Muhlleitner, R. Santos, and H. Ziesche, "Higgs-to-Higgs boson decays in a 2HDM at next-to-leading order," *Phys. Rev. D* **95** no. 7, (2017) 075019, arXiv:1609.04185 [hep-ph].

[87] M. Krause, D. Lopez-Val, M. Muhlleitner, and R. Santos, "Gauge-independent Renormalization of the N2HDM," *JHEP* **12** (2017) 077, arXiv:1708.01578 [hep-ph].

[88] M. Krause and M. Mühlleitner, "Impact of Electroweak Corrections on Neutral Higgs Boson Decays in Extended Higgs Sectors," *JHEP* **04** (2020) 083, arXiv:1912.03948 [hep-ph].

[89] A. Denner, S. Dittmaier, and J.-N. Lang, "Renormalization schemes for mixing angles in extended Higgs sectors," in *14th International Symposium on Radiative Corrections: Application of Quantum Field Theory to Phenomenology.* 12, 2019. arXiv:1912.02425 [hep-ph].

[90] A. Denner, S. Dittmaier, and J.-N. Lang, "Renormalization of mixing angles," *JHEP* **11** (2018) 104, arXiv:1808.03466 [hep-ph].

[91] A. Denner, "Techniques for calculation of electroweak radiative corrections at the one loop level and results for W physics at LEP-200," *Fortsch. Phys.* **41** (1993) 307–420, arXiv:0709.1075 [hep-ph].

[92] M. E. Peskin and D. V. Schroeder, *An Introduction to quantum field theory.* Addison-Wesley, Reading, USA, 1995.

[93] J. Fleischer and F. Jegerlehner, "Radiative corrections to higgs-boson decays in the weinberg-salam model," *Phys. Rev. D* **23** (May, 1981) 2001–2026. https://link.aps.org/doi/10.1103/PhysRevD.23.2001.

[94] F. Staub, "SARAH 4 : A tool for (not only SUSY) model builders," *Comput. Phys. Commun.* **185** (2014) 1773–1790, arXiv:1309.7223 [hep-ph].

[95] F. Staub, "SARAH 3.2: Dirac Gauginos, UFO output, and more," *Comput. Phys. Commun.* **184** (2013) 1792–1809, arXiv:1207.0906 [hep-ph].

[96] F. Staub, "Automatic Calculation of supersymmetric Renormalization Group Equations and Self Energies," *Comput. Phys. Commun.* **182** (2011) 808–833, arXiv:1002.0840 [hep-ph].

[97] F. Staub, "From Superpotential to Model Files for FeynArts and CalcHep/CompHep," *Comput. Phys. Commun.* **181** (2010) 1077–1086, arXiv:0909.2863 [hep-ph].

[98] S. Profumo, L. Giani, and O. F. Piattella, "An Introduction to Particle Dark Matter," *Universe* **5** no. 10, (2019) 213, arXiv:1910.05610 [hep-ph].

[99] M. Bauer and T. Plehn, *Yet Another Introduction to Dark Matter: The Particle Physics Approach*, vol. 959 of *Lecture Notes in Physics*. Springer, 2019. arXiv:1705.01987 [hep-ph].

[100] P. D. Group, "Review of Particle Physics," *Progress of Theoretical and Experimental Physics* **2020** no. 8, (08, 2020) , https://academic.oup.com/ptep/article-pdf/2020/8/083C01/33653179/ptaa104.pdf. https://doi.org/10.1093/ptep/ptaa104. 083C01.

[101] A. De Rujula, S. Glashow, and U. Sarid, "CHARGED DARK MATTER," *Nucl. Phys. B* **333** (1990) 173–194.

[102] J. M. Cline, Z. Liu, and W. Xue, "Millicharged Atomic Dark Matter," *Phys. Rev. D* **85** (2012) 101302, arXiv:1201.4858 [hep-ph].

[103] **Planck** Collaboration, P. Ade *et al.*, "Planck 2015 results. XIII. Cosmological parameters," *Astron. Astrophys.* **594** (2016) A13, arXiv:1502.01589 [astro-ph.CO].

[104] N. W. Evans, C. A. O'Hare, and C. McCabe, "Refinement of the standard halo model for dark matter searches in light of the Gaia Sausage," *Phys. Rev. D* **99** no. 2, (2019) 023012, arXiv:1810.11468 [astro-ph.GA].

[105] G. Jungman, M. Kamionkowski, and K. Griest, "Supersymmetric dark matter," *Phys. Rept.* **267** (1996) 195–373, arXiv:hep-ph/9506380.

[106] J. Lewin and P. Smith, "Review of mathematics, numerical factors, and corrections for dark matter experiments based on elastic nuclear recoil," *Astroparticle Physics* **6** no. 1, (1996) 87 – 112. http://www.sciencedirect.com/science/article/pii/S0927650596000473.

[107] P. J. Fox, J. Liu, and N. Weiner, "Integrating Out Astrophysical Uncertainties," *Phys. Rev. D* **83** (2011) 103514, arXiv:1011.1915 [hep-ph].

[108] A. Fitzpatrick, W. Haxton, E. Katz, N. Lubbers, and Y. Xu, "The Effective Field Theory of Dark Matter Direct Detection," *JCAP* **02** (2013) 004, arXiv:1203.3542 [hep-ph].

[109] M. Hoferichter, P. Klos, J. Menéndez, and A. Schwenk, "Analysis strategies for general spin-independent WIMP-nucleus scattering," *Phys. Rev. D* **94** no. 6, (2016) 063505, arXiv:1605.08043 [hep-ph].

[110] D. Gazda, R. Catena, and C. Forssén, "Ab initio nuclear response functions for dark matter searches," *Phys. Rev. D* **95** no. 10, (2017) 103011, arXiv:1612.09165 [hep-ph].

[111] M. Hoferichter, P. Klos, J. Menéndez, and A. Schwenk, "Nuclear structure factors for general spin-independent WIMP-nucleus scattering," *Phys. Rev. D* **99** no. 5, (2019) 055031, arXiv:1812.05617 [hep-ph].

[112] E. Epelbaum, H.-W. Hammer, and U.-G. Meissner, "Modern Theory of Nuclear Forces," *Rev. Mod. Phys.* **81** (2009) 1773–1825, arXiv:0811.1338 [nucl-th].

[113] R. Machleidt and D. Entem, "Chiral effective field theory and nuclear forces," *Phys. Rept.* **503** (2011) 1–75, arXiv:1105.2919 [nucl-th].

[114] H.-W. Hammer, A. Nogga, and A. Schwenk, "Three-body forces: From cold atoms to nuclei," *Rev. Mod. Phys.* **85** (2013) 197, arXiv:1210.4273 [nucl-th].

[115] J. Hisano, K. Ishiwata, and N. Nagata, "Gluon contribution to the dark matter direct detection," *Phys. Rev. D* **82** (2010) 115007, arXiv:1007.2601 [hep-ph].

[116] J. Hisano, R. Nagai, and N. Nagata, "Effective Theories for Dark Matter Nucleon Scattering," *JHEP* **05** (2015) 037, arXiv:1502.02244 [hep-ph].

[117] G. Bélanger, F. Boudjema, A. Goudelis, A. Pukhov, and B. Zaldivar, "micrOMEGAs5.0 : Freeze-in," *Comput. Phys. Commun.* **231** (2018) 173–186, arXiv:1801.03509 [hep-ph].

[118] J. Pumplin, D. Stump, J. Huston, H. Lai, P. M. Nadolsky, and W. Tung, "New generation of parton distributions with uncertainties from global QCD analysis," *JHEP* **07** (2002) 012, arXiv:hep-ph/0201195.

[119] K. Ishiwata and T. Toma, "Probing pseudo Nambu-Goldstone boson dark matter at loop level," *JHEP* **12** (2018) 089, arXiv:1810.08139 [hep-ph].

[120] J. Hisano, K. Ishiwata, and N. Nagata, "QCD Effects on Direct Detection of Wino Dark Matter," *JHEP* **06** (2015) 097, arXiv:1504.00915 [hep-ph].

[121] J. Hisano, K. Ishiwata, N. Nagata, and M. Yamanaka, "Direct Detection of Vector Dark Matter," *Prog. Theor. Phys.* **126** (2011) 435–456, arXiv:1012.5455 [hep-ph].

[122] M. A. Shifman, A. Vainshtein, and V. I. Zakharov, "Remarks on Higgs Boson Interactions with Nucleons," *Phys. Lett. B* **78** (1978) 443–446.

[123] J. Hisano, "Effective theory approach to direct detection of dark matter," *Les Houches Lect. Notes* **108** (2020) , arXiv:1712.02947 [hep-ph].

[124] B. A. Kniehl and M. Spira, "Low-energy theorems in Higgs physics," *Z. Phys. C* **69** (1995) 77–88, arXiv:hep-ph/9505225.

[125] F. Ertas and F. Kahlhoefer, "Loop-induced direct detection signatures from CP-violating scalar mediators," *JHEP* **06** (2019) 052, arXiv:1902.11070 [hep-ph].

[126] D. Azevedo, M. Duch, B. Grzadkowski, D. Huang, M. Iglicki, and R. Santos, "One-loop contribution to dark-matter-nucleon scattering in the pseudo-scalar dark matter model," *JHEP* **01** (2019) 138, arXiv:1810.06105 [hep-ph].

[127] G. Devaraj and R. G. Stuart, "Reduction of one loop tensor form-factors to scalar integrals: A General scheme," *Nucl. Phys. B* **519** (1998) 483–513, arXiv:hep-ph/9704308.

[128] R. G. Stuart, "Algebraic Reduction of One Loop Feynman Diagrams to Scalar Integrals," *Comput. Phys. Commun.* **48** (1988) 367–389.

[129] K. Park, "Reduction of one-loop n-point integrals," arXiv:0912.0310 [hep-ph].

[130] A. Denner and S. Dittmaier, "Reduction schemes for one-loop tensor integrals," *Nucl. Phys. B* **734** (2006) 62–115, arXiv:hep-ph/0509141.

[131] J. M. Campbell, E. Glover, and D. Miller, "One loop tensor integrals in dimensional regularization," *Nucl. Phys. B* **498** (1997) 397–442, arXiv:hep-ph/9612413.

[132] T. Binoth, J. Guillet, G. Heinrich, E. Pilon, and C. Schubert, "An Algebraic/numerical formalism for one-loop multi-leg amplitudes," *JHEP* **10** (2005) 015, arXiv:hep-ph/0504267.

[133] R. Pittau, "A Simple method for multileg loop calculations," *Comput. Phys. Commun.* **104** (1997) 23–36, arXiv:hep-ph/9607309.

[134] T. Hahn, "Generating Feynman diagrams and amplitudes with FeynArts 3," *Comput. Phys. Commun.* **140** (2001) 418–431, arXiv:hep-ph/0012260.

[135] V. Shtabovenko, R. Mertig, and F. Orellana, "New Developments in FeynCalc 9.0," *Comput. Phys. Commun.* **207** (2016) 432–444, arXiv:1601.01167 [hep-ph].

[136] T. Abe, M. Fujiwara, and J. Hisano, "Loop corrections to dark matter direct detection in a pseudoscalar mediator dark matter model," *JHEP* **02** (2019) 028, arXiv:1810.01039 [hep-ph].

[137] **LHC Higgs Cross Section Working Group** Collaboration, S. Dittmaier *et al.*, "Handbook of LHC Higgs Cross Sections: 1. Inclusive Observables," arXiv:1101.0593 [hep-ph].

[138] G. Belanger, F. Boudjema, A. Pukhov, and A. Semenov, "micrOMEGAs_3: A program for calculating dark matter observables," *Comput. Phys. Commun.* **185** (2014) 960–985, arXiv:1305.0237 [hep-ph].

[139] F. Staub, "Exploring new models in all detail with SARAH," *Adv. High Energy Phys.* **2015** (2015) 840780, arXiv:1503.04200 [hep-ph].

[140] A. Denner, S. Dittmaier, and L. Hofer, "Collier: a fortran-based Complex One-Loop LIbrary in Extended Regularizations," *Comput. Phys. Commun.* **212** (2017) 220–238, arXiv:1604.06792 [hep-ph].

[141] A. Drukier and L. Stodolsky, "Principles and Applications of a Neutral Current Detector for Neutrino Physics and Astronomy,".

[142] **COHERENT** Collaboration, D. Akimov *et al.*, "Observation of Coherent Elastic Neutrino-Nucleus Scattering," *Science* **357** no. 6356, (2017) 1123–1126, arXiv:1708.01294 [nucl-ex].

[143] **XENON** Collaboration, E. Aprile *et al.*, "Projected WIMP Sensitivity of the XENONnT Dark Matter Experiment," arXiv:2007.08796 [physics.ins-det].

[144] T. Hambye, "Hidden vector dark matter," *JHEP* **01** (2009) 028, arXiv:0811.0172 [hep-ph].

[145] O. Lebedev, H. M. Lee, and Y. Mambrini, "Vector Higgs-portal dark matter and the invisible Higgs," *Phys. Lett. B* **707** (2012) 570–576, arXiv:1111.4482 [hep-ph].

[146] Y. Farzan and A. R. Akbarieh, "VDM: A model for Vector Dark Matter," *JCAP* **10** (2012) 026, arXiv:1207.4272 [hep-ph].

[147] S. Baek, P. Ko, W.-I. Park, and E. Senaha, "Higgs Portal Vector Dark Matter : Revisited," *JHEP* **05** (2013) 036, arXiv:1212.2131 [hep-ph].

[148] S. Baek, P. Ko, and W.-I. Park, "Invisible Higgs Decay Width vs. Dark Matter Direct Detection Cross Section in Higgs Portal Dark Matter Models," *Phys. Rev. D* **90** no. 5, (2014) 055014, arXiv:1405.3530 [hep-ph].

[149] M. Duch, B. Grzadkowski, and M. McGarrie, "A stable Higgs portal with vector dark matter," *JHEP* **09** (2015) 162, arXiv:1506.08805 [hep-ph].

[150] D. Azevedo, M. Duch, B. Grzadkowski, D. Huang, M. Iglicki, and R. Santos, "Testing scalar versus vector dark matter," *Phys. Rev. D* **99** no. 1, (2019) 015017, arXiv:1808.01598 [hep-ph].

[151] R. Costa, M. Mühlleitner, M. O. P. Sampaio, and R. Santos, "Singlet Extensions of the Standard Model at LHC Run 2: Benchmarks and Comparison with the NMSSM," *JHEP* **06** (2016) 034, arXiv:1512.05355 [hep-ph].

[152] A. Denner, E. Kraus, and M. Roth, "Physical renormalization condition for the quark mixing matrix," *Phys. Rev. D* **70** (2004) 033002, arXiv:hep-ph/0402130.

[153] S. Weinberg, *The quantum theory of fields. Vol. 2: Modern applications*. Cambridge University Press, 8, 2013.

[154] E. J. Weinberg, *Radiative corrections as the origin of spontaneous symmetry breaking*. PhD thesis, Harvard U., 1973. arXiv:hep-th/0507214.

[155] T. Matsubara, "A New approach to quantum statistical mechanics," *Prog. Theor. Phys.* **14** (1955) 351–378.

[156] A. K. Das, *Finite Temperature Field Theory*. World Scientific, New York, 1997.

[157] R. Kubo, "Statistical mechanical theory of irreversible processes. 1. General theory and simple applications in magnetic and conduction problems," *J. Phys. Soc. Jap.* **12** (1957) 570–586.

[158] P. C. Martin and J. S. Schwinger, "Theory of many particle systems. 1.," *Phys. Rev.* **115** (1959) 1342–1373.

[159] P. M. Bakshi and K. T. Mahanthappa, "Expectation value formalism in quantum field theory. 1.," *J. Math. Phys.* **4** (1963) 1–11.

[160] L. Keldysh, "Diagram technique for nonequilibrium processes," *Zh. Eksp. Teor. Fiz.* **47** (1964) 1515–1527.

[161] K.-c. Chou, Z.-b. Su, B.-l. Hao, and L. Yu, "Equilibrium and Nonequilibrium Formalisms Made Unified," *Phys. Rept.* **118** (1985) 1–131.

[162] S. R. Coleman and E. J. Weinberg, "Radiative Corrections as the Origin of Spontaneous Symmetry Breaking," *Phys. Rev. D* **7** (1973) 1888–1910.

[163] M. Carrington, "The Effective potential at finite temperature in the Standard Model," *Phys. Rev. D* **45** (1992) 2933–2944.

[164] P. Arnold, "Phase transition temperatures at next-to-leading order," *Phys. Rev. D* **46** (Sep, 1992) 2628–2635. https://link.aps.org/doi/10.1103/PhysRevD.46.2628.

[165] R. R. Parwani, "Resummation in a hot scalar field theory," *Phys. Rev. D* **45** (1992) 4695, arXiv:hep-ph/9204216. [Erratum: Phys.Rev.D 48, 5965 (1993)].

[166] P. B. Arnold and O. Espinosa, "The Effective potential and first order phase transitions: Beyond leading-order," *Phys. Rev. D* **47** (1993) 3546, arXiv:hep-ph/9212235. [Erratum: Phys.Rev.D 50, 6662 (1994)].

[167] J. E. Camargo-Molina, A. P. Morais, R. Pasechnik, M. O. P. Sampaio, and J. Wessén, "All one-loop scalar vertices in the effective potential approach," *JHEP* **08** (2016) 073, arXiv:1606.07069 [hep-ph].

[168] P. Basler and M. Mühlleitner, "BSMPT (Beyond the Standard Model Phase Transitions): A tool for the electroweak phase transition in extended Higgs sectors," *Comput. Phys. Commun.* **237** (2019) 62–85, arXiv:1803.02846 [hep-ph].

[169] P. Basler, M. Krause, M. Muhlleitner, J. Wittbrodt, and A. Wlotzka, "Strong First Order Electroweak Phase Transition in the CP-Conserving 2HDM Revisited," *JHEP* **02** (2017) 121, arXiv:1612.04086 [hep-ph].

[170] C. Caprini *et al.*, "Detecting gravitational waves from cosmological phase transitions with LISA: an update," *JCAP* **03** (2020) 024, arXiv:1910.13125 [astro-ph.CO].

[171] C. Caprini *et al.*, "Science with the space-based interferometer eLISA. II: Gravitational waves from cosmological phase transitions," *JCAP* **04** (2016) 001, arXiv:1512.06239 [astro-ph.CO].

[172] C. Caprini, R. Durrer, and G. Servant, "The stochastic gravitational wave background from turbulence and magnetic fields generated by a first-order phase transition," *JCAP* **12** (2009) 024, arXiv:0909.0622 [astro-ph.CO].

[173] M. Dine, R. G. Leigh, P. Y. Huet, A. D. Linde, and D. A. Linde, "Towards the theory of the electroweak phase transition," *Phys. Rev. D* **46** (1992) 550–571, arXiv:hep-ph/9203203.

[174] M. Quiros, "Finite temperature field theory and phase transitions," in *ICTP Summer School in High-Energy Physics and Cosmology*, pp. 187–259. 1, 1999. arXiv:hep-ph/9901312.

[175] G. W. Anderson and L. J. Hall, "Electroweak phase transition and baryogenesis," *Phys. Rev. D* **45** (Apr, 1992) 2685–2698. https://link.aps.org/doi/10.1103/PhysRevD.45.2685.

[176] S. Profumo, M. J. Ramsey-Musolf, and G. Shaughnessy, "Singlet Higgs phenomenology and the electroweak phase transition," *JHEP* **08** (2007) 010, arXiv:0705.2425 [hep-ph].

[177] M. Misiak and M. Steinhauser, "Weak radiative decays of the B meson and bounds on $M_{H^\pm}$ in the Two-Higgs-Doublet Model," *Eur. Phys. J. C* **77** no. 3, (2017) 201, arXiv:1702.04571 [hep-ph].

[178] P. Athron, C. Balázs, A. Fowlie, and Y. Zhang, "PhaseTracer: tracing cosmological phases and calculating transition properties," *Eur. Phys. J. C* **80** no. 6, (2020) 567, arXiv:2003.02859 [hep-ph].

[179] M. Carena, G. Nardini, M. Quiros, and C. Wagner, "The Baryogenesis Window in the MSSM," *Nucl. Phys. B* **812** (2009) 243–263, arXiv:0809.3760 [hep-ph].

[180] G. Dorsch, S. Huber, K. Mimasu, and J. No, "The Higgs Vacuum Uplifted: Revisiting the Electroweak Phase Transition with a Second Higgs Doublet," *JHEP* **12** (2017) 086, arXiv:1705.09186 [hep-ph].

[181] S. Kanemura, S. Kiyoura, Y. Okada, E. Senaha, and C. Yuan, "New physics effect on the Higgs selfcoupling," *Phys. Lett. B* **558** (2003) 157–164, arXiv:hep-ph/0211308.

[182] V. Rubakov and M. Shaposhnikov, "Electroweak baryon number nonconservation in the early universe and in high-energy collisions," *Usp. Fiz. Nauk* **166** (1996) 493–537, arXiv:hep-ph/9603208.

[183] J. M. Cline, "Baryogenesis," in *Les Houches Summer School - Session 86: Particle Physics and Cosmology: The Fabric of Spacetime*. 9, 2006. arXiv:hep-ph/0609145.

[184] A. G. Cohen, D. Kaplan, and A. Nelson, "Progress in electroweak baryogenesis," *Ann. Rev. Nucl. Part. Sci.* **43** (1993) 27–70, arXiv:hep-ph/9302210.

[185] F. Stecker, "On the Nature of the Baryon Asymmetry," *Nucl. Phys. B* **252** (1985) 25–36.

[186] A. De Rujula, "Avatars of a matter - antimatter universe," in *32nd Rencontres de Moriond: High-Energy Phenomena in Astrophysics*, pp. 363–378. 1997. arXiv:astro-ph/9705045.

[187] S. L. Adler, "Axial-vector vertex in spinor electrodynamics," *Phys. Rev.* **177** (Jan, 1969) 2426–2438. https://link.aps.org/doi/10.1103/PhysRev.177.2426.

[188] G. 't Hooft, "Symmetry breaking through bell-jackiw anomalies," *Phys. Rev. Lett.* **37** (Jul, 1976) 8–11. https://link.aps.org/doi/10.1103/PhysRevLett.37.8.

[189] V. Kuzmin, V. Rubakov, and M. Shaposhnikov, "On the Anomalous Electroweak Baryon Number Nonconservation in the Early Universe," *Phys. Lett. B* **155** (1985) 36.

[190] F. R. Klinkhamer and N. Manton, "A Saddle Point Solution in the Weinberg-Salam Theory," *Phys. Rev. D* **30** (1984) 2212.

[191] P. B. Arnold, D. Son, and L. G. Yaffe, "The Hot baryon violation rate is O (alpha-w**5 T**4)," *Phys. Rev. D* **55** (1997) 6264–6273, arXiv:hep-ph/9609481.

[192] P. B. Arnold, "Hot B violation, the lattice, and hard thermal loops," *Phys. Rev. D* **55** (1997) 7781–7796, arXiv:hep-ph/9701393.

[193] G. D. Moore, C.-r. Hu, and B. Muller, "Chern-Simons number diffusion with hard thermal loops," *Phys. Rev. D* **58** (1998) 045001, arXiv:hep-ph/9710436.

[194] G. D. Moore, "The Sphaleron rate: Where we stand," in *3rd International Conference on Strong and Electroweak Matter*, pp. 23–33. 12, 1998. arXiv:hep-ph/9902464.

[195] J. M. Cline and K. Kainulainen, "Electroweak baryogenesis at high bubble wall velocities," *Phys. Rev. D* **101** no. 6, (2020) 063525, arXiv:2001.00568 [hep-ph].

[196] T. Konstandin, "Quantum Transport and Electroweak Baryogenesis," *Phys. Usp.* **56** (2013) 747–771, arXiv:1302.6713 [hep-ph].

[197] G. D. Moore and T. Prokopec, "How fast can the wall move? A Study of the electroweak phase transition dynamics," *Phys. Rev. D* **52** (1995) 7182–7204, arXiv:hep-ph/9506475.

[198] G. D. Moore and T. Prokopec, "Bubble wall velocity in a first order electroweak phase transition," *Phys. Rev. Lett.* **75** (1995) 777–780, arXiv:hep-ph/9503296.

[199] J. M. Cline, M. Joyce, and K. Kainulainen, "Supersymmetric electroweak baryogenesis in the WKB approximation," *Phys. Lett. B* **417** (1998) 79–86, arXiv:hep-ph/9708393. [Erratum: Phys.Lett.B 448, 321–321 (1999)].

[200] J. M. Cline, M. Joyce, and K. Kainulainen, "Supersymmetric electroweak baryogenesis," *JHEP* **07** (2000) 018, arXiv:hep-ph/0006119.

[201] C. Lee, V. Cirigliano, and M. J. Ramsey-Musolf, "Resonant relaxation in electroweak baryogenesis," *Phys. Rev. D* **71** (2005) 075010, arXiv:hep-ph/0412354.

[202] J. de Vries, M. Postma, J. van de Vis, and G. White, "Electroweak Baryogenesis and the Standard Model Effective Field Theory," *JHEP* **01** (2018) 089, arXiv:1710.04061 [hep-ph].

[203] J. De Vries, M. Postma, and J. van de Vis, "The role of leptons in electroweak baryogenesis," *JHEP* **04** (2019) 024, arXiv:1811.11104 [hep-ph].

[204] A. Riotto, "Towards a nonequilibrium quantum field theory approach to electroweak baryogenesis," *Phys. Rev. D* **53** (1996) 5834–5841, arXiv:hep-ph/9510271.

[205] A. Riotto, "Supersymmetric electroweak baryogenesis, nonequilibrium field theory and quantum Boltzmann equations," *Nucl. Phys. B* **518** (1998) 339–360, arXiv:hep-ph/9712221.

[206] M. Postma and J. Van De Vis, "Source terms for electroweak baryogenesis in the vev-insertion approximation beyond leading order," *JHEP* **02** (2020) 090, arXiv:1910.11794 [hep-ph].

[207] M. Carena, M. Quiros, M. Seco, and C. Wagner, "Improved Results in Supersymmetric Electroweak Baryogenesis," *Nucl. Phys. B* **650** (2003) 24–42, arXiv:hep-ph/0208043.

[208] T. Konstandin, T. Prokopec, M. G. Schmidt, and M. Seco, "MSSM electroweak baryogenesis and flavor mixing in transport equations," *Nucl. Phys. B* **738** (2006) 1–22, arXiv:hep-ph/0505103.

[209] V. Cirigliano, C. Lee, M. J. Ramsey-Musolf, and S. Tulin, "Flavored Quantum Boltzmann Equations," *Phys. Rev. D* **81** (2010) 103503, arXiv:0912.3523 [hep-ph].

[210] V. Cirigliano, C. Lee, and S. Tulin, "Resonant Flavor Oscillations in Electroweak Baryogenesis," *Phys. Rev. D* **84** (2011) 056006, arXiv:1106.0747 [hep-ph].

[211] Boost, "Boost C++ Libraries." http://www.boost.org/, 2017.

[212] G. D. Moore, "Computing the strong sphaleron rate," *Phys. Lett. B* **412** (1997) 359–370, arXiv:hep-ph/9705248.

[213] G. D. Moore and M. Tassler, "The Sphaleron Rate in SU(N) Gauge Theory," *JHEP* **02** (2011) 105, arXiv:1011.1167 [hep-ph].

[214] P. Ferreira, R. Guedes, M. O. Sampaio, and R. Santos, "Wrong sign and symmetric limits and non-decoupling in 2HDMs," *JHEP* **12** (2014) 067, arXiv:1409.6723 [hep-ph].

[215] **Particle Data Group** Collaboration, K. Olive *et al.*, "Review of Particle Physics," *Chin. Phys. C* **38** (2014) 090001.